

JUNE 2023

AJNR

VOLUME 44 • PP 625-747

AJNR

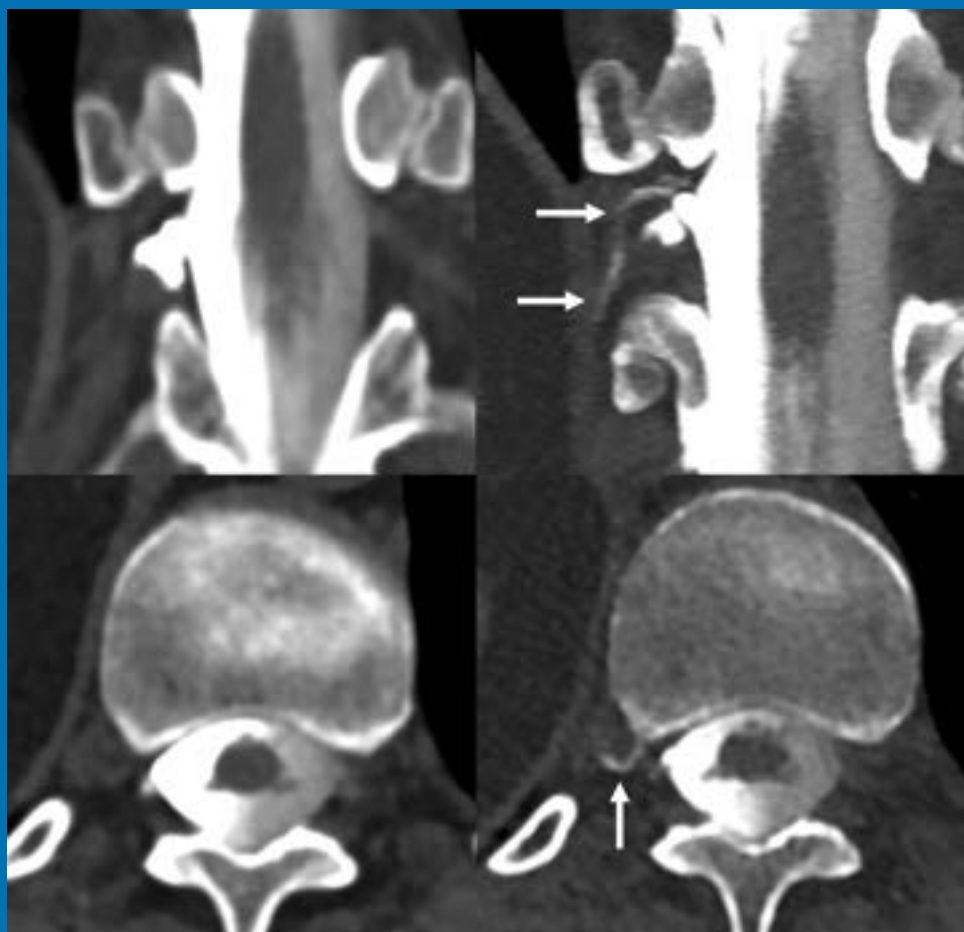
AMERICAN JOURNAL OF NEURORADIOLOGY

JUNE 2023
VOLUME 44
NUMBER 6
WWW.AJNR.ORG

THE JOURNAL OF DIAGNOSTIC AND
INTERVENTIONAL NEURORADIOLOGY

Photon-counting detector CT myelography for CSF-venous fistula
Surgical clipping and endovascular treatment of unruptured intracranial aneurysms
Early-versus-late endovascular stroke treatment
Algorithm for screening patients with MS with new lesion activity

Official Journal ASNR • ASFNR • ASHNR • ASPNR • ASSR



FRED™ X™

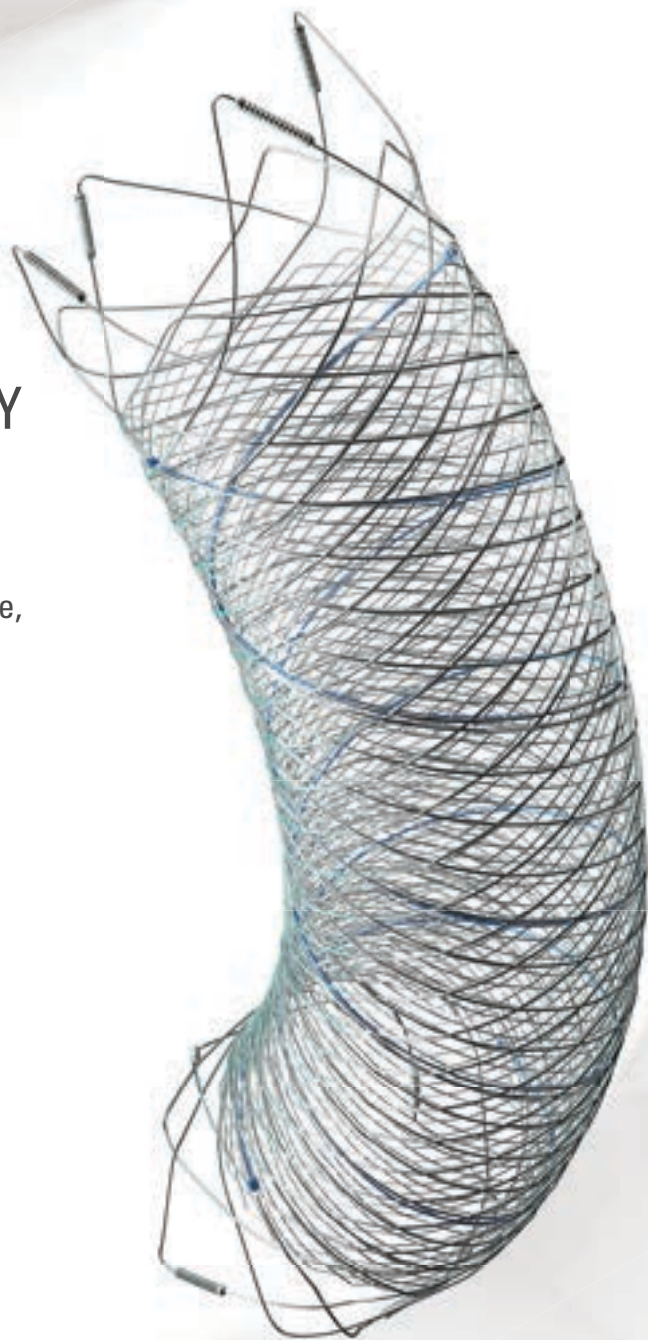
Flow Diverter Stent

THE NEXT ADVANCEMENT IN FLOW DIVERSION TECHNOLOGY

The FRED™ X Flow Diverter features the same precise placement and immediate opening of the FRED™ Device, now with X Technology. X Technology is a covalently bonded, nanoscale surface treatment, designed to:

- **REDUCE MATERIAL THROMBOGENICITY¹**
- **MAINTAIN NATURAL VESSEL HEALING RESPONSE^{2,3,4}**
- **IMPROVE DEVICE DELIVERABILITY AND RESHEATHING¹**

The only FDA PMA approved portfolio with a 0.021" delivery system for smaller device sizes, and no distal lead wire.



For more information, contact your local MicroVention sales representative or visit our website. www.microvention.com



^{*} Data is derived from in vivo and ex vitro testing and may not be representative of clinical performance.

¹ Data on file

² Tanaka M et al. Design of biocompatible and biodegradable polymers based on intermediate water concept. Polymer Journal. 2015;47:114-121.

³ Tanaka M et al. Blood compatible aspects of poly(2-methoxyethylacrylate) (PMEA) – relationship between protein adsorption and platelet adhesion on PMEA surface. Biomaterials. 2000;21:1471-1481.

⁴ Schiel L et al. X Coating™: A new biopassive polymer coating. Canadian Perfusion Canadienne. June 2001;11(2):9.

Indications for Use: The FRED X System is indicated for use in the internal carotid artery from the petrous segment to the terminus for the endovascular treatment of adult patients (22 years of age or older) with wide-necked (neck width 4 mm or dome-to-neck ratio < 2) saccular or fusiform intracranial aneurysms arising from a parent vessel with a diameter 2.0 mm and 5.0 mm.

Rx Only: Federal (United States) law restricts this device to sale by or on the order of a physician. For Healthcare professionals intended use only.

MICROVENTION, FRED and HEADWAY are registered trademarks of MicroVention, Inc. in the United States and other jurisdictions. Stylized X is a trademark of MicroVention, Inc. © 2022 MicroVention, Inc. MM1222 US 03/22

WEB™ 17

Aneurysm Embolization System

LOWER PROFILE



NEW SIZES



MORE ACCESS OPTIONS



INDICATIONS FOR USE:

The WEB Aneurysm Embolization System is intended for the endovascular embolization of ruptured and unruptured intracranial aneurysms and other neurovascular abnormalities such as arteriovenous fistulae (AVF). The WEB Aneurysm Embolization System is also intended for vascular occlusion of blood vessels within the neurovascular system to permanently obstruct blood flow to an aneurysm or other vascular malformation.

POTENTIAL COMPLICATIONS:

Potential complications include but are not limited to the following: hematoma at the site of entry, aneurysm rupture, emboli, vessel perforation, parent artery occlusion, hemorrhage, ischemia, vasospasm, clot formation, device migration or misplacement, premature or difficult device detachment, non-detachment, incomplete aneurysm filling, revascularization, post-embolization syndrome, and neurological deficits including stroke and death. For complete indications, potential complications, warnings, precautions, and instructions, see instructions for use (IFU provided with the device).

VIA 21, 27, 33 - The VIA Microcatheter is intended for the introduction of interventional devices (such as the WEB device/stents/flow diverters) and infusion of diagnostic agents (such as contrast media) into the neuro, peripheral, and coronary vasculature.

VIA 17, 17 Preshaped - The VIA Microcatheter is intended for the introduction of interventional devices (such as the WEB device/stents/flow diverters) and infusion of diagnostic agents (such as contrast media) into the neuro, peripheral, and coronary vasculature.

The VIA Microcatheter is contraindicated for use with liquid embolic materials, such as n-butyl 2-cyanoacrylate or ethylene vinyl alcohol & DMSO (dimethyl sulfoxide).

The device should only be used by physicians who have undergone training in all aspects of the WEB Aneurysm Embolization System procedure as prescribed by the manufacturer.

RX Only: Federal law restricts this device to sale by or on the order of a physician.

For healthcare professional intended use only.



MicroVention Worldwide
Innovator Center PH +1.714.247.8000

35 Enterprise
Aliso Viejo, CA 92656 USA
MicroVention UK Limited
MicroVention Europe, S.A.R.L.
MicroVention Deutschland GmbH
Website
PH +44 (0) 191 258 6777
PH +33 (1) 39 21 77 46
PH +49 211 210 798-0
microvention.com



WEB™ and VIA™ are registered trademarks
of Sequent Medical, Inc. in the United States.

©2021 MicroVention, Inc. MM1184 WW 11/2021

LIFE IS FULL OF COMPROMISES.
IT'S TIME TO TAKE A STAND.

NO COMPROMISE

HIGH RELAXIVITY, HIGH STABILITY:^{1,2}
I CHOOSE BOTH.

The individual who appears is for illustrative purposes. The person depicted is a model and not a real healthcare professional.
Please see Brief Summary of Prescribing Information including Boxed Warning on adjacent page.

VUEWAY™ (gadopichlenol) solution for injection

Indications

VUEWAY injection is indicated in adults and children aged 2 years and older for use with magnetic resonance imaging (MRI) to detect and visualize lesions with abnormal vascularity in:

- the central nervous system (brain, spine and surrounding tissues),
- the body (head and neck, thorax, abdomen, pelvis, and musculoskeletal system).

IMPORTANT SAFETY INFORMATION

WARNING: NEPHROGENIC SYSTEMIC FIBROSIS (NSF)

Gadolinium-based contrast agents (GBCAs) increase the risk for NSF among patients with impaired elimination of the drugs. Avoid use of GBCAs in these patients unless the diagnostic information is essential and not available with non-contrast MRI or other modalities. NSF may result in fatal or debilitating fibrosis affecting the skin, muscle and internal organs.

- The risk for NSF appears highest among patients with:
 - Chronic, severe kidney disease (GFR < 30 mL/min/1.73 m²), or
 - Acute kidney injury.
- Screen patients for acute kidney injury and other conditions that may reduce renal function. For patients at risk for chronically reduced renal function (e.g. age > 60 years,

hypertension, diabetes), estimate the glomerular filtration rate (GFR) through laboratory testing.

- For patients at highest risk for NSF, do not exceed the recommended VUEWAY dose and allow a sufficient period of time for elimination of the drug from the body prior to any re-administration.

Contraindications

VUEWAY injection is contraindicated in patients with history of hypersensitivity reactions to VUEWAY.

Warnings


Risk of **nephrogenic systemic fibrosis** is increased in patients using GBCA agents that have impaired elimination of the drugs, with the highest risk in patients chronic, severe kidney disease as well as patients with acute kidney injury. Avoid use of GBCAs among these patients unless the diagnostic information is essential and not available with non-contrast MRI or other modalities.

Hypersensitivity reactions, including serious hypersensitivity reactions, could occur during use or shortly following VUEWAY administration. Assess all patients for any history of a reaction to contrast media, bronchial asthma and/or allergic disorders, administer VUEWAY only in situations where trained personnel and therapies are promptly available for the treatment of hypersensitivity reactions, and observe patients for signs and symptoms of hypersensitivity reactions after administration.



IN MRI

INTRODUCING


Vueway™
(gadopiclenol) injection
485.1 mg/mL

HALF THE GADOLINIUM DOSE COMPARED TO OTHER
MACROCYCLIC GBCAs IN APPROVED INDICATIONS.^{1,3-6}
FROM BRACCO, YOUR TRUSTED PARTNER IN MRI.



Gadolinium retention can be for months or years in several organs after administration. The highest concentrations (nanomoles per gram of tissue) have been identified in the bone, followed by other organs (brain, skin, kidney, liver and spleen). Minimize repetitive GBCA imaging studies, particularly closely spaced studies, when possible.

Acute kidney injury requiring dialysis has occurred with the use of GBCAs in patients with chronically reduced renal function. The risk of acute kidney injury may increase with increasing dose of the contrast agent.

Ensure catheter and venous patency before injecting as **extravasation** may occur, and cause tissue irritation.

VUEWAY may **impair the visualization of lesions** seen on non-contrast MRI. Therefore, caution should be exercised when Vueway MRI scans are interpreted without a companion non-contrast MRI scan.

The most common adverse reactions (incidence $\geq 0.5\%$) are injection site pain (0.7%), and headache (0.7%).

You are encouraged to report negative side effects of prescription drugs to the FDA. Visit www.fda.gov/medwatch or call 1-800-FDA-1088.

Please see BRIEF SUMMARY of Prescribing Information for VUEWAY, including BOXED WARNING on Nephrogenic Systemic Fibrosis.

Manufactured for Bracco Diagnostics Inc. by Liebel-Flarsheim Company LLC - Raleigh, NC, USA 27616.

VUEWAY is a trademark of Bracco Imaging S.p.A.

References: 1. Vueway™ (gadopiclenol) Injection Full Prescribing Information. Monroe Twp., NJ: Bracco Diagnostics Inc.; September 2022. 2. Robic C, Port M, Rousseaux O, et al. Physicochemical and Pharmacokinetic Profiles of Gadopiclenol: A New Macrocyyclic Gadolinium Chelate With High T1 Relaxivity. *Invest Radiol*. 2019 Aug;54: 475–484. 3. GADAVIST® (gadobutrol) Injection. Full Prescribing Information. Bayer HealthCare Pharmaceuticals Inc. Whippany, NJ; April 2022. 4. DOTAREM® (gadoterate meglumine) Injection. Full Prescribing Information. Guerbet LLC. Princeton, NJ; April 2022. 5. CLARISCAN™ (gadoterate meglumine) injection for intravenous use. Full Prescribing Information. GE Healthcare. Marlborough, MA; February 2020. 6. ProHance® (Gadoteridol) Injection. Full Prescribing Information and Patient Medication Guide. Monroe Twp., NJ: Bracco Diagnostics Inc.; December 2020.

Bracco Diagnostics Inc.
259 Prospect Plains Road, Building H
Monroe Township, NJ 08831 USA
Phone: 609-514-2200
Toll Free: 1-877-272-2269 (U.S. only)
Fax: 609-514-2446
© 2022 Bracco Diagnostics Inc.
All Rights Reserved. US-VW-2200012 10/22

VISIT
VUEWAY.COM
FOR MORE
INFORMATION



Vueway™

(gadopiclenol) injection, for intravenous use

BRIEF SUMMARY: Please see package insert of full prescribing information.

WARNING: NEPHROGENIC SYSTEMIC FIBROSIS (NSF)

Gadolinium-based contrast agents (GBCAs) increase the risk for NSF among patients with impaired elimination of the drugs. Avoid use of GBCAs in these patients unless the diagnostic information is essential and not available with non-contrast MRI or other modalities. NSF may result in fatal or debilitating fibrosis affecting the skin, muscle and internal organs.

- The risk for NSF appears highest among patients with:
 - Chronic, severe kidney disease (GFR < 30 mL/min/1.73 m²), or
 - Acute kidney injury.
- Screen patients for acute kidney injury and other conditions that may reduce renal function. For patients at risk for chronically reduced renal function (e.g. age > 60 years, hypertension, diabetes), estimate the glomerular filtration rate (GFR) through laboratory testing.
- For patients at highest risk for NSF, do not exceed the recommended Vueway dose and allow a sufficient period of time for elimination of the drug from the body prior to any re-administration [see Warnings and Precautions (5.1) in the full Prescribing Information].

INDICATIONS AND USAGE

Vueway™ (gadopiclenol) is a gadolinium-based contrast agent indicated in adult and pediatric patients aged 2 years and older for use with magnetic resonance imaging (MRI) to detect and visualize lesions with abnormal vascularity in:

- the central nervous system (brain, spine, and associated tissues),
- the body (head and neck, thorax, abdomen, pelvis, and musculoskeletal system).

CONTRAINDICATIONS

Vueway is contraindicated in patients with history of hypersensitivity reactions to gadopicholol.

WARNINGS AND PRECAUTIONS

Nephrogenic Systemic Fibrosis Gadolinium-based contrast agents (GBCAs) increase the risk for nephrogenic systemic fibrosis (NSF) among patients with impaired elimination of the drugs. Avoid use of GBCAs among these patients unless the diagnostic information is essential and not available with non-contrast MRI or other modalities. The GBCA-associated NSF risk appears highest for patients with chronic, severe kidney disease (GFR < 30 mL/min/1.73 m²) as well as patients with acute kidney injury. The risk appears lower for patients with chronic, moderate kidney disease (GFR 30-59 mL/min/1.73 m²) and little, if any, for patients with chronic, mild kidney disease (GFR 60-89 mL/min/1.73 m²). NSF may result in fatal or debilitating fibrosis affecting the skin, muscle, and internal organs. Report any diagnosis of NSF following Vueway administration to Bracco Diagnostics Inc. (1-800-257-5181) or FDA (1-800-FDA-1088 or www.fda.gov/medwatch).

Screen patients for acute kidney injury and other conditions that may reduce renal function. Features of acute kidney injury consist of rapid (over hours to days) and usually reversible decrease in kidney function, commonly in the setting of surgery, severe infection, injury or drug-induced kidney toxicity. Serum creatinine levels and estimated GFR may not reliably assess renal function in the setting of acute kidney injury. For patients at risk for chronically reduced renal function (e.g., age > 60 years, diabetes mellitus or chronic hypertension), estimate the GFR through laboratory testing.

Among the factors that may increase the risk for NSF are repeated or higher than recommended doses of a GBCA and the degree of renal impairment at the time of exposure. Record the specific GBCA and the dose administered to a patient. For patients at highest risk for NSF, do not exceed the recommended Vueway dose and allow a sufficient period of time for elimination of the drug prior to re-administration. For patients receiving hemodialysis, physicians may consider the prompt initiation of hemodialysis following the administration of a GBCA in order to enhance the contrast agent's elimination [see Use in Specific Populations (8.6) and Clinical Pharmacology (12.3) in the full Prescribing Information]. The usefulness of hemodialysis in the prevention of NSF is unknown.

Hypersensitivity Reactions With GBCAs, serious hypersensitivity reactions have occurred. In most cases, initial symptoms occurred within minutes of GBCA administration and resolved with prompt emergency treatment.

- Before Vueway administration, assess all patients for any history of a reaction to contrast media, bronchial asthma and/or allergic disorders. These patients may have an increased risk for a hypersensitivity reaction to Vueway.
- Vueway is contraindicated in patients with history of hypersensitivity reactions to Vueway [see Contraindications (4) in the full Prescribing Information].
- Administer Vueway only in situations where trained personnel and therapies are promptly available for the treatment of hypersensitivity reactions, including personnel trained in resuscitation.
- During and following Vueway administration, observe patients for signs and symptoms of hypersensitivity reactions.

Gadolinium Retention Gadolinium is retained for months or years in several organs. The highest concentrations (nanomoles per gram of tissue) have been identified in the bone, followed by other organs (e.g. brain, skin, kidney, liver, and spleen). The duration of retention also varies by tissue and is longest in bone. Linear GBCAs cause more retention than macrocyclic GBCAs. At equivalent doses, gadolinium retention varies among the linear agents with gadodiamide causing greater retention than other linear agents such as gadoxetate disodium, and gadobenate dimeglumine. Retention is lowest and similar

among the macrocyclic GBCAs such as gadoterate meglumine, gadobutrol, gadoteridol, and gadopicholol.

Consequences of gadolinium retention in the brain have not been established. Pathologic and clinical consequences of GBCA administration and retention in skin and other organs have been established in patients with impaired renal function [see Warnings and Precautions (5.1) in the full Prescribing Information]. There are rare reports of pathologic skin changes in patients with normal renal function. Adverse events involving multiple organ systems have been reported in patients with normal renal function without an established causal link to gadolinium.

While clinical consequences of gadolinium retention have not been established in patients with normal renal function, certain patients might be at higher risk. These include patients requiring multiple lifetime doses, pregnant and pediatric patients, and patients with inflammatory conditions. Consider the retention characteristics of the agent when choosing a GBCA for these patients. Minimize repetitive GBCA imaging studies, particularly closely spaced studies, when possible.

Acute Kidney Injury In patients with chronically reduced renal function, acute kidney injury requiring dialysis has occurred with the use of GBCAs. The risk of acute kidney injury may increase with increasing dose of the contrast agent. Do not exceed the recommended dose.

Extravasation and Injection Site Reactions Injection site reactions such as injection site pain have been reported in the clinical studies with Vueway [see Adverse Reactions (6.1) in the full Prescribing Information]. Extravasation during Vueway administration may result in tissue irritation [see Nonclinical Toxicology (13.2) in the full Prescribing Information]. Ensure catheter and venous patency before the injection of Vueway.

Interference with Visualization of Lesions Visible with Non-Contrast MRI As with any GBCA, Vueway may impair the visualization of lesions seen on non-contrast MRI. Therefore, caution should be exercised when Vueway MRI scans are interpreted without a companion non-contrast MRI scan.

ADVERSE REACTIONS

The following serious adverse reactions are discussed elsewhere in labeling:

- Nephrogenic Systemic Fibrosis [see Warnings and Precautions (5.1) in the full Prescribing Information]
- Hypersensitivity Reactions [see Contraindications (4) and Warnings and Precautions (5.2) in the full Prescribing Information]

Clinical Trials Experience Because clinical trials are conducted under widely varying conditions, adverse reaction rates observed in the clinical trials of a drug cannot be directly compared to rates in the clinical trials of another drug and may not reflect the rates observed in clinical practice.

The safety of Vueway was evaluated in 1,047 patients who received Vueway at doses ranging from 0.025 mmol/kg (one half the recommended dose) to 0.3 mmol/kg (six times the recommended dose). A total of 708 patients received the recommended dose of 0.05 mmol/kg. Among patients who received the recommended dose, the average age was 51 years (range 2 years to 88 years) and 56% were female. The ethnic distribution was 79% White, 10% Asian, 7% American Indian or Alaska native, 2% Black, and 2% patients of other or unspecified ethnic groups.

Overall, approximately 4.7% of subjects receiving the labeled dose reported one or more adverse reactions.

Table 1 lists adverse reactions that occurred in > 0.2% of patients who received 0.05 mmol/kg Vueway.

TABLE 1. ADVERSE REACTIONS REPORTED IN > 0.2% OF PATIENTS RECEIVING VUEWAY IN CLINICAL TRIALS	
Adverse Reaction	Vueway 0.05 mmol/kg (n=708) (%)
Injection site pain	0.7
Headache	0.7
Nausea	0.4
Injection site warmth	0.4
Injection site coldness	0.3
Dizziness	0.3
Local swelling	0.3

Adverse reactions that occurred with a frequency < 0.2% in patients who received 0.05 mmol/kg Vueway included: maculopapular rash, vomiting, worsened renal impairment, feeling hot, pyrexia, oral paresthesia, dysgeusia, diarrhea, pruritus, allergic dermatitis, erythema, injection site paresthesia, Cystatin C increase, and blood creatinine increase.

Adverse Reactions in Pediatric Patients

One study with a single dose of Vueway (0.05 mmol/kg) was conducted in 80 pediatric patients aged 2 years to 17 years, including 60 patients who underwent a central nervous system (CNS) MRI and 20 patients who underwent a body MRI. One adverse reaction (maculopapular rash of moderate severity) in one patient (1.3%) was reported in the CNS cohort.

USE IN SPECIFIC POPULATIONS

Pregnancy Risk Summary There are no available data on Vueway use in pregnant women to evaluate for a drug-associated risk of major birth defects, miscarriage or other adverse maternal or fetal outcomes. GBCAs cross the human placenta and result in fetal exposure and gadolinium retention. The available human data on GBCA exposure during pregnancy and adverse fetal outcomes are limited and inconclusive (see Data). In animal reproduction studies, there were no adverse developmental effects observed in rats or rabbits with intravenous administration of Vueway during organogenesis (see Data). Because of the potential risks of gadolinium to the fetus, use Vueway only if imaging is essential during pregnancy and cannot be delayed. The estimated background risk of major birth defects and miscarriage for the indicated population(s) are unknown. All pregnancies have a background risk of birth defect, loss, or other adverse outcomes. In the U.S. general population, the estimated background risk of major birth defects and miscarriage in clinically recognized pregnancies is 2% to 4% and 15% to 20% respectively. Data Human Data Contrast enhancement is visualized in the placenta and fetal tissues after maternal GBCA administration. Cohort studies and case reports on exposure to GBCAs during pregnancy have not reported a clear association between GBCAs and adverse effects in the exposed neonates. However, a retrospective cohort study comparing pregnant women who had a GBCA MRI to pregnant women who did not have an MRI reported a higher occurrence of stillbirths and neonatal deaths in the group receiving GBCA MRI. Limitations of this study include a lack of comparison with non-contrast MRI and lack of information about the maternal indication for MRI. Overall, these data preclude

a reliable evaluation of the potential risk of adverse fetal outcomes with the use of GBCAs in pregnancy.

Animal Data Gadolinium Retention: GBCAs administered to pregnant non-human primates (0.1 mmol/kg on gestational days 85 and 135) result in measurable gadolinium concentration in the offspring in bone, brain, skin, liver, kidney, and spleen for at least 7 months. GBCAs administered to pregnant mice (2 mmol/kg daily on gestational days 16 through 19) result in measurable gadolinium concentrations in the pups in bone, brain, kidney, liver, blood, muscle, and spleen at one-month postnatal age.

Reproductive Toxicology: Animal reproduction studies conducted with gadopicholol showed some signs of maternal toxicity in rats at 10 mmol/kg and rabbits at 5 mmol/kg (corresponding to 52 times and 57 times the recommended human dose, respectively). This maternal toxicity was characterized in both species by swelling, decreased activity, and lower gestation weight gain and food consumption.

No effect on embryo-fetal development was observed in rats at 10 mmol/kg (corresponding to 52 times the recommended human dose). In rabbits, a lower mean fetal body weight was observed at 5 mmol/kg (corresponding to 57 times the recommended human dose) and this was attributed as a consequence of the lower gestation weight gain.

Lactation Risk Summary There are no data on the presence of gadopicholol in human milk, the effects on the breastfed infant, or the effects on milk production. However, published lactation data on other GBCAs indicate that 0.01% to 0.04% of the maternal gadolinium dose is excreted in breast milk. Additionally, there is limited GBCA gastrointestinal absorption in the breast-fed infant. Gadopicholol is present in rat milk. When a drug is present in animal milk, it is likely that the drug will be present in human milk (see Data). The developmental and health benefits of breastfeeding should be considered along with the mother's clinical need for Vueway and any potential adverse effects on the breastfed infant from Vueway or from the underlying maternal condition. Data In lactating rats receiving single intravenous injection of [¹⁵³Gd]-gadopiclenol, 0.3% and 0.2% of the total administered radioactivity was transferred to the pups via maternal milk at 6 hours and 24 hours after administration, respectively. Furthermore, in nursing rat pups, oral absorption of gadopicholol was 3.6%.

Pediatric Use The safety and effectiveness of Vueway for use with MRI to detect and visualize lesions with abnormal vascularity in the CNS (brain, spine, and associated tissues), and the body (head and neck, thorax, abdomen, pelvis, and musculoskeletal system) have been established in pediatric patients aged 2 years and older.

Use of Vueway in this age group is supported by evidence from adequate and well-controlled studies in adults with additional pharmacokinetic and safety data from an open-label, uncontrolled, multicenter, single dose study of Vueway (0.05 mmol/kg) in 80 pediatric patients aged 2 to 17 years. The 80 patients consisted of 60 patients who underwent a CNS MRI and 20 patients who underwent a body MRI [see Adverse Reactions (6.1) and Clinical Pharmacology (12.3) in the full Prescribing Information].

The safety and effectiveness of Vueway have not been established in pediatric patients younger than 2 years of age.

Geriatric Use Of the total number of Vueway-treated patients in clinical studies, 270 (26%) patients were 65 years of age and over, while 62 (6%) patients were 75 years of age and over. No overall differences in safety or efficacy were observed between these subjects and younger subjects.

This drug is known to be substantially excreted by the kidney, and the risk of adverse reactions to this drug may be greater in patients with impaired renal function. Because elderly patients are more likely to have decreased renal function, it may be useful to monitor renal function.

Renal Impairment In patients with renal impairment, the exposure of gadopicholol is increased compared to patients with normal renal function. This may increase the risk of adverse reactions such as nephrogenic systemic fibrosis (NSF). Avoid use of GBCAs among these patients unless the diagnostic information is essential and not available with non-contrast MRI or other modalities. No dose adjustment of Vueway is recommended for patients with renal impairment. Vueway can be removed from the body by hemodialysis [see Warnings and Precautions (5.1, 5.3, 5.4) and Clinical Pharmacology (12.3) in the full Prescribing Information].

OVERDOSAGE

Among subjects who received a single 0.3 mmol/kg intravenous dose of gadopicholol (6 times the recommended dose of Vueway), headache and nausea were the most frequently reported adverse reactions. Gadopicholol can be removed from the body by hemodialysis [see Clinical Pharmacology (12.3) in the full Prescribing Information].

PATIENT COUNSELING INFORMATION Advise the patient to read the FDA-approved patient labeling (Medication Guide).

Nephrogenic Systemic Fibrosis Inform the patient that Vueway may increase the risk for NSF among patients with impaired elimination of the drugs and that NSF may result in fatal or debilitating fibrosis affecting the skin, muscle and internal organs.

Instruct the patients to contact their physician if they develop signs or symptoms of NSF following Vueway administration, such as burning, itching, swelling, scaling, hardening and tightening of the skin; red or dark patches on the skin; stiffness in joints with trouble moving, bending or straightening the arms, hands, legs or feet; pain in the hip bones or ribs; or muscle weakness [see Warnings and Precautions (5.1) in the full Prescribing Information].

Gadolinium Retention Advise patients that gadolinium is retained for months or years in brain, bone, skin, and other organs following Vueway administration even in patients with normal renal function. The clinical consequences of retention are unknown. Retention depends on multiple factors and is greater following administration of linear GBCAs than following administration of macrocyclic GBCAs [see Warnings and Precautions (5.3) in the full Prescribing Information].

Injection Site Reactions Inform the patient that Vueway may cause reactions along the venous injection site, such as mild and transient burning or pain or feeling of warmth or coldness at the injection site [see Warnings and Precautions (5.5) in the full Prescribing Information].

Pregnancy Advise pregnant women of the potential risk of fetal exposure to Vueway [see Use in Specific Populations (8.1) in the full Prescribing Information].

Rx only

US Patent No. 10,973,934
Manufactured for Bracco Diagnostics Inc. by Liebel-Flarsheim Company LLC
- Raleigh, NC, USA 27616.
Toll Free: 1-877-272-2269 (U.S. only)
Revised November 2022

I am a global citizen.

I am patient-centered care.

I am committed to health equity.

I am a teacher.

I am a life-long learner.

I am determined.

I am curious.

I am a collaborative team player.

I am a volunteer.

I am ASNR.

Don't miss out on the tools, resources and relationships you've come to rely on. Log in and renew your ASNR membership today! www.asnr.org



The ASNR Career Center

The Go-To Job Site for Neuroradiology Employers and Job Seekers

For Job Seekers

- Access to an expanded network of jobs via the National Healthcare Career Network
- Confidential resume posting
- Professional online profile

For Employers

- Employer resources to help you recruit top talent
- Multiple pricing options, including free Fellowship listings
- Resume search

Start here: careers.asnr.org

AJNR *go green*

***AJNR* urges American Society of Neuroradiology members to reduce their environmental footprint by voluntarily suspending their print subscription.**

The savings in paper, printing, transportation, and postage directly fund new electronic enhancements and expanded content.

The digital edition of *AJNR* presents the print version in its entirety, along with extra features including:

- Publication Preview
- Case Collection
- Podcasts
- The *AJNR* News Digest
- The *AJNR* Blog

It also reaches subscribers much faster than print. An electronic table of contents will be sent directly to your mailbox to notify you as soon as it publishes.

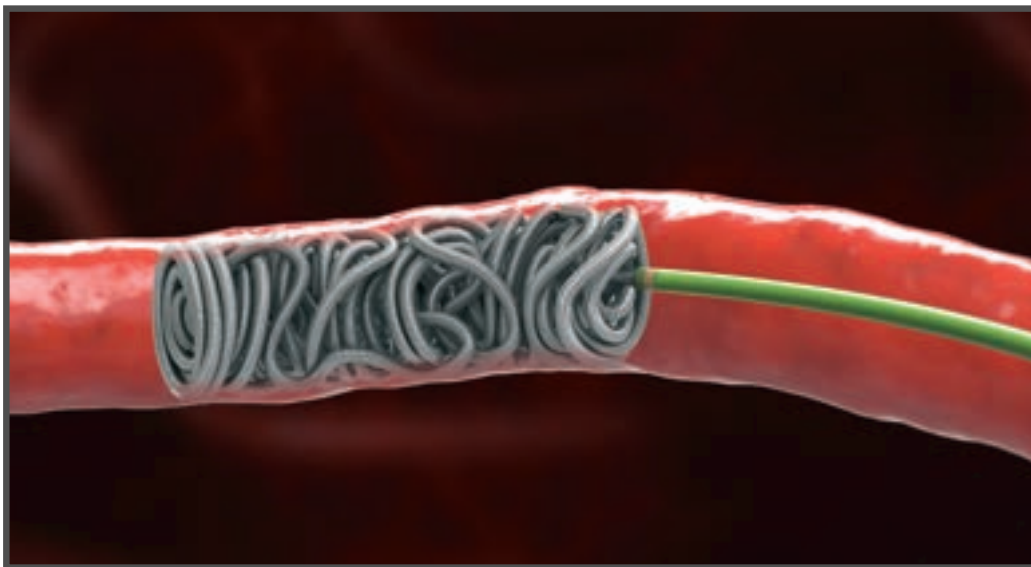
Readers can search, reference, and bookmark current and archived content 24 hours a day on www.ajnr.org.

ASNR members who wish to opt out of print can do so by using the *AJNR* Go Green link on the *AJNR* Website (<http://www.ajnr.org/content/subscriber-help-and-services>). Just type your name in the email form to stop print and spare our ecosystem.

OPTIBLOCKTM

COIL

PRECISION PLACEMENT



EFFICIENT OCCLUSION

- Precision Anchoring • Concise, Dense Pack • Unique Design and Long Lengths
- $\geq .0165$ Microcatheter Compatible

Visit our products page at baltgroup.com for more information.

Balt USA
29 Parker, Irvine, CA 92618 • tel 949.788.1443 fax 949.788.1444
baltgroup.com
© 2023 BALT USA MKTG-370 Rev. A



AJNR

AMERICAN JOURNAL OF NEURORADIOLOGY

JUNE 2023
VOLUME 44
NUMBER 6
WWW.AJNR.ORG

Publication Preview at www.ajnr.org features articles released in advance of print. Visit www.ajnrblog.org to comment on AJNR content and chat with colleagues and AJNR's News Digest at <http://ajnrndigest.org> to read the stories behind the latest research in neuroimaging.



625 **PERSPECTIVES** J.S. Ross

REVIEW ARTICLE

-  626 **Comprehensive Update and Review of Clinical and Imaging Features of SMART Syndrome** Y. Ota, et al.




ADULT BRAIN

LEVEL 1 EBM EXPEDITED PUBLICATION


-    634 **A Pragmatic Randomized Trial Comparing Surgical Clipping and Endovascular Treatment of Unruptured Intracranial Aneurysms** T.E. Darsaut, et al.

INTERVENTIONAL

GENERAL CONTENTS

-    641 **Automated Segmentation of Intracranial Thrombus on NCCT and CTA in Patients with Acute Ischemic Stroke Using a Coarse-to-Fine Deep Learning Model** K. Zhu, et al.

ADULT BRAIN

-  649 **Evaluation of the Statistical Detection of Change Algorithm for Screening Patients with MS with New Lesion Activity on Longitudinal Brain MRI** M. Homssi, et al.

ADULT BRAIN

- 656 **Commentary**
Revolutionizing MS Monitoring: The Impact of Postprocessing Techniques on Lesion Detection A. Lecler

ADULT BRAIN

-    658 **NCCT Markers of Intracerebral Hemorrhage Expansion Using Revised Criteria: An External Validation of Their Predictive Accuracy** C. Ducroux, et al.

ADULT BRAIN

-  665 **Evaluation of Motion-Corrected Multishot Echo-Planar Imaging as an Alternative to Gradient Recalled-Echo for Blood-Sensitive Imaging** J.A. Murchison, et al.

ADULT BRAIN

-   668 **Medical Imaging Compatibility of Magnesium- and Iron-Based Bioresorbable Flow Diverters** A.A. Oliver, et al.

INTERVENTIONAL

-  675 **Comprehensive Venous Outflow Predicts Functional Outcomes in Patients with Acute Ischemic Stroke Treated by Thrombectomy** G. Adusumilli, et al.

INTERVENTIONAL

AJNR (Am J Neuroradiol ISSN 0195–6108) is a journal published monthly, owned and published by the American Society of Neuroradiology (ASNR), 820 Jorie Boulevard, Oak Brook, IL 60523. Annual dues for the ASNR include approximately 19% for a journal subscription. The journal is printed by Intellicor Communications, 330 Eden Road, Lancaster, PA 17601; Periodicals postage paid at Oak Brook, IL and additional mailing offices. Printed in the U.S.A. POSTMASTER: Please send address changes to American Journal of Neuroradiology, P.O. Box 3000, Denver, NJ 07834, U.S.A. Subscription rates: nonmember \$452 (\$530 foreign) print and online, \$320 online only; institutions \$520 (\$594 foreign) print and basic online, \$1029 (\$1103 foreign) print and extended online, \$380 online only (basic), \$825 online only (extended); single copies are \$35 each (\$40 foreign). Indexed by PubMed/MEDLINE, BIOSIS Previews, Current Contents (Clinical Medicine and Life Sciences), EMBASE, Google Scholar, HighWire Press, Q-Sensei, RefSeek, Science Citation Index, SCI Expanded, ReadCube, and Semantic Scholar. Copyright © American Society of Neuroradiology.

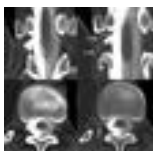
- 681 **Femoral Access-Site Complications with Tenecteplase versus Alteplase before Mechanical Thrombectomy for Large-Vessel-Occlusion Stroke** *P. Hendrix, et al.* **INTERVENTIONAL**
-   687 **Early-versus-Late Endovascular Stroke Treatment: Similar Frequencies of Nonrevascularization and Postprocedural Cerebrovascular Complications in a Large Single-Center Cohort Study** *E. Maslias, et al.* **INTERVENTIONAL**
-  693 **Ultrasound-Guided Radiofrequency Ablation versus Thyroidectomy for the Treatment of Benign Thyroid Nodules in Elderly Patients: A Propensity-Matched Cohort Study** *L. Yan, et al.* **HEAD & NECK INTERVENTIONAL**
-   700 **Improved Myelination following Camp Leg Power, a Selective Motor Control Intervention for Children with Spastic Bilateral Cerebral Palsy: A Diffusion Tensor MRI Study** *A. Vuong, et al.* **PEDIATRICS FUNCTIONAL**
-   707 **Doppler Ultrasound Flow Reversal in the Superior Sagittal Sinus to Detect Cerebral Venous Congestion in Vein of Galen Malformation** *S. Schwarz, et al.* **PEDIATRICS**
-  716 **Subarachnoid Space Measurements in Apparently Healthy Fetuses Using MR Imaging** *A. Wandel, et al.* **PEDIATRICS**
-  722 **Why, How Often, and What Happens When We Fail: A Retrospective Analysis of Failed Fluoroscopically Guided Lumbar Punctures** *M. Gerasymchuk, et al.* **SPINE**
-   730 **Efficacy of Epidural Blood Patching or Surgery in Spontaneous Intracranial Hypotension: A Systematic Review and Evidence Map** *T.J. Amrhein, et al.* **SPINE**
-  740 **Utility of Photon-Counting Detector CT Myelography for the Detection of CSF-Venous Fistulas** *A.A. Madhavan, et al.* **SPINE**
- 745 **Conebeam CT as an Additional Tool in Digital Subtraction Myelography for the Detection of Spinal Lateral Dural Tears** *N. Lützen, et al.* **SPINE**

ONLINE FEATURES

E31 ERRATUM

BOOK REVIEWS *R.M. Quencer, Section Editor*

Please visit www.ajnrblog.org to read and comment on Book Reviews.



Use of photon-counting detector CT myelography for detection of CSF-venous fistula from A.A. Madhavan, et al, in this issue.



Indicates Editor's Choices selection



Indicates article with supplemental online video

Indicates Fellows' Journal Club selection



Evidence-Based Medicine Level 1



Indicates open access to non-subscribers at www.ajnr.org



Evidence-Based Medicine Level 2



Indicates article with supplemental online data

EDITOR-IN-CHIEF

Jeffrey S. Ross, MD

Professor of Radiology, Department of Radiology,
Mayo Clinic College of Medicine, Phoenix, AZ

SENIOR EDITORS

Harry J. Cloft, MD, PhD

Professor of Radiology and Neurosurgery,
Department of Radiology, Mayo Clinic College of
Medicine, Rochester, MN

Christopher G. Filippi, MD

Professor and Alice Ettinger-Jack R. Dreyfuss
Chair of Radiology,
Tufts University School of Medicine,
Radiologist-in-Chief
Tufts University Medical Center, Boston, MA

Thierry A.G.M. Huisman, MD, PD, FICIS, FACR

Radiologist-in-Chief and Chair of Radiology, Texas
Children's Hospital,
Professor of Radiology, Pediatrics, Neurosurgery,
and OBGYN, Baylor College of Medicine,
Houston, TX

Yvonne W. Lui, MD

Associate Professor of Radiology,
Chief of Neuroradiology,
New York University School of Medicine,
New York, NY

C.D. Phillips, MD, FACR

Professor of Radiology, Weill Cornell Medical
College, Director of Head and Neck Imaging,
New York-Presbyterian Hospital, New York, NY

Lubdhra M. Shah, MD, MS

Professor of Radiology and Director of Spine
Imaging, University of Utah Department of
Radiology and Imaging Sciences, Salt Lake City, UT

STATISTICAL SENIOR EDITOR

Bryan A. Comstock, MS

Senior Biostatistician,
Department of Biostatistics,
University of Washington, Seattle, WA

ARTIFICIAL INTELLIGENCE DEPUTY EDITOR

Peter D. Chang, MD

Assistant Professor-in-Residence,
Departments of Radiological Sciences,
Computer Sciences, and Pathology,
Director, Center for Artificial Intelligence in
Diagnostic Medicine (CAIDM),
University of California, Irvine, Irvine, CA

EDITORIAL BOARD

Ashley H. Aiken, *Atlanta, GA*

Matthew D. Alexander, *Salt Lake City, UT*

Lea M. Alhilali, *Phoenix, AZ*

Jason W. Allen, *Atlanta, GA*

Mohammed A. Almekhlafi, *Calgary, Alberta, Canada*

Niranjan Balu, *Seattle, WA*

Matthew J. Barkovich, *San Francisco, CA*

Joachim Berkefeld, *Frankfurt, Germany*

Karen Buch, *Boston, MA*

Judah Burns, *New York, NY*

Danielle Byrne, *Dublin, Ireland*

Federico Cagnazzo, *Montpellier, France*

Gloria C. Chiang, *New York, NY*

Daniel Chow, *Irvine, CA*

Kars C.J. Compagne, *Rotterdam, The Netherlands*

Yonghong Ding, *Rochester, MN*

Birgit Ertl-Wagner, *Toronto, Ontario, Canada*

Aaron Field, *Madison, WI*

Nils D. Forkert, *Calgary, Alberta, Canada*

Frank Gaillard, *Melbourne, Australia*

Joseph J. Gemmete, *Ann Arbor, Michigan*

Brent Griffith, *Detroit, MI*

Michael J. Hoch, *Philadelphia, PA*

Joseph M. Hoxworth, *Phoenix, AZ*

Raymond Y. Huang, *Boston, MA*

Susie Y. Huang, *Boston, MA*

Ferdinand K. Hui, *Honolulu, HI*

Christof Karmonik, *Houston, TX*

Gregor Kasprian, *Vienna, Austria*

Timothy J. Kaufmann, *Rochester, MN*

Hillary R. Kelly, *Boston, MA*

Toshibumi Kinoshita, *Akita, Japan*

Ioannis Koktzoğlu, *Evanston, IL*

Stephen F. Kralik, *Houston, TX*

Luke Ledbetter, *Los Angeles, CA*

Franklin A. Marden, *Chicago, IL*

Markus A. Möhlenbruch, *Heidelberg, Germany*

Mahmud Mossa-Basha, *Morrisville, NC*

Renato Hoffmann Nunes, *Sao Paulo, Brazil*

Sam Payabvash, *New Haven, CT*

Johannes A.R. Pfaff, *Salzburg, Austria*

Eike I. Piechowiak, *Bern, Switzerland*

Laurent Pierot, *Reims, France*

Alexander R. Podgorsak, *Chicago, IL*

Eytan Raz, *New York, NY*

Jeff Rudie, *San Diego, CA*

Paul M. Ruggieri, *Cleveland, OH*

Fatih Seker, *Heidelberg, Germany*

Maksim Shapiro, *New York, NY*

Timothy Shepherd, *New York, NY*

Mark S. Shiroishi, *Los Angeles, CA*

Neetu Soni, *Rochester, NY*

Ashok Srinivasan, *Ann Arbor, MI*

Jason F. Talbott, *San Francisco, CA*

Anderanik Tomasian, *Los Angeles, CA*

Fabio Triulzi, *Milan, Italy*

Arastoo Vossough, *Philadelphia, PA*

Richard Watts, *New Haven, CT*

Elysa Widjaja, *Toronto, Ontario, Canada*

Ronald Wulz, *Philadelphia, Pennsylvania*

Shuang Xia, *Tianjin, China*

Leonard Yeo, *Singapore*

Woong Yoon, *Gwangju, South Korea*

David M. Yousem, *Evergreen, CO*

Carlos Zamora, *Chapel Hill, NC*

Chengcheng Zhu, *Seattle, WA*

EDITORIAL FELLOW

Alexandre Boutet, *Toronto, Ontario, Canada*

SPECIAL CONSULTANTS TO THE EDITOR

AJNR Blog Editor

Neil Lall, *Denver, CO*

Case of the Month Editor

Nicholas Stence, *Aurora, CO*

Case of the Week Editors

Matylda Machnowska, *Toronto, Ontario, Canada*

Anvita Pauranik, *Calgary, Alberta, Canada*

Classic Case Editor

Sandy Cheng-Yu Chen, *Taipei, Taiwan*

Health Care and Socioeconomics Editor

Pina C. Sanelli, *New York, NY*

Physics Editor

Greg Zaharchuk, *Stanford, CA*

Podcast Editor

Kevin Hiatt, *Winston-Salem, NC*

Twitter Editor

Jacob Ormsby, *Albuquerque, NM*

Official Journal:

American Society of Neuroradiology

American Society of Functional Neuroradiology

American Society of Head and Neck Radiology

American Society of Pediatric Neuroradiology

American Society of Spine Radiology

Founding Editor
Juan M. Taveras

Editors Emeriti
Mauricio Castillo, Robert I. Grossman,
Michael S. Huckman, Robert M. Quencer

Managing Editor
Karen Halm
Assistant Managing Editor
Laura Wilhelm
Executive Director, ASNR
Mary Beth Hepp



Title: The Andromeda Galaxy. Also known as M31, this is a barred spiral galaxy located approximately 2.5 million light-years away from Earth in the constellation Andromeda. It is the nearest galaxy to our Milky Way and is estimated to be around 150,000 light-years across, making it one of the largest galaxies in the Local Group of galaxies. The Andromeda Galaxy contains more than a trillion stars, and its mass is believed to be about 1.5 times that of our Milky Way. It is also home to a supermassive black hole at its center, which has a mass of about 100 million times that of the sun. This image was acquired as a series of fifty 5-minute images (4 hours) using red, green, and blue filters. The telescope was a Takahashi FSQ Fluorite refractor with a 106-mm aperture on a Paramount ME mount. The camera was a SBIG STL-11000M CCD, with Astrodon filters. The images were processed using PixInsight, Photoshop, and Topaz Labs Adjust AI and DeNoise AI.

Jeffrey S. Ross, Mayo Clinic, Phoenix, Arizona

Comprehensive Update and Review of Clinical and Imaging Features of SMART Syndrome

Y. Ota, E. Liao, G. Shah, A. Srinivasan, and A.A. Capizzano



ABSTRACT

SUMMARY: Stroke-like migraine attacks after radiation therapy (SMART) syndrome is a delayed complication of cranial irradiation, with subacute onset of stroke-like symptoms including seizures, visual disturbance, speech impairment, unilateral hemianopsia, facial droop, and aphasia, often associated with migraine-type headache. The diagnostic criteria were initially proposed in 2006. However, the diagnosis of SMART syndrome is challenging because clinical symptoms and imaging features of SMART syndrome are indeterminate and overlap with tumor recurrence and other neurologic diseases, which may result in inappropriate clinical management and unnecessary invasive diagnostic procedures. Recently, various imaging features and treatment recommendations for SMART syndrome have been reported. Radiologists and clinicians should be familiar with updates on clinical and imaging features of this delayed radiation complication because recognition of this entity can facilitate proper clinical work-up and management. This review provides current updates and a comprehensive overview of the clinical and imaging features of SMART syndrome.

ABBREVIATIONS: ALERT = acute late-onset encephalopathy after radiation therapy; ATP = adenosine triphosphate; MELAS = mitochondrial myopathy, encephalopathy, lactic acidosis, and stroke-like episodes; PIPG = peri-ictal pseudoprogression; PRES = posterior reversible encephalopathy syndrome; ROS = reactive oxygen species; SMART = stroke-like migraine attacks after radiation therapy

Stroke-like migraine attacks after radiation therapy (SMART) syndrome is considered a delayed complication of cranial irradiation, associated with migraine-like headaches and subacute onset of stroke-like symptoms in both adult and pediatric populations previously treated for intracranial malignancies.¹⁻⁸ SMART syndrome is often reversible, but resolution can be delayed or have permanent sequelae in some cases.^{5,8} A radiation dose of >50 Gy has been suggested as a threshold, but lower doses have also been reported. In 2006, Black et al⁶ proposed diagnostic criteria for SMART syndrome, including the following: 1) a remote history of external beam cranial irradiation; 2) prolonged, reversible signs and symptoms referable to a unilateral cortical region beginning years after cranial irradiation, including seizure, migraine with or without an aura, and stroke-like symptoms; 3) transient, diffuse, unilateral gyriform enhancement sparing the white matter within a previous radiation field; and 4) not attributed to another disorder.⁶ However, since the initial diagnostic criteria were proposed, further reported cases of SMART syndrome have revealed

additional clinical and imaging manifestations that fail to strictly fit within these criteria despite otherwise matching the features of SMART syndrome. As well, updates regarding clinical and imaging prognostic factors and a spectrum of SMART syndrome variants including peri-ictal pseudoprogression (PIPG) and acute late-onset encephalopathy after radiation therapy (ALERT) have been proposed.^{9,10} In this review, we discuss clinical and radiologic updates on SMART syndrome along with a comprehensive review covering pathophysiology, clinical and radiologic features, management, and its mimics on imaging.

Epidemiology

SMART syndrome can affect both adult and pediatric populations with a male predominance.^{2,3} The overall incidence remains to be revealed due to its rarity. The age of onset ranges from 3.5 to 88 years of age, with a mean age of approximately 45 years and a mean time to symptom development of 14 years after brain irradiation.⁷ Radiation therapy is performed via whole-brain radiation therapy or focal irradiation such as stereotactic radiosurgery, intensity-modulated radiation therapy, or 3D conformal radiation therapy; a radiation dose of ≥ 50 Gy is often reported in SMART syndrome.⁵ Patients typically recover from symptoms within 1.5–2.5 months,³ but some patients experience either incomplete recovery^{4,5} or recurrent episodes of SMART syndrome.^{5,8}

Recently, it has been reported that older patients are more likely to have incomplete recovery and a longer duration of symptoms of

Received January 31, 2023; accepted after revision March 20.

From The Division of Neuroradiology, Department of Radiology, University of Michigan, Ann Arbor, Michigan.

Please address correspondence to Yoshiaki Ota, MD, 1500 E Medical Center Dr, UH B2, Ann Arbor, MI 48109; e-mail: yoshiako@med.umich.edu; @GattsukiRadiol

Indicates open access to non-subscribers at www.ajnr.org

<http://dx.doi.org/10.3174/ajnr.A7859>

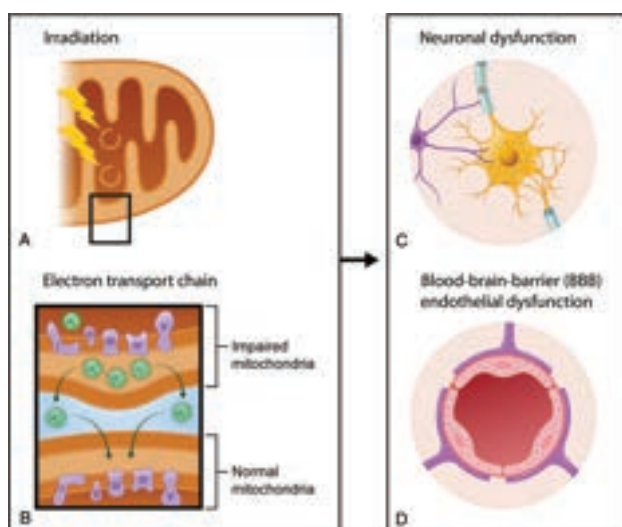


FIG 1. A, Ionizing irradiation causes mitochondrial DNA damage directly or secondarily via the production of reactive oxygen species (O_2) and free radicals, which result in injury to the mitochondrial DNA. B, These changes alter the function of the electron transport chain, which is composed of complex proteins (I–V) and mediates creation of adenosine triphosphate, and can result in impaired mitochondria. Also, O_2 can function as a signaling molecule in intermitochondrial communication and diffuse to the nearby mitochondria, resulting in further mitochondrial dysfunction. C and D, Mitochondrial dysfunction in neurons and endothelial cells can lead to a decrease of available ATP and consequent neuronal and BBB endothelial dysfunction. Inadequate availability of ATP in both neuron and BBB endothelial cells can impair the ion homeostasis within the intracellular and extracellular compartments and lead to neuronal hyperexcitability, which can trigger subsequent cortical spreading depression.

SMART syndrome and that female patients tend to have higher rates of recurrent episodes of SMART syndrome compared with male patients.^{5,8}

Pathophysiology

The pathophysiology of SMART syndrome has yet to be fully elucidated and is postulated to be multifactorial. Delayed brain irradiation injury involves white matter necrosis, vascular endothelial damage, demyelination, and gliosis.¹ There is little histologic evidence of the above-mentioned pathophysiology of SMART syndrome.^{2,4} Furthermore, radiation-induced mitochondrial dysfunction has been implicated in SMART syndrome pathophysiology (Fig 1).^{11,12}

Radiation-Induced Mitochondrial Dysfunction

Ionizing radiation therapy causes DNA damage not only in tumor cells but also in the normal brain tissues within the irradiation field directly or secondarily via the production of free radicals and reactive oxygen species (ROS) in the mitochondria.^{1,11} Ionizing radiation permanently impairs the mitochondria, leading to a persistent production of mitochondrial ROS.¹¹ Mitochondrial ROS can function as signaling molecules in intermitochondrial and mitochondrial-nuclear communication and promote subsequent long-term radiation effects.¹¹ Impairment of the mitochondria in neurons and endothelial cells can lead to

altered function of the electron transport chain. Consequently, impaired mitochondria in neurons and endothelial cells leads to a decrease in available adenosine triphosphate (ATP),¹² resulting in neuronal and BBB endothelial dysfunction. Inadequate availability of ATP in both neuron and BBB endothelial cells can impair the ion homeostasis within both intracellular and extracellular compartments and result in neuronal hyperexcitability.

Similarly, inadequate availability of ATP due to mitochondrial dysfunction has been also postulated in mitochondrial myopathy, encephalopathy, lactic acidosis, and stroke-like episodes (MELAS), which is related to pathogenic mitochondrial DNA gene mutations.¹³

Neuronal Dysfunction

Impaired neurons with radiation-induced mitochondrial dysfunction have Na, K-ATPase dysfunction due to a decrease of available ATP. Na, K-ATPase is important in maintaining extracellular ion homeostasis. When Na, K-ATPase is impaired, the K^+ ion and glutamate are shifted from the intracellular space to the extracellular space. Glutamate binds to *N*-methyl-*D*-aspartate receptors and α -amino-3-hydroxy-5-methyl-4-isoxazole propionic acid receptors, both of which are predominantly located in the dendritic spine and perisynaptic and extrasynaptic regions.¹⁴ The consequent elevation in extracellular glutamate results in a massive influx of Na^+ and Ca^{2+} into neurons through *N*-methyl-*D*-aspartate receptors. While Na^+ influx results in neuronal swelling, which is reversible, elevated intracellular Ca^{2+} contributes to neuronal hyperexcitability.^{14–16}

BBB Endothelial Dysfunction

BBB endothelial cells preserve ion homeostasis in the extracellular fluid, where the K^+ level is strictly regulated by BBB ion transports such as Na, K-ATPase.¹³ Reduced functioning of BBB ion transports due to insufficient available ATP can cause an increase in K^+ concentration in CSF and resulting neuronal hyperexcitability.¹³

Neuronal hyperexcitability is thought to trigger cortical spreading depression,¹⁷ which is a slowly propagating wave of transient regional depolarization of neurons, accompanied by suppression of all spontaneous or evoked electrical activity in that region,^{2,15,18} and can be observed in the acute phase of MELAS, hemiplegic migraine, and status epilepticus.

On nuclear and perfusion imaging, neuronal excitability is characterized by hypermetabolism/hyperperfusion, while subsequent spreading depression demonstrates hypometabolism/hypoperfusion. These imaging features can be used for differentiation from other etiologies such as a neoplastic process (tumor recurrence, intracranial metastasis, and leptomeningeal carcinomatosis).

Other Postulated Pathophysiology

Delayed radiation brain injury¹⁹ is postulated to induce vascular dysregulation resulting in BBB disruption and cerebral edema,²⁰ which is similar to the proposed etiology of posterior reversible encephalopathy syndrome (PRES). Posterior circulation vessels appear to be more vulnerable to dysregulation or injury.²¹ However, whether there is a degree of commonality underlying the pathophysiology remains to be determined, particularly given the disparate etiologic mechanisms of vascular injury as

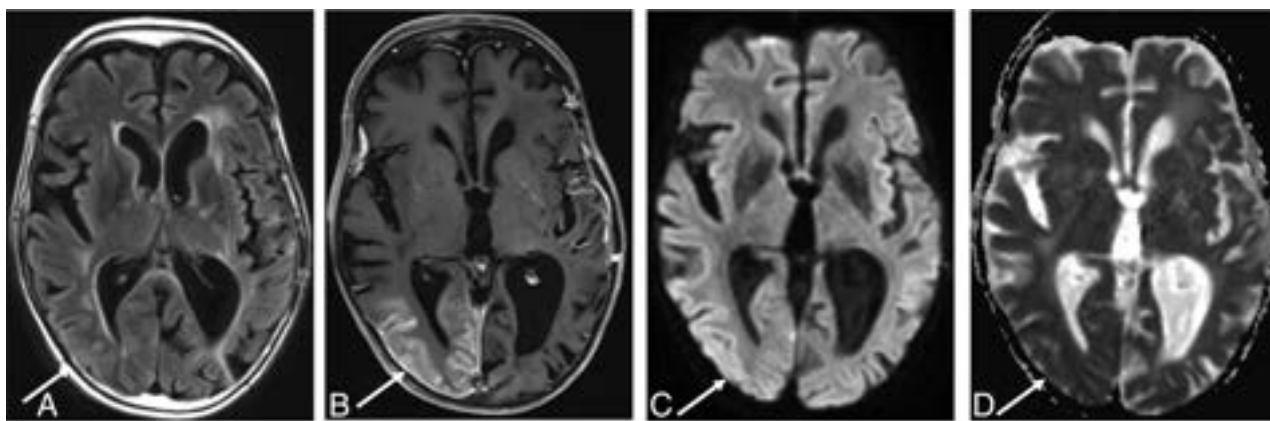


FIG 2. A 51-year-old man with a history of juvenile left posterior fossa tumor treated by surgery and whole-brain irradiation 45 years ago presented with acute visual changes and seizures. He was diagnosed with SMART syndrome and treated with corticosteroids and recovered from the symptoms. A FLAIR image (A) shows cortical hyperintensity, and the postcontrast T1 image (B) shows gyriform enhancement in the right temporo-occipital region (arrows), with an incidental right temporal dural-based meningioma. There is high signal on diffusion-weighted imaging (C) without low signal on ADC (D) (facilitated diffusion) (arrows).

well as the variance in distribution, because PRES usually involves the bilateral posterior circulation, while SMART syndrome usually occurs unilaterally and fails to respect vascular boundaries.

Symptoms, Clinical Work-Up, and Treatment

Symptoms. Patients with SMART syndrome often present with migraine-type headaches (35%–72%), which have been described as being severe and unilateral and can be associated with nausea, vomiting, and light sensitivity (photophobia) with or without an aura.^{2,3,22} Seizure is also a common symptom of SMART syndrome (35%–83%), which can be focal or generalized and is potentially lethal, warranting rapid control by antiseizure medications.^{22,23} Patients with SMART syndrome can develop stroke-like neurologic deficits (33%–87%), including visuospatial deficits (complete or partial), hemisensory deficits, hemiparesis, and speech impairment.^{3,5,8} The incidence of subsequent infarction is reported to be 14%–18%,^{8,22} and the rate of recurrence of SMART syndrome is 55%–62%.^{5,8,22}

A recent study has suggested that hemiparesis, speech impairment, and visual impairment may be likely to incompletely recover.⁵

Clinical Work-Up. For the assessment of SMART syndrome, MR imaging plays a crucial role in making the diagnosis, but CSF testing and electroencephalography are also important to exclude an infectious or neoplastic process and thus are often included in the work-up.^{4,5} Results of the CSF analysis are usually nonspecific, without evidence of neoplastic, inflammation, or an infectious process.^{2,5,23} Electroencephalography, especially with a long-term video, can show electrographic activities in nonconvulsive and convulsive status epilepticus in many cases,^{4,5,23} allowing clinicians to prescribe antiseizure medications as appropriate.

Treatment. Currently, there are no standard treatment guidelines for SMART syndrome due to the rarity of cases and the lack of uniformity in the approach to treatment, and treatment of symptoms is commonly performed.²⁴

Migraines and seizures are usually controlled by antimigraine and antiseizure medications, respectively. Aspirin and verapamil are thought to help reduce the recurrence and severity of SMART syndrome episodes.^{2,6} Antiplatelet therapy and blood pressure drugs are conventionally used in cases in which patients with SMART syndrome are suspected of having acute infarction following an acute SMART syndrome attack. In cases in which patients with SMART syndrome have severe headache and neurologic deficits, steroids (corticosteroids) are often used mainly for reducing focal cerebral edema.^{3,25} However, steroid use in the acute phase has been suggested to be related to incomplete symptom recovery,⁵ so the risks and benefits of steroid use in SMART syndrome should be carefully considered before administration.

L-arginine, which improves endothelial function and is used in stroke-like episodes of MELAS, is reported to be a potential treatment option based on the similarity of clinical and imaging features and postulated pathophysiology.²⁶

Imaging Features

Imaging plays a crucial role of the diagnosis of SMART syndrome, and brain MR imaging is the primary imaging technique of choice.^{2–4} In the acute phase of SMART syndrome, the typical MR imaging features are seen as reversible, unilateral, gyriform enhancement with T2 and FLAIR hyperintense cortical swelling in a distribution not consistent with vascular territories (Fig 2).^{2–5} Findings are typically unilateral, likely reflecting the distribution of the high-dose radiation treatment field, though there are a few reports of bilateral cerebral involvement.²² Involvement of the temporal and parietal lobes is often reported, followed by the occipital and frontal lobes.^{4,8,22} In the delayed phase, the conventional MR imaging features as well as symptoms resolve or become mitigated. Previous reports showed that gyriform enhancement typically resolves in 14–35 days but may last up to 84 days.⁴ There have been many reports regarding additional imaging features of conventional neuroimaging, advanced neuroimaging, and nuclear medicine imaging. In this section, we discuss additional imaging features of SMART syndrome that are not currently included in the diagnostic criteria but are important for assessment and

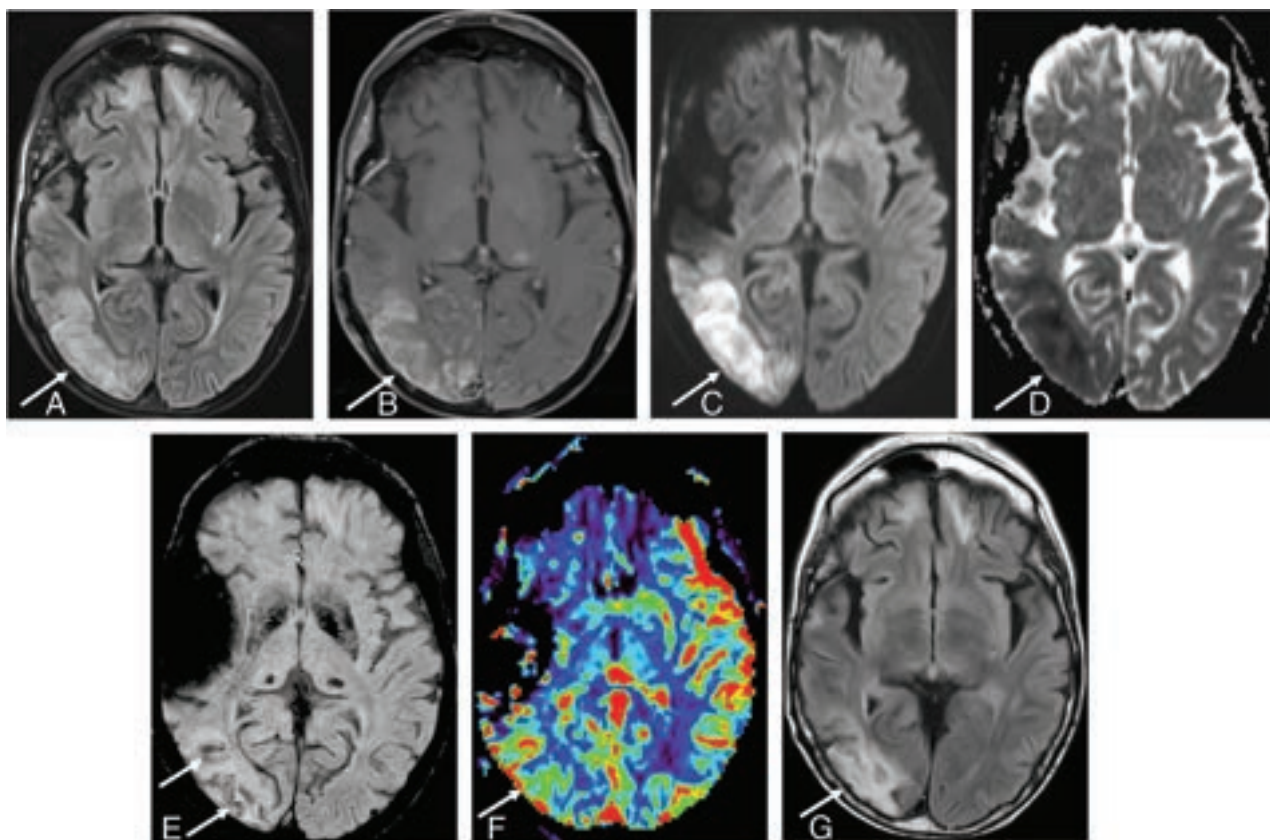


FIG 3. A 50-year-old man diagnosed with SMART syndrome. He had a history of pilocytic astrocytoma treated by resection and 60 Gy of radiation therapy 30 years ago and presented with left-sided hemiparesis, speech impairment, seizure, and migraine-like headache. He was diagnosed with SMART syndrome and treated by verapamil and aspirin, but residual symptoms (hemiparesis and speech impairment) remained. *A*, A FLAIR image shows cortical hyperintensity and involvement of subcortical white matter in the right temporo-occipital region (*arrow*). There is bifrontal subcortical white matter hyperintensity likely due to prior radiation injury. *B*, There is gyriform enhancement in the right temporo-occipital region (*arrow*) with restricted diffusion (*C* and *D*) (high signal on DWI and low signal on ADC) (*arrow*). *E*, SWI shows linear hypointensity along the subcortical white matter (*arrow*). *F*, Dynamic susceptibility contrast perfusion MR imaging shows an increase of CBV in the same area. *G*, After 3 months, FLAIR shows residual hyperintensity in the cortical and subcortical area (*arrow*).

prognosis. We also review imaging features of variants of SMART syndrome including PIPG and ALERT.

Conventional MR Imaging. In addition to classically described MR imaging features in the diagnostic criteria, white matter involvement adjacent to the gyriform enhancement and cortical swelling are observed in some cases, likely reflecting edema in severe SMART syndrome cases (Fig 3). The white matter involvement of SMART syndrome is suspected to portend worse recovery.⁵

DWI. DWI detects differences in Brownian motion of water molecules, and diffusion signal abnormalities are thought to reflect alterations in the random movement of water molecules in tissues secondary to altered internal microarchitecture and can be seen in many neurologic conditions. DWI also can characterize the neuronal hypertoxicity/cortical spreading phenomenon caused by transient neuronal cell Na, K-ATPase pump impairment due to abnormal synaptic ion homeostasis, resulting in restricted diffusion.^{27,28} Restricted diffusion is occasionally seen in acute SMART attack regions involving the subjacent white matter. When present, restricted diffusion is suggested to be related to delayed or incomplete recovery.^{5,8}

SWI and T2*WI. SWI and T2*WI are sensitive to susceptibility effects of iron within hemosiderin²⁹ and have been shown to identify microhemorrhage and radiation-induced intracranial cavernomas, which are commonly seen delayed complications of intracranial radiation therapy. SWI is more sensitive than T2*WI.³⁰⁻³² SWI and T2*WI show linear hypointensity in the subcortical white matter of the acute SMART attack region (Fig 3).⁵ There is no pathologic confirmation of this SWI white matter abnormality, but hemorrhagic transformation acutely affected by SMART syndrome is proposed.⁵ Also, patients with SMART syndrome with this SWI feature are suggested to experience incomplete recovery more frequently than patients without this SWI feature.⁵ Given that susceptibility imaging is consistently included in the routine brain protocol of many institutions, reporting of findings on SWI or T2*WI, even if negative, is important for radiologists and clinicians in terms of appropriate clinical management.

Perfusion Imaging. CT perfusion and DSC MR imaging findings have been reported in SMART syndrome. CT perfusion evaluates iodinated contrast passing from the intravascular to extravascular space of the ROI,³³ and DSC MR imaging uses the first pass of a

Table 1: Modified diagnostic criteria in addition to the criteria of Black et al⁶ for SMART syndrome

Criteria
A) Remote history of external beam cranial irradiation.
B) Prolonged signs and symptoms, which may be reversible or persistent, attributable to a unilateral cortical region. Clinical manifestations may include migraine-type headache with or without an aura, seizures, confusion, and stroke-like symptoms, including visuospatial deficits, hemisensory deficits, hemiparesis, and aphasia.
C) Reversible or sustained unilateral gyriform enhancement with or without T2WI/FLAIR hyperintensity involving the cortex and subjacent cerebral white matter in the irradiated area.
D) No definitive evidence of residual or recurrent brain tumor, and not attributable to other disorders.

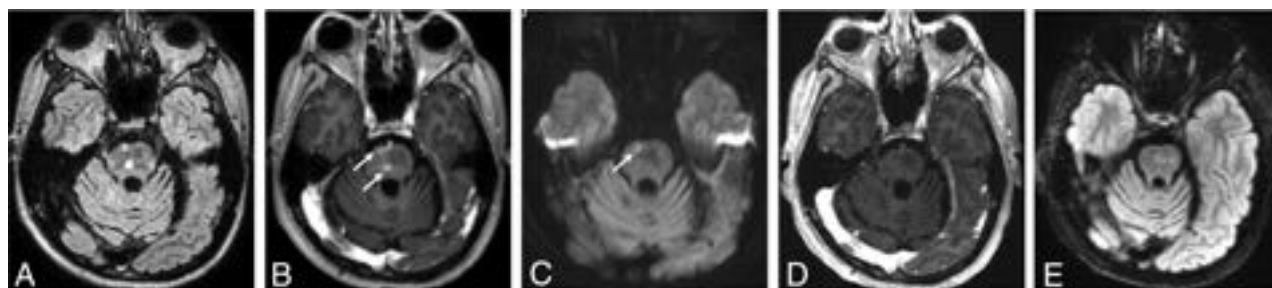


FIG 4. A 60-year-old man with brainstem SMART syndrome. He had a history of posterior fossa medulloblastoma treated with resection and 30 Gy of radiation therapy 16 years ago and presented with emotional lability and slurred speech. He completely recovered from the symptoms. A FLAIR image (A) shows hyperintensity in the central pons with peripheral patchy enhancement on the axial postcontrast T1-weighted image (arrows, B). C, DWI shows focal restricted diffusion in the corresponding area of the enhancing lesion (arrow). D and E, After 6 months, a post-contrast T1-weighted image shows resolution of enhancement with residual slight FLAIR hyperintensity.

paramagnetic contrast agent through the ROI monitored by a dynamic series of T2- or T2*-weighted images.³⁴ Both techniques allow assessment of local perfusion from first-pass contrast bolus analysis, including CBV and CBF. In the acute phase of a SMART syndrome attack, both CBV and CBF are increased (Fig 3), reflecting increased perfusion in the acute region,³⁵⁻³⁷ while in the postictal phase, CBV and CBF are suggested to decrease or become normalized.^{35,38} This perfusion pattern can help distinguish SMART syndrome from other etiologies such as local recurrence or carcinomatosis, which typically manifest as persistent elevated perfusion in the absence of targeted treatments, warranting sequential perfusion imaging.

MR Spectroscopy. MR spectroscopy is a noninvasive MR imaging technique that assesses the concentration of biomolecules in an ROI. One report demonstrated a decrease in NAA and an increase in Cr and Cho peaks,³⁹ while another article failed to find such differences.⁴⁰ There appear to be insufficient data currently available to verify the role of MR spectroscopy in SMART syndrome.

Nuclear Imaging. [¹⁸F] FDG-PET assesses regional cerebral glucose metabolism as a biomarker of neural activity and can allow localization of an epileptogenic zone in refractory epilepsy.⁴¹⁻⁴³ Some reports demonstrated hypermetabolism in the affected area of a SMART syndrome attack.^{41,42,44} Similarly, [¹⁸F] fluoroethyl-L-tyrosine amino acid (FET) PET has been used for status epilepticus^{45,46} and is suggested to show increased radiotracer uptake in the region of an acute SMART syndrome attack.^{36,45} Ictal brain perfusion SPECT using technetium Tc99m hexamethylpropyleneamine oxime was reported to show an increase of perfusion in the acute area of the SMART syndrome region,⁴⁴ while the opposite pattern was reported in the interictal period,⁴⁴ suggesting that

endothelial dysfunction, one of the postulated pathophysiologies of SMART syndrome, is transient.

Modified Diagnostic Criteria. SMART syndrome is a rare late-delayed brain irradiation complication, which occurs from 1 to 37 years after radiation therapy.⁴⁷ In 1995, Shuper et al⁴⁸ first reported 4 pediatric cases of complicated migraine-like episodes 1–3 years after brain irradiation without detailed MR imaging features, and in 2006, Black et al⁶ proposed diagnostic criteria of SMART syndrome, including clinical and imaging features. However, the signs and symptoms are known to occasionally be persistent, recurrent, or followed by infarction.^{4,8} Furthermore, migraines are one of the common clinical features but do not always occur, despite migraines being eponymous of this entity.⁵ Regarding imaging features, apart from classic cortical changes, the brainstem has been suggested to be involved (Fig 4),^{47,49} and T2WI and FLAIR hyperintensity in the cortical and subjacent white matter may occur and last for an extended period.⁵ DWI, SWI, and T2*WI, which are commonly included in brain MR imaging protocols, could show alterations in acute attack regions and provide a prognostic factor for clinical recovery.⁵ With reference to these clinical and imaging characteristics, the diagnostic criteria proposed in 2006 could be modified as suggested in Table 1, with the above-mentioned clinical and imaging updates. The main additions to the criteria proposed in 2006 are as follows: 1) The clinical signs and symptoms may be persistent, and 2) T2WI and FLAIR hyperintensity in the cortex and subjacent white matter in the irradiated areas may occur and persist.

Neuroimaging of SMART Syndrome Spectrum. Other reported delayed radiation therapy complications, which are proposed within the spectrum of SMART syndrome, include PIPG and ALERT.^{9,10}

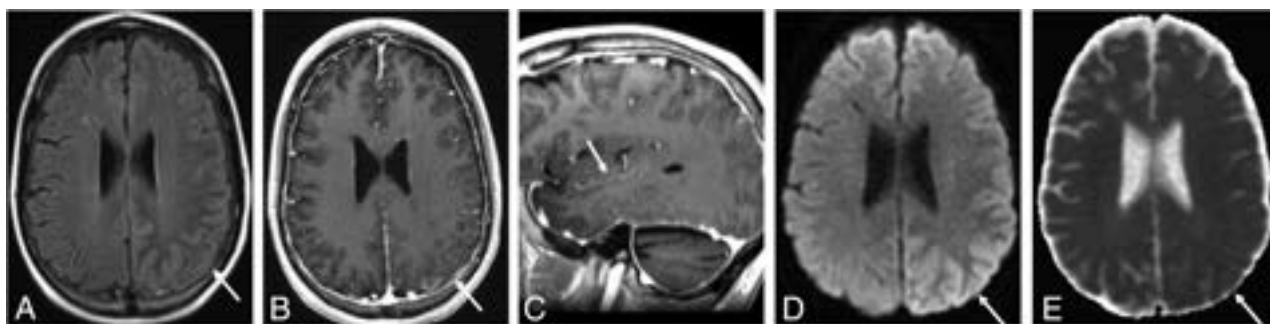


FIG 5. A 37-year-old man diagnosed with PIPG. He had a history of pineoblastoma treated with resection and a posterior fossa meningioma treated by resection and whole-brain irradiation 12 years before, and he presented with migraine-like headache, seizure, right-sided hemiparesis, and aphasia. He was treated with verapamil, aspirin, and valproic acid. He completely recovered from the symptoms. A FLAIR image (A) shows hyperintensity (arrow) with leptomenigeal enhancement in the left temporoparietal region on the axial (B) and sagittal (C) postcontrast T1-weighted images (arrows). Diffusion-weighted imaging (D) and ADC (E) show vasogenic edema (high signal on DWI without low signal on ADC) (arrows).

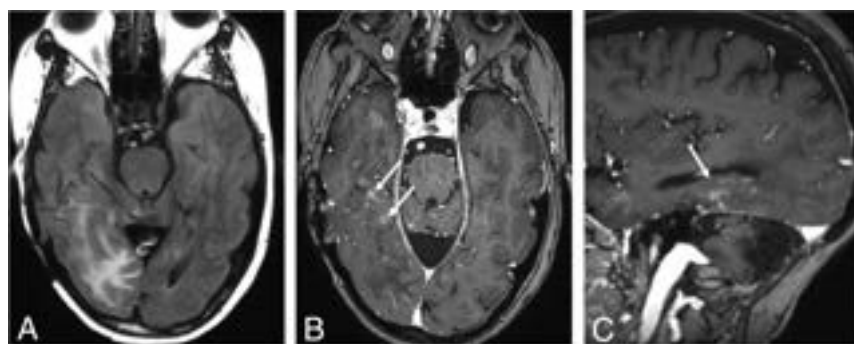


FIG 6. A 60-year-old man with ALERT syndrome. He had a history of atypical meningioma treated with resection and radiation therapy 12 years ago and presented with impaired consciousness, left homonymous hemianopia, and left-sided weakness. He was treated with steroids, but left-sided weakness persisted. The FLAIR (A) image shows hyperintensity with patchy enhancement in the right temporoparietal region on the axial (B) and sagittal (C) postcontrast T1-weighted images (arrows).

Table 2: Differential diagnosis of SMART syndrome

Category and Differential Diagnosis
Neoplastic process:
Tumor recurrence, leptomenigeal carcinomatosis
Ischemic or vascular process:
Subacute brain infarction, cortical vein thrombosis, PRES
Infectious process:
Cerebritis, meningoencephalitis
Hyperexcitability:
Hemiplegic migraine, status epilepticus
Genetic disease (hyperexcitability):
MELAS

PIPG was postulated in 2011, with clinical features of absence of acute headache, stroke-like deficits, and MR imaging features of focal cortical or leptomenigeal enhancement overlying an ictal region without adjacent white matter involvement (Fig 5).⁹ Unlike SMART syndrome, PIPG is observed in all cortical regions, while SMART syndrome occurs with predominance in the temporal, parietal, and occipital lobes. A correlation between steroid introduction and clinical improvement could not be established in patients with PIPG, unlike in patients with SMART syndrome or ALERT syndrome.²²

ALERT syndrome was established in 2013 and is characterized by clinical features of long-lasting impaired consciousness,

seizures, and stroke-like symptoms and by MR imaging features of multifocal patchy enhancement or focal leptomenigeal enhancement associated with T2/FLAIR intensity in the corresponding area (Fig 6).^{10,22} Steroid efficacy was shown to be evident in patients with ALERT syndrome, with rapid symptom recovery within a few days following steroid introduction.²²

Differential Diagnosis. Table 2 summarizes the differential diagnosis of SMART syndrome.

Neoplastic Process. Given that patients with SMART syndrome typically have a history of primary or secondary CNS

tumors treated with intracranial irradiation, the main differential diagnoses to consider include tumor recurrence and leptomenigeal carcinomatosis. These diseases should be ruled out because clinical management and treatment strategies are vastly different from those of SMART syndrome.

Tumor recurrence can show leptomenigeal or gyriform enhancement similar to imaging features of SMART syndrome and its spectrum on conventional MR imaging when the initial treated lesions are aggressive neoplasms or metastatic lesions,⁵⁰ like leptomenigeal carcinomatosis. Therefore, confirming the original tumor and referring to the images before brain irradiation are beneficial for a differential diagnosis. In addition, transient abnormalities on perfusion and nuclear imaging between the ictal and interictal or postictal phase may help differentiate tumor recurrence from SMART syndrome and its spectrum,^{35,38,40,44} because imaging abnormalities of tumor recurrence and metastasis do not resolve without antineoplastic treatment. Relatively short-interval MR imaging follow-up (2–3 weeks) after therapy to reduce symptoms may also be warranted because gyriform enhancement of SMART syndrome may resolve in a short interval, while tumor recurrence and intracranial metastasis do not.⁴ Leptomenigeal carcinomatosis is also unlikely in the setting of resolving gyriform or leptomenigeal

enhancement on follow-up MR imaging in the absence of treatment. CSF cytology, which is the criterion standard for leptomeningeal carcinomatosis with a high specificity (>95%), can be helpful for the diagnosis, though it has a low sensitivity (<50%).⁵¹

Ischemic or Vascular Process. Subacute brain infarction can present as cortical enhancement with T2 and FLAIR hyperintensity⁵² and can mimic the MR imaging findings of SMART syndrome. However, subacute brain infarction typically occurs along vascular territories. Consistency with a vascular territory of subacute brain infarction can be useful to differentiate it from SMART syndrome, which often involves the temporal, parietal, and occipital lobes and does not respect vascular boundaries. If there is concern for venous ischemia, adding MR venography to a brain MR imaging protocol could be beneficial to exclude cortical vein thrombosis.⁵³ PRES can mimic clinical features of SMART syndrome such as headache, neurologic deficits, and seizures but can typically show bilateral imaging features,⁵⁴ making SMART syndrome unlikely because SMART syndrome is unilateral.

Infectious Process. Cerebritis and meningoencephalitis can be ruled out on the basis of CSF analysis without evidence of an inflammatory or infectious process, as well as a clinical history and physical examination.

Hyperexcitable Processes. Hemiplegic migraine or status epilepticus can also mimic clinical and imaging features of SMART syndrome.^{55,56} Typically, patients with hemiplegic migraine have a family history of this condition. Lack of personal or family history of hemiplegic migraine and prior intracranial irradiation make the diagnosis of SMART syndrome more likely. Status epilepticus can overlap the clinical and imaging features of SMART syndrome, making differentiation from SMART syndrome difficult.

Genetic Disease. MELAS can show clinical features similar to those of SMART syndrome such as migraine-like headache, seizures, and stroke-like episodes. MR imaging of MELAS can also demonstrate a T2/FLAIR hyperintense cortex and subcortical white matter with leptomeningeal or cortical enhancement.^{13,57} The lesions of MELAS are usually multiple and asymmetric and can show an increased lactate peak with a decreased N-acetylaspartate peak on MR spectroscopy,⁵⁸ while those of SMART syndrome are typically localized in a region without established MR spectroscopy findings. The diagnosis of MELAS can be confirmed by clinical tests, molecular genetic testing, muscle biopsy showing an increase of lactate and pyruvate concentrations, mitochondrial mutations, and muscle biopsy showing ragged red fibers.

CONCLUSIONS

The diagnosis, clinical assessment, and management of SMART syndrome are challenging for radiologists and clinicians due to perplexing symptoms and imaging features that can overlap with other etiologies. This review has provided an updated comprehensive overview of SMART syndrome. This rare, delayed complication of radiation therapy is still scarcely reported, and further investigation is needed to concretely establish the

pathophysiology, treatment, and imaging features. Recognizing the updated clinical and imaging features of SMART syndrome can help to aid in proper clinical work-up and management.

ACKNOWLEDGMENTS

The authors thank Danielle Dobbs, graphic designer at the University of Michigan, Ann Arbor, Michigan, for creating Figure 1.

Disclosure forms provided by the authors are available with the full text and PDF of this article at www.ajnr.org.

REFERENCES

1. Turnquist C, Harris BT, Harris CC. **Radiation-induced brain injury: current concepts and therapeutic strategies targeting neuroinflammation.** *Neurooncol Adv* 2020;2:vdaa057 CrossRef Medline
2. Zheng Q, Yang L, Tan LM, et al. **Stroke-like migraine attacks after radiation therapy syndrome.** *Chin Med J (Engl)* 2015;128:2097–101 CrossRef Medline
3. Dominguez M, Malani R. **Stroke-like migraine attacks after radiation therapy (SMART) syndrome: a comprehensive review.** *Curr Pain Headache Rep* 2021;25:33 CrossRef Medline
4. Black DF, Morris JM, Lindell EP, et al. **Stroke-like migraine attacks after radiation therapy (SMART) syndrome is not always completely reversible: a case series.** *AJNR Am J Neuroradiol* 2013;34:2298–303 CrossRef Medline
5. Ota Y, Leung D, Lin E, et al. **Prognostic factors of stroke-like migraine attacks after radiation therapy (SMART) syndrome.** *AJNR Am J Neuroradiol* 2022;43:396–401 CrossRef Medline
6. Black DF, Bartleson JD, Bell ML, et al. **SMART: stroke-like migraine attacks after radiation therapy.** *Cephalalgia* 2006;26:1137–42 CrossRef Medline
7. Rigamonti A, Lauria G, Mantero V, et al. **SMART (stroke-like migraine attack after radiation therapy) syndrome: a case report with review of the literature.** *Neurol Sci* 2016;37:157–61 CrossRef Medline
8. Singh TD, Hajeb M, Rabinstein AA, et al. **SMART syndrome: retrospective review of a rare delayed complication of radiation.** *Eur J Neurol* 2021;28:1316–23 CrossRef Medline
9. Rheims S, Ricard D, van den Bent M, et al. **Peri-ictal pseudoprogression in patients with brain tumor.** *Neuro Oncol* 2011;13:775–82 CrossRef Medline
10. Di Stefano AL, Berzero G, Vitali P, et al. **Acute late-onset encephalopathy after radiotherapy: an unusual life-threatening complication.** *Neurology* 2013;81:1014–17 CrossRef Medline
11. Kam WW, Banati RB. **Effects of ionizing radiation on mitochondria.** *Free Radic Biol Med* 2013;65:607–19 CrossRef Medline
12. Averbek D, Rodriguez-Lafrasse C. **Role of mitochondria in radiation responses: epigenetic, metabolic, and signaling impacts.** *Int J Mol Sci* 2021;22:11047 CrossRef Medline
13. Iizuka T, Sakai F, Suzuki N, et al. **Neuronal hyperexcitability in stroke-like episodes of MELAS syndrome.** *Neurology* 2002;59:816–24 CrossRef Medline
14. Verma M, Lizama BN, Chu CT. **Excitotoxicity, calcium and mitochondria: a triad in synaptic neurodegeneration.** *Transl Neurodegener* 2022;11:3 CrossRef Medline
15. Ayata C, Lauritzen M. **Spreading depression, spreading depolarizations, and the cerebral vasculature.** *Physiol Rev* 2015;95:953–93 CrossRef Medline
16. Auffenberg E, Hedrich UB, Barbieri R, et al. **Hyperexcitable interneurons trigger cortical spreading depression in an Scn1a migraine model.** *J Clin Invest* 2021;131:e142202 CrossRef Medline
17. Vinogradova LV. **Initiation of spreading depression by synaptic and network hyperactivity: insights into trigger mechanisms of migraine aura.** *Cephalalgia* 2018;38:1177–87 CrossRef Medline
18. Dreier JP, Major S, Pannek HW, et al; COSBID study group. **Spreading convulsions, spreading depolarization and epileptogenesis in human cerebral cortex.** *Brain* 2012;135:259–75 CrossRef Medline

19. Greene-Schloesser D, Robbins ME, Peiffer AM, et al. **Radiation-induced brain injury: a review.** *Front Oncol* 2012;2:73 CrossRef Medline
20. Kessler AT, Bhatt AA. **Brain tumour post-treatment imaging and treatment-related complications.** *Insights Imaging* 2018;9:1057–75 CrossRef Medline
21. Anderson RC, Patel V, Sheikh-Bahaei N, et al. **Posterior reversible encephalopathy syndrome (PRES): pathophysiology and neuro-imaging.** *Front Neurol* 2020;11:463 CrossRef Medline
22. Di Stefano AL, Berzero G, Ducray F, et al. **Stroke-like events after brain radiotherapy: a large series with long-term follow-up.** *Eur J Neurol* 2019;26:639–50 CrossRef Medline
23. Fan EP, Heiber G, Gerard EE, et al. **Stroke-like migraine attacks after radiation therapy: a misnomer?** *Epilepsia* 2018;59:259–68 CrossRef Medline
24. Winter SF, Klein JP, Vaios EJ, et al. **Clinical presentation and management of SMART syndrome.** *Neurology* 2021 May 4. [Epub ahead of print] CrossRef
25. Jia W, Saito R, Kanamori M, et al. **SMART (stroke-like migraine attacks after radiation therapy) syndrome responded to steroid pulse therapy: report of a case and review of the literature.** *eNeurologicalSci* 2018;12:1–4 CrossRef Medline
26. Wai K, Balabanski A, Chia N, et al. **Reversible hemispheric hypoperfusion in two cases of SMART syndrome.** *J Clin Neurosci* 2017;43:146–48 CrossRef Medline
27. Pai V, Sitoh YY, Purohit B. **Gyriform restricted diffusion in adults: looking beyond thrombo-occlusions.** *Insights Imaging* 2020;11:20 CrossRef Medline
28. Moritani T, Smoker WR, Sato Y, et al. **Diffusion-weighted imaging of acute excitotoxic brain injury.** *AJNR Am J Neuroradiol* 2005;26:216–28 Medline
29. Greenberg SM, Vernooij MW, Cordonnier C, et al; Microbleed Study Group. **Cerebral microbleeds: a guide to detection and interpretation.** *Lancet Neurol* 2009;8:165–74 CrossRef Medline
30. Khanipour Roshan S, Salmela MB, McKinney AM. **Susceptibility-weighted imaging in stroke-like migraine attacks after radiation therapy syndrome.** *Neuroradiology* 2015;57:1103–09 CrossRef Medline
31. Goos JD, van der Flier WM, Knol DL, et al. **Clinical relevance of improved microbleed detection by susceptibility-weighted magnetic resonance imaging.** *Stroke* 2011;42:1894–900 CrossRef Medline
32. Cheng AL, Batool S, McCreary CR, et al. **Susceptibility-weighted MRI for detecting microbleeds.** *Stroke* 2013;44:2782–86 CrossRef Medline
33. Hoeffner EG, Case I, Jain R, et al. **Cerebral perfusion CT: technique and clinical applications.** *Radiology* 2004;231:632–44 CrossRef Medline
34. Welker K, Boxerman J, Kalnin A, et al; American Society of Functional Neuroradiology MR Perfusion Standards and Practice Subcommittee of the ASFNR Clinical Practice Committee. **ASFNR recommendations for clinical performance of MR dynamic susceptibility contrast perfusion imaging of the brain.** *AJNR Am J Neuroradiol* 2015;36:E41–51 CrossRef Medline
35. Nar Senol P, Gocmen R, Karli Oguz K, et al. **Perfusion imaging insights into SMART syndrome: a case report.** *Acta Neurol Belg* 2015;115:807–10 CrossRef Medline
36. Teske N, Albert NL, Forbrig R, et al. **Advanced imaging findings in stroke-like migraine attacks after radiation therapy (SMART) syndrome.** *Eur J Nucl Med Mol Imaging* 2023;50:1264–65 CrossRef Medline
37. Biju RD, Dower A, Moon BG, et al. **SMART (stroke-like migraine attacks after radiation therapy) syndrome: a case study with imaging supporting the theory of vascular dysfunction.** *Am J Case Rep* 2020;21:e921795 CrossRef Medline
38. Gelfand JM, Wintermark M, Josephson SA. **Cerebral perfusion-CT patterns following seizure.** *Eur J Neurol* 2010;17:594–601 CrossRef Medline
39. Gomez-Cibeira E, Calleja-Castano P, Gonzalez de la Aleja J, et al. **Brain magnetic resonance spectroscopy findings in the stroke-like migraine attacks after radiation therapy (SMART) syndrome.** *J Neuroimaging* 2015;25:1056–58 CrossRef Medline
40. Farid K, Meissner WG, Samier-Foubert A, et al. **Normal cerebrovascular reactivity in stroke-like migraine attacks after radiation therapy syndrome.** *Clin Nucl Med* 2010;35:583–85 CrossRef Medline
41. Pruitt A, Dalmau J, Detre J, et al. **Episodic neurologic dysfunction with migraine and reversible imaging findings after radiation.** *Neurology* 2006;67:676–78 CrossRef Medline
42. Bund C, Fahrner P, Gebus O, et al. **Sequential FDG PET and MRI findings in a case of SMART syndrome.** *Seizure* 2017;51:50–51 CrossRef Medline
43. Ponisio MR, Zempel JM, Day BK, et al. **The role of SPECT and PET in epilepsy.** *AJR Am J Roentgenol* 2021;216:759–68 CrossRef Medline
44. Jaraba S, Puig O, Miro J, et al. **Refractory status epilepticus due to SMART syndrome.** *Epilepsy Behav* 2015;49:189–92 CrossRef Medline
45. von Oertzen TJ. **PET and ictal SPECT can be helpful for localizing epileptic foci.** *Curr Opin Neurol* 2018;31:184–91 CrossRef Medline
46. Hutterer M, Ebner Y, Riemenschneider MJ, et al. **Epileptic activity increases cerebral amino acid transport assessed by 18F-fluoroethyl-L-tyrosine amino acid PET: a potential brain tumor mimic.** *J Nucl Med* 2017;58:129–37 CrossRef Medline
47. Ota Y, Leung D, Moritani T, et al. **Atypical imaging findings of presumed stroke-like migraine attacks after radiation therapy syndrome in the brainstem.** *Neuroradiology* 2021;63:1377–81 CrossRef Medline
48. Shuper A, Packer RJ, Vezina LG, et al. **“Complicated migraine-like episodes” in children following cranial irradiation and chemotherapy.** *Neurology* 1995;45:1837–40 CrossRef Medline
49. Maramattom BV, Panikar D. **Brainstem SMART syndrome: Be-SMART.** *Neurol India* 2022;70:1731–33 CrossRef Medline
50. Andersen BM, Miranda C, Hatzoglou V, et al. **Leptomeningeal metastases in glioma: the Memorial Sloan Kettering Cancer Center experience.** *Neurology* 2019;92:e2483–91 CrossRef Medline
51. Chamberlain MC, Glantz M, Groves MD, et al. **Diagnostic tools for neoplastic meningitis: detecting disease, identifying patient risk, and determining benefit of treatment.** *Semin Oncol* 2009;36:S35–45 CrossRef Medline
52. Karonen JO, Partanen PL, Vanninen RL, et al. **Evolution of MR contrast enhancement patterns during the first week after acute ischemic stroke.** *AJNR Am J Neuroradiol* 2001;22:103–11 Medline
53. Idiculla PS, Gurala D, Palanisamy M, et al. **Cerebral venous thrombosis: a comprehensive review.** *Eur Neurol* 2020;83:369–79 CrossRef Medline
54. Fugate JE, Rabinstein AA. **Posterior reversible encephalopathy syndrome: clinical and radiological manifestations, pathophysiology, and outstanding questions.** *Lancet Neurol* 2015;14:914–25 CrossRef Medline
55. Guerriero RM, Gaillard WD. **Imaging modalities to diagnose and localize status epilepticus.** *Seizure* 2019;68:46–51 CrossRef Medline
56. Pellerin A, Marois C, Mezouar N, et al. **Neuronal injuries evidenced by transient cortical magnetic resonance enhancement in hemiplegic migraine: a case report.** *Cephalalgia* 2019;39:323–25 CrossRef Medline
57. Bhatia KD, Krishnan P, Kortman H, et al. **Acute cortical lesions in MELAS syndrome: anatomic distribution, symmetry, and evolution.** *AJNR Am J Neuroradiol* 2020;41:167–73 CrossRef Medline
58. Cheng W, Zhang Y, He L. **MRI features of stroke-like episodes in mitochondrial encephalomyopathy with lactic acidosis and stroke-like episodes.** *Front Neurol* 2022;13:843386 CrossRef Medline

A Pragmatic Randomized Trial Comparing Surgical Clipping and Endovascular Treatment of Unruptured Intracranial Aneurysms

T.E. Darsaut, J.M. Findlay, M.W. Bojanowski, C. Chalaala, D. Iancu, D. Roy, A. Weill, W. Boisseau, A. Diouf, E. Magro, M. Kotowski, M.B. Keough, L. Estrade, N. Bricout, J.-P. Lejeune, M.M.C. Chow, C.J. O'Kelly, J.L. Rempel, R.A. Ashforth, H. Lesiuk, J. Sinclair, U.-E. Erdenebold, J.H. Wong, F. Scholtes, D. Martin, B. Otto, A. Bilocq, E. Truffer, K. Butcher, A.J. Fox, A.S. Arthur, L. Létourneau-Guillon, F. Guilbert, M. Chagnon, J. Zehr, B. Farzin, G. Gevry, and J. Raymond



ABSTRACT

BACKGROUND AND PURPOSE: Surgical clipping and endovascular treatment are commonly used in patients with unruptured intracranial aneurysms. We compared the safety and efficacy of the 2 treatments in a randomized trial.

MATERIALS AND METHODS: Clipping or endovascular treatments were randomly allocated to patients with one or more 3- to 25-mm unruptured intracranial aneurysms judged treatable both ways by participating physicians. The study hypothesized that clipping would decrease the incidence of treatment failure from 13% to 4%, a composite primary outcome defined as failure of aneurysm occlusion, intracranial hemorrhage during follow-up, or residual aneurysms at 1 year, as adjudicated by a core lab. Safety outcomes included new neurologic deficits following treatment, hospitalization of >5 days, and overall morbidity and mortality (mRS > 2) at 1 year. There was no blinding.

RESULTS: Two hundred ninety-one patients were enrolled from 2010 to 2020 in 7 centers. The 1-year primary outcome, ascertainable in 290/291 (99%) patients, was reached in 13/142 (9%; 95% CI, 5%–15%) patients allocated to surgery and in 28/148 (19%; 95% CI, 13%–26%) patients allocated to endovascular treatments (relative risk: 2.07; 95% CI, 1.12–3.83; $P = .021$). Morbidity and mortality (mRS > 2) at 1 year occurred in 3/143 and 3/148 (2%; 95% CI, 1%–6%) patients allocated to surgery and endovascular treatments, respectively. Neurologic deficits (32/143, 22%; 95% CI, 16%–30% versus 19/148, 12%; 95% CI, 8%–19%; relative risk: 1.74; 95% CI, 1.04–2.92; $P = .04$) and hospitalizations beyond 5 days (69/143, 48%; 95% CI, 40%–56% versus 12/148, 8%; 95% CI, 5%–14%; relative risk: 0.18; 95% CI, 0.11–0.31; $P < .001$) were more frequent after surgery.

CONCLUSIONS: Surgical clipping is more effective than endovascular treatment of unruptured intracranial aneurysms in terms of the frequency of the primary outcome of treatment failure. Results were mainly driven by angiographic results at 1 year.

ABBREVIATIONS: EVT = endovascular treatment; RR = relative risk; UIA = unruptured intracranial aneurysm

Unruptured intracranial aneurysms (UIAs) are increasingly discovered as incidental imaging findings, with an estimated

prevalence of 2%–5% of the adult population, but most remain asymptomatic.^{1–3} Ruptures are infrequent, on the order of 1% per

Received February 27, 2023; accepted after revision April 10.

From the Division of Neurosurgery (T.E.D., J.M.F., M.B.K., M.M.C.C., C.J.O.), Department of Surgery, and Department of Radiology and Diagnostic Imaging (J.L.R., R.A.A.), Mackenzie Health Sciences Centre, University of Alberta Hospital, Edmonton, Alberta, Canada; Service of Neurosurgery (M.W.B., C.C.), Department of Surgery, and Service of Neuroradiology (D.J., D.R., A.W., W.B., A.D., M.K., L.L.-G., F.G., J.R.), Department of Radiology, Centre Hospitalier de l'Université de Montréal, Montreal, Québec, Canada; Service of Neurosurgery (E.M.), Centre Hospitalier Universitaire Cavale Blanche, Institut National de la Santé et de la Recherche Médicale Unité Mixte de Recherche 1101 LaTIM, Brest, France; Interventional Neuroradiology (L.E., N.B.), and Service of Neurosurgery (J.-P.L.), Centre Hospitalier Universitaire de Lille, Lille, France; Section of Neurosurgery (H.L., J.S.), Department of Surgery, and Department of Medical Imaging (U.-E.E.), Section of Interventional Neuroradiology, Ottawa Hospital, University of Ottawa, Ottawa, Ontario, Canada; Division of Neurosurgery (J.H.W.), Foothills Medical Centre, University of Calgary, Calgary, Alberta, Canada; Departments of Neurosurgery (F.S., D.M.) and Medical Physics (B.O.), Division of Medical Imaging, Centre Hospitalier Universitaire de Liège, Liège, Belgium; Service of Neurosurgery (A.B., E.T.), Centre Hospitalier Régional de Trois-Rivières, Trois-Rivières, Québec, Canada; Clinical Neurosciences (K.B.), Prince of Wales Clinical School, University of New South Wales, Randwick, New South Wales, Australia; Department of Medical Imaging (A.J.F.), University of Toronto, Toronto,

Ontario, Canada; Department of Neurosurgery (A.S.A.), University of Tennessee Health Science Center and Semmes-Murphey Clinic, Memphis, Tennessee; Department of Mathematics and Statistics (M.C., J.Z.), Université de Montréal, Montréal, Québec, Canada; and Research Centre of the University of Montreal Hospital Centre (B.F., G.G., J.R.), Interventional Neuroradiology Research Laboratory, Montreal, Québec, Canada.

This work was funded by Canadian Institutes of Health Research (MOP119554).

Please address correspondence to Jean Raymond, MD, Centre Hospitalier de l'Université de Montréal, Department of Radiology; Service of Neuroradiology, 1000 Saint-Denis St, Room D03-5462B, Montreal, Québec, Canada H2X 0C1; e-mail: jean.raymond@umontreal.ca; @RaymondJeanMD1

Indicates open access to non-subscribers at www.ajnr.org

Indicates article with online supplemental data.

Evidence-Based Medicine Level 1.

<http://dx.doi.org/10.3174/ajnr.A7865>

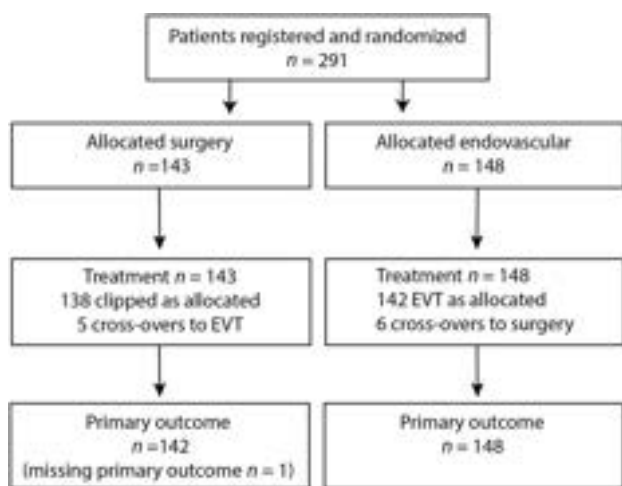


FIG 1. Study flowchart.

year.⁴⁻⁶ The best management of patients with UIAs is uncertain, with significant variability and disagreement among clinicians.⁷ Despite the lack of level 1 evidence of benefit, preventive endovascular or surgical treatments are commonly used.⁶ Endovascular treatment (EVT) has progressively supplanted surgical clipping after coiling was shown to be superior for ruptured aneurysms in 2002.⁸ However, for unruptured aneurysms, the safety and efficacy of the 2 treatments have never been previously compared in a randomized trial.⁹

It remains unclear whether UIAs should be repaired, and if so, which treatment is best. A proper answer to these questions would require nearly a thousand patients to be followed for many years, using a hard clinical outcome such as disabling stroke or death as a primary end point. An attempt to address the question of whether UIAs should be treated was interrupted in 2009 due to insufficient recruitment.¹⁰ Surgical clipping, though more invasive, is reputed to be more effective than endovascular treatment, but this possibility has never been proved.¹¹ The Collaborative UnRuptured Endovascular versus Surgery (CURES) trial was designed to test the hypothesis that surgical clipping of intradural, saccular UIAs was superior to endovascular management in decreasing the proportion of patients experiencing treatment failure, a composite primary outcome defined as failure of the allocated treatment technique to occlude the aneurysm, aneurysmal rupture during follow-up, or a residual aneurysm on angiography at 1 year, decreasing from 14% to 3%.¹² We here report the final results of the CURES trial.

MATERIALS AND METHODS

This report follows the CONSolidated Standards Of Reporting Trials (CONSORT) guidelines. CURES was an investigator-led, pragmatic, multicenter, randomized (1:1) parallel-group trial conducted in 5 Canadian and 2 European centers (Montreal, Edmonton, Ottawa, Trois-Rivières, and Calgary in Canada; and Liège, Belgium, and Lille, France). The trial, conceived as a pilot before a larger pivotal effort, was initially funded by the Canadian Institutes of Health Research (MOP 119554). The protocol, published in 2011,¹² was approved by the local institutional review boards of all participating centers, and all patients provided written informed consent. Data capture and

management were through secure servers in compliance with Good Clinical Practice requirements. The trial was monitored in Montreal, Canada. Electronic case report forms were simple, and data collection was kept to a minimum to facilitate completion by ordinary care personnel. Neuropsychological tests were not required by protocol. There were no preplanned interim efficacy analyses or stopping rules for safety or futility because both treatments were in common clinical use. The number of patients to be recruited was estimated to be 118 per group (with a statistical power of 0.80 and a 2-sided α of .05), or 260 patients (to account for losses and cross-overs). The trial was launched in September 2010, but participation was below expectations. The Steering Committee decided to publish interim results in 2016 to encourage center participation and before re-submission for financial support.¹³ Further funding was declined in 2016, but the Steering Committee opted for trial continuation until the initiation of the Comprehensive Aneurysm Management (CAM) study on UIAs in 2020.¹⁴ The last patient was recruited in May 2020. In May 2021, after examination of the blinded 1-year outcome data, the Data Safety Monitoring Committee recommended trial continuation, but the Steering Committee decided to report the CURES trial.

Patients

CURES was designed to address the question of the best treatment for patients with UIAs eligible for both surgical or endovascular options. Patients were recruited from outpatient neurosurgery or neuroradiology clinics by participating physicians at each study site, which all offer specialized neurovascular care. Independent (mRS of <3) patients 18 years of age and older with any intradural, saccular, nonbasilar UIA, 3–25 mm (in maximal cross-sectional diameter), were offered participation if they had at least 10 years of life expectancy. Patients were excluded if their aneurysms were thought to require endovascular flow diversion or parent vessel occlusion, with or without surgical bypass. Patients with multiple aneurysms were not excluded, but 1 index aneurysm was to be chosen as the main target. The protocol was modified on October 22, 2014, to include patients with recurrent but previously treated aneurysms ($n = 10$); on May 9, 2016, to allow prerandomization when approved by the local institutional review board;¹⁵ and on June 25, 2019, to include patients considered for endovascular flow diversion ($n = 9$). A prospective screening log of potential participants was not required.

Interventions

Patients were treated with surgical clipping or endovascular methods as per local practices, with technical details left to the individual operators.

Outcome Measures

The composite primary outcome measure, “treatment failure,” occurred under the following circumstances: 1) failure of aneurysm occlusion using the allocated treatment technique, 2) intracranial hemorrhage during follow-up, or 3) when a residual or recurrent index aneurysm was found using CTA, MRA, or conventional angiography at 1 year. Cross-overs to the other treatment arm, with no attempt to occlude the aneurysm, were not considered treatment failures. Additional procedures directed against the index aneurysm performed during the follow-up period were considered treatment failures. One primary poor efficacy

Table 1: Patient and index aneurysm characteristics

Characteristics	Surgical (<i>n</i> = 143)	Endovascular (<i>n</i> = 148)
Patient		
Age at treatment (mean) (SD) (yr)	56.1 (10)	56.9 (10)
Female sex (No.) (%)	98 (69%)	105 (71%)
Pretreatment mRS score (No.) (%)		
0	120 (84)	114 (77)
1	22 (15)	29 (20)
2	1 (1)	5 (3)
Patients with multiple aneurysms (No.) (%)	26 (18)	38 (26)
Index aneurysm location (No.) (%)		
Anterior circulation (No.) (%)	139 (97)	143 (97)
ICA		
Ophthalmic/paraophthalmic	17 (12)	18 (12)
Posterior communicating/anterior choroidal	16 (11)	29 (20)
Carotid terminus	13 (9)	12 (8)
MCA		
MCA bifurcation/M1	43 (30)	48 (32)
ACA		
Anterior communicating	43 (30)	31 (21)
Pericallosal	5 (3)	5 (3)
Other	2 (1)	0
Posterior circulation (No.) (%)	4 (3)	5 (3)
PCA	0	1 (1)
SCA	0	2 (1)
PICA	4 (3)	2 (1)
Index aneurysm size (mean) (range) (mm)	7.7 (3–20)	7.9 (3–24)
3–9 mm (%)	112 (78)	115 (78)
10–15 mm (%)	26 (18)	28 (19)
>15 mm (%)	5 (3)	5 (3)
Aneurysm neck ≥ 4 mm	56 (39)	56 (38)
Recurrent, previously treated index aneurysm	7 (5)	3 (2)
Medical history		
Pain/headache	15 (10)	19 (13)
Cranial nerve palsy	4 (3)	4 (3)
Stroke/TIA	5 (3)	3 (2)
History of previous SAH from another aneurysm	19 (13)	18 (12)
Hypertension	73 (51)	71 (48)
Current smoker	56 (39)	62 (42)
Excessive alcohol	14 (10)	9 (6)
Positive family history	27 (19)	26 (18)
Treatment		
Time from randomization to treatment (mean) (SD) (wk)	17.8 (22)	9.4 (18)
Adherence to assigned treatment (No.) (%)	138 (97)	142 (96)
Index aneurysm rupture after randomization, before treatment	1 (1)	0
Additional nonindex aneurysms treated at same time	14 (10)	15 (10)
Stent-assisted coiling (non-flow-diverting stent) (No.) (%)	NA	29 (19)
Flow-diverting stent (No.) (%)	NA	9 (6)

Note:—NA indicates not applicable.

outcome was allocated per patient; when a patient reached >1 outcome, the following hierarchical order was used to classify each patient: intracranial hemorrhage during follow-up > initial treatment failure > residual aneurysm at 12-month imaging follow-up.

Secondary end points included the individual components of the composite primary outcome, as well as treatment safety outcomes: overall morbidity (mRS > 2) and mortality at 1 year, new perioperative (30 days) neurologic deficits (defined as any new weakness, sensory abnormality, decreased level of consciousness, or cranial nerve deficit), perioperative morbidity (mRS > 2) measured at discharge, peritreatment hospitalization lasting >5 days, and discharge to a location other than home.

Follow-up tests and visits were standard per local practices, including neurologic examinations, brain imaging studies, and a functional assessment according to the mRS at discharge, 6 weeks, and 1 year using a standardized questionnaire.¹⁶

A vascular imaging study (conventional angiography, CTA, or MRA) at a mean of 12 (± 2) months to verify aneurysm occlusion was expected as standard care, to be centrally adjudicated by an independent core lab according to a previously validated classification system.^{17,18} The protocol did not impose a common follow-up imaging technique to be used in all patients because surgical patients are typically followed by CTA, while patients undergoing EVT are followed by MRA. Blinding of the core lab assessors for the presence of surgical clips or endovascular devices was not possible.

Randomization

Parallel-group randomization (1:1) was concealed, generated through a web-based platform (<https://www.medscinet.com/cures>), and minimized for age older than 60 years, aneurysm size of ≥ 15 mm, and posterior circulation location (posterior communicating artery aneurysms were considered to be in the anterior circulation). Blinding to treatment assignment of patients, physicians, and outcome assessors was not done.

Statistical Analyses

All data were analyzed by statisticians (J.Z., M.C.). Patient and aneurysm characteristics and primary and secondary outcomes are described by group using mean and SD for continuous variables and percentages for categorical variables. Analyses were intent-to-treat, but as-treated analyses were also performed.

The impact of missing data on the primary outcome results was studied using a worst-case-scenario sensitivity analysis, in which the missing data ($n = 1$) were replaced by a bad outcome. Relative risk (RR) was estimated using a generalized estimating equation with a binomial distribution and a log-link function reporting 95% confidence intervals. No adjustments for residual confounding factors were made. The analyses of interactions between prespecified subgroups of interest and treatment were made by adding subgroup variables and interaction in the generalized estimating equation models. Subgroups predefined according to minimization criteria (age, aneurysm size, and location) were examined, regardless of the results of tests for interactions. There were no corrections

Table 2: Primary and secondary outcomes

	Surgical (<i>n</i> = 142)	Endovascular (<i>n</i> = 148)
Primary outcome ^a (composite) ^b (No.) (%)	13 (9)	28 (19)
Failure to occlude aneurysm with allocated technique	1 (1)	5 (3)
Intracranial hemorrhage during FU	2 (2)	1 (1)
Saccular residual aneurysm	10 (7)	22 (15)
Missing primary outcome	1 (1)	0
Secondary outcomes	<i>n</i> = 143	<i>n</i> = 148
No. of days hospitalized per treatment (mean) (median) (range)	6.7 (5) (1–25)	3.8 (1) (0–122)
No. of patients hospitalized for >5 days (No.) (%)	69 (48)	12 (8)
Patients with postoperative morbidity (discharge mRS > 2) (No.) (%)	3 (2)	4 (3)
Patients with new neurologic deficits following treatment (No.) (%)	32 (22)	19 (12)
Discharge location		
Home (No.) (%)	135 (94)	142 (96)
Other hospital (No.) (%)	4 (3)	2 (1)
Rehabilitation center (No.) (%)	3 (2)	3 (2)
Death (No.) (%)	1 (1)	1 (1)
1-year mRS (No.) (%)		
0	79 (55)	93 (63)
1	55 (38)	41 (28)
2	6 (4)	11 (7)
3	1 (1)	1 (1)
4	1 (1)	1 (1)
5	0	0
6	1 (1)	1 (1)
Death and dependency (mRS > 2) at 1 year (No.) (%)	3 (2)	3 (2)
Mean (SD) time of 1-year mRS assessment (mo)	15.1 (9.4)	15.4 (6.4)
Retreatment of index aneurysm during follow-up (No.) (%)	3 (2)	8 (5)
Angiographic outcome at 1 year		
Complete aneurysm occlusion (No.) (%)	114 (80)	84 (57)
Residual aneurysm neck (No.) (%)	16 (11)	40 (27)
Saccular residual aneurysm (No.) (%)	11 (8)	23 (16)
1-year imaging not available (No.) (%) ^c	2 (1)	1 (1)
CTA/MRA/catheter angiographic determinations (No.) (%)	116 (81), 14 (10), 11 (8)	14 (10), 106 (72), 27 (18)
Mean (SD) time of 1-year imaging assessment (mo)	15.7 (10.0)	15.2 (8.2)

Note:—FU indicates follow-up.

^a RR for the primary outcome: 2.07; 95% CI, 1.12–3.83; *P* = .021.

^b One primary outcome was assigned per patient. When a patient had >1 primary outcome, it was assigned on the basis of the following hierarchy: intracranial hemorrhage > failure of technique > residual aneurysm.

^c There was 1 death in each group.

for multiplicity of analyses. Analyses were performed using SAS software, Version 9.4 (SAS Institute) and SPSS, Version 26 (IBM) with a significance level of 5%.

Roles of the Funding Source and Data Integrity

Neither the funding agency (Canadian Institutes of Health Research) nor the sponsor (Université de Montréal) had any part in the study design, data collection, analysis, or reporting and had no access to the data or source documents.

RESULTS

From September 2010 to May 2020, two hundred ninety-one patients with 376 UIAs (291 index aneurysms and 85 additional aneurysms) were recruited. Patients who registered and had treatment randomly allocated are presented in the flow chart (Fig 1).

Baseline patient and aneurysm characteristics were similar (Table 1). Of 291 patients, 138/143 patients randomly allocated to surgery underwent clipping; 5 were treated with EVT. Of the 148 patients randomly allocated EVT, 142 underwent EVT and 6 were treated by surgery.

The 1-year primary outcome data are available for 290/291 patients (99%; Table 2): 13/142 patients (9%; 95% CI, 5%–15%) in the surgical group and 28/148 (19%; 95% CI, 13%–26%) in the EVT group reached the primary outcome (RR: 2.07; 95% CI, 1.12–3.83; *P* = .021). No primary outcomes occurred in patients who crossed over, and the as-treated analysis of the primary end point gave similar results (RR: 2.10; 95% CI, 1.13–3.88; *P* = .019). A worst-case-scenario analysis in which a poor outcome was imputed for the 1 missing surgical primary outcome did not significantly change the results. In the endovascular group, the “treatment failure” primary outcome was assigned because of immediate failure in 5 patients, a fatal treatment-related subarachnoid hemorrhage in 1, and saccular aneurysmal recurrences at 1 year in 22 patients (2 retreated by EVT; 6, by clipping; or 14 left untreated). In the surgical group, treatment failure was assigned as follows: 1 patient who awoke hemiparetic from the operation and was immediately returned to the operating room for clip removal, 1 surgical patient who died from aneurysmal rupture the day before scheduled treatment, 1 patient who died 2.5 years after treatment due to rupture of a contralateral coiled aneurysm (the clipped aneurysm remained occluded), and 10 patients who had residual saccular aneurysms at 1 year. These recurrences were treated with stent-assisted coiling (*n* = 3) or left untreated at the time of reporting (*n* = 7).

Intent-to-treat exploratory subgroup analyses are detailed and illustrated in the forest plot (Fig 2). The interaction test was not significant for age, size, or neck width. There was a significant interaction with location (*P* = .001), with treatment failures more frequent in patients with MCA aneurysms in the EVT group (RR: 13.44; 95% CI, 1.85–97.5).

Secondary outcomes, including the individual components of the primary outcome and safety outcomes, as well as pretreatment, discharge, and 1-year follow-up mRS scores are presented in Table 2 and Fig 3. Perioperative safety outcomes were in favor of EVT: New neurologic deficits occurred in 32/143 surgical patients (22%; 95% CI, 16%–30%) compared with 19/148 (12%;

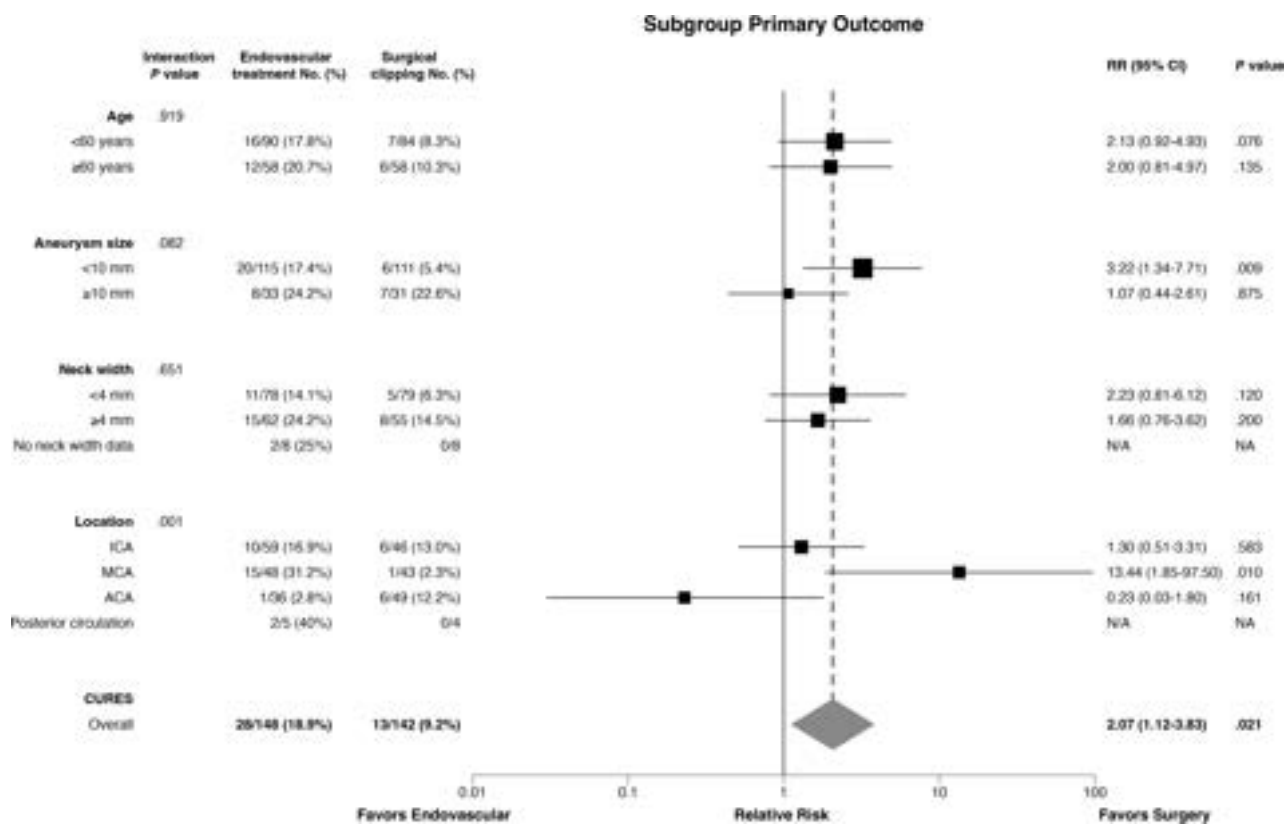


FIG 2. Subgroup analyses of primary outcome. NA indicates not applicable.

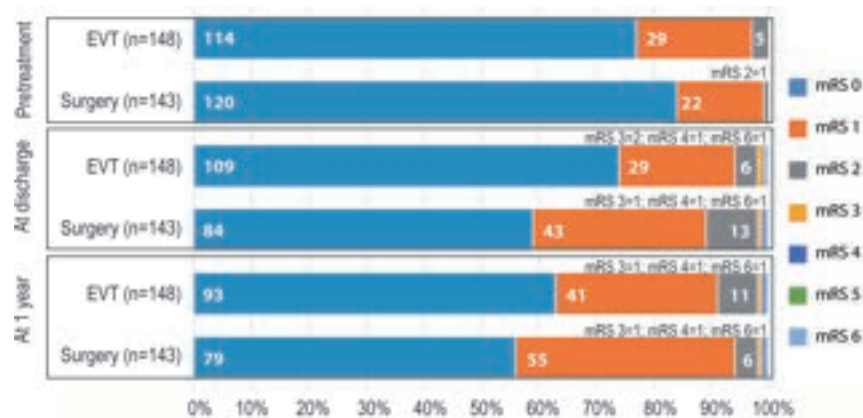


FIG 3. Clinical status at baseline, hospital discharge, and 1-year follow-up.

95% CI, 8%–19%) patients allocated to EVT ($P = .04$). Hospitalization for > 5 days occurred in 69/143 (48%; 95% CI, 40%–56%) surgical patients, compared with 12/148 (8%; 95% CI, 5%–14%) patients treated endovascularly (RR: 0.18; 95% CI, 0.11–0.31; $P < .001$). Perioperative safety outcomes, such as death or dependency at discharge or discharge to a location other than home, were similar. Patients with a discharge mRS of 0 were more frequent in the endovascular group (Fig 3). All 291 patients had clinical follow-up data: By 1 year, 1 surgical patient had died and 2 were disabled (mRS > 2), 1 patient allocated to EVT had died, and 2 were disabled.

Serious adverse events occurred in 31/143 (22%; 95% CI, 16%–29%) surgical patients and 15/148 (10%; 95% CI, 6%–16%) patients treated endovascularly ($P = .01$) (details in the Online Supplemental Data). One-year follow-up imaging is available for 288 patients: Complete occlusions were more frequent in patients allocated to surgical management, while saccular aneurysms and residual necks were more frequent in patients allocated to EVT (Table 2).

DISCUSSION

CURES provides randomized evidence that clipping is more effective than EVT in terms of angiographic results at 1 year. This benefit comes at the cost of a more invasive intervention, associated with a longer hospitalization and a greater risk of posttreatment neurologic deficits. However, death and dependency at discharge and 1 year were similarly infrequent in both groups.

The primary end point of the trial was a composite that attempted to capture in 1 judgment the efficacy of treatment. This outcome combined immediate results (failure of the allocated treatment technique) and aneurysm rupture during follow-up and, to account for the short follow-up, an angiographic outcome of “residual aneurysm” at 1 year. Angiographic outcomes are

necessary in practice because clinicians cannot wait until aneurysms rupture to judge the results of each procedure.¹⁹ Angiography is the most common primary outcome of aneurysm trials.^{18,20-23} Residual aneurysm was used to judge treatment failure because this angiographic category has been shown to be reliable and its clinical significance has been constant across raters, imaging modalities, and treatments.^{17,18} This reliability is important because different angiographic imaging modalities are routinely used to follow surgically clipped (mostly CTA) versus endovascularly treated aneurysms (mostly MRA). Had we used “complete occlusion” as the angiographic measure of efficacy, the conclusion would not have been different.

The 1-year timeframe was selected to be long enough for patients to recover from transient morbidity and to allow postcoiling aneurysm recurrences to occur.^{24,25}

The clinical significance of angiographic recurrences in terms of aneurysm rupture is unclear, but recurrences are potentially concerning. There were no posttreatment ruptures of index aneurysms during the course of this study. Case series and meta-analyses have reported hemorrhages after endovascular coiling in <1% of patients, but retreatments were performed in 10%–22% of patients.^{26,27} The better angiographic outcomes of surgery may translate into clinical benefits if, with time, delayed recurrent aneurysms rupture or if there are complications from retreatment of recurrent aneurysms.

CURES was fully integrated into clinical practice, with no extra risks, tests, or costs, and data were collected by ordinary care personnel at the time of routine follow-up visits.²⁸ The main drawback of the approach is the lack of blinding. To decrease the risk of bias, we used death or dependency (mRS > 2) as the clinical outcome at 1 year, a choice that has been shown to be reliable.²⁹

Subgroup exploratory findings suggest that surgery is particularly more effective than EVT in MCA aneurysms. A trial dedicated to MCA aneurysms has recently been proposed.³⁰

The use of surgical clipping for aneurysms is declining, and concerns have been raised that this trend may lead to a decrease in open surgical expertise.³¹⁻³³ The surgical angiographic results presented here are promising, but they come with added initial morbidity. It would be ill-advised to prematurely abandon a treatment that could provide better long-term clinical outcomes, but this remains to be shown. Whether patients with UIAs should be treated at all also remains a dilemma. These questions are now being addressed by the CAM study.^{14,34}

The limitations to this study include the relatively small number of patients, slowly accrued during >10 years. Indications, techniques, and treatments may have substantially changed across time. In particular, relatively few patients were treated with newer stents, flow diverters, or intrasaccular flow disruptors. The noninvasive imaging technique most commonly used to assess angiographic results at 1 year differed between groups. There were a few patients with posterior circulation aneurysms to whom the results of this trial may not apply. Other limitations are the absence of blinding of outcome assessors and the lack of adjustment for a multiplicity of analyses. The follow-up period may have been insufficient to capture all recurrences that can occur after 1 year, and it was too short to assess efficacy in the prevention of long-term aneurysm rupture.²⁶

Only 7 centers actively participated. Despite the limitations, results are expected to apply to a variety of patients, operators, and settings.

CONCLUSIONS

Surgical clipping is more effective than endovascular treatment of UIAs in terms of the frequency of the primary outcome measure, treatment failure. Results were mainly driven by angiographic results at 1 year. Additional trials are required to assess long-term clinical outcome results of the preventive treatment of UIAs.

ACKNOWLEDGMENT

We thank Dr Bryce Weir for his contributions to an early version of this manuscript.

Disclosure forms provided by the authors are available with the full text and PDF of this article at www.ajnr.org.

REFERENCES

1. Vernooij MW, Ikram MA, Tanghe HL, et al. **Incidental findings on brain MRI in the general population.** *N Engl J Med* 2007;357:1821–28 CrossRef Medline
2. Vlak MH, Algra A, Brandenburg R, et al. **Prevalence of unruptured intracranial aneurysms, with emphasis on sex, age, comorbidity, country, and time period: a systematic review and meta-analysis.** *Lancet Neurol* 2011;10:626–36 CrossRef Medline
3. Etminan N, de Sousa DA, Tiseo C, et al. **European Stroke Organisation (ESO) guidelines on management of unruptured intracranial aneurysms.** *Eur Stroke J* 2022;7:V CrossRef Medline
4. Villablanca JP, Duckwiler GR, Jahan R, et al. **Natural history of asymptomatic unruptured cerebral aneurysms evaluated at CT angiography: growth and rupture incidence and correlation with epidemiologic risk factors.** *Radiology* 2013;269:258–65 CrossRef Medline
5. Backes D, Vergouwen MD, Tiel Groenestege AT, et al. **PHASES score for prediction of intracranial aneurysm growth.** *Stroke* 2015;46:1221–26 CrossRef Medline
6. Thompson BG, Brown RD Jr, Amin-Hanjani S, et al; American Heart Association Stroke Council, Council on Cardiovascular and Stroke Nursing, and Council on Epidemiology and Prevention; American Heart Association; American Stroke Association. **Guidelines for the Management of Patients With Unruptured Intracranial Aneurysms: A Guideline for Healthcare Professionals From the American Heart Association/American Stroke Association.** *Stroke* 2015;46:2368–400 CrossRef Medline
7. Darsaut TE, Estrade L, Jamali S, et al. **Uncertainty and agreement in the management of unruptured intracranial aneurysms.** *J Neurosurg* 2014;120:618–23 CrossRef Medline
8. Molyneux A, Kerr R, Stratton I, et al; International Subarachnoid Aneurysm Trial (ISAT) Collaborative Group. **International Subarachnoid Aneurysm Trial (ISAT) of neurosurgical clipping versus endovascular coiling in 2143 patients with ruptured intracranial aneurysms: a randomised trial.** *Lancet* 2002;360:1267–74 CrossRef Medline
9. Pontes FG, da Silva EM, Baptista-Silva JC, et al. **Treatments for unruptured intracranial aneurysms.** *Cochrane Database Syst Rev* 2021;5:CD013312 CrossRef Medline
10. Raymond J, Darsaut TE, Molyneux AJ; TEAM Collaborative Group. **A trial on unruptured intracranial aneurysms (the TEAM trial): results, lessons from a failure and the necessity for clinical care trials.** *Trials* 2011;12:64 CrossRef Medline
11. Kotowski M, Naggara O, Darsaut TE, et al. **Safety and occlusion rates of surgical treatment of unruptured intracranial aneurysms: a systematic review and meta-analysis of the literature from 1990 to 2011.** *J Neurol Neurosurg Psychiatry* 2013;84:42–48 CrossRef Medline

12. Darsaut TE, Findlay JM, Raymond J; CURES Collaborative Group. **The design of the Canadian UnRuptured Endovascular versus Surgery (CURES) trial.** *Can J Neurol Sci* 2011;38:236–41 CrossRef Medline
13. Darsaut TE, Findlay JM, Magro E, et al. **Surgical clipping or endovascular coiling for unruptured intracranial aneurysms: a pragmatic randomised trial.** *J Neurol Neurosurg Psychiatry* 2017;88:663–68 CrossRef Medline
14. Darsaut TE, Desal H, Cognard C, et al. **Comprehensive Aneurysm Management (CAM): an all-inclusive care trial for unruptured intracranial aneurysms.** *World Neurosurg* 2020;141:e770–77 CrossRef Medline
15. Raymond J, Darsaut TE, Roy DJ. **Recruitment in clinical trials: the use of Zelen's prerandomization in recent neurovascular studies.** *World Neurosurg* 2017;98:403–10 CrossRef Medline
16. Bruno A, Akinwuntan AE, Lin C, et al. **Simplified modified Rankin scale questionnaire: reproducibility over the telephone and validation with quality of life.** *Stroke* 2011;42:2276–79 CrossRef Medline
17. Benomar A, Farzin B, Gevry G, et al. **Noninvasive angiographic results of clipped or coiled intracranial aneurysms: an inter- and intra-observer reliability study.** *AJNR Am J Neuroradiol* 2021;42:1615–20 CrossRef Medline
18. Benomar A, Farzin B, Volders D, et al. **Angiographic results of surgical or endovascular treatment of intracranial aneurysms: a systematic review and inter-observer reliability study.** *Neuroradiology* 2021;63:1511–19 CrossRef Medline
19. Darsaut TE, Chapot R, Raymond J. **Changing the rules of the game: the problem of surrogate angiographic outcomes in the evaluation of aneurysm treatments.** *AJNR Am J Neuroradiol* 2020;41:2174–75 CrossRef Medline
20. White PM, Lewis SC, Gholkar A; HELPS Trial Collaborators, et al. **Hydrogel-Coated Coils Versus Bare Platinum Coils for the Endovascular Treatment of Intracranial Aneurysms (HELPS): a randomised controlled trial.** *Lancet* 2011;377:1655–62 CrossRef Medline
21. Raymond J, Klink R, Chagnon M, et al. **Hydrogel versus bare platinum coils in patients with large or recurrent aneurysms prone to recurrence after endovascular treatment: a randomized controlled trial.** *AJNR Am J Neuroradiol* 2017;38:432–41 CrossRef Medline
22. Coley S, Sneade M, Clarke A, et al. **Cerecyte Coil Trial: procedural safety and clinical outcomes in patients with ruptured and unruptured intracranial aneurysms.** *AJNR Am J Neuroradiol* 2012;33:474–80 CrossRef Medline
23. Darsaut TE, Raymond J; STAT Collaborative Group. **The design of the STenting in Aneurysm Treatments (STAT) trial.** *J Neurointerv Surg* 2012;4:178–81 CrossRef Medline
24. Zhang Q, Jing L, Liu J, et al. **Predisposing factors for recanalization of cerebral aneurysms after endovascular embolization: a multivariate study.** *J Neurointerv Surg* 2018;10:252–57 CrossRef Medline
25. Lee J, Lim JW, Cho YD. **Follow-up outcomes after re-embolization for recanalized aneurysms after initial coiling: further recurrence rates and related risk factors.** *World Neurosurg* 2018;114:e508–17 CrossRef Medline
26. Lecler A, Raymond J, Rodriguez-Regent C, et al. **Intracranial aneurysms: recurrences more than 10 years after endovascular treatment: a prospective cohort study, systematic review, and meta-analysis.** *Radiology* 2015;277:173–80 CrossRef Medline
27. Raymond J, Guilbert F, Weill A, et al. **Long-term angiographic recurrences after selective endovascular treatment of aneurysms with detachable coils.** *Stroke* 2003;34:1398–403 CrossRef Medline
28. Raymond J, Darsaut TE, Altman DG. **Pragmatic trials can be designed as optimal medical care: principles and methods of care trials.** *J Clin Epidemiol* 2014;67:1150–56 CrossRef Medline
29. Bacchus E, Kate MP, Benomar A, et al. **Inter-rater reliability of the simplified modified Rankin scale as an outcome measure for treated cerebral aneurysm patients.** *Neurochirurgie* 2022;68:488–92 CrossRef Medline
30. Darsaut TE, Keough MB, Boisseau W, et al. **Middle Cerebral Artery Aneurysm Trial (MCAAT): a randomized care trial comparing surgical and endovascular management of MCA aneurysm patients.** *World Neurosurg* 2022;160:e49–54 CrossRef Medline
31. Huang MC, Baaj AA, Downes K, et al. **Paradoxical trends in the management of unruptured cerebral aneurysms in the United States: analysis of nationwide database over a 10-year period.** *Stroke* 2011;42:1730–35 CrossRef Medline
32. Andaluz N, Zuccarello M. **Recent trends in the treatment of cerebral aneurysms: analysis of a nationwide inpatient database.** *J Neurosurg* 2008;108:1163–69 CrossRef Medline
33. Macdonald RL. **Editorial: clip or coil? Six years of follow-up in BRAT.** *J Neurosurg* 2015;123:605–07 CrossRef Medline
34. Iancu D, Collins J, Farzin B, et al. **Recruitment in a pragmatic randomized trial on the management of unruptured intracranial aneurysms.** *World Neurosurg* 2022;163:e413–19 CrossRef Medline

Automated Segmentation of Intracranial Thrombus on NCCT and CTA in Patients with Acute Ischemic Stroke Using a Coarse-to-Fine Deep Learning Model

K. Zhu, F. Bala, J. Zhang, F. Benali, P. Cimflova, B.J. Kim, R. McDonough, N. Singh, M.D. Hill, M. Goyal, A. Demchuk, B.K. Menon, and W. Qiu



ABSTRACT

BACKGROUND AND PURPOSE: Identifying the presence and extent of intracranial thrombi is crucial in selecting patients with acute ischemic stroke for treatment. This article aims to develop an automated approach to quantify thrombus on NCCT and CTA in patients with stroke.

MATERIALS AND METHODS: A total of 499 patients with large-vessel occlusion from the Safety and Efficacy of Nerinetide in Subjects Undergoing Endovascular Thrombectomy for Stroke (ESCAPE-NA1) trial were included. All patients had thin-section NCCT and CTA images. Thrombi contoured manually were used as reference standard. A deep learning approach was developed to segment thrombi automatically. Of 499 patients, 263 and 66 patients were randomly selected to train and validate the deep learning model, respectively; the remaining 170 patients were independently used for testing. The deep learning model was quantitatively compared with the reference standard using the Dice coefficient and volumetric error. The proposed deep learning model was externally tested on 83 patients with and without large-vessel occlusion from another independent trial.

RESULTS: The developed deep learning approach obtained a Dice coefficient of 70.7% (interquartile range, 58.0%–77.8%) in the internal cohort. The predicted thrombi length and volume were correlated with those of expert-contoured thrombi ($r = 0.88$ and 0.87 , respectively; $P < .001$). When the derived deep learning model was applied to the external data set, the model obtained similar results in patients with large-vessel occlusion regarding the Dice coefficient (66.8%; interquartile range, 58.5%–74.6%), thrombus length ($r = 0.73$), and volume ($r = 0.80$). The model also obtained a sensitivity of 94.12% (32/34) and a specificity of 97.96% (48/49) in classifying large-vessel occlusion versus non-large-vessel occlusion.

CONCLUSIONS: The proposed deep learning method can reliably detect and measure thrombi on NCCT and CTA in patients with acute ischemic stroke.

ABBREVIATIONS: AIS = acute ischemic stroke; ASSD = average symmetric surface distance; DC = Dice coefficient; DL = deep learning; EVT = endovascular therapy; HD95 = 95th percentile of the Hausdorff distance; IQR = interquartile range; LVO = large-vessel occlusion; MeVO = medium-vessel occlusion; STAPLE = simultaneous truth and performance level estimation

Randomized controlled trials in patients with acute ischemic stroke (AIS) have demonstrated the efficacy and safety of

endovascular therapy (EVT) compared with medical therapy in patients with large-vessel occlusion (LVO).^{1,2} Identifying the presence, location, and extent of thrombi on NCCT and CTA images is important when selecting patients with AIS for reperfusion therapy. Thrombus characteristics such as location, length, volume, and permeability are helpful in predicting recanalization after both thrombolysis and EVT.^{3,4} Recent studies have also shown that thrombus radiomics is able to predict recanalization with IV alteplase⁵ and first-attempt recanalization with thromboaspiration.⁶

Received October 18, 2022; accepted after revision April 20, 2023.

From the Department of Clinical Neurosciences and Hotchkiss Brain Institute (K.Z., F. Bala, J.Z., F. Benali, P.C., R.M., N.S., M.D.H., M.G., A.D., B.K.M.), Department of Community Health Sciences (M.D.H.), Department of Medicine, and Department of Radiology (P.C., M.D.H., A.D.), Cumming School of Medicine, University of Calgary, Calgary, Alberta, Canada; College of Electronic Engineering (K.Z.), Xi'an Shiyou University, Xi'an, Shaanxi, China; St. Anne's University Hospital Brno and Faculty of Medicine (P.C.), Masaryk University, Brno, Czech Republic; Department of Neurology and Cerebrovascular Center (B.J.K.), Seoul National University Bundang Hospital, Seongnam-si, Gyeonggi-do, Korea; Department of Diagnostic and Interventional Neuroradiology (R.M.), University Hospital Hamburg, Hamburg, Germany; and School of Life Science and Technology (W.Q.), Huazhong University of Science and Technology, Wuhan, Hubei, China.

This work was supported by the Natural Science Basic Research Plan in Shaanxi Province of China (No. 2021JM-413), the Distinguished Young Scholars of the National Natural Science Foundation of China (Overseas), and the National Key Research and Development Program (No. 2022YFE0209900).

Please address correspondence to Wu Qiu, PhD, Room 701, Innovation Research Institute, Luoyu Rd 1037, School of Life Science and Technology, Huazhong University of Science and Technology, Wuhan, Hubei, China, 430074; e-mail: qiu.wu.ch@gmail.com

Indicates open access to non-subscribers at www.ajnr.org

Indicates article with online supplemental data.

<http://dx.doi.org/10.3174/ajnr.A7878>

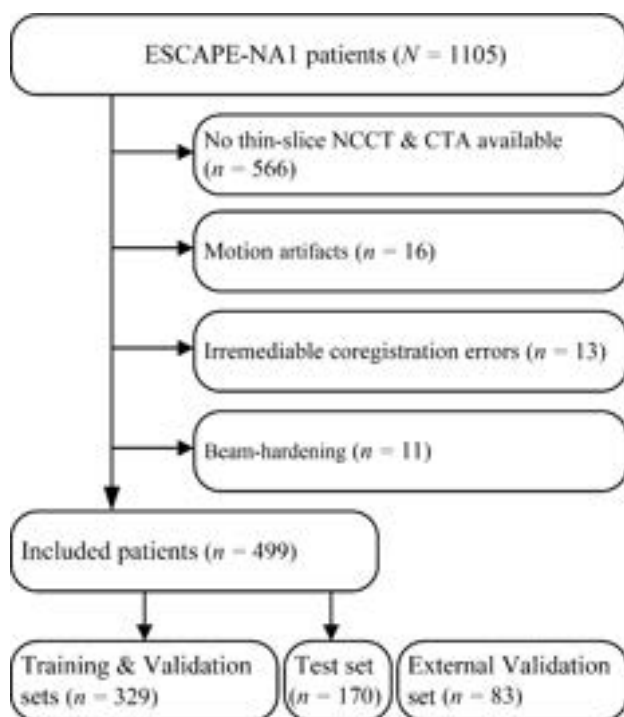


FIG 1. Flowchart of patient inclusion.

Accurate segmentation of thrombi on baseline imaging is the first step in assessing thrombus characteristics. Manual delineation of the thrombus is still the criterion standard in assessing thrombus characteristics in clinical practice.⁷ It requires expertise in imaging interpretation and is observer-dependent. Semiautomated segmentation techniques use clinicians' input to help with this task, but the variability introduced by user input is still a concern.⁸ A fully-automated thrombus segmentation approach readily available in the acute setting is, therefore, desirable.

Automated segmentation of thrombi on NCCT or CTA is, however, challenging due to various reasons. These include the low signal-to-noise ratio on CT-based imaging, partial volume effects, CT image artifacts, and intracranial calcification, and so forth, all of which hinder accurate delineation of the thrombus. These challenges imply that the traditional model-based or thresholding-based segmentation methods may not be able to achieve accurate or acceptable results.^{9–12} To the best of our knowledge, there are very few established approaches to automatically segment intracranial thrombi on CT images. This study, therefore, aims to develop and externally validate an automated thrombus-segmentation approach on NCCT and CTA images in patients with acute stroke presenting with intracranial vessel occlusion.

MATERIALS AND METHODS

Study Participants

Patients were retrospectively selected from the Safety and Efficacy of Nerinetide in Subjects Undergoing Endovascular Thrombectomy for Stroke (ESCAPE-NA1) randomized controlled trial (ClinicalTrials.gov: NCT02930018).¹³ Study approval was obtained from the ethics board at each site and the responsible regulatory

authorities. Signed informed consent was obtained from the patients or their legally authorized representatives. Inclusion criteria for the main study were the following: 1) 18 years of age or older with LVO (intracranial ICA, MCA M1, or functional M1 [proximal occlusion of all M2 branches]), 2) NIHSS score of ≥ 5 , 3) time from last seen well <12 hours, 4) pial collateral filling of $\geq 50\%$ of the ischemic MCA territory, and 5) ASPECTS ≥ 5 . For this study, we included only patients with available thin-section (≤ 2.5 mm) baseline NCCT and CTA images (single-phase or 1 phase of multiphase CTA). We excluded patients whose imaging showed the following: 1) irremediable coregistration errors ($n = 13$), 2) severe motion artifacts ($n = 16$), or 3) beam-hardening artifacts ($n = 11$). A total of 499 patients were included, of whom 329 were randomly selected for the training ($n = 263$) and internal validation ($n = 66$); the remaining 170 patients (independent of the derivation cohort) were used to internally test the derived model (Fig 1).

An external validation set was also used to test the generalizability of the derived DL model. This data set comprised 83 randomly chosen patients with AIS with anterior circulation occlusions from the Precise and Rapid Assessment of Collaterals Using Multi-Phase CTA in the Triage of Patients with Acute Ischemic Stroke for IV or IA Therapy (PRoVe-IT) study.^{14,15} Of the 83 patients, 34 had LVO, 28 had medium-vessel occlusion (MeVO) (M2/M3/M4 segments of the MCA or A2/A3/A4 segments of the anterior cerebral artery), and 21 had no identifiable intracranial occlusion.

Reference Standard: Manual Segmentation of Thrombi

The thin-section NCCT images were automatically coregistered onto the CTA images (using the second phase if multiphase CTA was available) using rigid-body transformation (the SimpleITK packages in Python; <https://pypi.org/project/SimpleITK/>),¹⁶ followed by skull-stripping.¹⁷ An expert neuroradiologist visually inspected the registration results and performed manual corrections by using the 3D Slicer software (Version 4.1, <https://www.slicer.org/>) when the coregistration was suboptimal.¹⁸ Four trained readers (3 neuroradiologists with >5 years' experience in vascular imaging and 1 vascular neurologist with >10 years of stroke imaging experience) manually segmented intracranial thrombi section-by-section on NCCT images while referring to the coregistered CTA images using ITK-SNAP (<http://www.itksnap.org/>).¹⁹ Four readers were each responsible for one-fourth of the entire data set, and they were blinded to clinical information and follow-up imaging.

All 4 readers segmented a subset of 10 patients randomly selected from the internal test set. An expectation-maximization algorithm for simultaneous truth and performance level estimation (STAPLE) algorithm was performed to generate a computational "golden reference standard" based on the 4 experts' segmentations, which was used to assess the variability of manual segmentations.²⁰

Deep Learning Model

A 2-stage coarse-to-fine thrombus segmentation neural network was proposed on the basis of the U-net architecture.²¹ The proposed deep learning (DL) model used a multiscale training

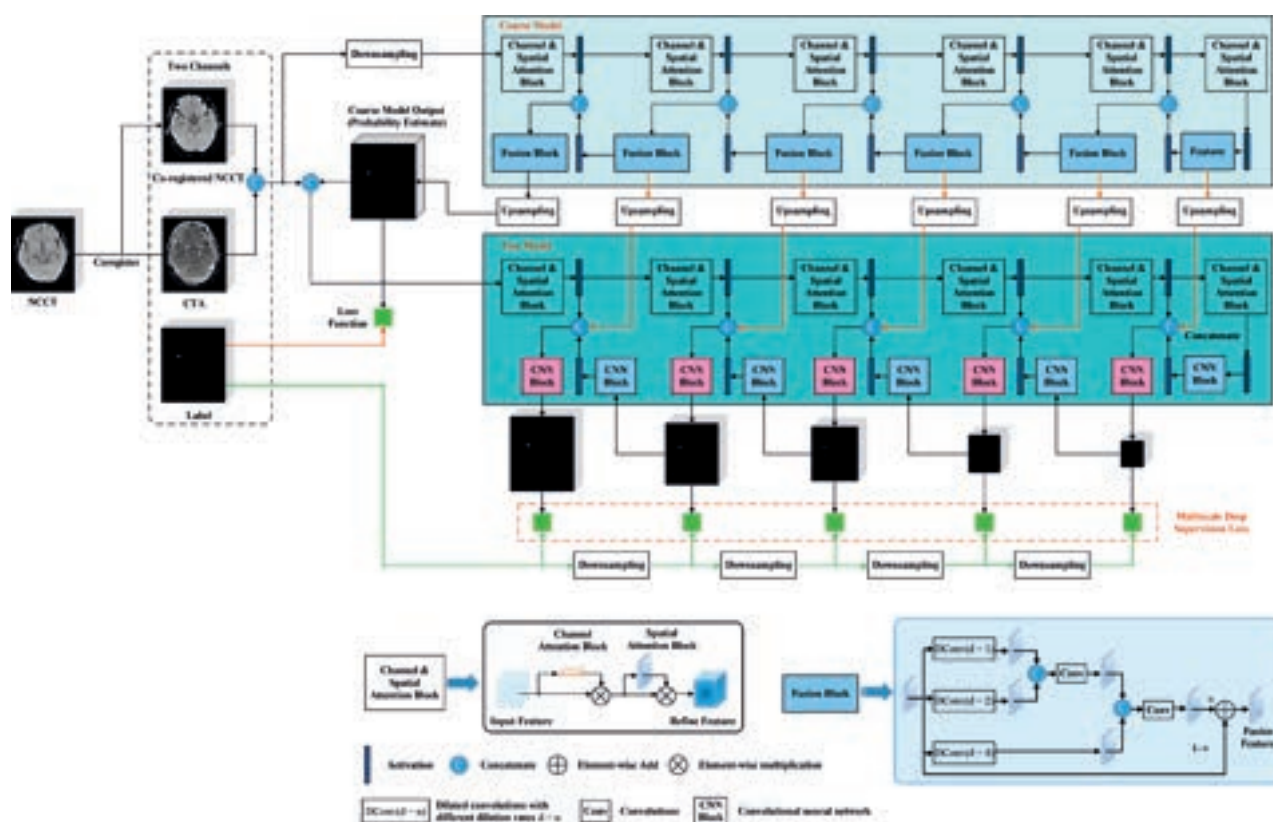


FIG 2. The proposed coarse-to-fine DL architecture. A 2-stage coarse-to-fine thrombus segmentation neural network used a multiscale training strategy with a deep-supervision mechanism, which consisted of the channel and spatial attention blocks and the scale-aware pyramid fusion module.

strategy with a deep-supervision mechanism. In particular, a channel and spatial attention block was designed to make the model focus more on the salient areas on images at different scales and obtain more conducive features.²² The spatial attention module generates a spatial attention map using the interspatial relationship of features. Different from channel attention, spatial attention focuses on where an informative part is, which is complementary to channel attention. To compute the spatial attention, we apply average-pooling and max-pooling operations along the channel axis first and concatenate them to generate an efficient feature descriptor.²² On the concatenated feature descriptor, we apply a convolution layer to generate a spatial attention map, which encodes where to emphasize or suppress. In this article, the patch size for spatial transform was $96 \times 160 \times 160$ voxels. To make full use of multiscale context information, we used a scale-aware pyramid fusion module, in which 3 parallel dilated convolutions with different dilation rates were used to capture information at different scales.²³

The detailed architecture of the proposed model is shown in Fig 2, and the details around the model architecture and hyperparameter optimization are summarized as follows: The 3D kernel size for convolutions was $3 \times 3 \times 3$. Feature numbers at each layer were 32, 64, 128, 256, and 320 (limited to 320 to ensure sufficient context aggregation). Batch normalization was used in the proposed network, which took a step toward reducing the internal covariate shift and, in doing so, dramatically accelerated the training of deep neural nets. The batch size of the networks was

2, to enable large patch sizes, and the leaky Rectified Linear Unit nonlinearity was implemented. Stochastic gradient descent with Nesterov momentum ($\mu = 0.99$) was used as the optimizer. The initial learning rate, dampening, batch size, and decay weight were 0.01, 0, 2, and 3×10^{-5} , respectively. The learning rate was decayed throughout the training following $lr_{init} \times (1 - epoch/epochmax)^{0.9}$, where lr_{init} is 0.01 and $epochmax$ is the maximum of the epoch.

Specifically, NCCT images after skull-stripping were downsampled from the original spacing of $0.625 \times 0.488 \times 0.488 \text{ mm}^3$ ($257 \times 456 \times 436$ voxels) to $1.08 \times 0.844 \times 0.844 \text{ mm}^3$ ($149 \times 264 \times 252$ voxels) and passed into the coarse model to obtain maximal contextual information and localize thrombi candidates at the first coarse stage. The output of the prediction maps at the coarse stage was upsampled to the original resolution and fed into the fine stage together with the original images to obtain more detailed segmentation. In particular, the fused features of each layer at the coarse stage were upsampled and concatenated to the features of the corresponding layer at the fine stage to use both global contextual information and local detail information obtained at coarse and fine stages.

Additionally, 5-fold cross-validation on the training data set was performed to select the optimal model at the coarse and fine stages. Spatial augmentations (rotation, scaling, low-resolution simulation, and so forth) were applied in 3D to increase the diversity of the training data. The combined Dice and cross-entropy were used as the loss function.²⁴ At each level of deep

Table 1: Patient characteristics in the derivation data and in the internal and external test data^a

Characteristic	Derivation Set (n = 329)	Internal Test Set (n = 170)	External Test Set (n = 83)
Age (yr) ^b	69 (59–78)	68 (59–79)	71 (63–79)
Male	173 (52.6)	89 (52.4)	43 (51.8)
Race			
White	261 (79.3)	142 (83.5)	NA
Asian	26 (7.9)	10 (5.9)	
African American	35 (10.6)	14 (8.2)	
Other	7 (2.1)	4 (2.4)	
Onset-to-CT time ^b	160 (82–268)	154 (79–284)	120 (89–184)
Baseline NIHSS score ^b	17 (12–21)	16 (13–20)	9 (5–15)
ASPECTS ^b	8 (7–9)	8 (7–9)	10 (8–10)
Hypertension	222 (67.5)	127 (74.7)	49 (59.0)
Hyperlipidemia	140 (42.6)	79 (46.5)	NA
Diabetes	70 (21.3)	36 (21.2)	9 (10.8)
IV alteplase	193 (58.7)	99 (58.2)	66 (79.5)
IV nerinetide	155 (47.1)	87 (51.2)	0
Occlusion site			
ICA	71 (21.6)	39 (23.0)	8 (9.6)
M1, MCA	248 (75.4)	125 (73.5)	26 (31.3)
M2, MCA	10 (3.0)	6 (3.5)	10 (12.1)
M3/M4, MCA	0	0	13 (15.7)
ACA (A2/A3)	0	0	3 (3.6)
PCA (P2)	0	0	2 (2.4)
No occlusion	0	0	21 (25.3)

Note:—ACA indicates anterior cerebral artery; PCA, posterior cerebral artery; NA, not applicable.

^a Except where indicated, data are number of patients, with percentages in parentheses.

^b Data are the median with the IQR in parentheses.

supervision, the ground truth segmentation mask was correspondingly downsampled for loss computation on the basis of the size of the feature maps. The training objective was the sum of the losses (L) at all resolutions, $L = W_1 \times L_1 + W_2 \times L_2 + \dots$. Hereby, the weights (W) were halved with each decrease in resolution, resulting in $W_2 = 0.5W_1$, $W_3 = 0.25W_1$, and so forth, and were normalized to sum 1.

Statistical Methods

Patient demographics, including clinical and imaging variables, were compared across the derivation and internal test sets using the χ^2 and Student t tests as appropriate.

The proposed segmentation method was quantitatively evaluated using the spatial overlap metric of the Dice coefficient (DC) and 2 boundary distance error metrics: average symmetric surface distance (ASSD) and 95th percentile of the Hausdorff Distance (HD95),²⁵ compared with the reference standard of manual (expert) segmentation. The DC is a spatial overlap index ranging from 0 to 1, where 1 indicates a perfect overlap between the reference standard and the predicted segmentation and vice versa. The ASSD and HD95 represent the average and largest HD95 errors between the 2 surfaces derived from the segmented and reference objects in 3D space. For ASSD and HD95, 0 mm indicates perfect segmentation. The correlations regarding thrombus length and volume between the DL-derived model and manual measurements were analyzed using the Pearson correlation and Spearman correlation as appropriate to the data distribution.²⁶ The correlation was considered excellent if ≥ 0.70 and good if between 0.5 and 0.7.²⁶ Absolute and relative errors of thrombus volume and length were also calculated. These metrics

were all calculated in 3D space at a patient level and applied onto both the internal data set (ESCAPE-NA1) and the external test data set (PRoVe-IT) for internal and external validation, respectively. On the basis of the segmentation results, the model predictions can be also used to distinguish the patients with LVO versus without LVO after localizing the segmented thrombus and thresholding thrombus volume. We further assessed the specificity and sensitivity of the DL model in classifying intracranial thrombi (LVO versus non-LVO and occlusion versus nonocclusion) in the external data set.

All statistical analyses were performed using the SciPy package (<https://scipy.org/>). All P values were 2-sided, and statistical significance was defined as $P < .05$.

RESULTS

Patient Characteristics

Patient characteristics of the derivation and internal and external test data are summarized in Table 1. There were no statistically significant differences in baseline characteristics between the derivation and internal test data (all, $P > .05$, Table 1). The choice of the external test data, with different characteristics than the internal data, was deliberate.

Internal Validation

All patients had ICA or M1 segment MCA occlusions. Figure 3 shows 2 examples predicted by the proposed DL model compared with the reference standard. Quantitative results on the internal test data of 170 patients are shown in Table 2. The proposed DL model obtained a median DC of 70.7% (interquartile range [IQR], 58.0%–77.8%), a median ASSD of 0.38 mm (IQR, 0.24–0.77 mm), and a median HD95 of 1.31 mm (IQR, 0.79–3.83 mm). The median thrombus length measured by the DL model was 13.94 mm (IQR, 6.32–25.76 mm) and was strongly correlated with that of the expert segmented thrombi ($r = 0.88$, $P < .001$). The median difference δL_{diff} (mm) and median absolute difference $|\delta L_{diff}|$ (mm) of thrombus length between the expert segmentation and algorithm predictions were -5.41 mm (IQR, -11.34 to -0.5 mm) and 5.79 mm (IQR, 1.79 – 11.37 mm), respectively. The median thrombus volume of 71.9 mm³ (IQR, 39.25 – 126.15 mm³) obtained by the DL model also strongly correlated with that obtained by expert segmentation ($r = 0.87$, $P < .001$). The median volume difference δV_{diff} (mm³) and the median absolute volume difference $|\delta V_{diff}|$ (mm³) between the expert segmentation and algorithm predictions were -0.9 mm³ (IQR, -3.41 – 0.33 mm³) and 1.76 mm³ (IQR, 0.71 – 4.23 mm³), respectively.

External Validation

The prevalence of LVO, MeVo, and no occlusions in the external data was 34 (41%), 28 (33.7%), and 21 (25.3%), respectively. Quantitative results from the 34 patients with LVO in the external data are shown in Table 2. In these 34 patients with LVO, the proposed DL model obtained a median DC of 66.8% (IQR,

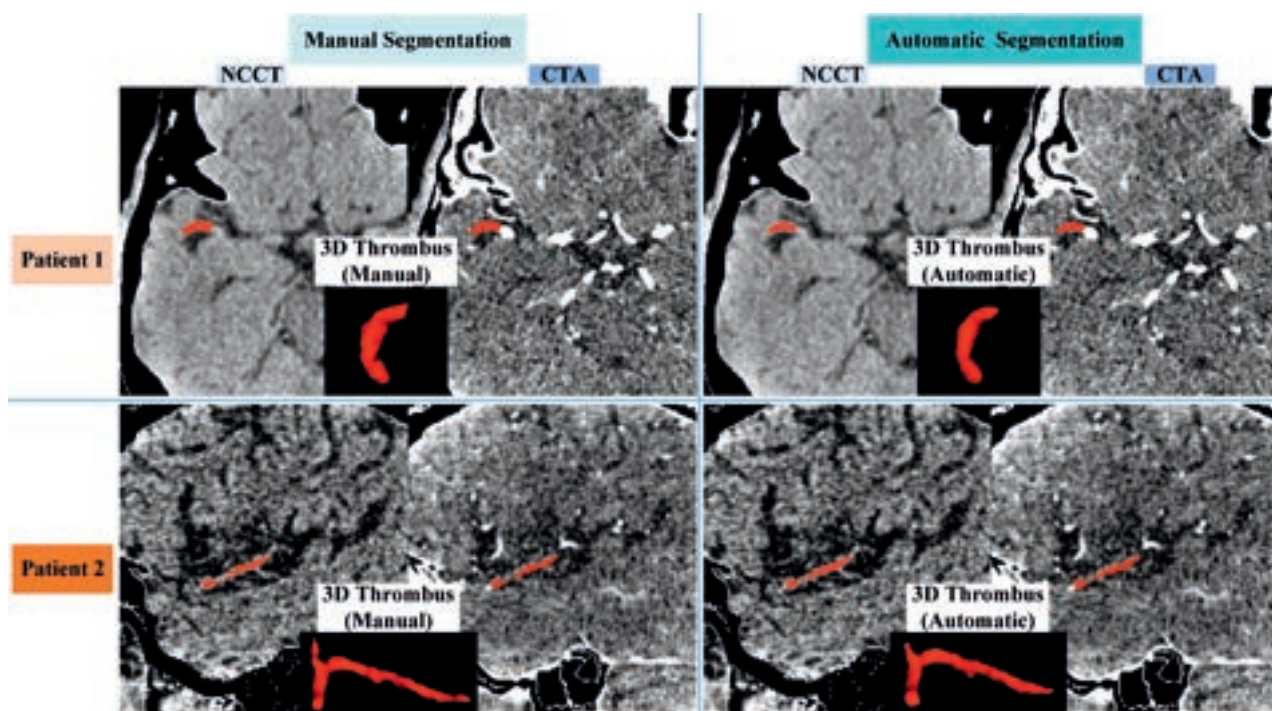


FIG 3. Two segmentation examples obtained by the proposed model. The images are shown as NCCT/CTA overlaid with the manually or algorithm-segmented thrombi in red.

Table 2: Quantitative evaluation of thrombus measurement in the internal test data (170 patients) and external validation data (34 patients with LVO) of PRoVe-IT^a

	Internal Validation Data (<i>n</i> = 170)	External Validation Data (<i>n</i> = 34)
DC (%)	70.7 (58.0–77.8)	66.8 (58.5–74.6)
ASSD (mm)	0.38 (0.24 to 0.77)	0.56 (0.19–1.21)
HD95 (mm)	1.31 (0.79–3.83)	3.05 (1.37–8.19)
Reference length (mm)	20.3 (10.25–34.73)	12.11 (5.73–19.51)
Prediction length (mm)	13.94 (6.32–25.76)	9.0 (3.4–21.74)
δL_{diff} (mm)	–5.41 (–11.34 to –0.5)	0.0 (–6.12–8.2)
$ \delta L_{diff} $ (mm)	5.79 (1.79–11.37)	6.14 (2.81–12.27)
Reference volume (mm ³)	80.53 (49.92–155.39)	37.51 (29.19–78.3)
Prediction volume (mm ³)	71.9 (39.25–126.15)	58.14 (32.96–104.68)
δV_{diff} (mm ³)	–0.9 (–3.41–0.33)	0.59 (–0.17–4.53)
$ \delta V_{diff} $ (mm ³)	1.76 (0.71–4.23)	1.47 (0.5–4.62)
Volume correlation	0.95 (0.89–0.98)	0.91 (0.84–0.96)

^a Values are shown as medians with the IQR in parentheses. $\delta()$ and $|\delta()|$ represent relative and absolute error, respectively.

58.5%–74.6%), a median ASSD of 0.56 mm (IQR, 0.19–1.21 mm), and a median HD95 of 3.05 mm (IQR, 1.37–8.19 mm) compared with the reference standard. The median thrombus length measured by the proposed DL model was 9.0 mm (IQR, 3.4–21.74 mm), which correlated significantly with expert manual segmentation ($r = 0.73$, $P < .001$). The median difference δL_{diff} (mm) and the median absolute difference $|\delta L_{diff}|$ (mm) of thrombus length between the expert segmentation and algorithm predictions were 0.0 mm (IQR, –6.12–8.2 mm) and 6.14 mm (IQR, 2.81–12.27 mm), respectively. The median thrombus volume of 58.14 mm³ (IQR, 32.96–104.68 mm³) obtained by the DL model strongly correlated with manual segmentation ($r = 0.80$, $P < .001$). The median volume

difference δV_{diff} (mm³) and the median absolute volume difference $|\delta V_{diff}|$ (mm³) between the expert segmentation and algorithm predictions were 0.59 mm³ (IQR, –0.17–4.53 mm³) and 1.47 mm³ (IQR, 0.5–4.62 mm³), respectively.

The accuracy, specificity, and sensitivity of the DL model in classifying intracranial thrombi were further investigated in the external data. The DL model obtained a sensitivity of 94.12% (32/34) and a specificity of 97.96% (48/49) in classifying patients with LVO versus non-LVO (including patients with MeVO and no occlusion). The DL model obtained a sensitivity of 69.35% (43/62) and a specificity of 100% (21/21) in classifying patients with occlusion versus no occlusion.

Analysis of Variability in Manual Segmentations

The median thrombus length and volume derived from the 10 patients using the STAPLE algorithm were 20.53 mm (IQR, 18.05–42.17 mm) and 52.49 mm³ (IQR, 22.99–166.42 mm³), respectively. Compared with the criterion standard generated by the STAPLE algorithm, the median DCs were 54.4% (IQR, 49.4%–70.7%), 57.5% (IQR, 49.1%–64.6%), 82.9% (IQR, 39.9%–94.1%), and 88.3% (IQR, 58.6%–93.5%) for the 4 raters, respectively. The proposed DL model achieved a median DC of 64.7% (IQR, 45.7%–73.7%), approaching an average performance of the 4 experts' manual contouring. Other metrics, ie, ASSD, HD95, and volume correlations, showed consistent results (Online Supplemental Data).

DISCUSSION

This study describes a fully automated DL model for intracranial thrombus segmentation on NCCT and CTA images in patients with AIS. This model used a coarse-to-fine DL network with multilevel and multiscale feature fusion and deep-supervision strategy. It was developed using a large data set of 329 patients and tested internally and externally for generalizability. Both internal and external validations demonstrate that the developed model can accurately detect and segment intracranial thrombi, especially in patients with LVO, compared with manual segmentation by experts.

There are no well-established methods for automated thrombus segmentation, and only a few that use semiautomated methods.^{7–11} Existing methods of thrombus segmentation rely on manual or semiautomated measurements of thrombus density on NCCT. This method of density assessment by using small ROIs is prone to interobserver variability due to the heterogeneity in thrombus composition and the small size of intracranial thrombi and is sensitive to partial volume effects, image noise, and the presence of vessel wall calcification.⁷ Santos et al²⁷ developed a semiautomated region-growing segmentation method that was limited by a low observer agreement and variability in thrombus density. Qazi et al¹² used linear regression to build statistical models to predict patient-specific optimal Hounsfield unit thresholds, which replaced a universal single Hounsfield unit threshold for thrombus segmentation favored by Riedel et al.²⁸ However, these thrombus density threshold-based methods are subject to image-intensity variability, and their generalizability is a concern. Lucas et al²⁹ proposed a cascaded neural network to segment thrombi. Unfortunately, this method was restricted to 2D images and limited to the MCA + ICA region, used fixed ROIs, and was developed using a small data set (the segmentation network was trained on only the 216 positive cases). Mojtahedi et al³⁰ used dual-modality U-Net-based CNNs to detect the thrombus location and then limited the search area by creating a bounding box around the detected thrombus location, which would allow the first-level prediction errors to stack up later. To the best of our knowledge, our study represents the largest data set of automated intracranial thrombus segmentation on NCCT/CTA with internal and external validation. The proposed method can automatically segment small thrombi in 3D whole-brain NCCT images, which overcomes the limitations of segmentation methods such as intensity-based and fixed ROI annotations.

Among the 170 patients with LVO in the internal validation, the DL model failed to detect thrombus in only 10 cases. Visual inspection showed that these false-negative cases could be attributed to one or a combination of reasons: 1) small thrombi ($<30 \text{ mm}^3$) ($n = 4$); 2) isodense (to surrounding tissue) thrombi ($n = 7$); and 3) the presence of severe beam-hardening artifacts on the thrombus ($n = 5$). Only 7.5% of training data had such imaging characteristics in the retrospective analysis. Including more sample images with such characteristics in the training data could have improved the performance of the derived DL model.

The volumetric analyses regarding thrombus length and volume also show excellent internal and external validation. However, the difference in thrombus length and HD95 seems to be large, possibly explained by the challenges in segmenting

thrombi in curved vessels. Nonetheless, this study reports HD95 values, 3.05 (range, 1.37–8.19), similar to those reported in the Multicenter Randomized Clinical Trial of Endovascular Treatment for Acute Ischemic Stroke in the Netherlands (MR CLEAN) study, 5.67 (range, 4.30–7.04).³⁰ The median DC was 70.7% in internal validation in the LVO-only ESCAPE NA1 study and 66.8% in the 34 LVO cases in external validation in the PRoVe-IT study. This slight difference could be because patients in the PRoVe-IT study had less severe stroke than patients in the ESCAPE-NA1 trial (NIHSS score 8 versus 16) and, therefore, less extensive thrombi. Indeed, the median thrombus volume of the patients with LVO in the PRoVe-IT data (37.51 mm^3 ; IQR, $29.19\text{--}78.3 \text{ mm}^3$) was much smaller than that in the internal data set of ESCAPE-NA1 (80.53 mm^3 ; IQR, $49.92\text{--}155.39 \text{ mm}^3$).

Moreover, the DC of the proposed model in the external validation set was 66.8%, suggesting a good agreement between the predicted and the measured thrombi. Our DC is similar to the algorithm developed from the MR CLEAN data, which achieved a DC of 62%.³⁰ Despite the smaller thrombus burden, the developed DL model obtained a high specificity in identifying the presence of thrombus in the external validation. The sensitivity of 77.42% (48/62) was comparably low because 14 of 28 MeVO cases were identified as having no occlusions by the model, which might be because the derived DL model was trained using only LVO cases. Including more patients with distal occlusions or without occlusions in the training data could have improved the accuracy of the model in detecting small thrombi.

The results of our study have several implications in clinical practice. Automated segmentation can be used to extract radiologic thrombus characteristics, such as thrombus length and volume, which were shown to be associated with clinical outcomes and reperfusion success.^{31,32} Although not included in the output of our proposed model, thrombus density and permeability are also useful in predicting clinical and angiographic outcomes,³¹ thus justifying future work to automate their calculations. Physicians can use the output of our model to inform their decisions regarding bridging therapy; for instance, long and large thrombi might benefit more from adjunctive IV thrombolysis compared with smaller thrombi; however, this possibility needs to be validated in future work.³³ Furthermore, information about the precise location and length of the thrombus is useful for neurointerventionalists to plan the EVT procedure and choose the best device to achieve fast and effective reperfusion. Last, automated segmentation can be applied on big databases to extract thrombus characteristics in a faster and easier manner compared with humans and, thus, could be used to improve the design of EVT devices.

Detection and segmentation of thrombi on NCCT/CTA are tedious and time-consuming for physicians.^{5,27,34,35} Improvements in image quality, better training, and systematic assessments of thrombus characteristics (parameterization and morphology) are useful to help humans improve thrombus detection on NCCT and CTA. Regardless of these strategies, detecting thrombi on NCCT and CTA continues to be challenging for humans, especially with small thrombi. Furthermore, the results using the reference standard generated by the STAPLE algorithm show the variability of manual segmentations across different raters and thus highlight

the need for an automated process to standardize the extraction of thrombus characteristics.

Our study has several limitations. First, patients with unavailable thin-section NCCT and CTA images were excluded, therefore introducing selection bias; however, we chose to do so to decrease measurement error from thick-section scans. Second, 4 well-trained experts manually contoured the data for evaluation. Even though the reproducibility of manual segmentations in our experiments was acceptable, the variability introduced by cognitive biases and heuristics and image misalignment should be considered. The variability in the results is partly explained by the difference in experience and training among the 4 raters. Two raters were neuroradiologists (raters 1 and 3), one was a neuroradiology resident (rater 2), and one was a vascular neurologist (rater 4). The 2 neuroradiologists achieved the highest DCs. Moreover, intracranial thrombi are small and occur in curved vessels. Annotation of lesions that are small with curved shapes can also result in variability compared with larger-sized lesions where variability will be inherently less. Third, the internal data sets did not include MeVO occlusions, explaining the low model performance for these cases. Future studies focusing on this occlusion subgroup would improve detection and delineation of these thrombi. Fourth, the proposed model did not show good performance in small and isodense thrombi; however, we chose to keep these cases, contrary to a prior study, to increase the generalizability of our results. Including more studies with artifacts (beam-hardening and so forth) would also improve the generalizability. Fifth, the developed model can be applied only on thin-section NCCT and CTA images. The extension to a more widely used NCCT with 5-mm-thick slices should be investigated.

CONCLUSIONS

An automated method based on DL is capable of detecting and segmenting thrombi reliably, especially those causing LVOs, on NCCT and CTA images in patients with AIS. Extensive validations demonstrate the efficacy of the proposed technique compared with the reference standard (ie, manual segmentation). If translated into a clinical setting, this algorithm could help physicians in their decision-making for AIS.

Disclosure forms provided by the authors are available with the full text and PDF of this article at www.ajnr.org.

REFERENCES

- Goyal M, Menon BK, van Zwam WH, et al; HERMES Collaborators. Endovascular thrombectomy after large-vessel ischaemic stroke: a meta-analysis of individual patient data from five randomised trials. *Lancet* 2016;387:1723–31 CrossRef Medline
- Menon BK, Hill MD, Davalos A, et al. Efficacy of endovascular thrombectomy in patients with M2 segment middle cerebral artery occlusions: meta-analysis of data from the HERMES Collaboration. *J Neurointerv Surg* 2019;11:1065–69 CrossRef Medline
- Menon BK, Al-Ajlan FS, Najm M, et al; INTERSeCT Study Investigators. Association of clinical, imaging, and thrombus characteristics with recanalization of visible intracranial occlusion in patients with acute ischemic stroke. *JAMA* 2018;320:1017–26 CrossRef Medline
- Riedel CH, Zimmermann P, Jensen-Kondering U, et al. The importance of size: successful recanalization by intravenous thrombolysis in acute anterior stroke depends on thrombus length. *Stroke* 2011;42:1775–77 CrossRef Medline
- Qiu W, Kuang H, Nair J, et al. Radiomics-based intracranial thrombus features on CT and CTA predict recanalization with intravenous alteplase in patients with acute ischemic stroke. *AJNR Am J Neuroradiol* 2019;40:39–44 CrossRef Medline
- Hofmeister J, Bernava G, Rosi A, et al. Clot-based radiomics predict a mechanical thrombectomy strategy for successful recanalization in acute ischemic stroke. *Stroke* 2020;51:2488–94 CrossRef Medline
- Santos EM, Yoo AJ, Beenen LF, et al; MR CLEAN Investigators. Observer variability of absolute and relative thrombus density measurements in patients with acute ischemic stroke. *Neuroradiology* 2016;58:133–39 CrossRef Medline
- Lalys F, Yan V, Kaladji A, et al. Generic thrombus segmentation from pre- and post-operative CTA. *Int J Comput Assist Radiol Surg* 2017;12:1501–10 CrossRef Medline
- Lee K, Johnson RK, Yin Y, et al. Three-dimensional thrombus segmentation in abdominal aortic aneurysms using graph search based on a triangular mesh. *Comput Biol Med* 2010;40:271–78 CrossRef Medline
- Freiman M, Esses SJ, Joskowicz L, et al. An iterative model-constrained graph-cut algorithm for abdominal aortic aneurysm thrombus segmentation. In: *Proceedings of the 2010 IEEE International Conference on Biomedical Imaging: from Nano to Macro*, Rotterdam, the Netherlands. April 14, 2010:672–75
- Zhugue F, Rubin GD, Sun S, et al. An abdominal aortic aneurysm segmentation method: level set with region and statistical information. *Med Phys* 2006;33:1440–53 CrossRef Medline
- Qazi S, Qazi E, Wilson AT, et al. Identifying thrombus on non-contrast CT in patients with acute ischemic stroke. *Diagnostics (Basel)* 2021;11:1919 CrossRef Medline
- Hill MD, Goyal M, Menon BK, et al; ESCAPE-NA1 Investigators. Efficacy and Safety of Nerinetide for the Treatment of Acute Ischaemic Stroke (ESCAPE-NA1): a multicentre, double-blind, randomised controlled trial. *Lancet* 2020;395:878–87 CrossRef Medline
- Menon BK, d'Este CD, Qazi EM, et al. Multiphase CT angiography: a new tool for the imaging triage of patients with acute ischemic stroke. *Radiology* 2015;275:510–20 CrossRef Medline
- Ospel JM, Volny O, Qiu W, et al. Impact of multiphase computed tomography angiography for endovascular treatment decision-making on outcomes in patients with acute ischemic stroke. *J Stroke* 2021;23:377–87 CrossRef Medline
- Beare R, Lowekamp B, Yaniv Z. Image segmentation, registration and characterization in R with SimpleITK. *J Stat Soft* 2018;86:8 CrossRef Medline
- Najm M, Kuang H, Federico A, et al. Automated brain extraction from head CT and CTA images using convex optimization with shape propagation. *Comput Methods Programs Biomed* 2019;176:1–8 CrossRef Medline
- Fedorov A, Beichel R, Kalpathy-Cramer J, et al. 3D Slicer as an image computing platform for the Quantitative Imaging Network. *Magn Reson Imaging* 2012;30:1323–41 CrossRef Medline
- Yushkevich PA, Piven J, Hazlett HC, et al. User-guided 3D active contour segmentation of anatomical structures: significantly improved efficiency and reliability. *Neuroimage* 2006;31:1116–28 CrossRef Medline
- Warfield SK, Zou KH, Wells WM. Simultaneous truth and performance level estimation (STAPLE): an algorithm for the validation of image segmentation. *IEEE Trans Med Imaging* 2004;23:903–21 CrossRef Medline
- Ronneberger O, Fischer P, Brox T. U-Net: Convolutional Networks for Biomedical Image Segmentation. In: Navab N, Hornegger J, Wells W, et al, eds. In: *Medical Image Computing and Computer-Assisted Intervention*, Munich, Germany. October 5–9, 2015

22. Woo S, Park J, Lee JY, et al. **CBAM: Convolutional Block Attention Module.** *arXiv* July 17, 2018. <https://arxiv.org/pdf/1807.06521v1.pdf>. Accessed October 6, 2018
23. Feng S, Zhao H, Shi F, et al. **CPFNet: Context Pyramid Fusion Network for Medical Image Segmentation.** *IEEE Trans Med Imaging* 2020;39:3008–18 CrossRef Medline
24. Ma J, Chen J, Ng M, et al. **Loss odyssey in medical image segmentation.** *Med Image Anal* 2021;71:102035 CrossRef Medline
25. Mourya GK, Gogoi M, Talbar SN, et al. **Cascaded dilated deep residual network for volumetric liver segmentation from CT image.** *International Journal of E-Health and Medical Communications* 2021;12:34–45 CrossRef
26. Mukaka MM. **Statistics corner: a guide to appropriate use of correlation coefficient in medical research.** *Malawi Med J* 2012;24:69–71 Medline
27. Santos EM, Marquering HA, Berkhemer OA, et al; MR CLEAN Investigators. **Development and validation of intracranial thrombus segmentation on CT angiography in patients with acute ischemic stroke.** *PLoS One* 2014;9:e101985 CrossRef Medline
28. Riedel CH, Jensen U, Rohr A, et al. **Assessment of thrombus in acute middle cerebral artery occlusion using thin-slice nonenhanced computed tomography reconstructions.** *Stroke* 2010;41:1659–64 CrossRef Medline
29. Lucas C, Schöttler JJ, Kemmling A, et al. **Automatic detection and segmentation of the acute vessel thrombus in cerebral CT.** *Informatik Aktuell* Springer; 2019:74–79 CrossRef
30. Mojtahedi M, Kappelhof M, Ponomareva E, et al. **Fully automated thrombus segmentation on CT images of patients with acute ischemic stroke.** *Diagnostics (Basel)* 2022;12:698 CrossRef Medline
31. Dutra BG, Tolhuisen ML, Alves HC; MR CLEAN Registry Investigators, et al. **Thrombus imaging characteristics and outcomes in acute ischemic stroke patients undergoing endovascular treatment.** *Stroke* 2019;50:2057–64 CrossRef Medline
32. Yoo J, Baek JH, Park H, et al. **Thrombus volume as a predictor of nonrecanalization after intravenous thrombolysis in acute stroke.** *Stroke* 2018;49:2108–15 CrossRef Medline
33. Campbell BC, Kappelhof M, Fischer U. **Role of intravenous thrombolytics prior to endovascular thrombectomy.** *Stroke* 2022;53:2085–92 CrossRef Medline
34. Huang C, Tian J, Yuan C, et al. **Fully automated segmentation of lower extremity deep vein thrombosis using convolutional neural network.** *Biomed Res Int* 2019;2019:3401683 CrossRef Medline
35. Santos EM, Niessen WJ, Yoo AJ, et al; MR CLEAN Investigators. **Automated entire thrombus density measurements for robust and comprehensive thrombus characterization in patients with acute ischemic stroke.** *PLoS One* 2016;11:e0145641 CrossRef Medline

Evaluation of the Statistical Detection of Change Algorithm for Screening Patients with MS with New Lesion Activity on Longitudinal Brain MRI

M. Homssi, E.M. Sweeney, E. Demmon, W. Mannheim, M. Sakirsky, Y. Wang, S.A. Gauthier, A. Gupta, and T.D. Nguyen



ABSTRACT

BACKGROUND AND PURPOSE: Identification of new MS lesions on longitudinal MR imaging by human readers is time-consuming and prone to error. Our objective was to evaluate the improvement in the performance of subject-level detection by readers when assisted by the automated statistical detection of change algorithm.

MATERIALS AND METHODS: A total of 200 patients with MS with a mean interscan interval of 13.2 (SD, 2.4) months were included. Statistical detection of change was applied to the baseline and follow-up FLAIR images to detect potential new lesions for confirmation by readers (Reader + statistical detection of change method). This method was compared with readers operating in the clinical workflow (Reader method) for a subject-level detection of new lesions.

RESULTS: Reader + statistical detection of change found 30 subjects (15.0%) with at least 1 new lesion, while Reader detected 16 subjects (8.0%). As a subject-level screening tool, statistical detection of change achieved a perfect sensitivity of 1.00 (95% CI, 0.88–1.00) and a moderate specificity of 0.67 (95% CI, 0.59–0.74). The agreement on a subject level was 0.91 (95% CI, 0.87–0.95) between Reader + statistical detection of change and Reader, and 0.72 (95% CI, 0.66–0.78) between Reader + statistical detection of change and statistical detection of change.

CONCLUSIONS: The statistical detection of change algorithm can serve as a time-saving screening tool to assist human readers in verifying 3D FLAIR images of patients with MS with suspected new lesions. Our promising results warrant further evaluation of statistical detection of change in prospective multireader clinical studies.

ABBREVIATIONS: PPV = positive predictive value; SDC = statistical detection of change

Detection of new lesion activity on serial MR imaging is important for the disease diagnosis, monitoring, and evaluation of treatment response in patients with MS.¹ In most clinical workflows, expert readers manually view baseline and follow-up brain MR images side-by-side on a PACS monitor to look for voxels with sufficiently large changes in image intensity and size

to be considered a potentially clinically relevant new MS lesion.² The state-of-the-art 3D T2-weighted FLAIR images, acquired in a routine clinical MS imaging protocol¹ as recommended by the most recent clinical consensus,³ provide high 1-mm isotropic resolution and excellent soft-tissue contrast for lesion detection. However, native images obtained at 2 different time points are often imperfectly aligned due to differences in patient positioning and acquisition technique. Therefore, detecting new lesions by visual matching on the unregistered longitudinal images (when image registration tools are not readily available on the reading workstation) in the presence of noise is a time-consuming, error-prone, and highly observer-dependent task, even for human experts.⁴

A number of automated and semiautomated algorithms have been developed to overcome these challenges.^{5–7} In the classic approach, serially acquired images are intensity-normalized and coregistered, from which a dissimilarity map (eg, obtained by subtraction) is calculated and then automatically segmented (eg, by thresholding or statistical inference methods) or reviewed by humans to yield the final lesion

Received February 3, 2023; accepted after revision April 3.

From the Department of Radiology (M.H., Y.W., A.G., T.D.N.), Department of Neurology (E.D., W.M., M.S., S.A.G.), and The Feil Family Brain & Mind Institute (S.A.G.), Weill Cornell Medicine, New York, New York; and Penn Statistics in Imaging and Visualization Endeavor (PennSIVE) Center, Department of Biostatistics, Epidemiology, and Informatics (E.M.S.), University of Pennsylvania, Philadelphia, Pennsylvania.

M. Homssi and E.M. Sweeney contributed equally to this work.

Paper previously presented, in part, at: Annual Meeting of the American Society of Neuroradiology, May 16–28, 2022; New York, New York.

This work was supported in part by grants from the National Institutes of Health (R01 NS105144, R01 NS090464, R01 NS104283) and the National Multiple Sclerosis Society (RR-1602-0767).

Please address correspondence to Thanh D. Nguyen, PhD, 407 East 61st St, RR-120, New York, NY 10065; e-mail: tdn2001@med.cornell.edu

Indicates open access to non-subscribers at www.ajnr.org

<http://dx.doi.org/10.3174/ajnr.A7858>

change mask.^{2,8-15} More recently, supervised deep learning-based convolutional neural network models have become the predominant approach.¹⁶⁻²⁰ Despite rapid advances in research, the detection sensitivity and specificity remain moderate on a voxel or lesion level (sensitivity and specificity; <0.8).^{4,7} We previously introduced the statistical detection of change (SDC) algorithm as an automated lesion-change detection tool to visually assist human readers. This algorithm applies an optimal binary change detector to the subtraction of 2 longitudinally registered FLAIR images to delineate brain areas with potential new lesions.¹⁴ The purpose of this study was to evaluate the improvement in the performance of subject-level detection by human readers when assisted by SDC, in comparison with the benchmark of human readers operating in the clinical workflow.

MATERIALS AND METHODS

Study Cohort

This was a retrospective longitudinal study conducted in a cohort of 200 patients with MS (145 women [72.5%], 55 men [27.5%]; mean age, 47.6 [SD, 10.9] years; range, 18.5–75.8 years) who were enrolled in an ongoing prospective imaging and clinical database for MS research. The database was approved by the local institutional review board (Judith Jaffe Multiple Sclerosis Center clinical and MR imaging database, IRB No. 0711009544; Weill Cornell Medicine), and written informed consent was obtained from all participants before their entry into the database. Consecutive patients who underwent 2 MR imaging scans between September 20, 2017, and July 7, 2021, with a mean follow-up interval of 13.2 (SD, 2.4) months (range, 7.5–24.8 months) were included. The final cohort consisted of 6 patients with clinically isolated syndrome, 181 with relapsing-remitting MS, 6 with primary-progressive MS, and 7 with secondary-progressive MS. The mean disease duration was 14.7 (SD, 7.4) years (range, 2.6–54.9 years), and the mean Expanded Disability Status Scale score was 1.3 (SD, 1.6) (range, 0.0–7.0; median, 1.0; interquartile range, 2.0). A total of 183 patients (91.5%) were treated with disease-modifying therapies. Of these, 88 (48.1%) received treatment by injection; 60 (32.8%), orally; and 35 (19.1%), by infusion.

MR Imaging Examinations

All patients were scanned on 3T MR imaging scanners (Magnetom Skyra and Vida; Siemens) using a product 20-channel head/neck coil. The scanning protocol included pre- and postgadolinium 3D T1-weighted MPRAGE sequences for anatomic definition and detection of active lesions, respectively, and 3D T2-weighted FLAIR and a sampling-perfection with application optimized contrasts by using different flip angle evolution (SPACE; Siemens) sequence for lesion identification, using the following imaging parameters: 1) 3D sagittal T1-weighted MPRAGE: TR/TE/TI = 2300.0/2.3/900 ms, flip angle = 8°, bandwidth = 200 Hz/pixel, acquired voxel size = 1.0-mm isotropic, number of slices = 176, parallel imaging factor = 2.0, scan time = 5 minutes 21 seconds; 2) 3D sagittal T2-weighted FLAIR SPACE: TR/TE/TI = 7600/448/2450 ms, flip angle = 90°, bandwidth = 781 Hz/pixel, echo spacing = 3.42 ms, turbo factor = 284, acquired voxel size = 1.0-mm isotropic, number of slices = 176, parallel imaging factor = 4.0, scan time = 5 minutes 6 seconds.

Image Postprocessing

At each time point, T1-weighted and FLAIR images were brain-extracted using the FMRIB Software Library (FSL) BET command (FSL Brain Extraction Tool (<http://fsl.fmrib.ox.ac.uk/fsl/fslwiki/BET>)²¹ and corrected for spatial inhomogeneity and segmented into gray matter, white matter, and CSF masks using the FSL FAST command (<https://fsl.fmrib.ox.ac.uk/fsl/fslwiki/FAST>).²² The FLAIR image was then linearly registered to the T1-weighted structural image using the FSL FLIRT command (Linear Image Registration Tool; FLIRT; <http://www.fmrib.ox.ac.uk/fsl/fslwiki/FLIRT>)²³ with 6 *df* (rigid body transformation). For longitudinal registration, the baseline and follow-up brain-extracted T1-weighted images were first linearly aligned to a half-way space⁹ using the Advanced Normalization Tools algorithm (<http://stnava.github.io/ANTs/>) with 12 *df* (rigid body and affine transformation),²⁴ followed by registration of the corresponding FLAIR images into the same half-way space using the concatenated transformation matrices obtained from the previous steps. The purpose of spatially aligning longitudinal images to the half-way space was to ensure that the degree of blurring introduced by the registration algorithm was similar among images, which improves image subtraction.

Next, the SDC algorithm,¹⁴ implemented in Matlab R2020 (MathWorks) on a Linux Ubuntu 18.04 computer equipped with a 64-bit Intel Core i9-9940X 3.30 GHz CPU and 128 GB of RAM, was applied to the registered and intensity-normalized FLAIR images in the half-way space to detect brain voxels with positive signal change (indicating new lesions or growth of existing lesions). Briefly, for each voxel, the SDC test statistic was calculated from the FLAIR subtraction image over a 3-voxel connected neighborhood and compared with a threshold (chosen to achieve a false-positive rate of 0.0001) to generate a binary positive change mask. Additional constraints were imposed on the minimum lesion volume (15 mm³) and location (lesions located within 2 voxels of the CSF border and the GM/WM tissue border had to be part of a larger lesion that extended outside this border) to reduce the number of false-positives. The constraint on the lesion location was useful for eliminating the thin layer of bright voxels lining the ventricles on the FLAIR image and also for dealing with spurious voxels at the tissue edge on the FLAIR difference image due to imperfect subtraction.

Finally, the detected changed voxels were registered back to the follow-up FLAIR image. A binary mask was generated by the SDC algorithm, which was overlaid on the baseline and follow-up FLAIR image pair to delineate potential new lesions with a red box (Fig 1) to facilitate subsequent visual confirmation of the detected new lesions by human readers. The processing time of the SDC algorithm was recorded in 5 randomly chosen subjects.

Visual Identification of New Lesions

The registered baseline and follow-up FLAIR images, along with the red boxes marking the potential new lesions detected by SDC (Fig 1), were displayed side-by-side in the axial plane using ITK-SNAP Version 3.8 software (www.itksnap.org).²⁵ Two expert readers, a board-certified neuroradiologist with 16 years of experience and an MR imaging physicist with 20 years of experience, both of whom were blinded to clinical and other imaging

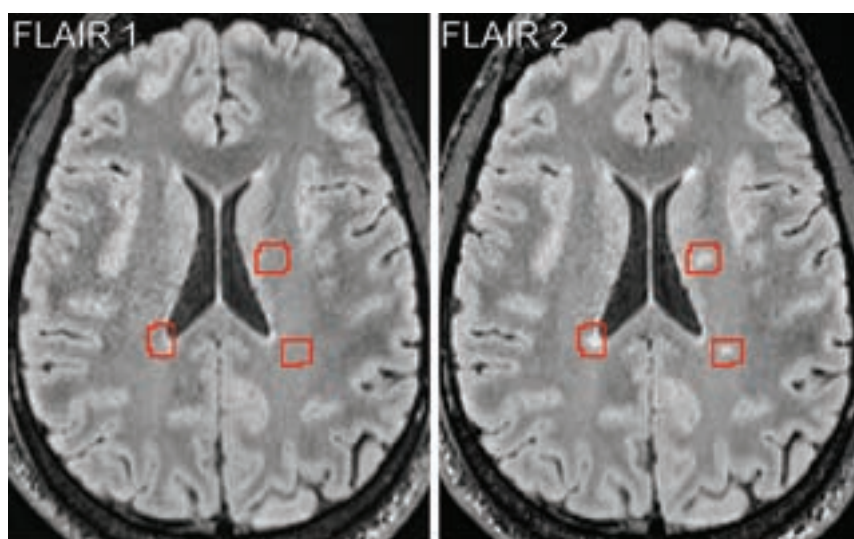


FIG 1. Longitudinal axial FLAIR images acquired from a patient with MS approximately 10.5 months apart, showing an example of 3 new lesions detected by human readers who were assisted visually by the SDC algorithm, which delineates brain areas containing potential new lesions for human confirmation (red boxes) (referred to as Reader + SDC method).

information, jointly reviewed the FLAIR images with visual assistance from SDC-detected areas of lesion growth to identify new lesions on the basis of consensus (Reader + SDC method). The readers assessed all available FLAIR images both inside and outside the areas of change detected by SDC algorithm. A lesion was considered as new if it could be seen on the follow-up FLAIR image but could not be ascertained on the baseline FLAIR image.

For comparison, the official radiology reports created by board-certified neuroradiologists at the time of the clinical encounters were retrieved from the EPIC electronic medical record system (Epic Systems) and manually parsed for the mention of at least 1 new lesion. In our clinical workflow occurring in the context of a routine outpatient imaging practice affiliated with a large academic health system, new lesions are detected on the basis of the visual interpretation of baseline and follow-up native brain images acquired with FLAIR as well as T1-weighted, T2-weighted, and gadolinium-enhanced T1-weighted sequences (hereafter referred to as the Reader method). In this setting, faculty neuroradiologists, all of whom are board-certified, reviewed these brain MR imaging studies as they appeared in real time on a clinical worklist. Cases were variably interpreted alongside radiology clinical trainees (diagnostic radiology residents and/or neuroradiology fellows) with the benefit of full access to the electronic health record and all patient records. During the time period of this study (approximately 4 years), all image interpretation was performed on a PACS system. The total number of new lesions and their precise anatomic locations were variably recorded in the reports, subject to the clinical scenario and preferences of the interpreting radiologist. Therefore, in this study, lesion detection outcome for the 3 methods (Reader, SDC, and Reader + SDC) was defined at a subject level as a binary indicator of having at least 1 new lesion.

Statistical Analysis

All statistical analyses were performed in R statistical and computing software, Version 4.1.2 (<http://www.r-project.org>).²⁶ We

were interested in the detection of ≥ 1 new lesion at a subject level. A change in size of existing lesions (growth or shrinkage) and lesions of $<15 \text{ mm}^3$ was excluded from the analysis. This minimum lesion volume cutoff was calculated assuming a spherical lesion shape with a diameter of 3 mm (3 voxels on our FLAIR image) using the formula $V_{\min} = \pi d^3 / 6 = 14.1 \text{ mm}^3$, which is in accordance with the currently accepted minimum lesion dimension on MR imaging.¹ For each subject and each method (Reader, SDC, and Reader + SDC), a binary indicator of the incidence of new lesions was created. Contingency tables at a subject level were investigated, and sensitivity, specificity, and positive predictive value (PPV) were assessed using the Reader + SDC method as a reference. Exact binomial 95% CIs were calculated for these measures.²⁷ Agreement among all the

methods was calculated with nonparametric bootstrapped 95% CIs.²⁸ For the Reader and SDC methods, the Breslow-Day test²⁹ was used to test whether the OR was the same for the subject group imaged on the same scanner versus the group imaged on 2 different scanners.

RESULTS

All 200 pairs of baseline and follow-up FLAIR scans were interpretable. Of these, 80 pairs (40.0%) were acquired on the same MR imaging scanner. The fully-automated SDC algorithm detected 86 subjects (43.0%) with at least 1 potential new lesion. The semiautomated Reader + SDC method, in which 2 readers identified new lesions by comparing the 2 longitudinally registered FLAIR images with visual assistance from SDC showing potential new lesions (Fig 1), detected 41 subjects (20.5%) with at least 1 new lesion. After excluding lesions of $<15 \text{ mm}^3$, Reader + SDC found 30 individuals (15.0%) with new lesions. In comparison, the traditional Reader method, performed by radiologists in the routine clinical workflow, identified 20 subjects (10.0%) with at least 1 new lesion.

Table 1 shows the contingency table for subject-level detection of new lesions on FLAIR images obtained by the Reader and SDC methods using the Reader + SDC method as a reference (note that lesions of $<15 \text{ mm}^3$ were excluded from the statistical analysis for SDC and Reader + SDC methods, while the Reader method did not provide information on lesion size). In 200 cases of MS, Reader failed to detect new lesions in 14/30 individuals, resulting in a moderate sensitivity of 0.53 (95% CI, 0.34–0.72), with an excellent specificity of 0.98 (95% CI, 0.94–0.99) and a good PPV of 0.80 (95% CI, 0.56–0.94). Of these 14 cases, 13 (92.9%) had only 1 new lesion and one (7.1%) had 2 new lesions. Most of these lesions were either periventricular (9/15, 60%) or in the central semiovale (5/15, 33%). The 4 subjects who were identified as having at least 1 new lesion by Reader but not by Reader + SDC

in Table 1 were all found to have new lesions less than the 15-mm³ cutoff. In comparison, SDC was able to detect all 30/30 patients with at least 1 new lesion, achieving a perfect sensitivity of 1.00 (95% CI, 0.88–1.00), though at the cost of a lower specificity of 0.67 (95% CI, 0.59–0.74) and a lower PPV of 0.35 (95% CI, 0.25–0.46). The agreement on a subject level was found to be 0.91 (95% CI, 0.87–0.95) between Reader + SDC and Reader; 0.72 (95% CI, 0.66–0.78) between Reader + SDC and SDC; and 0.64 (95% CI, 0.57–0.71) between Reader and SDC.

Table 2 shows the contingency tables for subject-level detection of new FLAIR lesions in the 2 groups of subjects who were imaged on the same scanner (80/200) and on 2 different scanners (120/200). Reader was found to perform better on FLAIR images acquired on the same scanner compared with those acquired on different scanners (sensitivity, 0.67; 95% CI, 0.38–0.88, versus 0.40; 95% CI, 0.16–0.68; specificity, 1.00; 95% CI, 0.94–1.00, versus 0.96; 95% CI, 0.91–0.99; and PPV 1.00; 95% CI, 0.69–1.00, versus 0.60; 95% CI, 0.26–0.88). While SDC detected 15/15 patients with at least 1 new lesion (sensitivity, 1.00; 95% CI, 0.78–1.00) in both groups, SDC correctly detected 49/65 patients without a new lesion (specificity, 0.75; 95% CI, 0.63–0.85) in the group scanned on the same scanner but only 65/105 patients without a new lesion (specificity, 0.62; 95% CI, 0.52–0.71) in the group scanned on 2 different scanners. Using the Breslow-Day test, we found that the OR for Reader versus Reader + SDC

differed across the group imaged on the same scanner and the one imaged on 2 different scanners ($P = .036$), indicating a different performance. On the other hand, we did not find a statistically significant difference in the OR for the SDC versus Reader + SDC case with regard to scanner change ($P = .762$).

Figure 2 shows examples of 4 new lesions of various sizes and locations from 4 different subjects with MS that were identified by SDC and confirmed by Reader + SDC but were not detected by Reader according to the radiology report. Figure 3 shows examples of 2 new punctate lesions, both of which were gadolinium-enhancing, that were identified by Reader in the clinical workflow but were not detected by SDC and Reader + SDC after applying a minimum lesion volume threshold of 15 mm³.

On average, the longitudinal FLAIR registration took 120.6 (SD, 10.7) seconds, and the SDC new lesion detection took 2.5 (SD, 0.3) seconds per case.

DISCUSSION

In this single-center study evaluating the utility of the automated SDC algorithm in assisting human readers to detect new lesions on longitudinal FLAIR images, we found that SDC was able to provide a perfect new lesion-detection sensitivity on a subject level. SDC achieved this excellent level of detection sensitivity while providing a moderate subject-level specificity of 0.67 (meaning about 2 of every 3 subjects without new lesion activity were correctly classified). These operating characteristics allow SDC to be used as a valuable screening tool and could accelerate the interpretation time of cases in which no new lesions are identified by SDC. In our study, for example, 114 of 200 patients had no new lesions on follow-up confirmed by SDC, suggesting that a more rapid expert human review of these cases (57% of our entire cohort) may be feasible. Such an increase in efficiency may enable expert human readers to allocate more time to interpret MR imaging cases flagged by SDC as being potentially positive for new lesions.

In the conventional radiology workflow, detecting new lesions that formed between 2 longitudinal scans of patients with MS is often performed by radiologists and other clinicians

manually on a PACS monitor by comparing a large number of paired-but-imperfectly aligned FLAIR images. This approach is often time-consuming, mentally demanding, and error-prone, especially if there is a substantial image misalignment due to the difference in head orientation between the 2 scans. SDC overcomes these challenges by providing an automated detection of potential new lesions, which are then visually indicated to the reader on a pair of longitudinally registered images (Fig 1). Conceptually, SDC is formulated as an optimal change detector applied to the subtraction image, which can be proved mathematically by the Neyman-Pearson lemma to provide the best detection power for a given false-positive rate.³⁰

Table 1: Contingency table comparing the subject-level detection of new lesions obtained from longitudinal FLAIR images of 200 patients with MS using the Reader (manual), SDC (fully automated), and Reader + SDC (semiautomated) methods^a

		Reader + SDC		Total
		New Lesions	No New Lesions	
Reader	New Lesions	16	4	20
	No new lesions	14	166	180
SDC	New lesions	30	56	86
	No new lesions	0	114	114
Total		30	170	200

^a Reader + SDC was considered a reference method to provide the ground truth for comparison.

Table 2: Contingency table comparing the subject-level detection of new lesions obtained from longitudinal FLAIR images acquired on the same MR imaging scanner from 80 patients with MS and those acquired on 2 different scanners from 120 patients with MS using the Reader (manual), SDC (fully automated), and Reader + SDC (semiautomated) methods

		Reader + SDC		
		New Lesions	No New Lesions	Total
Same MR imaging scanner from 80 patients with MS				
Reader	New lesions	10	0	10
	No new lesions	5	65	70
SDC	New lesions	15	16	31
	No new lesions	0	49	49
Total		15	65	80
Two different scanners from 120 patients with MS				
Reader	New lesions	6	4	10
	No new lesions	9	101	110
SDC	New lesions	15	40	55
	No new lesions	0	65	65
Total		15	105	120

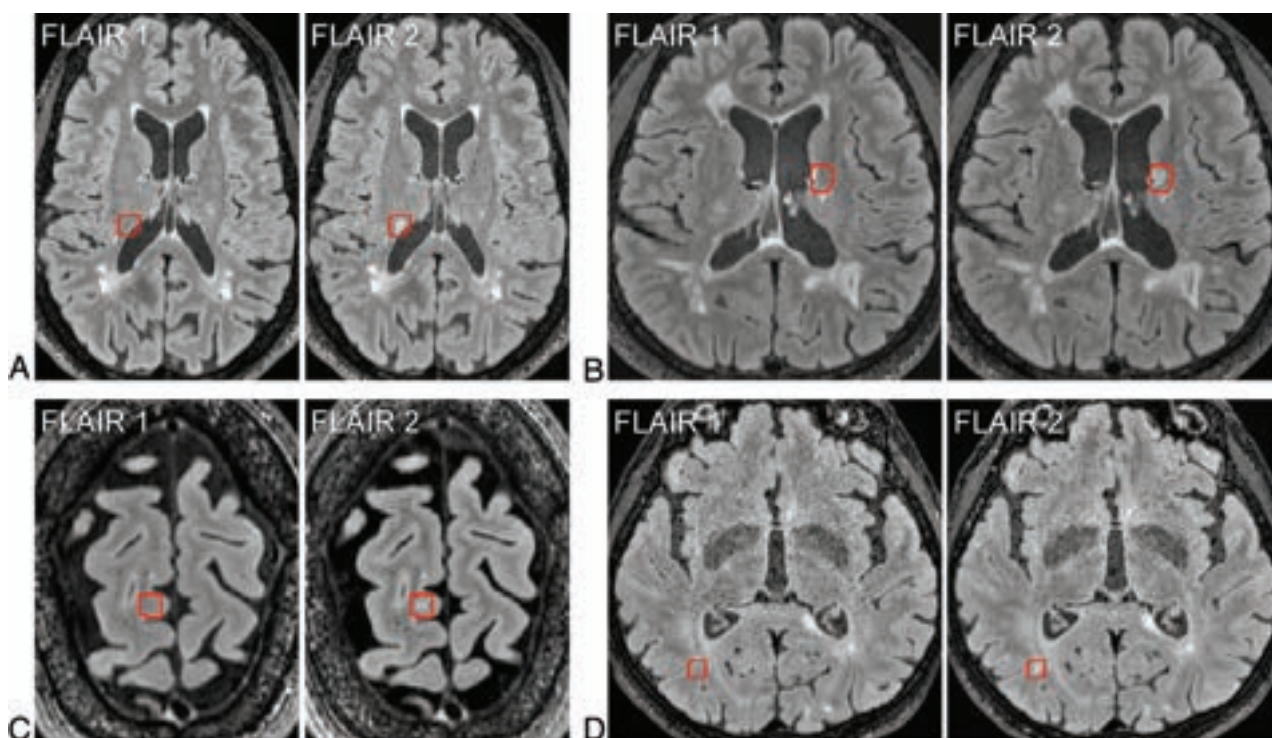


FIG 2. Examples of new lesions varying in size and location on longitudinal FLAIR images obtained from 4 different subjects with MS. These lesions were initially identified by SDC (marked by red boxes) and later confirmed by the Reader + SDC method but were not detected by the Reader method using the conventional radiology workflow.

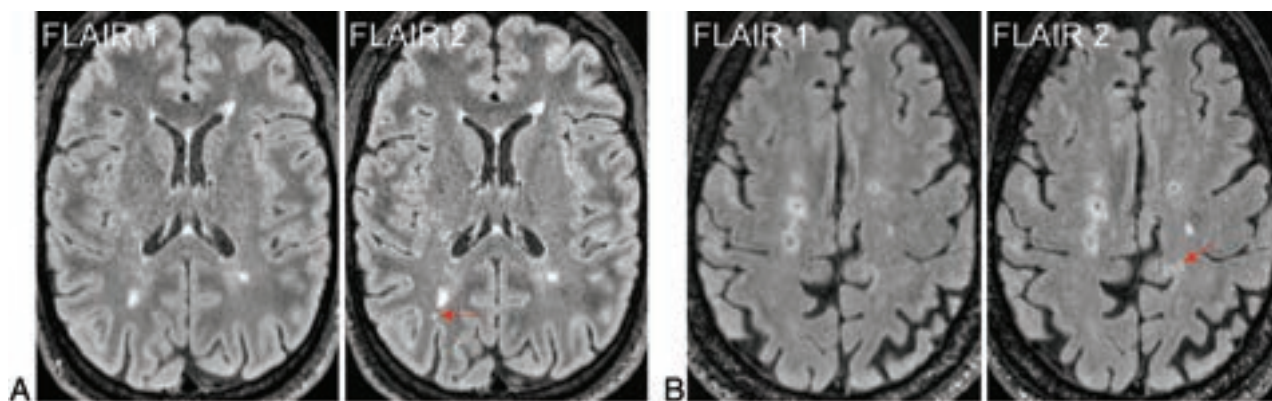


FIG 3. Examples of new punctate lesions (arrows) on longitudinal FLAIR images acquired from 2 different subjects with MS, identified by the Reader method in the clinical workflow but not detected by the SDC and Reader + SDC methods after applying a minimum lesion volume cut-off of 15 mm³. Both lesions were enhancing on the postgadolinium T1-weighted images.

By design, SDC mimics a human reader in 2 key aspects: First, it applies an adaptive intensity threshold to the subtraction image on the basis of the level of noise in the image. For example, the threshold for the longitudinal signal change is automatically increased by SDC for more noisy images, which can be regarded as equivalent to setting a higher level of trust as often performed by a human reader when dealing with noise. Second, SDC uses signal from voxels in a local neighborhood to calculate the test statistic, helping to increase the detection reliability. Similar to change detection by humans, spatially spurious signals on the subtraction image are encoded by the algorithm to have a lower likelihood of being identified as true change. By virtue of being

capable of operating at a very high sensitivity and a reasonable specificity, SDC enables the new lesion identification problem to be shifted from the traditionally difficult task of locating new lesions on unmarked images to a much easier task of confirming true-positives and eliminating false-positives in areas already marked by SDC. Therefore, SDC has a great potential to shorten new-lesion detection time while reducing reader fatigue.

Several studies have demonstrated the benefits of detecting new lesions on a subject level on longitudinally registered or subtracted standard 1-mm isotropic 3D FLAIR images. A study by Galletto Pregliasco et al,¹⁵ performed in 94 patients with MS, showed that using an automated coregistration-fusion method

improved the detection rate of subjects with at least 1 new lesion from 46% to 59%. In another study conducted by Eichinger et al,¹³ in 106 patients with MS, 58% of subjects were identified as having at least 1 new lesion on the FLAIR subtraction image, with a similar proportion (59%) identified using the conventional reading method. In this study of 200 patients with MS, we saw an improvement from 8% by Reader to 15% by Reader + SDC in the subject-level detection rate using a minimum lesion volume threshold of 15 mm³. The observed relatively rare event of a new lesion occurring in our cohort is likely related to different patient characteristics.

Compared with the emerging neural network-based deep learning approaches for new lesion detection, the SDC algorithm does not require data labeling and specialized hardware (such as a powerful graphics processing unit) for network training. SDC can also be used as a computer-assisted detection and segmentation tool to help humans create labeled image data for network training more efficiently. In addition to the ease of implementation, SDC provides relatively fast processing of the subtraction image, taking only a few seconds per case using our Matlab implementation, which can be further improved for interactive use by a C/C++ implementation. However, the longitudinal registration step to generate the subtraction image takes about 2 minutes per case in our processing pipeline. The development of rapid image registration algorithms³¹⁻³³ will, therefore, be essential for a successful deployment of SDC in a routine interactive workflow. Alternatively, SDC can be implemented as part of the image-reconstruction process, assuming that images from the prior study are available on the scanner. Further studies are needed to evaluate the clinical feasibility of these approaches.

The coregistration steps involved in the SDC processing pipeline are key elements of the SDC approach and offer a highly precise registration not possible in routine image-interpretation software solutions embedded in clinical PACS systems. In our pipeline implementation, we chose to perform longitudinal FLAIR image registration by registering the image to the T1-weighted half-space for 2 reasons: 1) The T1-weighted image has the same resolution (1-mm isotropic) but much better GM/WM contrast than the FLAIR image, and 2) in our data, the T1-weighted image has less noise than the FLAIR image because T1-weighted imaging was acquired with an acceleration factor of 2, while FLAIR was acquired with an acceleration factor of 4 (to keep the scan time reasonable). Consequently, the longitudinal registration was found to be generally more accurate when using T1-weighted images rather than FLAIR images. While a 1-mm isotropic 3D T1-weighted sequence is part of the MS brain MR imaging protocol recommended by the most recent clinical consensus,³ performing direct registration between the 2 longitudinal FLAIR images is a viable option when such T1-weighted images are not available.

This study has several limitations. First, the ground truth was determined on the basis of expert readings from only 1 experienced board-certified neuroradiologist in consensus with an MR imaging physicist with expertise in MS brain image analysis. Furthermore, because these readers were aware of the use of SDC, our study design was unable to fully eliminate the possibility of reader bias. While this study design is appropriate for the

current early-stage evaluation of SDC technology development, the diagnostic performance metrics such as sensitivity and specificity reported in this study require further clinical validation in future multireader multicase studies³⁴ involving multiple board-certified radiologists and using a clinical consensus as the criterion standard. This is a key validation step to ensure that image-analysis techniques are ready for regulatory approval and clinical adoption.

Second, intracortical and subpial GM lesions were not considered because these lesions are difficult to visualize reliably with existing routine 3T imaging sequences, including FLAIR.³⁵ Third, in the current study design, the Reader method was performed in the routine clinical workflow by readers different from those involved in the Reader + SDC method. These differences make it difficult to determine the clinical significance, if any, of discrepancies in new lesion identification noted between the clinical radiologic report and retrospectively performed SDC-enhanced readings. For example, the radiologist issuing the clinical report in the Reader method had real-time access to the electronic health record and contrast-enhanced imaging while being subject to time constraints imposed in the clinical workflow and being responsible for total brain MR imaging interpretation, not only new lesion detection on FLAIR.

While our study design allows a direct comparison of SDC with the radiology report, regarded as a clinically established benchmark, future work will be focused on integrating the SDC algorithm into the clinical workflow, which will allow prospective comparison studies to be performed in a real-world setting. In the context of active MS, this will also enable the comparison of gadolinium-based T1-weighted sequences with emerging non-contrast approaches for new acute lesion detection such as those combining FLAIR subtraction with quantitative susceptibility mapping.³⁶ Fourth, a minimum lesion volume cutoff of 15 mm³ was used to mitigate the effect of noise on the false-positive rate of the SDC algorithm. Such punctate MS lesions are often considered inconsequential,¹ though further evidence on their role in the disease progression and outcome may be needed. Fifth, the PACS system used for clinical interpretations was not equipped with the capability to adjust for differences in scan angle or patient positioning or to coregister 3D images to enable section-by-section comparisons accurately. This capability is being enhanced in more modern PACS systems but was not readily available in the version of the PACS system used during the time of the study scanning. Sixth, validation on FLAIR images acquired on MR imaging scanners from other vendors or with different acquisition parameters is very important for successful clinical translation of SDC and will be addressed in a future study. Finally, linear longitudinal brain registration was used in this study, which was deemed sufficiently accurate for the annual follow-up interval in our cohort but may not capture nonlinear changes in the brain morphology during a longer interscan period. The use of a deformable motion model in the registration algorithm may be considered in such scenario.^{12,24}

CONCLUSIONS

The SDC algorithm can serve as a time-saving screening tool to assist human readers in verifying 3D FLAIR images of patients

with MS with suspected new lesions. Our promising results warrant further evaluation of SDC in prospective multireader clinical studies.

Disclosure forms provided by the authors are available with the full text and PDF of this article at www.ajnr.org.

REFERENCES

- Filippi M, Rocca MA, Ciccarelli O, et al; MAGNIMS Study Group. **MRI criteria for the diagnosis of multiple sclerosis: MAGNIMS consensus guidelines.** *Lancet Neurol* 2016;15:292–303 CrossRef Medline
- Moraal B, Wattjes MP, Geurts JJ, et al. **Improved detection of active multiple sclerosis lesions: 3D subtraction imaging.** *Radiology* 2010;255:154–63 CrossRef Medline
- Wattjes MP, Ciccarelli O, Reich DS, et al; North American Imaging in Multiple Sclerosis Cooperative MRI Guidelines Working Group. **2021 MAGNIMS-CMSC-NAIMS consensus recommendations on the use of MRI in patients with multiple sclerosis.** *Lancet Neurol* 2021;20:653–70 CrossRef Medline
- Carass A, Roy S, Jog A, et al. **Longitudinal multiple sclerosis lesion segmentation: resource and challenge.** *Neuroimage* 2017;148:77–102 CrossRef Medline
- Patriarche J, Erickson B. **A review of the automated detection of change in serial imaging studies of the brain.** *J Digit Imaging* 2004;17:158–74 CrossRef Medline
- Llado X, Ganiler O, Oliver A, et al. **Automated detection of multiple sclerosis lesions in serial brain MRI.** *Neuroradiology* 2012;54:787–807 CrossRef Medline
- Diaz-Hurtado M, Martinez-Heras E, Solana E, et al. **Recent advances in the longitudinal segmentation of multiple sclerosis lesions on magnetic resonance imaging: a review.** *Neuroradiology* 2022;64:2103–17 CrossRef Medline
- Sweeney EM, Shinohara RT, Shea CD, et al. **Automatic lesion incidence estimation and detection in multiple sclerosis using multisequence longitudinal MRI.** *AJNR Am J Neuroradiol* 2013;34:68–73 CrossRef Medline
- Battaglini M, Rossi F, Grove RA, et al. **Automated identification of brain new lesions in multiple sclerosis using subtraction images.** *J Magn Reson Imaging* 2014;39:1543–49 CrossRef Medline
- Ganiler O, Oliver A, Diez Y, et al. **A subtraction pipeline for automatic detection of new appearing multiple sclerosis lesions in longitudinal studies.** *Neuroradiology* 2014;56:363–74 CrossRef Medline
- Jain S, Ribbens A, Sima DM, et al. **Two time point MS lesion segmentation in brain MRI: an expectation-maximization framework.** *Front Neurosci* 2016;10:576 CrossRef Medline
- Cabezas M, Corral JF, Oliver A, et al. **Improved automatic detection of new T2 lesions in multiple sclerosis using deformation fields.** *AJNR Am J Neuroradiol* 2016;37:1816–23 CrossRef Medline
- Eichinger P, Wiestler H, Zhang H, et al. **A novel imaging technique for better detecting new lesions in multiple sclerosis.** *J Neurol* 2017;264:1909–18 CrossRef Medline
- Nguyen TD, Zhang S, Gupta A, et al. **Fast and robust unsupervised identification of MS lesion change using the statistical detection of changes algorithm.** *AJNR Am J Neuroradiol* 2018;39:830–33 CrossRef Medline
- Galletto Pregliasco A, Collin A, Gueguen A, et al. **Improved detection of new MS lesions during follow-up using an automated MR coregistration-fusion method.** *AJNR Am J Neuroradiol* 2018;39:1226–32 CrossRef Medline
- Birenbaum A, Greenspan H. **Multi-view longitudinal CNN for multiple sclerosis lesion segmentation.** *Eng Appl Artif Intel* 2017;65:111–18 CrossRef
- Fartaria MJ, Kober T, Granziera C, et al. **Longitudinal analysis of white matter and cortical lesions in multiple sclerosis.** *Neuroimage Clin* 2019;23:101938 CrossRef Medline
- Salem M, Valverde S, Cabezas M, et al. **A fully convolutional neural network for new T2-w lesion detection in multiple sclerosis.** *Neuroimage Clin* 2020;25:102149 CrossRef Medline
- Schmidt-Mengin M, Soulier T, Hamzaoui M, et al. **Online hard example mining vs. fixed oversampling strategy for segmentation of new multiple sclerosis lesions from longitudinal FLAIR MRI.** *Front Neurosci* 2022;16:1004050 CrossRef Medline
- Basaran BD, Matthews PM, Bai W. **New lesion segmentation for multiple sclerosis brain images with imaging and lesion-aware augmentation.** *Front Neurosci* 2022;16:1007453 CrossRef Medline
- Smith SM. **Fast robust automated brain extraction.** *Hum Brain Mapp* 2002;17:143–55 CrossRef Medline
- Zhang Y, Brady M, Smith S. **Segmentation of brain MR images through a hidden Markov random field model and the expectation-maximization algorithm.** *IEEE Trans Med Imaging* 2001;20:45–57 CrossRef Medline
- Jenkinson M, Bannister P, Brady M, et al. **Improved optimization for the robust and accurate linear registration and motion correction of brain images.** *Neuroimage* 2002;17:825–41 CrossRef Medline
- Avants BB, Tustison NJ, Song G, et al. **A reproducible evaluation of ANTs similarity metric performance in brain image registration.** *Neuroimage* 2011;54:2033–44 CrossRef Medline
- Yushkevich PA, Piven J, Hazlett HC, et al. **User-guided 3D active contour segmentation of anatomical structures: significantly improved efficiency and reliability.** *Neuroimage* 2006;31:1116–28 CrossRef Medline
- R Core Team. **R: A Language and Environment for Statistical Computing.** R Foundation for Statistical Computing, Vienna, Austria; 2021. <https://www.R-project.org>. Accessed April 20, 2023
- Collett D. **Modelling Binary Data.** 2nd ed. Taylor & Francis; 2002
- Efron B, Tibshirani RJ. **An Introduction to the Bootstrap.** CRC Press; 1994
- Breslow N, Day NE. **Statistical Methods in Cancer Research: The Analysis of Case-Control Studies.** IARC Scientific Publication; 1980
- Kay SM. **Fundamentals of Statistical Signal Processing: Detection Theory.** Vol. II. Prentice Hall; 1998
- Shamonin DP, Bron EE, Lelieveldt BP, et al; Alzheimer's Disease Neuroimaging Initiative. **Fast parallel image registration on CPU and GPU for diagnostic classification of Alzheimer's disease.** *Front Neuroinform* 2013;7:50 CrossRef Medline
- Balakrishnan G, Zhao A, Sabuncu MR, et al. **An unsupervised learning model for deformable medical image registration.** In: *Proceedings of the IEEE/CVF Conference on Computer Vision and Pattern Recognition*, Salt Lake City, Utah. June 18–23, 2018;9252–60
- Yang X, Kwitt R, Styner M, et al. **Quicksilver: fast predictive image registration—a deep learning approach.** *Neuroimage* 2017;158:378–96 CrossRef Medline
- Obuchowski NA, Bullen J. **Multireader diagnostic accuracy imaging studies: fundamentals of design and analysis.** *Radiology* 2022;303:26–34 CrossRef Medline
- Maranzano J, Dadar M, Rudko DA, et al. **Comparison of multiple sclerosis cortical lesion types detected by multicontrast 3T and 7T MRI.** *AJNR Am J Neuroradiol* 2019;40:1162–69 CrossRef Medline
- Zhang S, Nguyen TD, Zhao Y, et al. **Diagnostic accuracy of semiautomatic lesion detection plus quantitative susceptibility mapping in the identification of new and enhancing multiple sclerosis lesions.** *Neuroimage Clin* 2018;18:143–48 CrossRef Medline

Revolutionizing MS Monitoring: The Impact of Postprocessing Techniques on Lesion Detection

MS is the most common chronic inflammatory disease of the CNS, with approximately 2.5 million prevalent cases worldwide. It is the leading cause of nontraumatic disability among young adults. A major challenge in managing MS is monitoring disease activity, progression, and treatment response across time. However, detecting new brain lesions by side-by-side scrolling of 2 follow-up MR imaging examinations is time-consuming, prone to reading errors, and can be extremely difficult in cases of high lesion burden. With advancements in postprocessing techniques, new digital tools have emerged to help radiologists enhance their efficiency and reproducibility, while reducing reading time and error rates. Several methods using coregistration, intensity standardization, fusion, or image subtraction have been proposed. These tools have demonstrated substantial improvements in detecting new MS brain lesions, with performance gains ranging from 35% to 80%. A few studies have revealed that simple postprocessing techniques, such as coregistration fusion of 3D FLAIR sequences or coregistration subtraction with lesion color-coding of 2D FLAIR sequences, could enhance the detection of new T2/FLAIR hyperintense brain lesions in patients with MS.¹⁻³

In recent years, there has been a shift toward reducing the use of gadolinium contrast injection in MR images of patients with MS due to concerns about potential long-term health effects, making it even more critical for readers to detect new lesions on unenhanced MR images.⁴ This shift has led to a demand for alternative techniques to monitor disease activity and progression in patients with MS.⁵ The detection of new MS lesions is crucial in managing this chronic neurologic disease because it directly influences clinical decision-making and subsequent therapeutic strategies. Monitoring the formation of new lesions enables neurologists to assess the efficacy of the current treatment and, if necessary, adjust the therapeutic approach to prevent further disease progression. Early identification of new lesions allows the implementation of more aggressive treatment regimens, which have been shown to reduce disability accumulation, suppress inflammatory activity, and enhance long-term outcomes for patients. In this context, a vigilant approach to lesion detection is integral to the practice of precision medicine in MS because it facilitates the individualized tailoring of therapy to optimize patient outcomes while minimizing the risk of treatment-associated adverse effects.

Recently, numerous neural network–based deep learning approaches for new lesion detection have been developed to further improve the follow-up of patients with MS. These techniques can help identify new lesions and changes in lesion size or location with higher sensitivity and specificity than traditional imaging methods and can detect subtle and slight changes potentially undetectable by a human reader.⁶ According to the 2020 international guidelines for MR imaging standardization and the Magnetic Resonance Imaging in MS (MAGNIMS) consensus, the development and standardization of such postprocessing tools to aid radiologists in their interpretation would improve the follow-up of patients with MS.^{7,8}

In this *AJNR*-published study, Homssi et al⁹ evaluated a statistical detection of change (SDC) algorithm for screening patients with MS with new lesion activity on longitudinal brain MR imaging. They demonstrated the effectiveness of their SDC algorithm in assisting human readers in identifying new lesions in patients with MS. The study found that a Reader + SDC method, which combines the use of the SDC algorithm with human readers, outperformed the Reader method, in which only human readers were used, in detecting new lesions. Specifically, Reader + SDC identified 15.0% of subjects with at least 1 new lesion, while Reader detected only 8.0%. Moreover, the study found that the SDC algorithm achieved a perfect sensitivity of 1.00 and a moderate specificity of 0.67 as a subject-level screening tool. This outcome suggests that the SDC algorithm can be a valuable tool in assisting human readers in detecting new lesions in patients with MS and can help save time and reduce the potential for errors. As the authors emphasized, one of the advantages of the SDC technique compared with neural network–based deep learning approaches is that the SDC algorithm does not require data labeling and specialized hardware such as powerful graphics processing units for network training. However, it is not yet integrated into routine clinical practice, possibly limiting its adoption by radiologists worldwide, compared with simple postprocessing tools like coregistration fusion or coregistration subtraction techniques, which are widely accessible on most postprocessing devices.

The results of this study are promising and warrant further evaluation of the SDC algorithm in prospective multireader clinical studies. If the SDC algorithm proves to be effective in larger

clinical studies, it could become an invaluable tool for diagnosing and monitoring MS, leading to improved reader accuracy, efficiency, confidence, and reproducibility. The use of these tools in clinical practice aligns well with international guidelines oriented toward a more unified and harmonized approach for the follow-up of patients with MS, ultimately leading to improved patient outcomes.

REFERENCES

1. Galletto Pregliasco A, Collin A, Guéguen A, et al. **Improved detection of new MS lesions during follow-up using an automated MR coregistration-fusion method.** *AJNR Am J Neuroradiol* 2018;39:1226–32 CrossRef Medline
2. Schmidt MA, Linker RA, Lang S, et al. **FLAIR fusion processing with contrast inversion.** *Clin Neuroradiol* 2018;28:367–76 CrossRef Medline
3. Zopfs D, Laukamp KR, Paquet S, et al. **Follow-up MRI in multiple sclerosis patients: automated co-registration and lesion color-coding improves diagnostic accuracy and reduces reading time.** *Eur Radiol* 2019;29:7047–54 CrossRef Medline
4. Briset JC, Kremer S, Hannoun S, et al. **New OFSEP recommendations for MRI assessment of multiple sclerosis patients: special consideration for gadolinium deposition and frequent acquisitions.** *J Neuroradiol* 2020;47:250–58 CrossRef Medline
5. Boeken T, Feydy J, Lecler A, et al. **Artificial intelligence in diagnostic and interventional radiology: where are we now?** *Diagn Interv Imaging* 2023;104:1–5 CrossRef Medline
6. Roca P, Attie A, Colas L, et al; OFSEP Investigators; Steering Committee; Investigators; Imaging Group. **Artificial intelligence to predict clinical disability in patients with multiple sclerosis using FLAIR MRI.** *Diagn Interv Imaging* 2020;101:795–802 CrossRef Medline
7. Saslow L, Li DK, Halper J, et al. **An international standardized magnetic resonance imaging protocol for diagnosis and follow-up of patients with multiple sclerosis.** *Int J MS Care* 2020;22:226–32 CrossRef Medline
8. Filippi M, Rocca MA, Ciccarelli O, et al; MAGNIMS Study Group. **MRI criteria for the diagnosis of multiple sclerosis: MAGNIMS consensus guidelines.** *Lancet Neurol* 2016;15:292–303 CrossRef Medline
9. Homssi M, Sweeney EM, Demmon E, et al. **Evaluation of the statistical detection of change algorithm for screening patients with MS with new lesion activity on longitudinal brain MRI.** *AJNR Am J Neuroradiol* 2023;44:649–55 CrossRef Medline

● **A. Lecler**

Department of Neuroradiology
Adolphe de Rothschild Foundation Hospital
Paris, France
University of Paris
Paris, France

<http://dx.doi.org/10.3174/ajnr.A7868>

NCCT Markers of Intracerebral Hemorrhage Expansion Using Revised Criteria: An External Validation of Their Predictive Accuracy

C. Ducroux, A. Nehme, B. Rioux, M.-A. Panzini, R. Fahed, L.C. Gioia, and L. Létourneau-Guillon



ABSTRACT

BACKGROUND AND PURPOSE: Several NCCT expansion markers have been proposed to improve the prediction of hematoma expansion. We retrospectively evaluated the predictive accuracy of 9 expansion markers.

MATERIALS AND METHODS: Patients admitted for intracerebral hemorrhage within 24 hours of last seen well were retrospectively included from April 2016 to April 2020. The primary outcome was revised hematoma expansion, defined as any of a ≥ 6 -mL or $\geq 33\%$ increase in intracerebral hemorrhage volume, a ≥ 1 -mL increase in intraventricular hemorrhage volume, or de novo intraventricular hemorrhage. We assessed the predictive accuracy of expansion markers and determined their association with revised hematoma expansion.

RESULTS: We included 124 patients, of whom 51 (41%) developed revised hematoma expansion. The sensitivity of each marker for the prediction of revised hematoma expansion ranged from 4% to 78%; the specificity, 37%–97%; the positive likelihood ratio, 0.41–7.16; and the negative likelihood ratio, 0.49–1.06. By means of univariable logistic regressions, 5 markers were significantly associated with revised hematoma expansion: black hole (OR = 8.66; 95% CI, 2.15–58.14; $P = .007$), hypodensity (OR = 3.18; 95% CI, 1.49–6.93; $P = .003$), blend (OR = 2.90; 95% CI, 1.08–8.38; $P = .04$), satellite (OR = 2.84; 95% CI, 1.29–6.61; $P = .01$), and Barras shape (OR = 2.41; 95% CI, 1.17–5.10; $P = .02$). In multivariable models, only the black hole marker remained independently associated with revised hematoma expansion (adjusted OR = 5.62; 95% CI, 1.23–40.23; $P = .03$).

CONCLUSIONS: No single NCCT expansion marker had both high sensitivity and specificity for the prediction of revised hematoma expansion. Improved image-based analysis is needed to tackle limitations associated with current NCCT-based expansion markers.

ABBREVIATIONS: EM = expansion marker; HE = hematoma expansion; ICH = intracerebral hemorrhage; rHE = revised hematoma expansion; sHE = standard hematoma expansion

Spontaneous intracerebral hemorrhage (ICH) remains a major cause of morbidity and mortality worldwide.¹ Hematoma expansion (HE) is a potentially modifiable predictor of outcome and a promising therapeutic target.^{2,3} HE is most often defined as a ≥ 6 -mL absolute or $\geq 33\%$ relative increase in ICH volume on follow-up imaging performed 24–72 hours after a baseline NCCT

scan (herein considered a standard hematoma expansion [sHE] definition).⁴ A recent study redefined HE to include new or increasing intraventricular hemorrhage to capture HE that occurs within the ventricles.⁵ This revised hematoma expansion (rHE) definition better predicts 90-day functional outcomes than the sHE definition.^{5–7}

Received November 30, 2022; accepted after revision April 6, 2023.

From the Département des Neurosciences (C.D., A.N., B.R., M.-A.P., L.C.G.), Faculté de Médecine, and Département de Radiologie (L.L.-G.), Radio-oncologie et Médecine Nucléaire, Faculté de Médecine, Université de Montréal, Montréal, Québec, Canada; Département de Médecine (Neurologie) (C.D., A.N., B.R., M.-A.P., L.C.G.), Neurovascular Health Program (C.D., L.C.G.), and Département de Radiologie (L.L.-G.), Centre Hospitalier de l'Université de Montréal, Montréal, Québec, Canada; Department of Medicine (C.D., R.F.), Division of Neurology, The Ottawa Hospital Research Institute and University of Ottawa, Ottawa, Ontario, Canada; Centre for Clinical Brain Sciences (B.R.), University of Edinburgh, Edinburgh, UK; and Imaging and Engineering Axis (L.L.-G.), Centre de Recherche du Centre Hospitalier de l'Université de Montréal, Montréal, Québec, Canada.

Funding sources had no role in the design or conduct of the study.

C. Ducroux and A. Nehme contributed equally to the article.

L.C. Gioia and L. Létourneau-Guillon contributed equally to the article.

The project was partially funded through the following grants (LL.-G., principal investigator): the Radiological Society of North America Seed Grant (No. RSD2122), Fonds de recherche du Québec/Santé/Fondation de l'Association des Radiologistes du Québec, radiology research program (No. 299979), internal funding from the Department of Radiology, Radio-oncology, and Nuclear Medicine, Université de Montréal, and the Department of Radiology, Centre Hospitalier de l'Université de Montréal, Montréal, Canada. LL.-G. receives a scholarship from the Fonds de Recherche Québec Santé/Fondation de l'Association des Radiologistes du Québec (clinical research scholarship junior 1 salary award, 311203). A.N. acknowledges financial support from the Fonds de Recherche du Québec Santé. B.R. acknowledges financial support from the Fonds de Recherche du Québec Santé and the Ministère de la Santé et des Services Sociaux du Québec, and from the Center for Clinical Brain Sciences of the University of Edinburgh.

Please address correspondence to Céline Ducroux, MD, The Ottawa Hospital, Civic Campus, 1053 Carling Ave, Ottawa, ON, K1Y 4E9 Canada; e-mail: cducroux@toh.ca

Indicates open access to non-subscribers at www.ajnr.org

Indicates article with online supplemental data.
<http://dx.doi.org/10.3174/ajnr.A7871>

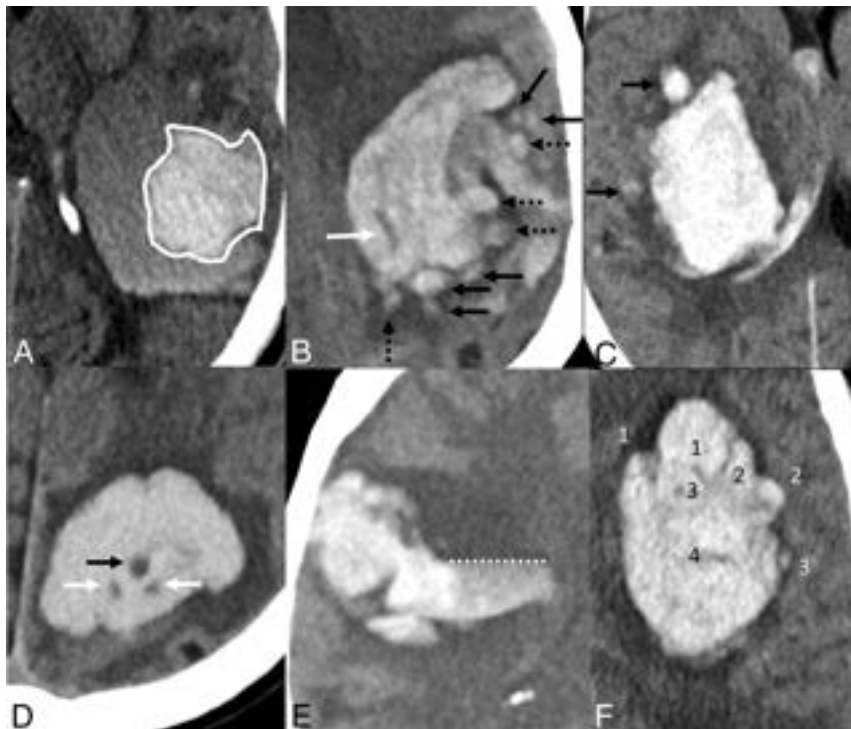


FIG 1. NCCT hematoma EMs. *A*, Blend sign: a relatively hypoattenuating area next to a hyperattenuating area of the hematoma, with a well-defined margin and a density difference of >18 HU between the 2 areas. *B*, Island sign: at least 3 scattered small hematomas all separate from the main hematoma (black arrows) or at least 4 small hematomas, some or all of which may connect with the main hematoma (dashed arrows), all visible on a single axial section. The white arrow identifies both a hypodensity (any hypodense region strictly encapsulated within the hemorrhage with any shape, size, and density) and a swirl sign (rounded, streak-like, or irregular region of hypo- or isoattenuation compared with the brain parenchyma that does not have to be encapsulated in the hematoma). *C*, Satellite sign: a small hematoma (diameter of <10 mm) separate from the main hemorrhage in at least 1 section and distinct from the main hematoma by a 1- to 20-mm separation (black arrows). *D*, Black hole sign: a hypoattenuating area with a density difference of >28 HU compared with the surrounding hematoma, which has no connection with the surface outside the hematoma (black arrow). This finding also corresponds to a hypodensity and a swirl sign. For the 2 hypodense foci labeled with white arrows, because the density difference with the hyperattenuating hematoma is <28 HU, they cannot be considered black hole signs. *E*, Fluid level: presence of 1 distinct hypoattenuating area (hypodense to the brain) above 1 hyperattenuating area (hyperdense to the brain), below a discrete straight line of separation (dashed line), irrespective of its density appearance. *F*, Barras density and shape signs are evaluated on the axial section showing the largest hematoma area and are based on a 5-point scale. Density is considered heterogeneous when there are ≥ 3 hypodensity foci within the hyperdense hematoma (scale of III, IV, or V). Shape is considered irregular when there are ≥ 2 focal hematoma margin irregularities, joined or separate from the hematoma edge (scale of III, IV, or V). Definitions from Morotti et al.⁴

The spot sign is among the most studied imaging-based predictors of HE.^{3,8} However, a CTA is not routinely available in the acute setting. The spot sign only mildly improves predictive accuracy when added to other established predictors of HE.⁸⁻¹⁰ Multiple NCCT hematoma expansion markers (EMs) have been recently developed (Fig 1) in an attempt to mitigate those limitations.⁴ These EMs may reflect the cascade phenomenon that occurs during HE, in which secondary hemorrhagic foci lead to irregular margins and heterogeneous density. They are classified as shape (Barras shape, island, and satellite) and density markers (Barras density, black hole, blend, fluid level, hypodensity, and swirl). EMs are associated with sHE, with ORs ranging from 2.01 to 7.87.¹¹ These markers may be integrated into prediction models

to select patients at higher risk of HE for more intensive monitoring and/or treatment or trials in acute ICH.^{12,13} They could also be used when other predictors of HE are not available, such as time in unknown-onset ICH.¹⁴

In a meta-analysis, the sensitivity and specificity of individual NCCT hematoma EMs for sHE varied substantially between studies. The Barras shape marker had the highest pooled sensitivity (68%), and the island marker had the highest pooled specificity (92%).¹⁵ However, the authors of the meta-analysis found an important risk of bias in the included studies. Whether the predictive accuracy of NCCT hematoma EMs is generalizable to rHE and routine clinical practice remains unknown. Despite recent standardized EM definitions, most studies evaluating EMs were conducted by expert readers who took part in their development, without external validation.^{4,16} Moreover, head-to-head comparisons of all 9 EMs within a single study are lacking. NCCT hematoma EMs are not currently used in routine clinical practice but could eventually help select patients at high risk of HE in future trials. To tackle these drawbacks and externally validate EMs, we designed a single-center retrospective diagnostic-accuracy study to assess the predictive accuracy of individual and combined EMs for rHE. We also aimed to evaluate whether EMs could improve the prediction of rHE when added to other established predictors of HE.

MATERIALS AND METHODS

This study was performed in accordance with the Standards for Reporting Diagnostic Accuracy Study (STARD)¹⁷ and the STrengthening the Reporting of

OBservational Studies in Epidemiology (STROBE) statement for observational cohort studies.¹⁸ Our study was approved by our institutional ethics review board, including a waiver of consent for the use of deidentified patient data.

Study Population

We retrospectively identified consecutive patients with ICH 18 years of age or older who presented to the Centre Hospitalier Universitaire de l'Université de Montréal between April 2016 and April 2020. The Centre Hospitalier Universitaire de l'Université de Montréal is a high-volume comprehensive stroke center and primarily uses NCCT as initial imaging for patients presenting with acute neurologic symptoms. At our institution, patients are

worked up for a secondary etiology of ICH in the absence of clinical or imaging findings that suggest small-vessel disease (ie, age, history of hypertension, leukoaraiosis, microbleeds), according to the physician's judgment. Patients were identified from all hospital departments through discharge codes in the medical archives and by query of our institution's prospectively collected stroke repository. We included patients with spontaneous ICH who were diagnosed <24 hours from symptom onset or last time seen well and had an available follow-up NCCT performed <72 hours after the initial imaging. We did not specify a minimum time between the initial and follow-up NCCT because patients may clinically deteriorate and develop HE on a follow-up CT performed shortly after the initial NCCT. Patients were excluded for the following reasons: 1) if ICH was known to be due to an underlying macrovascular cause (eg, intracranial aneurysm, arteriovenous malformation, cerebral cavernous malformation, dural arteriovenous fistula, or intracranial venous thrombosis), a brain neoplasm, trauma, or hemorrhagic transformation of a cerebral infarct; and/or 2) if patients underwent neurosurgical hematoma evacuation or external ventricular drainage before a follow-up NCCT. We used these criteria to enable adequate assessment of HE in our sample. Baseline characteristics and the time interval from symptom onset (or last seen well, if unknown) to the baseline NCCT scan were collected by chart review.

Image Analysis

The presence or absence of 9 EMs was evaluated by study investigators on baseline NCCT using standardized definitions.⁴ Images were pseudonymized and analyzed on a dedicated research platform to blind raters to subject identity, clinical information, and follow-up images as well as the other readers' interpretations. The Barras shape and density markers (5-point ordinal scales) were dichotomized to positive (3–5) versus negative (0–2), as previously published.⁴ Interobserver agreement was substantial to almost perfect for most EMs except for Barras density (reader 1 versus 2) and Barras shape (reader 1 versus 3) for which estimates were in the moderate-agreement range (Online Supplemental Data). Disagreements were resolved by adjudication of the third investigator.

Two study investigators, blinded to the double-read results of the EM assessment, measured ICH and intraventricular hemorrhage volumes on pseudonymized baseline and follow-up NCCT using semi-automated manual segmentation techniques (3D Slicer, Version 4.11; <http://www.slicer.org>) (Online Supplemental Data). If multiple NCCTs were available within 72 hours after the initial imaging, we selected the first available NCCT if rHE occurred and the latest available NCCT if rHE did not occur.

Outcomes

We evaluated the predictive accuracy of EMs for rHE as the primary outcome and sHE as a secondary end point. rHE was defined as any of the following: a ≥ 6 -mL absolute or $\geq 33\%$ relative increase in ICH volume, a ≥ 1 -mL increase in intraventricular hemorrhage volume, or de novo intraventricular hemorrhage. sHE was defined as a ≥ 6 -mL absolute or $\geq 33\%$ relative increase in ICH volume.²

Statistical Analyses

The sample size was based on a convenience sample of all available data within the specified timeframe. Baseline characteristics were compared using the χ^2 test of independence or the Fisher exact test for categorical variables and Student *t* test for continuous variables. We built 7 independent a priori composite variables using a combination of markers to evaluate a potential gain in the prediction of HE: 1) any shape marker (ie, at least 1 of Barras shape, island, or satellite), 2) any density marker (ie, at least 1 of Barras density, black hole, blend, fluid level, hypodensity, or swirl), 3) any EM, 4) shape count (ie, total number of shape markers), 5) density count (ie, total number of density markers), 6) EM count (ie, total number of EMs), and 7) the previously reported "expansion-prone hematoma" (≥ 1 of black hole, blend, or island).¹⁹

To evaluate the predictive accuracy of individual and combined EMs for rHE, we calculated their sensitivity, specificity, positive predictive value, negative predictive value, positive and negative likelihood ratios, diagnostic ORs, and accuracy. To determine the association between EMs and rHE, we calculated ORs with 2 sets of models using logistic regressions with maximum likelihood estimations. In our first set of models, we determined the association of each EM with rHE using univariable logistic regression. In our second set of models, we determined the added predictive value of each EM with likelihood ratio tests, used to compare a reduced model (established predictors of HE) nested into a full model (established predictors of HE plus 1 EM).²⁰ Established predictors of HE include antiplatelet use, anticoagulant use, ICH volume on baseline imaging, and time from symptom onset to baseline imaging, which were based on the findings of a large meta-analysis of individual patient-level data.⁸ We used time from last seen well to imaging in our analyses instead of time from symptom onset to include patients with unclear symptom onset, who are also at risk for HE.¹⁴ We used median imputation to replace missing values for last time seen well to imaging ($n = 10$). Otherwise, all other variables had complete data. We subsequently explored the potential incremental value of the EMs that were found to be independently associated with rHE (Online Supplemental Data). We replicated all analyses using sHE as a secondary end point. Statistical significance was defined as a $P < .05$, without adjustment for multiple comparisons. All analyses were performed with R Studio (Version 1.4; <http://rstudio.org/download/desktop>) and R statistical and computing software (Version 4.2.2; <http://www.r-project.org/>).

RESULTS

Demographics and Outcomes

A total of 270 patients with spontaneous ICH were identified during the study period. After we excluded 146 patients (Fig 2), the study population encompassed 124 patients, of whom 51 (41%) developed rHE and 35 (28%) developed sHE seen on follow-up CT. The median initial ICH volume was 16 mL (interquartile range: 6–37 mL). The median time from last-seen-well to initial CT was 107 minutes (interquartile range: 75–228 minutes). Twenty-six patients (21%) were treated with anticoagulants (Online Supplemental Data). A CT or MRA was performed in

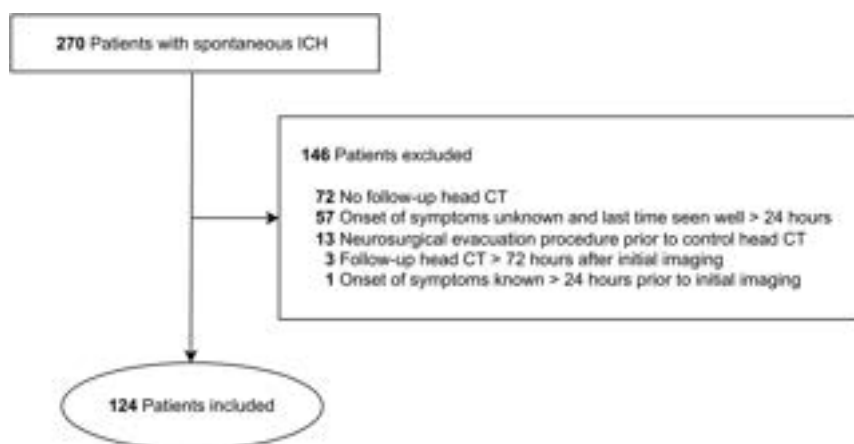


FIG 2. Flowchart.

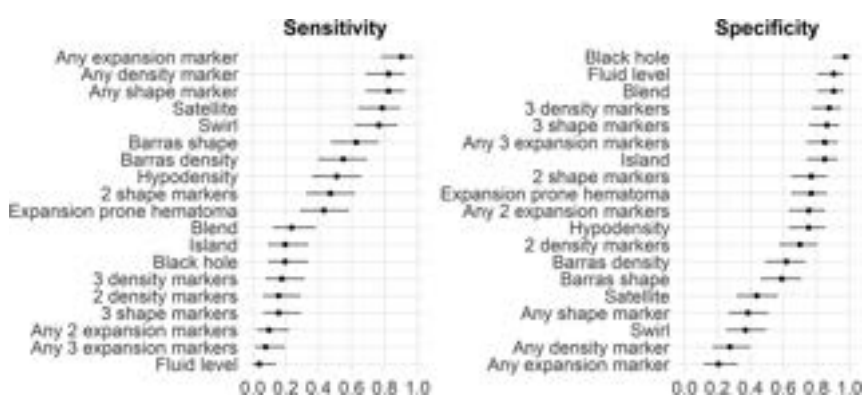


FIG 3. Sensitivity and specificity of NCCT expansion markers for rHE.

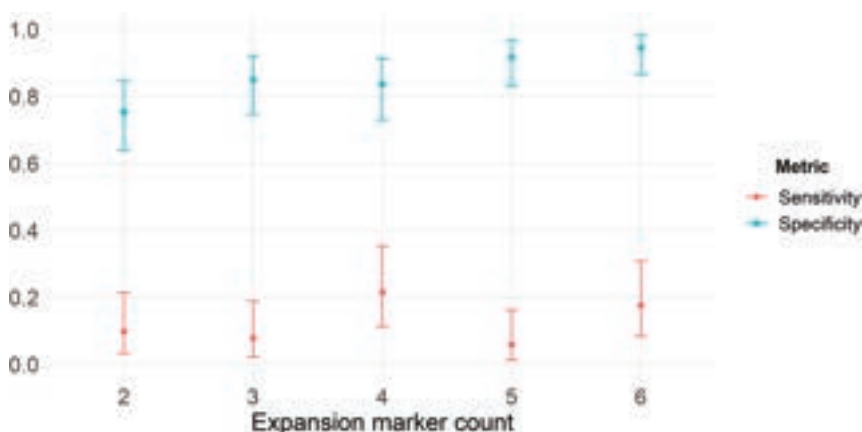


FIG 4. Sensitivity and specificity of expansion marker count for rHE.

100 patients (81%). A brain MR imaging and a DSA were performed in 40 (32%) and 4 patients (3%), respectively.

Predictive Accuracy of NCCT EMs

On baseline NCCT, 104 patients (84%) had at least 1 EM, 93 (75%) had at least 2 EMs, and 70 (56%) had ≥ 3 EMs. The most prevalent EMs were the swirl (69%), satellite (65%), and Barras

shape (50%) markers. The other 6 markers were present in $< 50\%$ of cases.

No marker had both high sensitivity and specificity for the prediction of rHE. The satellite marker had the highest sensitivity (78%; 95% CI, 65%–89%), while the black hole marker had the highest specificity (97%; 95% CI, 90%–100%) (Fig 3). Only the black hole marker had a positive likelihood ratio of > 5 , though it had a wide CI (7.16; 95% CI, 1.64–31.30). The negative likelihood ratios of individual EMs ranged from 0.49 to 1.06. All measures of predictive accuracy for rHE are available in the Online Supplemental Data.

The presence of any marker had a high sensitivity (90%; 95% CI, 79%–97%) for the prediction of rHE but low specificity (21%; 95% CI, 12%–32%). Nevertheless, with an estimated negative likelihood ratio of 0.48, the absence of any marker would only shift the probability of rHE from 41% (pretest probability, ie, prevalence) to 25% (posttest probability). Specificity for the prediction of rHE increased slightly with the number of positive EMs. However, combinations of 2–6 positive EMs had low sensitivity for rHE (6%–22%) (Fig 4).

Association of NCCT EMs with rHE

The results of logistic regressions are presented in the Table. In univariable logistic regressions, 5 markers were significantly associated with rHE: hypodensity (OR = 3.18; 95% CI, 1.49–6.93; $P = .003$), blend (OR = 2.90; 95% CI, 1.08–8.38; $P = .04$), black hole (OR = 8.66; 95% CI, 2.15–58.14; $P = .007$), satellite (OR = 2.84; 95% CI, 1.29–6.61; $P = .01$), and Barras shape (OR = 2.41; 95% CI, 1.17–5.10; $P = .02$). After adjustment for established predictors of HE, only the black hole marker (adjusted OR = 5.62; 95% CI, 1.23–40.23; $P = .03$) remained significantly associated with rHE. We replicated all our analyses on the original data set without median imputation and obtained similar results (data not shown).

All analyses were replicated using the sHE definition. Most predictive performance metrics were similar to the ones obtained using the rHE definition (Online Supplemental Data).

DISCUSSION

Our study provides an independent assessment of 9 NCCT hematoma EMs in a single cohort, including both standard and

Association of EMs with rHE^a

EM	Unadjusted		Adjusted ^b	
	OR (95% CI)	P Value	OR (95% CI)	P Value
Barras density	1.96 (0.95–4.08)	.07	1.11 (0.46–2.66)	.81
Black hole	8.66 (2.15–58.14)	.007 ^c	5.62 (1.23–40.23)	.03 ^c
Blend	2.90 (1.08–8.38)	.04 ^c	1.45 (0.43–4.99)	.55
Fluid level	0.38 (0.06–1.67)	.25	0.35 (0.05–1.60)	.18
Hypodensity	3.18 (1.49–6.93)	.003 ^c	2.01 (0.77–5.31)	.15
Swirl	1.91 (0.87–4.37)	.12	1.20 (0.48–3.05)	.70
Barras shape	2.41 (1.17–5.10)	.02 ^c	1.48 (0.63–3.51)	.37
Island	1.37 (0.53–3.55)	.51	0.49 (0.12–1.72)	.27
Satellite	2.84 (1.29–6.61)	.01 ^c	1.73 (0.68–4.57)	.25
Combined EMs				
Any shape marker	2.90 (1.26–7.18)	.02 ^c	1.87 (0.69–5.38)	.22
Any density marker	1.76 (0.74–4.44)	.21	0.93 (0.34–2.68)	.90
Shape marker count	1.57 (1.11–2.27)	.01 ^c	1.17 (0.73–1.87)	.51
Density marker count	1.51 (1.16–1.99)	.003 ^c	1.27 (0.87–1.86)	.21
Any EM	2.38 (0.85–7.75)	.12	1.33 (0.41–4.87)	.64
EM count	1.33 (1.12–1.60)	.002 ^c	1.20 (0.91–1.58)	.20
Expansion-prone hematoma	2.50 (1.16–5.50)	.02 ^c	1.30 (0.45–3.69)	.63

^a Revised hematoma expansion was defined as any of a ≥ 6 -mL or $\geq 33\%$ increase in ICH volume, a ≥ 1 -mL increase in intraventricular hemorrhage volume, or de novo intraventricular hemorrhage.

^b Adjusted for antiplatelet use, anticoagulant use, baseline ICH volume, and last-seen-well to initial CT.

^c $P < .05$.

revised definitions of HE.^{5,7} The predictive performance of prevalence-insensitive metrics (sensitivity, specificity, and positive and negative likelihood ratios) did not differ on the basis of both definitions. Combining EMs did not improve the predictive accuracy for rHE compared with the top-performing EMs. Only 5 of 9 EMs were associated with rHE, with ORs similar to those in a recent meta-analysis.¹² After we adjusted for established predictors of HE, only the black hole marker remained significantly associated with rHE.

In a meta-analysis of individual patient data, the strongest predictors of HE were time from symptom onset to baseline imaging, baseline ICH volume, and antithrombotic medication use.⁸ A new image-based prediction biomarker for HE should ideally improve on such established predictors. In our study, only the black hole marker remained associated with rHE in the multivariate analysis, and its added value in the full prediction model was only marginally significant, with an adjusted OR that had wide confidence intervals, partially resulting from its low prevalence. However, previous studies have shown that multiple other EMs (blend, hypodensity, island) are significant predictors of sHE and rHE.^{7,21} The latter studies did not include patients treated with anticoagulants, which could partially explain the difference from our findings. The impact of anticoagulation on the predictive performances of EMs is unknown, but at least 1 study suggested that EMs can be used in patients treated with anticoagulants.²² NCCT EMs may be necessary when other established markers are unavailable, such as the time from symptom onset in patients with an unwitnessed ICH.¹⁴

In addition to its independent association with rHE, the black hole marker had the highest specificity, positive likelihood ratio, and positive predictive value among EMs, in line with previous studies that evaluated this marker using the sHE²³ and rHE definitions.⁷ High specificity is important to reduce the rate of false-positive expansion predictions in a future trial, especially if the

experimental treatment is associated with serious adverse events, such as thrombotic complications. However, EMs with low sensitivity, such as the black hole marker, would miss a large proportion of patients at risk of rHE. Using the EMs with a low prevalence as an inclusion criterion in clinical trials could slow down recruitment. This issue was noticed in previous trials using the spot sign as an inclusion criterion.¹⁰

To improve the predictive accuracy of individual EMs, we evaluated different combinations of markers.²⁴ Li et al¹⁹ introduced the expansion-prone hematoma to tackle the low sensitivity associated with the most specific markers (black hole, blend, island) by allowing the presence of any of the latter. We found that the expansion-prone hematoma had lower sensitivity and specificity than previously reported, with its

estimated negative likelihood ratio not in a range that is generally considered clinically useful. The lack of improvement in predictive accuracy with such EM combinations has been described in some studies.^{21,25} One potential explanation is that different imaging markers capture similar information, with diminishing returns in predictive value when combined.

In our study, the swirl marker had lower specificity than previously reported.²⁶ Its higher than previously reported prevalence in our results may result from our inclusion of more diverse patients with ICH (ie, patients hospitalized in neurosurgery, patients treated with anticoagulants) or from a different interpretation of the marker by the raters in our study. This discrepancy raises the question of whether the predictive accuracy of EMs is generalizable to all patients with spontaneous ICH and whether the reliability of EMs is generalizable to all raters.²⁷ The heterogeneity of sensitivity and specificity metrics found in recent meta-analyses of EMs may partly reflect this issue.¹⁵ Thus, despite a positive association between EMs and HE, such markers might not be robust enough to guide medical decisions in clinical practice. A potential approach to improve the accuracy and reliability of NCCT-based HE prediction could include emerging machine learning approaches, such as those from the fields of radiomics or deep learning.²⁸ Finally, it is possible that outcome prediction based on baseline imaging might be inherently limited. Even though EMs have a pathophysiologic rationale, the fact that CT is only a snapshot of a dynamic process might limit its potential value as a predictive biomarker, despite optimal imaging analysis.²⁹ Likewise, it is also possible that the predictive performances of EMs decrease as the delay after stroke onset increases, similar to the spot sign.³⁰

Strengths and Limitations

The main strengths of our study include appraisal of all patients with ICH for inclusion, blinded evaluation of EMs and HE, and assessment of the 9 standardized EMs. Our results should be

interpreted with caution due to our relatively small sample size, which resulted in imprecise estimation of the prevalence of EMs and therefore of their predictive accuracy. Our small sample size also precluded a more comprehensive assessment of incremental prediction values, the detection of smaller associations, and the conduct of subgroup analyses. The time interval between the initial and follow-up NCCT was variable but was not associated with rHE. This study was performed at a single institution and should be repeated in a multicenter setting to mitigate potential selection biases inherent to a tertiary care center. In addition, we used a consensus evaluation of NCCT EMs in a retrospective setting, which differs from the acute setting and could impact the predictive performances. We included only patients with spontaneous ICH who did not undergo surgery before follow-up imaging, which may have potentially excluded patients with larger baseline ICH volumes. Similarly, we did not include patients who died before follow-up CT, which also may have led to a depletion of patients more likely to have HE.

Because of these exclusion criteria, the prevalence of rHE may be underestimated. The median ICH volume was low (16 mL) but similar to that reported in large trials.^{31,32} We did not evaluate functional outcome due to a significant proportion of missing follow-up data, because many patients were transferred to secondary stroke centers after their follow-up imaging. The established predictors of HE included in our models were initially reported with the sHE and not the rHE definition.⁸ However, the rHE definition is a refinement of the sHE definition and evaluates the same underlying process. We did not evaluate the interaction between time from ICH onset and the predictive performances of EMs. Finally, we performed multiple analyses without accounting for multiplicity, possibly having led to false-positive findings.

CONCLUSIONS

Most NCCT EMs were not found to be significantly associated with rHE after adjustment for established predictors of HE. No individual or combined NCCT EMs provided both the high sensitivity and specificity that would be required to identify patients at risk of HE. Larger and ideally multicenter studies are needed to further evaluate an NCCT-based approach to HE prediction before implementing these markers for decision-making in acute ICH.

Data Sharing

Data, analytic methods, and study materials will be made available to any researcher for reproducing the results or replicating the procedure. Requests to receive these materials should be sent to the corresponding author, who will maintain their availability.

Disclosure forms provided by the authors are available with the full text and PDF of this article at www.ajnr.org.

REFERENCES

- GBD 2019 Stroke Collaborators. **Global, regional, and national burden of stroke and its risk factors, 1990-2019: a systematic analysis for the Global Burden of Disease Study 2019.** *Lancet Neurol* 2021;20:795-820 CrossRef Medline
- Dowlathshahi D, Demchuk AM, Flaherty ML, et al; VISTA Collaboration. **Defining hematoma expansion in intracerebral hemorrhage: relationship with patient outcomes.** *Neurology* 2011;76:1238-44 CrossRef Medline
- Demchuk AM, Dowlathshahi D, Rodriguez-Luna D, et al; PREDICT/Sunnybrook ICH CTA Study Group. **Prediction of haematoma growth and outcome in patients with intracerebral haemorrhage using the CT-angiography spot sign (PREDICT): a prospective observational study.** *Lancet Neurol* 2012;11:307-14 CrossRef Medline
- Morotti A, Boulouis G, Dowlathshahi D, et al; International NCCT ICH Study Group. **Standards for detecting, interpreting, and reporting noncontrast computed tomographic markers of intracerebral hemorrhage expansion.** *Ann Neurol* 2019;86:480-92 CrossRef Medline
- Yogendrakumar V, Ramsay T, Fergusson DA, et al; PREDICT/Sunnybrook CTA Study Group. **Redefining hematoma expansion with the inclusion of intraventricular hemorrhage growth.** *Stroke* 2020;51:1120-27 CrossRef Medline
- Yogendrakumar V, Ramsay T, Fergusson D, et al; the PREDICT/Sunnybrook CTA Study Group. **New and expanding ventricular hemorrhage predicts poor outcome in acute intracerebral hemorrhage.** *Neurology* 2019;93:e879-88 CrossRef Medline
- Yang WS, Zhang SQ, Shen YQ, et al. **Noncontrast computed tomography markers as predictors of revised hematoma expansion in acute intracerebral hemorrhage.** *J Am Heart Assoc* 2021;10:e018248 CrossRef Medline
- Al-Shahi Salman R, Frantzijs J, Lee RJ, et al; ICH Growth Individual Patient Data Meta-analysis Collaborators. **Absolute risk and predictors of the growth of acute spontaneous intracerebral haemorrhage: a systematic review and meta-analysis of individual patient data.** *Lancet Neurol* 2018;17:885-94 CrossRef Medline
- Morotti A, Brouwers HB, Romero JM, et al; Antihypertensive Treatment of Acute Cerebral Hemorrhage II and Neurological Emergencies Treatment Trials Investigators. **Intensive blood pressure reduction and spot sign in intracerebral hemorrhage: a secondary analysis of a randomized clinical trial.** *JAMA Neurol* 2017;74:950-60 CrossRef Medline
- Gladstone DJ, Aviv RI, Demchuk AM, et al; SPOTLIGHT and STOP-IT Investigators and Coordinators. **Effect of recombinant activated coagulation factor VII on hemorrhage expansion among patients with spot sign-positive acute intracerebral hemorrhage: the SPOTLIGHT and STOP-IT Randomized Clinical Trials.** *JAMA Neurol* 2019;76:1493-501 CrossRef Medline
- Morotti A, Arba F, Boulouis G, et al. **Noncontrast CT markers of intracerebral hemorrhage expansion and poor outcome: a meta-analysis.** *Neurology* 2020;95:632-43 CrossRef Medline
- Parry-Jones AR, Sammut-Powell C, Paroutoglou K, et al. **An intracerebral hemorrhage care bundle is associated with lower case fatality.** *Ann Neurol* 2019;86:495-503 CrossRef Medline
- Song L, Hu X, Ma L, et al; INTERACT3 Investigators. **INTensive care bundle with blood pressure reduction in acute cerebral hemorrhage trial (INTERACT3): study protocol for a pragmatic stepped-wedge cluster-randomized controlled trial.** *Trials* 2021;22:943 CrossRef Medline
- Morotti A, Boulouis G, Charidimou A, et al. **Hematoma expansion in intracerebral hemorrhage with unclear onset.** *Neurology* 2021;96:e2363-71 CrossRef Medline
- Francesco A, Chiara R, Gregoire B, et al. **Noncontrast computed tomography markers of cerebral hemorrhage expansion: diagnostic accuracy meta-analysis.** *Int J Stroke* 2021 Nov 29. [Epub ahead of print] CrossRef Medline
- Dowlathshahi D, Morotti A, Al-Ajlan FS, et al. **Interrater and intrarater measurement reliability of noncontrast computed tomography predictors of intracerebral hemorrhage expansion.** *Stroke* 2019;50:1260-62 CrossRef Medline
- Bossuyt PM, Reitsma JB, Bruns DE, et al; STARD Group. **STARD 2015: an updated list of essential items for reporting diagnostic accuracy studies.** *BMJ* 2015;351:h5527 CrossRef Medline
- von Elm E, Altman DG, Egger M, et al; STROBE Initiative. **The Strengthening the Reporting of Observational Studies in Epidemiology**

(STROBE) Statement: guidelines for reporting observational studies. *Int J Surg* 2014;12:1495–99 CrossRef Medline

19. Li Q, Shen YQ, Xie XF, et al. **Expansion-prone hematoma: defining a population at high risk of hematoma growth and poor outcome.** *Neurocrit Care* 2019;30:601–08 CrossRef Medline
20. Cook NR. **Quantifying the added value of new biomarkers: how and how not.** *Diagn Progn Res* 2018;2:14 CrossRef Medline
21. Law ZK, Ali A, Krishnan K, et al; TICH-2 Investigators. **Noncontrast computed tomography signs as predictors of hematoma expansion, clinical outcome, and response to tranexamic acid in acute intracerebral hemorrhage.** *Stroke* 2020;51:121–28 CrossRef Medline
22. Zimmer S, Meier J, Minnerup J, et al. **Prognostic value of non-contrast CT markers and spot sign for outcome prediction in patients with intracerebral hemorrhage under oral anticoagulation.** *J Clin Med* 2020;9:1077 CrossRef Medline
23. He GN, Guo HZ, Han X, et al. **Comparison of CT black hole sign and other CT features in predicting hematoma expansion in patients with ICH.** *J Neurol* 2018;265:1883–90 CrossRef Medline
24. Katsanos AH, Gupta H, Morotti A, et al. **Increased prognostic yield by combined assessment of non-contrast computed tomography markers of antithrombotic-related spontaneous intracerebral hemorrhage expansion.** *J Clin Med* 2022;11:1596 CrossRef Medline
25. Morotti A, Boulouis G, Romero JM, et al; ATACH-II and NETT investigators. **Blood pressure reduction and noncontrast CT markers of intracerebral hemorrhage expansion.** *Neurology* 2017;89:548–54 CrossRef Medline
26. Yu Z, Zheng J, He M, et al. **Accuracy of swirl sign for predicting hematoma enlargement in intracerebral hemorrhage: a meta-analysis.** *J Neurol Sci* 2019;399:155–60 CrossRef Medline
27. Nehme A, Ducroux C, Panzini MA, et al. **Non-contrast CT markers of intracerebral hematoma expansion: a reliability study.** *Eur Radiol* 2022;32:6126–35 CrossRef Medline
28. Li H, Xie Y, Liu H, et al. **Non-contrast CT-based radiomics score for predicting hematoma enlargement in spontaneous intracerebral hemorrhage.** *Clin Neuroradiol* 2022;32:517–28 CrossRef Medline
29. Boulouis G, Dumas A, Betensky RA, et al. **Anatomic pattern of intracerebral hemorrhage expansion: relation to CT angiography spot sign and hematoma center.** *Stroke* 2014;45:1154–56 CrossRef Medline
30. Dowlatshahi D, Brouwers HB, Demchuk AM, et al. **Predicting intracerebral hemorrhage growth with the spot sign: the effect of onset-to-scan time.** *Stroke* 2016;47:695–700 CrossRef Medline
31. Qureshi AI, Palesch YY, Barsan WG, et al; ATACH-2 Trial Investigators and the Neurological Emergency Treatment Trials Network. **Intensive blood-pressure lowering in patients with acute cerebral hemorrhage.** *N Engl J Med* 2016;375:1033–43 CrossRef Medline
32. Anderson CS, Heeley E, Huang Y, et al; INTERACT2 Investigators. **Rapid blood-pressure lowering in patients with acute intracerebral hemorrhage.** *N Engl J Med* 2013;368:2355–65 CrossRef Medline

Evaluation of Motion-Corrected Multishot Echo-Planar Imaging as an Alternative to Gradient Recalled-Echo for Blood-Sensitive Imaging

J.A. Murchison, D. Shoshan, M.B. Ooi, Z. Li, and J.P. Karis



ABSTRACT

SUMMARY: We evaluated motion-corrected multishot EPI compared with gradient recalled-echo imaging to determine whether it can be used as a faster technique for blood-sensitive imaging in the emergency department setting. Multishot EPI was found to be superior to gradient recalled-echo ($P < .05$) in motion artifacts, overall image quality, and lesion detection. These results and reduced scan time make motion-corrected multishot EPI a viable alternative for blood-sensitive imaging in the emergency department setting.

ABBREVIATIONS: GRE = gradient recalled-echo; msEPI = multishot echo-planar imaging

MR imaging of the brain performed in the emergency department requires time-efficient acquisition protocols to provide timely patient care and maintain patient throughput.¹ In addition, a T2*-sensitive series that demonstrates pathologic hemorrhage is critically important when performing emergency department MR imaging examinations. Gradient recalled-echo (GRE) imaging is favored over SWI at our institution as a more time-efficient technique for obtaining T2*-weighted images. The GRE sequence at our institution uses approximately 30% of the total examination time (approximately 2 minutes of an 8-minute examination). We previously attempted to implement a T2* sequence using a multishot EPI (msEPI) technique, which permits more rapid image acquisition (~50% faster compared with GRE); however, the sequence was particularly vulnerable to patient motion (unpublished data). Recently developed motion-correction techniques for msEPI use a navigator echo that can reduce motion and phase errors, which are common in patients with acute medical conditions (Fig 1).²⁻⁴ In this study, we evaluated a novel 2D interleaved motion-corrected msEPI sequence to determine whether it can be used as a faster technique for blood-sensitive imaging in the emergency department.

MATERIALS AND METHODS

Patient Population

This prospective study was performed at a single clinical site, was approved by the institutional review board, and was compliant with

the Health Insurance Portability and Accountability Act. Patients in the emergency department undergoing nonemergent imaging for stroke were eligible for inclusion. Informed consent was waived for this minimum-risk study, and motion-corrected msEPI sequences were obtained in addition to the standard GRE sequences.

Imaging Methods

The msEPI sequence and reconstruction algorithm were developed by Li et al.⁵ The study was performed on a single Ingenia MR imaging scanner (Philips Healthcare) with a standard hardware configuration. A standard-of-care GRE sequence with compressed sensing was obtained, with a 230×230 mm² FOV, 1.0×1.1 mm² resolution, 5-mm section thickness, 1-mm section gap, 18° flip angle, 18-ms TE, ~25–32 slices, compressed sensing factor of 2, and ~105 Hz/pixel frequency-direction receiver bandwidth. The TR and total scan time varied with the number of prescribed slices. The typical TR used was ~860 ms, and the typical scan time was ~2 minutes 15 seconds. The proposed motion-corrected msEPI with a navigator echo scan was then obtained with matched geometric parameters. The image echo was acquired with an echo-train length of 27, eight shots, 24-ms TE, ~945 Hz/pixel frequency direction, and ~27 Hz/pixel phase-direction receiver bandwidths. The navigator echo was collected with an echo-train length of 23, sensitivity encoding acceleration factor of two, 72-ms TE, 2 signal averages, and ~1-minute scan time. Because the radiofrequency pulse must be refocused, T1-related tissue signal recovery is interrupted, resulting in altered tissue contrast compared with msEPI without a navigator echo. A 120° flip angle and ~3500-ms TR were chosen to match tissue contrast.

Radiologic Assessment

Two radiologists (1 staff neuroradiologist and 1 neuroradiology fellow) reviewed all subjects, and consensus scoring was obtained.

Received October 26, 2022; accepted after revision April 27, 2023.

From the Department of Neuroradiology (J.A.M., D.S., Z.L., J.P.K.), Barrow Neurological Institute, St. Joseph's Hospital and Medical Center, Phoenix, Arizona; and Philips Healthcare (M.B.O.), Houston, Texas.

This work was partially supported by Barrow Neurological Foundation.

Please address correspondence to John P. Karis, MD, c/o Neuroscience Publications; Barrow Neurological Institute, St. Joseph's Hospital and Medical Center, 350 W Thomas Rd, Phoenix, AZ 85013; e-mail: Neuropub@barrowneuro.org



Indicates article with online supplemental data.

<http://dx.doi.org/10.3174/ajnr.A7892>

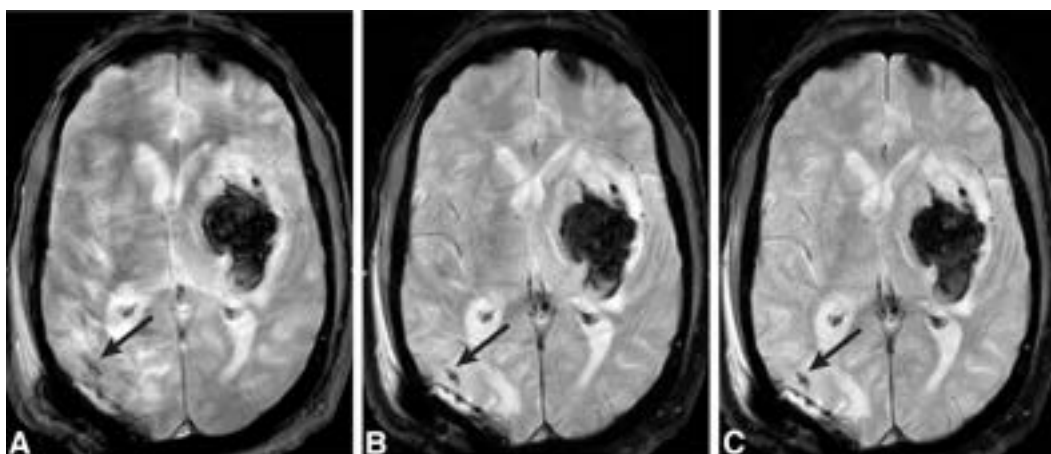


FIG 1. Axial MR images in a patient with a large left thalamic hemorrhage showing the effects of motion artifacts on standard GRE imaging (A) compared with non-motion-corrected (B) and motion-corrected (C) msEPI. Also note the increased conspicuity of a small parenchymal hemorrhage (arrow) in the right parietal region on msEPI compared with standard GRE. Reprinted with permission from the Barrow Neurological Institute, Phoenix, Arizona.

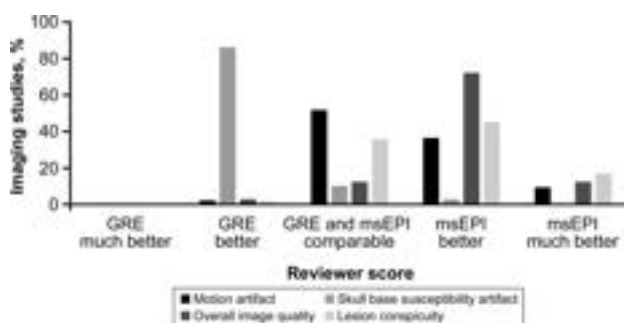


FIG 2. Results of scoring between GRE and msEPI for a total of 137 subjects with 53 subjects having T2* lesions. Motion-corrected msEPI was superior to GRE imaging in motion artifacts ($P < .001$), image quality ($P < .001$), and lesion conspicuity ($P < .001$). However, GRE was superior to motion-corrected msEPI in skull base artifacts ($P < .001$). Reprinted with permission from the Barrow Neurological Institute, Phoenix, Arizona.

For each subject, the matching pairs of GRE and motion-corrected msEPI were compared and scored relative to one another on motion artifacts, skull base susceptibility artifacts, overall image quality, and lesion conspicuity (marked NA if no lesion was visible). Each metric was scored on a 5-point Likert scale, in which 1 indicated that GRE was much better than msEPI, 2 indicated that GRE was better than msEPI, 3 indicated that the 2 modes were comparable, 4 indicated that msEPI was better than GRE, and 5 indicated that msEPI was much better than GRE. The position in which GRE and motion-corrected msEPI scans were presented was randomized (left versus right) and anonymized for review. Additional sequences were made available when requested to confirm the presence of a lesion. Susceptibility artifacts associated with adjustable shunt valves and postoperative pneumocephalus were also included in the evaluation of skull base susceptibility artifacts because they degrade image quality. Lesions bright on T2-weighted imaging (eg, arachnoid cysts and cystic encephalomalacia without hemosiderin staining) and lesions originating from the skull base were not considered for scoring lesion conspicuity

because these lesions do not show susceptibility and thus were not considered a T2* imaging lesion.

Statistical Analysis

Statistical analysis was performed using R statistical and computing software (Version 4.1.3; <http://www.r-project.org>). Nonparametric statistics were used because of the use of ordinal data. A 1-sample Wilcoxon signed-rank test was used to compare GRE versus motion-corrected msEPI. We tested the null hypothesis, $H_0: \Delta = 3$, where Δ is the average of the 2 scores over the subject population for a given metric because a score of 3 means that msEPI is comparable with GRE. Rejection of the null hypothesis suggests that the scoring distribution is not symmetric around 3 but in favor of either GRE $\Delta < 3$ or msEPI $\Delta > 3$. Significance was set at $P < .05$.

RESULTS

Imaging was performed and analyzed for a total of 137 subjects with 53 subjects having T2* lesions. The cohort included 57 male patients and 80 female patients (mean age, 50.9 years; range, 9–90 years). Motion-corrected msEPI was superior to GRE in motion artifacts ($P < .001$), image quality ($P < .001$), and lesion conspicuity ($P < .001$). However, GRE was superior to motion-corrected msEPI in skull base artifacts ($P < .001$) (Fig 2). Detailed assessment scores are included in the Online Supplemental Data.

DISCUSSION

Although the reduced overall signal due to the decreased scan time of the motion-corrected msEPI could have resulted in suboptimal imaging, we found that motion-corrected msEPI demonstrated improved overall image quality compared with GRE. Both reviewers noted that although overall signal intensity was less for motion-corrected msEPI compared with GRE, contrast resolution and sharpness were better with msEPI. Contrast between the lesions and the surrounding tissues was measured, and the mean values were 0.675 (range, 0.183–0.987) for GRE and 0.800 (range, 0.367–0.994) for msEPI. The results from 18

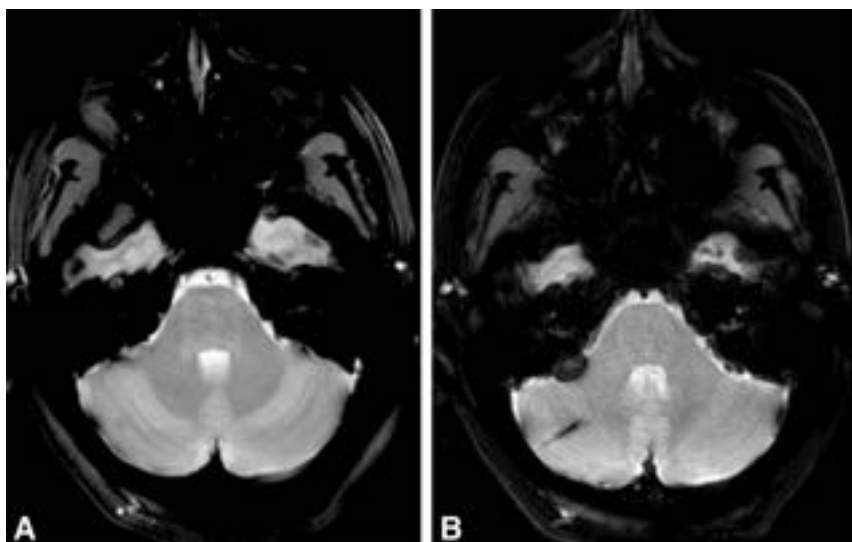


FIG 3. Axial standard GRE (A) and motion-corrected msEPI (B) in a subject with a developmental venous anomaly showing improved identification of tubular lesions in motion-corrected msEPI versus standard GRE imaging. Reprinted with permission from the Barrow Neurological Institute, Phoenix, Arizona.

measurable lesions showed that the msEPI had a greater difference between lesions and surrounding tissue compared with GRE, though this difference was not statistically significant. The lack of statistical significance might be partially due to the limited sample size.

Motion-corrected msEPI was rated as superior to GRE for motion artifacts. When significant motion artifacts were present, some GRE images were nondiagnostic and were repeated according to the protocol. This repeat sequence resulted in longer overall examination times for those patients. Only 3 subjects had worse motion artifacts associated with msEPI compared with GRE, possibly because of randomly increased patient motion during msEPI acquisition compared with during the GRE acquisition. Additional images of GRE and msEPI with and without motion correction are presented in the Online Supplemental Data.

Motion-corrected msEPI was also rated as superior to GRE for lesion detection. Every lesion identified on GRE was also identified on msEPI, but msEPI identified some lesions that were not identified on GRE (Fig 3).

As expected, GRE was found to have less susceptibility at the skull base compared with motion-corrected msEPI due to a designed longer effective TE resulting in increased susceptibility-induced signal loss. Skull base susceptibility artifact assessment also served as an internal control to ensure appropriate T2* weighting of msEPI. Note that increased skull base susceptibility artifacts did not negatively affect image quality or lesion detection. Although 3D msEPI provides fine section coverage and a high signal-to-noise ratio, it is still prone to motion artifacts, which are of great concern in the emergency department setting.

Motion-corrected 2D msEPI can potentially alleviate this concern through the use of a navigator echo.

Motion-corrected msEPI performed better than GRE in motion artifacts, overall image quality, and lesion detection. Skull base susceptibility artifacts were more prominent on msEPI than on GRE, consistent with the longer effective TE of msEPI, resulting in increased susceptibility-induced signal loss.

CONCLUSIONS

For institutions that have attempted implementation of non-motion-corrected msEPI but have been unsuccessful due to image degradation from patient motion, the improved image quality and reduced scan time achieved by replacing GRE with motion-corrected msEPI makes this new technique a viable

alternative for blood-sensitive imaging in the emergency department.

ACKNOWLEDGMENTS

We thank the staff of Neuroscience Publications at Barrow Neurologic Institute for assistance with manuscript preparation.

Disclosure forms provided by the authors are available with the full text and PDF of this article at www.ajnr.org.

REFERENCES

1. Sanchez Y, Yun BJ, Prabhakar AM, et al. **Magnetic resonance imaging utilization in an emergency department observation unit.** *West J Emerg Med* 2017;18:780–84 CrossRef Medline
2. Jeong HK, Gore JC, Anderson AW. **High-resolution human diffusion tensor imaging using 2-D navigated multishot SENSE EPI at 7 T.** *Magn Reson Med* 2013;69:793–802 CrossRef Medline
3. Steinhoff M, Mertins A, Bornert P. **SENSE-based multi-shot DWI reconstruction with extra-navigated rigid motion and contrast correction for brain EPI.** In: *Proceedings of the International Society for Magnetic Resonance in Medicine & the Society for MR Radiographers & Technologists Virtual Conference and Exhibition*, August 8–14, 2020:4339
4. Guhaniyogi S, Chu ML, Chang HC, et al. **Motion immune diffusion imaging using augmented MUSE for high-resolution multi-shot EPI.** *Magn Reson Med* 2016;75:639–52 CrossRef Medline
5. Li Z, Ooi MB, Karis J. **A rapid motion-corrected T2*-weighted multi-shot EPI technique for the emergency department setting.** In: *Proceedings of the Joint Annual Meeting International Society for Magnetic Resonance in Medicine-European Society for Magnetic Resonance in Medicine and Biology I and the International Society for MR Radiographers & Technologists*, London, UK. May 7–12, 2022

Medical Imaging Compatibility of Magnesium- and Iron-Based Bioresorbable Flow Diverters

A.A. Oliver,¹ E.K. Koons,² P.S. Trester,³ J.E. Kleinow,⁴ R.S. Jonsgaard,⁵ A.J. Vercnocke,⁶ C. Bilgin,⁷ R. Kadirvel,⁸ S. Leng,⁹ A. Lu,¹⁰ D. Dragomir-Daescu, and D.F. Kallmes¹¹



ABSTRACT

BACKGROUND AND PURPOSE: Bioresorbable flow diverters are under development to mitigate complications associated with conventional flow-diverter technology. One proposed advantage is the ability to reduce metal-induced artifacts in follow-up medical imaging. In the current work, the medical imaging compatibility of magnesium- and iron-based bioresorbable flow diverters is assessed relative to an FDA-approved control in phantom models.

MATERIALS AND METHODS: Bioresorbable flow diverters, primarily composed of braided magnesium or antiferromagnetic iron alloy wires, were compared with an FDA-approved control flow diverter. The devices were assessed for MR imaging safety in terms of magnetically induced force and radiofrequency heating using 1.5T, 3T, and 7T field strength clinical scanners. The devices were deployed in phantom models, and metal-induced image artifacts were assessed in the 3 MR imaging scanners and a clinical CT scanner following clinical scan protocols; device visibility was assessed under fluoroscopy.

RESULTS: The magnesium-based bioresorbable flow diverter, iron-based bioresorbable flow diverter, and the control device all demonstrated MR imaging safety in terms of magnetically induced force and radiofrequency heating at all 3 field strengths. The bioresorbable flow diverters did not elicit excessive MR imaging artifacts at any field strength relative to the control. Furthermore, the bioresorbable flow diverters appeared to reduce blooming artifacts in CT relative to the control. The iron-based bioresorbable flow diverter and control device were visible under standard fluoroscopy.

CONCLUSIONS: We have demonstrated the baseline medical imaging compatibility of magnesium and antiferromagnetic iron alloy bioresorbable flow diverters. Future work will evaluate the medical imaging characteristics of the bioresorbable flow diverters in large-animal models.

ABBREVIATIONS: BRFD = bioresorbable flow diverter; FD = flow-diverting device; FeBRFD = iron-based bioresorbable flow diverter; MgBRFD = magnesium-based bioresorbable flow diverter; RF = radiofrequency; T_g = gravitational torque; T_{max} = maximum torque

An estimated 5% of the US population has an intracranial aneurysm. Approximately 30,000 rupture annually, resulting in the death of one-half the patients within 6 months.¹ Therefore, it is critical to treat intracranial aneurysms before their rupture.

Received February 24, 2023; accepted after revision April 16.

From the Department of Biomedical Engineering and Physiology (A.A.O., E.K.K., S.L., D.D.-D., D.F.K.), Mayo Clinic Graduate School of Biomedical Sciences, Rochester, Minnesota; and Departments of Radiology (A.A.O., E.K.K., P.S.T., J.E.K., R.S.J., A.J.V., C.B., R.K., S.L., A.L., D.F.K.), Physiology and Biomedical Engineering (A.A.O., D.D.-D.), and Neurosurgery (R.K.), Mayo Clinic, Rochester, Minnesota.

This work was partially funded by National Institutes of Health, grant No. R01 NS076491. Alexander Oliver is supported by American Heart Association, grant No. 23PRE1012781.

Please address correspondence to Alexander A. Oliver, Alfred 9-446, Radiology, 200 First St SW, Mayo Clinic, Rochester, MN 55905; e-mail: Oliver.Alexander@mayo.edu

Indicates open access to non-subscribers at www.ajnr.org

Indicates article with online supplemental data.

<http://dx.doi.org/10.3174/ajnr.A7873>

Flow-diverting devices (FDs) are a rapidly growing endovascular approach for the treatment of intracranial aneurysms due to their high aneurysm occlusion rates in the clinic.² However, all FDA-approved FDs are composed of permanent materials that will remain in the patients for the duration of their lives. This outcome exacerbates complications such as device-induced thromboembolism^{3,4} and stenosis of the parent artery.⁵⁻⁷ Another limitation of FDs is metal-induced imaging artifacts.⁸ These artifacts impede noninvasive follow-up CT and MR imaging of FD performance.⁹ Metal-induced artifacts can obstruct the radiologist's view of tissues adjacent to the device, making it difficult to assess aneurysm healing, the degree of stenosis, and the presence of thrombi.

Bioresorbable flow diverters (BRFDs) are emerging as the next generation of FD technology to mitigate these complications.¹⁰ BRFDs aim to serve their transient function of healing and occluding the aneurysm and subsequently to be safely resorbed into the body. BRFDs show promise in reducing metal-induced image

artifacts for 2 reasons: First, before any resorption, the innate material properties of many bioresorbable materials induce fewer metal artifacts than conventional FD materials.^{11–13} Second, the progressive and eventual complete resorption reduces device volume and, therefore, metal-induced artifacts with time.¹⁴

We have previously developed BRFDs out of magnesium (MgBRFD) and iron (FeBRFD) alloys.¹⁵ In the current work, we evaluate the medical imaging compatibility of the MgBRFD and FeBRFD relative to an FDA-approved control FD. MR imaging safety and both MR imaging and CT artifacts induced by the devices are assessed using phantom models. Device visibility for fluoroscopy-guided delivery is assessed using the same phantom models. This work serves as a baseline demonstration of the medical imaging compatibility of metallic bioresorbable vascular devices.

MATERIALS AND METHODS

Devices

The MgBRFDs and FeBRFDs have been previously described in detail.¹⁵ In short, the MgBRFDs and FeBRFDs contained 32 and 48 braided wires, respectively. Three-quarters of the wires in each device are composed of bioresorbable magnesium (50- μ m diameter) or iron (25- μ m diameter) alloys. The iron alloy is composed of an austenitic crystal structure, theoretically resulting in antiferromagnetic properties.^{16–18} The remaining wires are tantalum (30- μ m diameter) to provide radiopacity during device delivery in vivo. The MgBRFDs and FeBRFDs were 4.75 mm in diameter and 10 mm in length. Wire subcomponents for both BRFDs were manufactured by Fort Wayne Metals. The Pipeline Embolization Device (Chestnut Medical) was used as the FDA-approved control FD. The control FD was composed of a braid of 36 cobalt chromium alloy and 12 platinum-tungsten wires (25- to 32- μ m diameter). The control FD was 3.75 mm in diameter and 10 mm in length.

MR Imaging Evaluations

Magnetically Induced Force and Torque. The force induced on the devices by the magnetic field of clinical MR imaging scanners was evaluated with reference to ASTM F 2052–15 (ASNI Webstore).¹⁹ The devices were hung from a stand using a string of negligible mass. The stand started at a position 90 cm away from the bore opening to the MR imaging scanner. The stand was then advanced toward the bore opening in 10 increments until it was 13 cm within the bore. Advancing the stand further within the bore obstructed the view of the device and made it impossible to assess the deflection angle. At every increment, the deflection angle was assessed using a protractor attached to the stand, as previously described.¹⁴ Deflection angle estimations were rounded up to the nearest 5° increment to conservatively assess the magnetically induced force. Magnetically induced force, F_m , was calculated using the equation: $F_m = m \times g \times \tan(\alpha)$, where m is the mass of the device, g is the acceleration of gravity, and α is the deflection angle.¹⁴ This process was repeated for the MgBRFD, FeBRFD, and control FD using 1.5T (Signa HDxt; GE Healthcare), 3T (Signa Premier; GE Healthcare), and 7T (Magnetom Terra; Siemens) clinical MR imaging scanners. The maximum spatial gradient within our area of measurement was 320, 550, and 500 G/cm for the 1.5T, 3T, and 7T scanners, respectively.

Magnetically induced torque on the implant was calculated using magnetically induced force in accordance with ASTM F2213 (ANSI Webstore).²⁰ The maximum torque (T_{max}) was estimated using the equation: $T_{max} = (B_{sat} \times F_m) / (4 \times dB/dz)$, where B_{sat} is the magnetic saturation of the device material, F_m is the magnetically induced force described above, and dB/dz is the maximum spatial gradient within our area of measurement. The B_{sat} of the device materials was unknown and was, therefore, conservatively estimated at 2.2T, the value for pure iron. Maximum gravitational torque (T_g) was calculated by multiplying the force of gravity acting on the device length.

Radiofrequency Heating. Radiofrequency (RF)-induced heating of the devices was evaluated with reference to ASTM F 2182–1121 (ASTM). An MgBRFD, FeBRFD, or control FD was placed in a phantom composed of 1.32 g/L of NaCl and 10 g/L of polyacrylic acid in deionized water to simulate physiologic electrical and thermal properties.²¹ Two temperature probes were placed on the surface of the device, with one in the middle and one at the end of the device. The device was held in place in the phantom using a wooden dowel. A third temperature probe was placed in the phantom far from the device to measure background fluctuations in phantom temperature. The phantom and the device were placed as laterally as possible on the patient table where potential RF heating is expected to be worse than in the center of the bore. Each device type or phantom was imaged using a T1-weighted fast spin-echo sequence on the 1.5T, 3T, and 7T clinical MR imaging scanners. Specific scan parameters are presented in the Online Supplemental Data. Temperature was measured for 2 minutes before the scan and for the duration of the scan sequence. For each temperature probe, the difference in average temperature between the prescan and scan duration was calculated. The temperature changes from the 2 probes at the device surface were averaged together, and the temperature change from the background probe was subtracted from this average.

Imaging Artifacts. An MgBRFD, FeBRFD, or control FD was placed within the phantom described above and imaged with a T1-weighted fast spin-echo sequence and a gradient-echo sequence using the 1.5 T, 3T, and 7T clinical MR imaging scanners. The specific scan parameters for both sequences are presented in the Online Supplemental Data. All scans were completed in first level operating mode.

CT Artifacts. An MgBRFD, FeBRFD, or a control FD was deployed within silicone sidewall aneurysm models. The aneurysm neck was 4 mm, and the height and width were 8 mm. The parent artery diameter was 4 mm for the MgBRFD and FeBRFD and 3.75 mm for the control FD to appropriately match the device diameters. The devices containing aneurysm models were perfused with Omnipaque iodine contrast (GE Healthcare) diluted to a concentration of 20 mg/mL using deionized water and placed within a 20-cm water phantom to mimic contrast-enhanced neurovasculature and attenuation in the human head. The samples were scanned using a clinical energy-integrating detector CT scanner (Somatom Force; Siemens) following the dual-source, dual-energy clinical circle of Willis protocol at our institution. The scan parameters are presented in the Online

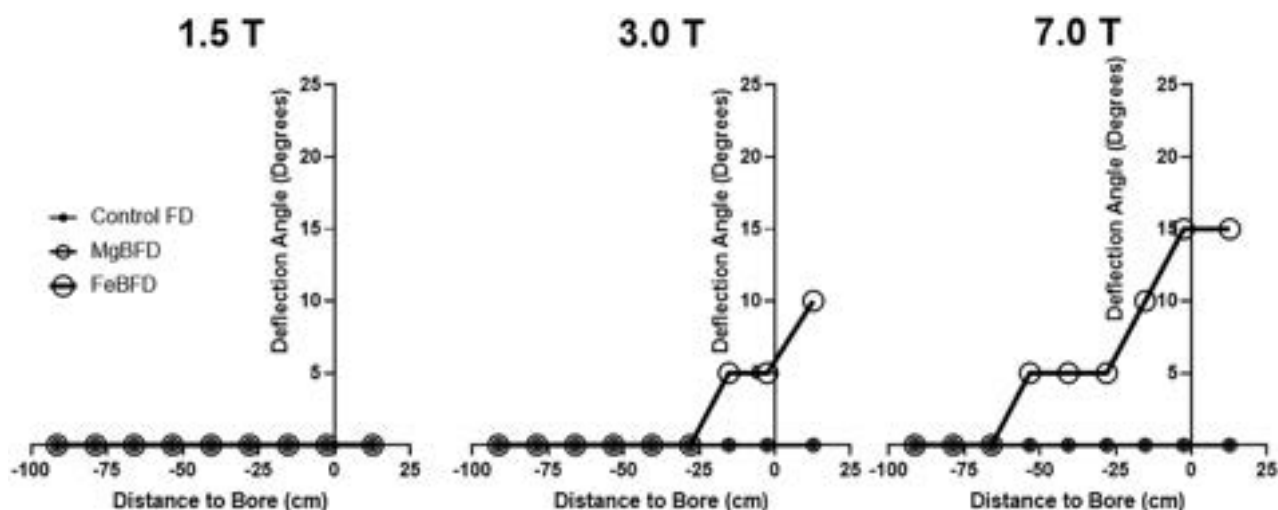


FIG 1. Deflection angle of the control FD, MgBRFD, and FeBRFD at various locations relative to the bore opening of 1.5T, 3T, and 7T field strength clinical MR imaging scanners. Negative values are outside the bore, with 0 cm representing the bore opening. Deflection angle estimates are rounded up to the next highest 5° increment.

Supplemental Data. The first scan before any device resorption was considered the 0-week time point.

The models containing MgBRFDs and FeBRFDs were then incorporated into a flow loop mimicking the physiologic environment to simulate device resorption using methods previously described in detail.¹⁵ At 1-, 5-, and 12-week time points, the devices were removed from the flow loop and imaged using a micro-CT scanner (SkyScan 1276; Bruker) to quantify reductions in device volume across time, as previously described.¹⁵ Immediately following micro-CT imaging, the device-containing models were perfused with contrast and re-imaged with the clinical CT scanner using the same technique as the 0-week time point. Following each scan, the device-containing models were re-incorporated into the flow loop until the next scan. This step allowed us to investigate changes in clinical CT artifacts associated with device resorption with time.

Fluoroscopy. A MgBRFD, FeBRFD, and control FD were deployed within the same silicone aneurysm models and placed within the 20-cm water phantom described above. The devices were then imaged using an Artis Zee angiography unit (Siemens) to assess their visibility for fluoroscopy-guided delivery. The devices containing the silicone aneurysm models were then removed from the 20-cm water phantom and imaged directly on the tabletop to more clearly depict the devices. The same x-ray tube position and angle were used for the water phantom and tabletop tests. The distance of the x-ray tube to aneurysm models was also standardized.

RESULTS

Magnetically Induced Force, Torque, and RF Heating

The deflection angles of the control FD, MgBRFD, and FeBRFD at various locations relative to the bore opening of 1.5T, 3T, and 7T clinical MR imaging scanners are presented in Fig 1. The magnetic fields of the MR imaging scanners did not induce any detectable deflection for the control FD and the MgBRFD at any

field strength. The FeBRFD deflected 5° and 15° at the bore opening of the 3T and 7T strength scanners, respectively. The calculated force of gravity (F_g), magnetically induced force (F_m) at the bore opening, and the ratio F_m/F_g are presented in the Online Supplemental Data for all device types and field strength scanners. Although the FeBRFD experienced detectable deflection at the bore opening of the 3T and 7T scanners, the magnetically induced force acting on the device from the MR imaging scanner was less than one-third of the force of gravity acting on the device ($F_m/F_g = 0.09$ at 3T, $F_m/F_g = 0.27$ at 7T) in the area tested. Because the highest spatial gradient of the magnetic field is <3 times the maximum spatial gradient within the area of our measurements, the magnetically induced force, therefore, does not present a notable safety concern for the control FD, MgBRFD, and FeBRFD.

In theory, the austenitic crystal structure of the iron alloy used in FeBRFD should result in a completely nonferromagnetic device and consequently no magnetically induced force. The small observed deflections are likely due to tiny ferromagnetic impurities within the crystal structure of the iron alloy. The T_{max} on the devices was estimated using F_m , T_{max} , and T_g , and the ratio of T_{max}/T_g is presented in Online Supplemental Data for all device types and field strength scanners. No torque was estimated for the control FD and MgBRFD at any scanner strength. The estimated T_{max} of the FeBRFD was less than the gravitational torque in the 3T scanner, but approximately 3 times greater than T_g in the 7T scanner ($T_{max}/T_g = 0.8$ at 3T, $T_{max}/T_g = 2.8$ at 7T). These estimations indicate that the FeBRFD is MR imaging-conditional at 3T, and further considerations would be required for evaluating safety at 7T. However, our T_{max} estimations are likely overestimates, because the B_{sat} for the antiferromagnetic resorbable iron alloy is likely much less than the 2.2T value conservatively used on the basis of pure iron.

For the evaluation of RF heating, no device type at any field strength resulted in a change in temperature of >0.34°C. The small observed RF heating temperature changes are within the range of fluctuations in room temperature and are negligible

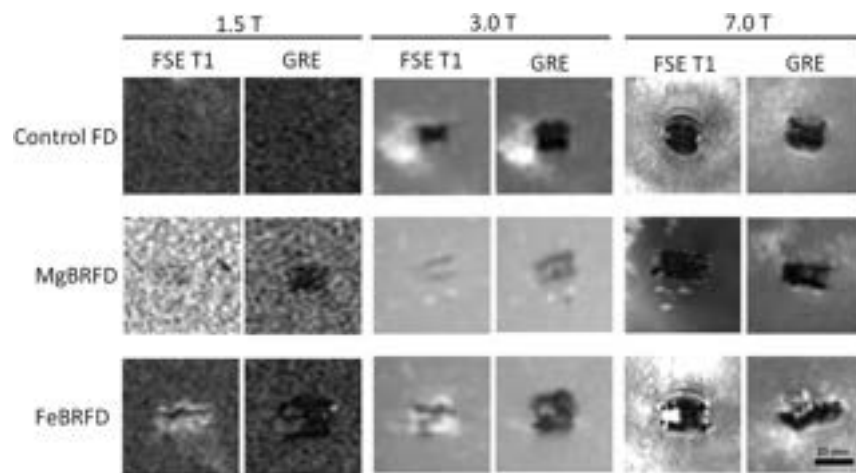


FIG 2. MR imaging artifacts induced by the control FD, MgBRFD, and FeBRFD using a fast spin-echo sequence with T1 weighting (FSE T1) and a gradient recalled-echo (GRE) scan sequence with 1.5T, 3T, and 7T field strength clinical MR imaging scanners.

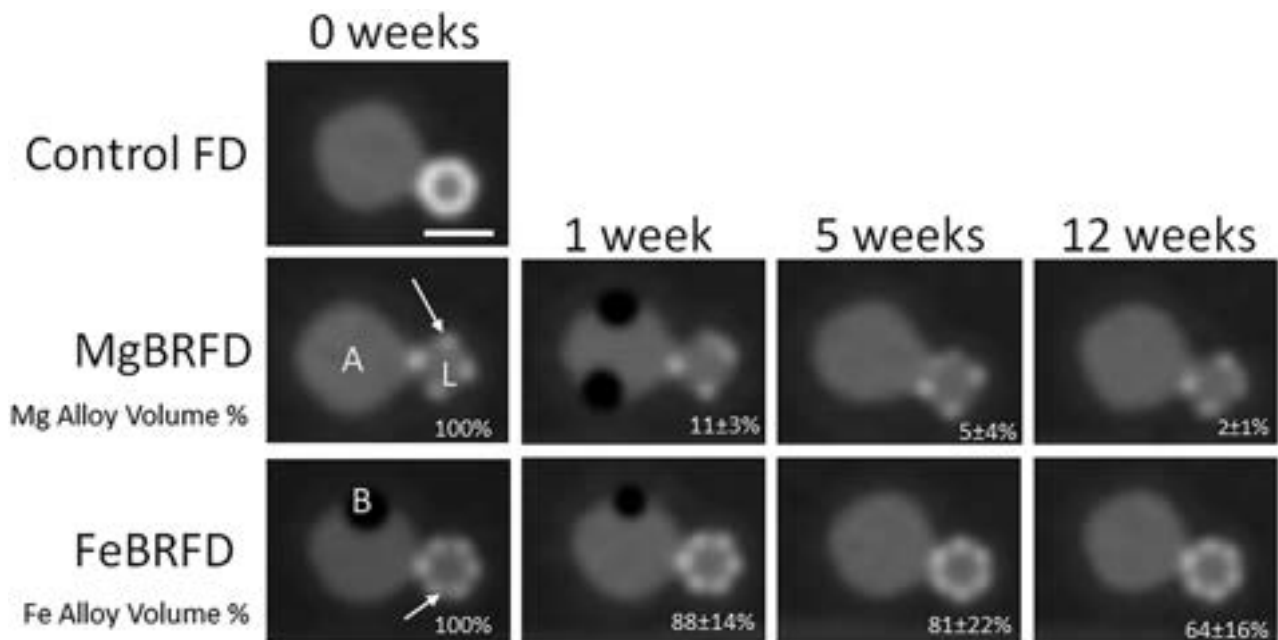


FIG 3. Representative CT images of the control FD, MgBRFD, and FeBRFD and reduction in resorbable device volume with time. A represents the aneurysm sac, L represents the lumen of the parent artery, and B represents trapped air bubbles. The arrows indicate examples of crossing tantalum marker wires. The scale bar is 5 mm.

from a physiologic safety standpoint. Therefore, these data suggest that the control FD, MgBRFD, and FeBRFD are MR imaging-conditional and can be safely scanned at the tested field strengths from the RF heating perspective.

MR Imaging Artifacts

MR imaging artifacts from the control FD, MgBRFD, and FeBRFD using both a T1-weighted fast spin-echo sequence and a gradient-echo scan sequence for all 3 field strength MR imaging scanners are presented in Fig 2. The MgBRFD imaged with the fast spin-echo sequence and the control FD for both scan sequences are barely detectable at 1.5T. Generally, for each device type, the gradient-echo sequence induced larger artifacts than the fast spin-echo sequence. However, the actual size of the artifacts

depends on many acquisition parameters such as TE, echo-train length, acquisition bandwidth, the orientation of the device in the scanner bore, and so forth. The FeBRFD appeared to induce slightly more artifacts than the control FD and MgBRFD when matched for scan sequence and scanner strength. Overall, MR imaging artifacts induced by the MgBRFD and FeBRFD are not excessive relative to the control FD, suggesting suitable MR imaging compatibility for the bioresorbable devices.

CT Artifacts

Representative CT images of the control FD, MgBRFD, and FeBRFD, as well as reductions in resorbable material volume are presented in Fig 3. The control FD induced the most blooming artifacts, resulting in the device appearing larger than its physical

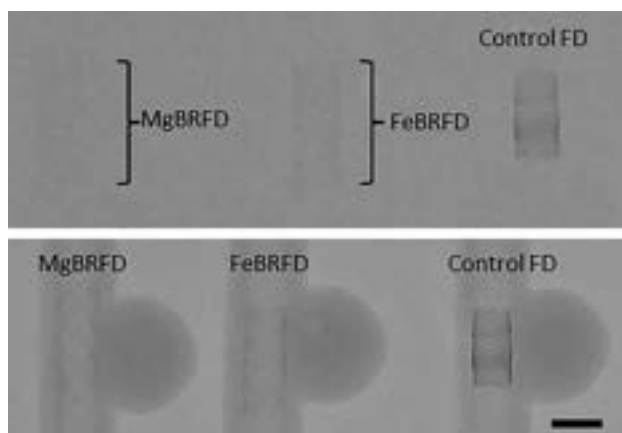


FIG 4. Fluoroscopic images of the MgBRFD, FeBRFD, and control FD placed within a 20-cm water phantom (*top*) and directly onto the tabletop (*bottom*). The scale bar is 5 mm.

size. No struts were visible in the control FD, making it appear as a solid cylinder due to blooming artifacts of highly attenuating metals. This feature obstructed the view of the aneurysm neck and made the parent vessel appear more stenosed. For the MgBRFD and FeBRFD, the only apparent struts were the tantalum radiopaque marker wires. Representative images for the MgBRFDs and FeBRFDs were selected at locations where the tantalum wires within the braid crossed, making it appear as if there were half the amount of tantalum wires than physically present. These locations were selected to create larger regions of bioresorbable wires unimpeded by the blooming of adjacent tantalum wires. The magnesium alloy resorbable wires were not detected at 0 weeks because their CT numbers were very similar to the contrast within the aneurysm model. Consequently, their resorption with time and near-complete resorption at 5 weeks did not have any visible implications for image quality. It is difficult to discern whether the iron alloy resorbable wires are detectable between the tantalum struts or if the increased CT number relative to the contrast is caused by blooming of the adjacent tantalum wires. A reduction down to 65% of the initial bioresorbable iron alloy volume as determined by micro-CT at 12 weeks did not appear to influence the resulting images.

Fluoroscopy

Fluoroscopy images of the MgBRFD, FeBRFD, and the control FD are presented in Fig 4. When placed in the 20-cm water phantom (FOV = 32 cm, kV = 70, mA = 258), the MgBRFD is barely detectable. The FeBRFD is more visible, owing to the greater number of tantalum wires within the braid in addition to the higher density of the iron alloy over the magnesium alloy. The control FD is the most apparent. When removed from the water phantom, all 3 devices are detectable, and the braided structure becomes more visible (FOV = 32 cm, kV = 70, mA = 31). Our incorporation of twelve 30- μ m-diameter tantalum wires in the FeBRFD resulted in an overall device radiopacity that would likely be suitable for fluoroscopy-guided delivery. However, these images also suggest that the device design could be improved in this respect. The ideal FD design requires a balance between fluoroscopic visibility and minimal CT artifacts.

DISCUSSION

In the current work, we demonstrate the medical imaging compatibility of a novel MgBRFD and FeBRFD relative to an FDA-approved control FD. With reference to the FDA guidance document “Testing and Labeling Medical Devices for Safety in the Magnetic Resonance Environment,”²² all 3 devices were MR imaging-conditional from a magnetically induced force and RF heating standpoint at all MR imaging scanner strengths. The FDA suggests that passive devices such as FDs <2 cm in all dimensions and <3 cm away from other implants do not require RF heating evaluations at ≤ 3 T, because they are not expected to generate a temperature change of $> 2^{\circ}\text{C}$.²² Our results validate this point and expand it up to a 7 T scanner. The magnetically induced torque of all 3 devices was less than the T_g in all 3 scanners, other than the FeBRFD in the 7 T scanner. Devices with a lower magnetically induced torque than T_g are considered MR imaging conditional.²² However, a greater magnetically induced torque may still be acceptable depending on the type of tissue adjacent to the device and how the device is fastened within it.²² In the case of stents and FDs, it may be necessary to wait several months until the device is encapsulated by tissue before obtaining MR images. Finally, the MgBRFD and FeBRFD did not induce excessive MR imaging artifacts relative to the control FD.

The MgBRFD and FeBRFD appeared to reduce blooming artifacts in CT images relative to the control FD, and the FeBRFD was still visible under fluoroscopy. This feature may result in a more accurate assessment of healing at the aneurysm neck and device-induced stenosis in follow-up imaging. The only obvious CT artifacts in the MgBRFD and FeBRFD images were caused by the tantalum marker wires. This feature suggests that an optimal BRFD design should contain the minimum volume of radiopaque markers required for fluoroscopy-guided delivery, while maximizing the amount of resorbable magnesium or iron alloy components within the device. Magnesium and iron alloys are regularly applied to other vascular scaffolding applications, such as coronary stenting.²³ This work can also serve as a baseline demonstration of medical imaging compatibility for these devices.

Other groups have investigated the medical imaging compatibility of BRFDs. Morrish et al¹¹ demonstrated suitable visibility for fluoroscopy-guided device delivery of their primarily polymer-based BRFD. Furthermore, they demonstrated a quantitative reduction in device-induced artifacts in MR imaging and CT images when their BRFD was compared with an FDA-approved control FD. They also showed that their BRFDs improved the image quality of MR imaging when assessed by 8 blinded neuroradiologists. Their work showcased the ability of BRFDs to reduce device-induced artifacts and improve medical imaging quality. Our work investigates and extends these results to the imaging compatibility of metallic BRFDs. Bian et al¹⁴ investigated the MR imaging compatibility of a bioresorbable iron-based coronary stent. Their stent was primarily composed of a ferromagnetic nitrided iron backbone. The ferromagnetic properties resulted in magnetically induced forces from the MR imaging scanners that were substantially larger than the force of gravity acting on the devices. However, RF heating and image artifacts were negligible relative to industry-standard controls. Most notably, their devices demonstrated the ability to reduce artifacts with their progressive resorption across time in vivo.

DSA is currently the criterion standard follow-up technique because its quality is not affected by device-related metallic artifacts.²⁴ However, DSA is an invasive procedure with potential complications that include cerebral microembolism and puncture site hematoma and pseudoaneurysm.²⁴ Therefore, there has been growing interest in the use of noninvasive techniques such as CT and MR imaging in the follow-up of aneurysms treated by endovascular means. The current literature indicates that noninvasive imaging methods are safer and more cost-effective compared with DSA as a primary follow-up technique.^{25,26} However, CT and MR imaging are susceptible to metal artifacts, which can affect the quality of scan and assessment. Vascular device design and material selection have implications for CT and MR imaging compatibility.^{9,27,28} Halitcan et al⁸ recently reported that nitinol FDs are advantageous for clinical TOF MR angiography follow-up of FD performance over cobalt-chromium FDs. In CT imaging, both the strut thickness and material selection affect the degree of x-ray attenuation and consequently the extent of metal-induced artifacts.^{29,30} Additionally, the improvement of medical imaging technology to mitigate metal-induced image artifacts and enhance the image quality of endovascular devices remains a growing topic of research.^{31,32} Follow-up quality assessment of medical imaging should be considered in the development and engineering of endovascular devices.

A limitation of the study was that the available control FD was 1 mm smaller in diameter than the MgBRFD and FeBRFD. However, the slightly decreased metal volume and dimensions in the control FD acted as a slightly more conservative benchmark standard for the BRFDs. Another limitation was the accuracy of deflection angle measurements, which were assessed visually relative to a mounted adjacent protractor. However, all observed deflection angles at multiple distances to the bore at all 3 field strengths and resulting calculations of magnetically induced force were less than one-third of the force of gravity acting on the devices; therefore, all measurement errors were negligible in the overall assessment of MR imaging safety.

Future work will focus on assessing the long-term aneurysm occlusion rates of the bioresorbable FDs relative to permanent controls in the rabbit elastase-induced aneurysm model.³³ A major direction for the field is to determine the optimal device resorption rate that allows the device to maintain structural integrity long enough for the aneurysm to heal before notable resorption.¹⁰ The medical imaging characteristics of the MgBRFD and FeBRFD relative to a control FD will also be assessed using animal models. Blinded interventional neuroradiologists will assess the deployability and image quality of the MgBRFDs and FeBRFDs relative to the control FDs using Likert scales. Future work will also focus on improving the MgBRFD and FeBRFD design by reducing the amount of radiopaque marker wires within the braid and/or adding platinum pledgets on either end of the device, with the intention of minimizing image artifacts at the aneurysm neck without sacrificing deployability.

CONCLUSIONS

We have demonstrated the MR imaging compatibility of magnesium- and antiferromagnetic iron alloy-based BRFDs. Furthermore, the BRFDs appeared to reduce metal-induced CT blooming artifacts

relative to the FDA-approved control FD. These data suggest that minimizing the volume of radiopaque markers required for fluoroscopy-guided device delivery, while maximizing the amount of bioresorbable metal components in the device, could reduce CT artifacts. This work serves as a baseline demonstration of the medical imaging compatibility of bioresorbable magnesium and antiferromagnetic iron alloy vascular devices. Future work will investigate the medical imaging characteristics of the BRFDs using large-animal models.

ACKNOWLEDGMENTS

The authors would like to thank Jeffrey Marsh, Liqiang Ren, and Tim Winfree for their help with CT scan acquisitions and Dr Daying Dai for her help formatting figures.

Disclosure forms provided by the authors are available with the full text and PDF of this article at www.ajnr.org.

REFERENCES

- King JT Jr. **Epidemiology of aneurysmal subarachnoid hemorrhage.** *Neuroimaging Clin N Am* 1997;7:659–68 Medline
- Brinjikji W, Murad MH, Lanzino G, et al. **Endovascular treatment of intracranial aneurysms with flow diverters: a meta-analysis.** *Stroke* 2013;44:442–47 CrossRef Medline
- Kallmes DF, Hanel R, Lopes D, et al. **International retrospective study of the Pipeline embolization device: a multicenter aneurysm treatment study.** *AJNR Am J Neuroradiol* 2015;36:108–15 CrossRef Medline
- Becske T, Brinjikji W, Potts MB, et al. **Long-term clinical and angiographic outcomes following Pipeline embolization device treatment of complex internal carotid artery aneurysms: five-year results of the Pipeline for Uncoilable or Failed Aneurysms Trial.** *Neurosurgery* 2017;80:40–48 CrossRef Medline
- Guédon A, Clarençon F, Di Maria F, et al. **Very late ischemic complications in flow-diverter stents: a retrospective analysis of a single-center series.** *J Neurosurg* 2016;125:929–35 CrossRef Medline
- Caroff J, Tamura T, King RM, et al. **Phosphorylcholine surface modified flow diverter associated with reduced intimal hyperplasia.** *J Neurointerv Surg* 2018;10:1097–101 CrossRef Medline
- Flood TF, van der Bom IM, Strittmatter L, et al. **Quantitative analysis of high-resolution, contrast-enhanced, cone-beam CT for the detection of intracranial in-stent hyperplasia.** *J Neurointerv Surg* 2015;7:118–25 CrossRef Medline
- Halitcan B, Bige S, Sinan B, et al. **The implications of magnetic resonance angiography artifacts caused by different types of intracranial flow diverters.** *J Cardiovasc Magn Reson* 2021;23:1–14 CrossRef Medline
- Bouillot P, Brina O, Delattre BM, et al. **Neurovascular stent artifacts in 3D-TOF and 3D-PCMRI: influence of stent design on flow measurement.** *Magn Reson Med* 2019;81:560–72 CrossRef Medline
- Oliver AA, Carlson KD, Bilgin C, et al. **Bioresorbable flow diverters for the treatment of intracranial aneurysms: review of current literature and future directions.** *J Neurointerv Surg* 2023;15:178–82 CrossRef
- Morrish R, Corcoran R, Cooke J, et al. **Fluoroscopy, CT, and MR imaging characteristics of a novel primarily bioresorbable flow-diverting stent for aneurysms.** *Interv Neuroradiol* 2022;28:660–67 CrossRef Medline
- Filli L, Luechinger R, Frauenfelder T, et al. **Metal-induced artifacts in computed tomography and magnetic resonance imaging: comparison of a biodegradable magnesium alloy versus titanium and stainless steel controls.** *Skeletal Radiol* 2015;44:849–56 CrossRef Medline
- Sonnow L, Könniker S, Vogt PM, et al. **Biodegradable magnesium Herbert screw: image quality and artifacts with radiography, CT and MRI.** *BMC Med Imaging* 2017;17:1–9 CrossRef Medline

14. Bian D, Qin L, Lin W, et al. **Magnetic resonance (MR) safety and compatibility of a novel iron bioresorbable scaffold.** *Bioact Mater* 2020;5:260–74 CrossRef Medline
15. Oliver AA, Bilgin C, Vercnocke AJ, et al. **Benchtop proof of concept and comparison of iron and magnesium-based bioresorbable flow diverters.** *J Neurosurg* 2022;1:1–7 CrossRef Medline
16. Schaffer JE, Nauman EA, Stanciu LA. **Cold-drawn bioabsorbable ferrous and ferrous composite wires: an evaluation of mechanical strength and fatigue durability.** *Metallurgical and Materials Transactions B* 2012;43:984–94 CrossRef
17. Schaffer JE. **Biodegradable alloy wire for medical devices.** *Google Patents* 2020. <https://patents.google.com/patent/WO2014011803A1/en>. Accessed April 29, 2023
18. Ishikawa Y, Endoh Y. **Antiferromagnetism of γ -FeMn alloys.** *J Appl Phys* 1968;39:1318–19 CrossRef
19. ASTM A. **F2052-15: Standard Test Method for Measurement of Magnetically Induced Displacement Force on Medical Devices in the Magnetic Resonance Environment.** *ANSI Webstore*. 2015. <https://webstore.ansi.org/standards/astm/astmf205215>. Accessed April 29, 2023
20. ASTM IF2213-17. **Standard Test Method for Measurement of Magnetically Induced Torque on Medical Devices in the Magnetic Resonance Environment.** *ASTM Compass* 2017. <https://www.astm.org/f2213-17.html>. Accessed April 29, 2023
21. ASTM F2182-11a. **Standard Test Method for Measurement of Radio Frequency Induced Heating on or Near Passive Implants during Magnetic Resonance Imaging.** *ASTM International West* 2011. <https://webstore.ansi.org/standards/astm/astmf218211a>. Accessed April 29, 2023
22. US Food and Drug Administration. **Testing and labeling medical devices for safety in the magnetic resonance (MR) environment: Guidance for industry and Food and Drug Administration Staff.** *Federal Register* 2021
23. Oliver AA, Sikora-Jasinska M, Demir AG, et al. **Recent advances and directions in the development of bioresorbable metallic cardiovascular stents: insights from recent human and in vivo studies.** *Acta Biomater* 2021;127:1–23 CrossRef Medline
24. Soize S, Gawlitza M, Raoult H, et al. **Imaging follow-up of intracranial aneurysms treated by endovascular means: why, when, and how?** *Stroke* 2016;47:1407–12 CrossRef Medline
25. Schaafsma JD, Koffijberg H, Buskens E, et al. **Cost-effectiveness of magnetic resonance angiography versus intra-arterial digital subtraction angiography to follow-up patients with coiled intracranial aneurysms.** *Stroke* 2010;41:1736–42 CrossRef Medline
26. Burel J, Gerardin E, Vannier M, et al. **Follow-up of intracranial aneurysms treated by flow diverters: evaluation of parent artery patency using 3D-T1 gradient recalled-echo imaging with 2-point Dixon in combination with 3D-TOF-MRA with compressed sensing.** *AJNR Am J Neuroradiol* 2022;43:554–59 CrossRef Medline
27. Lenhart M, Völk M, Manke C, et al. **Stent appearance at contrast-enhanced MR angiography: in vitro examination with 14 stents.** *Radiology* 2000;217:173–78 CrossRef Medline
28. Mahnken AH. **CT imaging of coronary stents: past, present, and future.** *ISRN Cardiol* 2012;2012:1–12 CrossRef Medline
29. Mahnken AH, Buecker A, Wildberger JE, et al. **Coronary artery stents in multislice computed tomography: in vitro artifact evaluation.** *Invest Radiol* 2004;39:27–33 CrossRef Medline
30. Maintz D, Burg MC, Seifarth H, et al. **Update on multidetector coronary CT angiography of coronary stents: in vitro evaluation of 29 different stent types with dual-source CT.** *Eur Radiol* 2009;19:42–49 CrossRef Medline
31. Leng S, Bruesewitz M, Tao S, et al. **Photon-counting detector CT: system design and clinical applications of an emerging technology.** *Radiographics* 2019;39:729–43 CrossRef Medline
32. Lee EM, Ibrahim E-SH, Dudek N, et al. **Improving MR image quality in patients with metallic implants.** *Radiographics* 2021;41:E126–37 CrossRef Medline
33. Fujiwara NH, Cloft HJ, Marx WF, et al. **Serial angiography in an elastase-induced aneurysm model in rabbits: evidence for progressive aneurysm enlargement after creation.** *AJNR Am J Neuroradiol* 2001;22:698–703 Medline

Comprehensive Venous Outflow Predicts Functional Outcomes in Patients with Acute Ischemic Stroke Treated by Thrombectomy

G. Adusumilli, T.D. Faizy, S. Christensen, M. Mlynash, Y. Loh, G.W. Albers, M.G. Lansberg, J. Fiehler, and J.J. Heit



ABSTRACT

BACKGROUND AND PURPOSE: Cortical venous outflow has emerged as a robust measure of collateral blood flow in acute ischemic stroke. The addition of deep venous drainage to this assessment may provide valuable information to further guide the treatment of these patients.

MATERIALS AND METHODS: We performed a multicenter retrospective cohort study of patients with acute ischemic stroke treated by thrombectomy between January 2013 and January 2021. The internal cerebral veins were scored on a scale of 0–2. This metric was combined with existing cortical vein opacification scores to create a comprehensive venous outflow score from 0 to 8 and stratify patients as having favorable-versus-unfavorable comprehensive venous outflow. Outcome analyses were primarily conducted using the Mann-Whitney *U* and χ^2 tests.

RESULTS: Six hundred seventy-eight patients met the inclusion criteria. Three hundred fifteen were stratified as having favorable comprehensive venous outflow (mean age, 73 years; range, 62–81 years; 170 men), and 363, as having unfavorable comprehensive venous outflow (mean age, 77 years; range, 67–85 years; 154 men). There were significantly higher rates of functional independence (mRS 0–2; 194/296 versus 37/352, 66% versus 11%, $P < .001$) and excellent reperfusion (TICI 2c/3; 166/313 versus 142/358, 53% versus 40%, $P < .001$) in patients with favorable comprehensive venous outflow. There was a significant increase in the association of mRS with the comprehensive venous outflow score compared with the cortical vein opacification score (-0.74 versus -0.67 , $P = .006$).

CONCLUSIONS: A favorable comprehensive venous profile is strongly associated with functional independence and excellent post-thrombectomy reperfusion. Future studies should focus on patients with venous outflow status that is discrepant with the eventual outcome.

ABBREVIATIONS: AIS = acute ischemic stroke; COVES = cortical vein opacification score; CVO = comprehensive venous outflow; CVO+ = favorable comprehensive venous outflow; CVO- = unfavorable comprehensive venous outflow; ICV = internal cerebral vein; IQR = interquartile range; LVO = large-vessel occlusion; VO = venous outflow

Collateral blood flow supplies critical blood flow to the penumbra and limits growth of the ischemic core in patients presenting with acute ischemic stroke (AIS).^{1–4} Robust collaterals are associated with higher rates of successful reperfusion and better clinical outcomes in patients with AIS with large-vessel occlusion (AIS-LVO) after endovascular thrombectomy.^{5,6} Although

collateral blood flow is governed by both arterial inflow and venous outflow (VO), arterial collaterals have historically been used to measure collateral robustness. More recently, the importance of cortical VO as a measure of collateral blood flow through ischemic brain tissue and into the veins draining this tissue has been recognized.^{6–18}

Currently VO is measured by the cortical vein opacification score (COVES), which characterizes opacification of the superficial middle cerebral vein, vein of Labbé, and sphenoparietal sinus, each on a scale of 0–2, with 0 representing zero opacification and 2 representing complete opacification and robust VO.¹⁰ Favorable cortical VO (dichotomized as COVES 3–6) is independently associated with excellent tissue reperfusion and favorable long-term functional outcomes.^{6,13,18} Although COVES has proved to be an excellent measure of ischemic brain perfusion and long-term outcomes, it measures only cortical venous drainage that represents just a portion of the venous egress from the MCA territory.

Received January 31, 2023; accepted after revision April 22.

From the Department of Radiology (G.A.), Massachusetts General Hospital, Boston, Massachusetts; Department of Neuroradiology (T.D.F., J.F.), University of Hamburg-Eppendorf, Hamburg, Germany; Stanford Stroke Center (S.C., M.M., G.W.A., M.G.L.) and Department of Radiology (J.J.H.), Stanford University, Stanford, California; and Comprehensive Stroke Center (Y.L.), Swedish Neuroscience Institute, Seattle, Washington.

Please address correspondence to Jeremy Heit, MD, PhD, Center for Academic Medicine, Department of Radiology, MC:5659, 453 Quarry Rd, Palo Alto, CA 94304; e-mail: jheit@stanford.edu; @JeremyHeitMDPHD

Indicates article with online supplemental data.

<http://dx.doi.org/10.3174/ajnr.A7879>

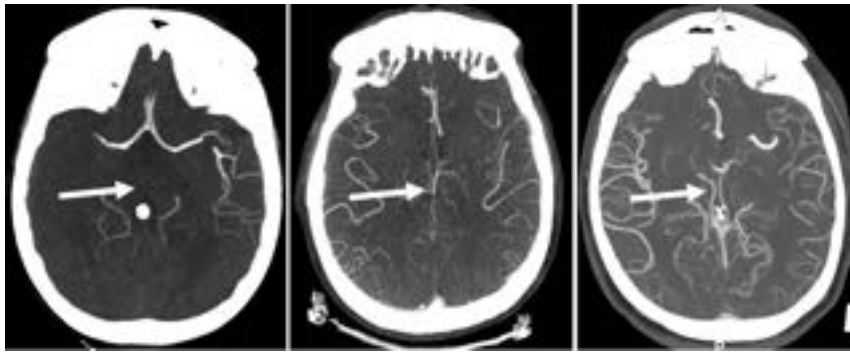


FIG 1. Degrees of internal cerebral vein opacification. From left to right, zero opacification of the ICV, moderate opacification of the ICV, and full opacification of the ICV.

The basal ganglia and striatum derive their arterial supply from the lenticulostriate arteries that arise from the M1 segment of the MCA, and the venous drainage of this territory is predominantly into the internal cerebral veins (ICVs).^{19,20} It is unclear whether assessment of venous opacification of the ICVs to the existing COVES score provides additional information to cortical venous outflow assessment.

In this study, we evaluated whether a comprehensive VO score that includes both cortical (COVES) and deep (ICV) veins that drain the MCA territory predicts favorable outcomes in patients with AIS-LVO who are treated by endovascular thrombectomy.

MATERIALS AND METHODS

Data generated or analyzed during the study are available from the corresponding author by request.

Study Design

We performed a multicenter retrospective cohort study of consecutive patients undergoing thrombectomy triage for AIS treatment at 2 comprehensive stroke centers between January 2013 and January 2021. The STrengthening the Reporting of OBservational studies in Epidemiology (STROBE) guidelines were followed to conduct this study.

Standard Protocol Approvals, Registrations, and Patient Consent

The study protocol was approved by the institution review boards of both study centers, complied with the Health Insurance Portability and Accountability Act, and followed the guidelines of the Declaration of Helsinki. Patient informed consent was waived by our review boards for this retrospective study.

Patient Inclusion and Exclusion Criteria

Patients were identified from prospectively maintained stroke databases at each center that had previously been processed for patients who underwent thrombectomy within 16 hours of stroke onset and had appropriate follow-up imaging. Demographic, imaging, and clinical data were obtained from the electronic medical records. Inclusion and exclusion criteria are detailed in the Online Supplemental Data.

Imaging Analysis

All CT and MR perfusion studies were automatically analyzed with RAPid processing of Perfusion and Diffusion (RAPID; iSchemaView). The ischemic core was defined as the volume of tissue with a 70% reduction in CBF relative to the contralateral cerebral hemisphere on CTP or the volume of tissue with restricted diffusion (ADC $< 620 \times 10^{-6} \text{ mm}^2/\text{s}$) on DWI.²¹

In all included patients, COVES had previously been scored by 2 neuroradiologists. The new ICV opacification metric was scored by 2 independent

radiologists on both the ipsilateral and contralateral ICVs in alignment with the COVES scoring system: 0 = not visible, 1 = moderate opacification, and 2 = full opacification (Fig 1).

COVES and the ICV metric were consolidated into a new comprehensive VO (CVO) score that measures both the cortical and deep venous opacification score. The CVO ranged from 0 (no opacification of the 1 deep and 3 cortical venous pathways) to 8 (full opacification of the 1 deep and 3 cortical venous pathways). Analogous to existing VO thresholds, the new CVO was defined as favorable (CVO+) by a score of 4–8 and unfavorable (CVO–) by a score of 0–3.

Postthrombectomy TIC1 scores were previously interpreted on DSA images. Successful reperfusion status was defined as TIC1 $\geq 2b$ (50%–100% revascularization).²² Excellent reperfusion status was defined as TIC1 2c/3 (95%–100% revascularization).²³

Infarct volume was acquired by manual segmentation on noncontrast CT images or $b = 1000$ DWIs using the software package Horos Project (Version 3.3.6; Horos) by a single neuroradiologist. Final infarct volumes were acquired on noncontrast CT images 48–72 hours after thrombectomy.

Readers were blinded to the clinical and outcome information of each patient during the scoring process.

Outcome Measures

Our primary outcome was functional independence at 90-day follow-up, defined by an mRS score of 0–2.²⁴ This score was previously obtained from each patient by a stroke neurologist or specialized study nurse at follow-up. Secondary outcomes included successful reperfusion status, excellent reperfusion status, excellent functional outcome (mRS 0–1), baseline ischemic core volume, final infarct volume, and change in infarct volume from the initial to follow-up examination.

Statistical Analyses

All statistical analyses were performed with SPSS Statistics, Version 29.0 (IBM). Patient demographics and imaging variables including infarct volume were compared between patients with CVO+ and CVO– by the Mann-Whitney U test; χ^2 analysis was performed to determine statistically significant differences in mRS and TIC1 score distributions between the 2 groups. The Kendall τ bivariate correlations were used to assess the relationships of CVO scores with mRS, TIC1, baseline ischemic core volume, final infarct

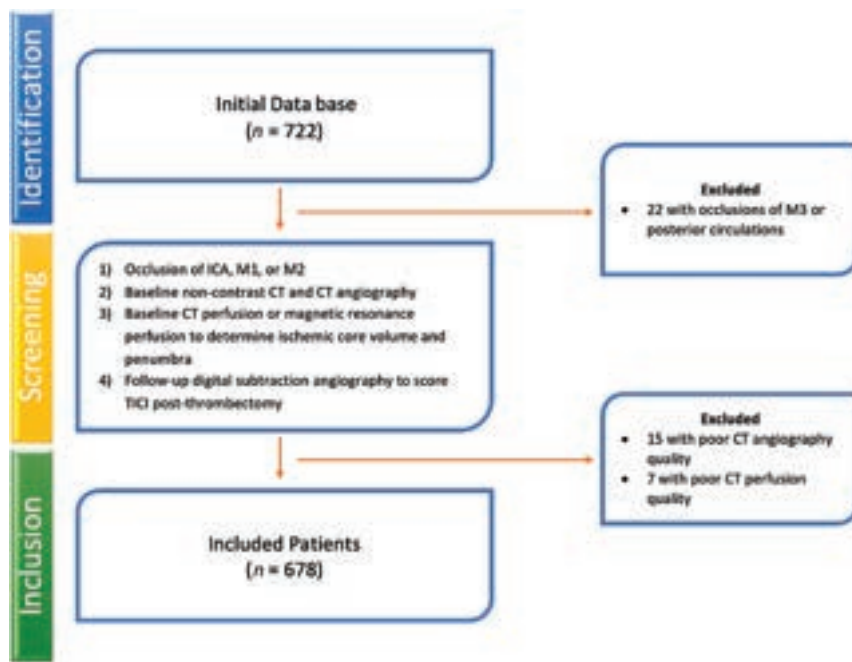


FIG 2. Patient screening and inclusion flowchart.

Table 1: Demographic profile of patients by VO status

	CVO+ (n = 315)	CVO- (n = 363)	P Value
Age (median) (IQR) (yr)	73 (62–81)	77 (67–85)	<.001
Female (No.) (%)	145 (46%)	209 (58%)	.003
Atrial fibrillation (No.) (%) (n = 311, 361)	115 (37%)	148 (41%)	.287
Hypertension (No.) (%) (n = 313, 361)	203 (65%)	261 (72%)	.037
Blood glucose level (median) (IQR) (mg/dL) (n = 272, 309)	117 (103–144)	123 (106–154)	.028
Diabetes (No.) (%) (n = 313, 360)	53 (17%)	78 (22%)	.122
Hyperlipidemia (No.) (%) (n = 276, 317)	82 (30%)	93 (29%)	.921
Smoker (current/prior) (No.) (%) (n = 292, 342)	85 (29%)	79 (23%)	.085
NIHSS score on presentation (median) (IQR)	11 (7–17)	17 (12–20)	<.001
tPA administration (No.) (%) (n = 311, 355)	189 (61%)	148 (42%)	<.001

volume, and change in infarct volume. Significant differences in correlations between COVES versus CVO against these variables were evaluated by converting the Kendall τ to the Pearson coefficient by the equation $r = \sin(0.5 \times \pi \times \tau)$ and performing a Fisher Z-test for comparison. We set α at the .05 level for significance and reported 2-tailed results for all tests.

RESULTS

Patient Inclusion and Exclusion

Of 722 patients who underwent thrombectomy and had appropriate follow-up imaging, 678 met the inclusion criteria (Fig 2). Twenty-two patients were excluded due to the occlusion being in the third segment of the MCA or in the posterior circulation. Fifteen patients were excluded due to poor CT angiogram quality, and 7 patients were excluded due to poor CTP image quality.

COVES versus CVO for VO Grading

COVES and the ICV metric were combined to create a new CVO score, as detailed in the Materials and Methods. Per the original COVES scoring, there would be 261 patients in the VO+ group

(38%) and 417 patients in the VO- group (62%). With the new CVO scoring, 315 patients were assigned to the favorable venous outflow group represented by CVO+ (46%), a significantly higher proportion than by the COVES scoring ($P < .001$). Accordingly, there were 363 patients in the CVO- group (54%). Interrater agreement for ICV opacification scoring on the affected side was substantial, $\kappa = (0.77; 95\% \text{ CI}, 0.60\text{--}0.94)$. Interrater agreement for ICV opacification scoring on the contralateral side was almost perfect, $\kappa = (0.90; 95\% \text{ CI}, 0.71\text{--}1.00)$.

Patient Demographics

Compared with patients with CVO-, those with CVO+ were younger (median age, 73 years; interquartile range [IQR], 62–81 years versus 77 years; IQR, 67–85 years; $P < .001$), presented with fewer baseline deficits (median NIHSS, 11; IQR, 7–17 versus 17; IQR, 12–20; $P < .001$), and were more likely to have received IV tPA (189/311 versus 148/355, 61% versus 42%; $P < .001$) (Table 1). There were fewer women in the CVO+ group than the CVO- group (145/315 versus 209/363, 46% versus 58%; $P = .003$).

Imaging Characteristics

The median baseline ischemic core volume in the CVO+ group was significantly smaller than in the CVO- group (5 versus 18 mL; $P < .001$). The final

infarct volume at 48–72 hours in the CVO+ group was also significantly smaller than in the CVO- group (12.4 versus 54.3 mL; $P < .001$). Concordantly, ischemic core volume growth occurred to a significantly less extent in the CVO+ group (+5.9 versus +32.1 mL; $P < .001$) (Table 2).

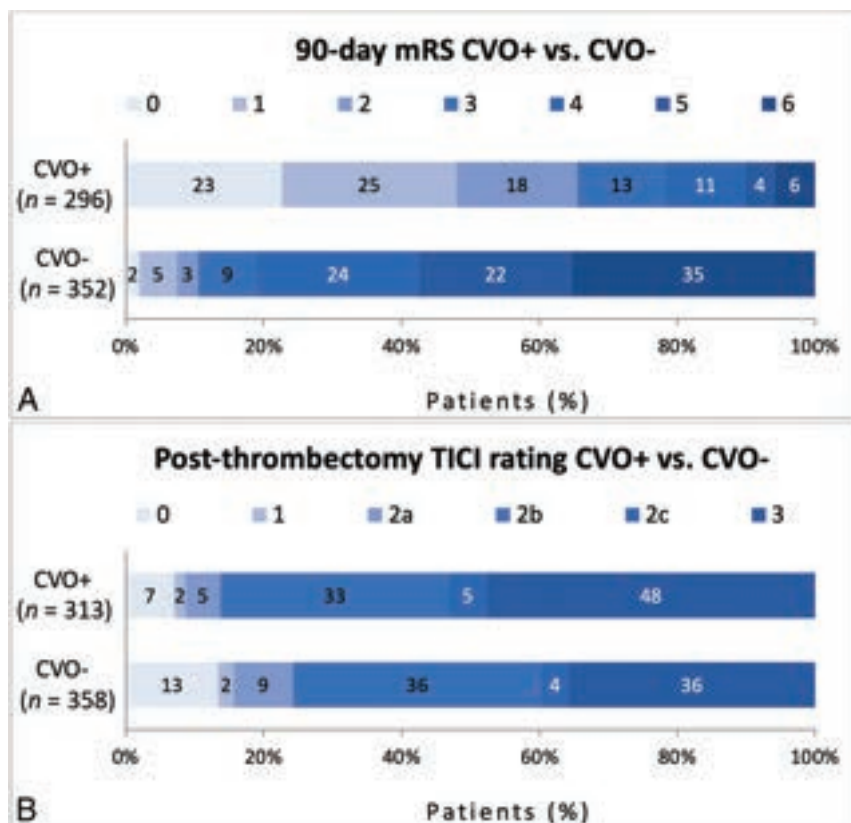
Cortical and Deep VO Associated with Functional Outcomes

A total of 648 patients presented for 90-day follow-up and had recorded mRS scores. The Kendall τ for the association of COVES with mRS was -0.47 , which indicates a moderate negative correlation. The Kendall τ for the association of the ICV metric with mRS was -0.49 , which denotes a similar relationship. With regard to the combined CVO score, the association with mRS was slightly stronger at -0.53 . The values of τ for COVES and CVO were converted to Pearson r , resulting in -0.67 and -0.74 , respectively. The increase in the association of mRS with CVO compared with COVES was significant at a Z-test statistic of 2.5 by the Fisher test ($P = .006$).

There were 296 patients in the CVO+ group and 352 patients in the CVO- group with recorded mRS scores. There was a

Table 2: Imaging metrics at baseline and follow-up by VO status

	CVO+ (n = 315)	CVO- (n = 363)	P Value
ASPECTS (median) (IQR)	8 (7–10)	7 (6–9)	<.001
Baseline infarct volume (median) (IQR) (n = 309, 359)	5 (0–17.5)	18 (3–48)	<.001
Follow-up infarct volume (median) (IQR) (n = 304, 343)	12.4 (4.8–34.2)	54.3 (22.1–120.3)	<.001
Change in infarct volume (median) (IQR) (n = 298, 340)	+5.9 (–0.4–22.1)	+32.1 (4.1–82.7)	<.001

**FIG 3.** mRS score (A) and TICI score (B) distribution of patients with CVO+ versus CVO-. Within each mRS or TICI score category, the percentage of patients with that score is noted.

significantly different distribution of mRS scores in the CVO+ group compared with the CVO- group ($P < .001$), with a greater proportion of favorable mRS scores observed in the CVO+ group. Concordantly, there were significantly higher rates of functional independence (mRS 0–2; 194/296 versus 37/352, 66% versus 11%; $P < .001$) and excellent functional outcome (mRS 0–1; 142/296 versus 26/352, 48% versus 7%; $P < .001$) in patients with CVO+ compared with those with CVO-. The mRS score distribution in patients with CVO+ versus those with CVO- is shown in Fig 3A. Level-by-level data may be found in the Online Supplemental Data.

Cortical and Deep VO Associated with Angiographic Success

The TICI was scored on a total of 671 patients after thrombectomy. There were 313 patients in the CVO+ group and 358 patients in the CVO- group. There were significantly higher rates

of successful reperfusion (TICI $\geq 2b$; 270/313 versus 271/358, 86% versus 76%; $P = .001$) and excellent reperfusion (TICI 2c/3; 166/313 versus 142/358, 53% versus 40%; $P < .001$) in patients with CVO+ compared with those with CVO-. The TICI score distribution in patients with CVO+ versus those with CVO- is shown in Fig 3B. Level-by-level data may be found in the Online Supplemental Data.

DISCUSSION

In this study, we describe a new comprehensive venous outflow score (CVO) for the assessment of venous outflow in patients with anterior circulation AIS-LVO. We found that CVO was strongly associated with functional outcomes to a significantly greater degree than the superficial cortical venous outflow (COVES) scale, and patients with favorable CVO (CVO+) were more likely to achieve functional independence and excellent functional outcome by 90-day follow-up compared with those with unfavorable CVO (CVO-).

Recently, the importance of considering collateral blood flow as a more complete cascade of blood flow^{15,16} or as a collaterome unit^{7,9} rather than as a dichotomous assessment of pial arteries has been appreciated. For example, the cerebral collateral cascade provides a complete assessment of collateral blood flow through the pial arteries, tissue-level collaterals, and VO. Each of these 3 components of collateral blood flow may be assessed through specific imaging parameters to determine the overall

robustness of collateral blood flow through ischemic brain tissue. Work on the cerebral collateral cascade ultimately showed that patients with a favorable metric in at least one of these components had significantly better functional outcomes than patients with a comprehensively unfavorable cerebral collateral cascade. However, these prior studies have not considered a more comprehensive assessment of VO from the anterior circulation that includes both deep venous and superficial cortical venous egress from this vascular territory.

Our finding that CVO+ has such a strong correlation with favorable functional outcomes further underscores VO as an important measure of collateral blood flow in patients with AIS-LVO. The association of CVO+ with favorable functional outcomes was stronger than that of superficial venous outflow (COVES) alone.^{6,10,13,18} These results parallel the evolution in thinking about collateral blood flow through the ischemic brain

more comprehensively, and the robustness of the correlation with CVO and outcome suggests that VO may be the most important component of collateral blood flow. Validation of these findings with prospective studies is warranted.

We also found that patients with CVO+ were significantly more likely to achieve successful (TICI 2b/2c/3) and excellent reperfusion (TICI 2c/3) after thrombectomy. This association of CVO with reperfusion success is a major finding because several prior studies have failed to demonstrate reperfusion differences between patients with favorable-versus-unfavorable collateral scores. Work on Endovascular Therapy Following Imaging Evaluation for Ischemic Stroke (DEFUSE 3) showed that good pial arterial collaterals alone were not predictive of reperfusion success or functional outcomes in patients with AIS.²⁵ The Tan score on pial arterial collaterals and the American Society of Interventional and Therapeutic Neuroradiology/Society of Interventional Radiology (ASITN/SIR) score of collaterals on DSA similarly were not able to distinguish reperfusion differences.^{26,27} Favorable cortical VO, however, has been independently associated with excellent vessel reperfusion after thrombectomy, regardless of arterial collateral status. Venous biomarkers of CBF may indeed be more sensitive for the assessment of tissue perfusion and collateral robustness because they reflect blood flow after ischemic tissue has been permeated.⁶ Our CVO scale increases the robustness of venous profile evaluation and contributes further to this association.

We also found baseline ischemic core volume, final infarct volume, and change in the infarct volume to be significantly lower in patients with CVO+. Although favorable cortical VO has already been associated with slower progression of infarct edema and lower rates of reperfusion hemorrhage, there is key information missing in cortical VO scoring.^{12,14} Cerebral tissue drained predominantly by deep veins, such as the striatocapsular region, often has a dearth of collateral supply and may be more susceptible to edema and reperfusion hemorrhage after mechanical thrombectomy. Robust deep venous outflow through the ICVs may, thus, play a key role in limiting infarct edema, decreasing the risk of reperfusion hemorrhage, and ultimately minimizing the evolution of the ischemic core in patients with stroke affecting those regions.^{19,20} Deep VO may, thus in part, explain the significantly better functional status of patients with favorable CVO at 90-day follow-up.

An additional interesting finding must be noted; patients with favorable and unfavorable CVO had similar rates of technical success of 50%–95% vessel reperfusion. The uncoupling of reperfusion success with functional outcomes at 90 days in this group comparison suggests the potential futility of sub-100% reperfusion in patients with poor CVO. This result warrants additional study because CVO may prove crucial in defining a population of high interest for neuroprotective trials.

Several limitations of our study must be noted. The retrospective design inherently introduces bias and may not be optimal at determining thresholds on scoring systems such as COVES or CVO.²⁸ Future prospective studies evaluating cortical and deep VO may be important in testing the thresholds we have discussed in this article. There may also be confounding variables that were not accounted for in the initial data collection, such as prior

carotid stenosis and endarterectomy, characteristics of atrial fibrillation in patients with this condition, prior history of venous thrombosis, or a history of cerebral endovascular or open procedures. This limitation cannot be corrected in a retrospective analysis of this nature. The imaging protocols at 2 separate comprehensive stroke centers were standardized, but given the variability of venous opacification with subtle changes in the timing of the contrast injection, this limitation must also be noted. Finally, single-phase CTA was used in this study, which may limit the evaluation of the entire venous phase. A recent study evaluated ICV opacification at different phases to stratify the degree of venous outflow, and this would be a valuable addition to our scoring system with the availability of multiphase imaging in future studies.²⁹

Considering the findings of our study and the poor collaterals of deep venous outflow regions, future work focusing on deep VO alone as a predictor of safety and functional outcomes would be valuable. Patients with reperfusion success but unfavorable VO should also be stratified further to determine what may, nonetheless, predict a good functional outcome at 90 days.

CONCLUSIONS

The addition of deep VO scoring to the COVES resulted in the new CVO score, which demonstrated a significantly greater association with functional outcomes at 90 days than COVES alone. Patients with favorable CVO had significantly higher rates of long-term functional independence and excellent reperfusion and significantly less baseline ischemic core burden and evolution by 48–72 hours. Our findings suggest that CVO is the most predictive marker of collateral blood flow and patient success after mechanical thrombectomy to date. Future work should study the uncoupling of reperfusion success with functional outcomes in patients with poor VO and evaluate deep VO by itself as a predictor of functional and reperfusion outcomes in patients with AIS.

Disclosure forms provided by the authors are available with the full text and PDF of this article at www.ajnr.org.

REFERENCES

1. Bang OY, Saver JL, Buck BH, et al; UCLA Collateral Investigators. **Impact of collateral flow on tissue fate in acute ischaemic stroke.** *J Neurol Neurosurg Psychiatry* 2008;79:625–29 CrossRef Medline
2. Bang OY, Saver JL, Kim SJ, et al. **Collateral flow predicts response to endovascular therapy for acute ischemic stroke.** *Stroke* 2011;42:693–99 CrossRef Medline
3. Bang OY, Goyal M, Liebeskind DS. **Collateral circulation in ischemic stroke.** *Stroke* 2015;46:3302–09 CrossRef Medline
4. Iwasawa E, Ichijo M, Ishibashi S, et al. **Acute development of collateral circulation and therapeutic prospects in ischemic stroke.** *Neural Regen Res* 2016;11:368–71 CrossRef Medline
5. Marks MP, Lansberg MG, Mlynash M, et al; Diffusion and Perfusion Imaging Evaluation for Understanding Stroke Evolution 2 Investigators. **Effect of collateral blood flow on patients undergoing endovascular therapy for acute ischemic stroke.** *Stroke* 2014;45:1035–39 CrossRef Medline
6. Faizy TD, Kabiri R, Christensen S, et al. **Association of venous outflow profiles and successful vessel reperfusion after thrombectomy.** *Neurology* 2021 May 5. [Epub ahead of print] CrossRef Medline
7. Liebeskind DS. **Mapping the collaterome for precision cerebrovascular health: theranostics in the continuum of stroke and dementia.** *J Cereb Blood Flow Metab* 2018;38:1449–60 CrossRef Medline

8. Liu L, Ding J, Leng X, et al. **Guidelines for evaluation and management of cerebral collateral circulation in ischaemic stroke 2017.** *Stroke Vasc Neurol* 2018;3:117–30 CrossRef Medline
9. Liebeskind DS. **Imaging the collaterome: a stroke renaissance.** *Curr Opin Neurol* 2015;28:1–3 CrossRef Medline
10. Hoffman H, Ziechmann R, Swarnkar A, et al. **Cortical vein opacification for risk stratification in anterior circulation endovascular thrombectomy.** *J Stroke Cerebrovasc Dis* 2019;28:1710–17 CrossRef Medline
11. Bhaskar S, Bivard A, Parsons M, et al. **Delay of late-venous phase cortical vein filling in acute ischemic stroke patients: associations with collateral status.** *J Cereb Blood Flow Metab* 2017;37:671–82 CrossRef Medline
12. Winkelmeier L, Heit JJ, Adusumilli G, et al. **Poor venous outflow profiles increase the risk of reperfusion hemorrhage after endovascular treatment.** *J Cereb Blood Flow Metab* 2023;43:72–83 CrossRef Medline
13. Faizy TD, Kabiri R, Christensen S, et al. **Favorable venous outflow profiles correlate with favorable tissue-level collaterals and clinical outcome.** *Stroke* 2021;52:1761–67 CrossRef Medline
14. Faizy TD, Kabiri R, Christensen S, et al. **Venous outflow profiles are linked to cerebral edema formation at noncontrast head CT after treatment in acute ischemic stroke regardless of collateral vessel status at CT angiography.** *Radiology* 2021;299:682–90 CrossRef Medline
15. Faizy TD, Mlynash M, Kabiri R, et al. **The cerebral collateral cascade: comprehensive blood flow in ischemic stroke.** *Neurology* 2022 April 28. [Epub ahead of print] CrossRef Medline
16. Faizy TD, Heit JJ. **Rethinking the collateral vasculature assessment in acute ischemic stroke: the comprehensive collateral cascade.** *Top Magn Reson Imaging* 2021;30:181–86 CrossRef Medline
17. Broocks G, Kemmling A, Faizy T, et al. **Effect of thrombectomy on oedema progression and clinical outcome in patients with a poor collateral profile.** *Stroke Vasc Neurol* 2021;6:222–29 CrossRef Medline
18. Jansen IGH, van Vuuren AB, van Zwam WH, et al; MR CLEAN Trial Investigators. **Absence of cortical vein opacification is associated with lack of intra-arterial therapy benefit in stroke.** *Radiology* 2018;286:731 CrossRef Medline
19. Shukir Muhammed Amin O, Aziz Abdullah A, Xaznadar A, et al. **Striatocapsular infarction; a single institutional experience.** *Acta Inform Med* 2012;20:106–12 CrossRef Medline
20. Amin OS, Zangana HM, Ameen NA. **The striatocapsular infarction and its aftermaths.** *BMJ Case Rep* 2010;2010:bcr0220102703 CrossRef Medline
21. Yu Y, Han Q, Ding X, et al. **Defining core and penumbra in ischemic stroke: a voxel- and volume-based analysis of whole brain CT perfusion.** *Sci Rep* 2016;6:20932 CrossRef Medline
22. Fugate JE, Klunder AM, Kallmes DF. **What is meant by “TICI”?** *AJNR Am J Neuroradiol* 2013;34:1792–97 CrossRef Medline
23. Goyal M, Fargen KM, Turk AS, et al. **2C or not 2C: defining an improved revascularization grading scale and the need for standardization of angiography outcomes in stroke trials.** *J Neurointerv Surg* 2014;6:83–86 CrossRef Medline
24. Banks JL, Marotta CA. **Outcomes validity and reliability of the modified Rankin scale: implications for stroke clinical trials: a literature review and synthesis.** *Stroke* 2007;38:1091–96 CrossRef Medline
25. de Havenon A, Mlynash M, Kim-Tenser MA, et al; DEFUSE 3 Investigators. **Results from DEFUSE 3: good collaterals are associated with reduced ischemic core growth but not neurologic outcome.** *Stroke* 2019;50:632–38 CrossRef Medline
26. Baydemir R, Aykaç Ö, Acar BA, et al. **Role of modified TAN score in predicting prognosis in patients with acute ischemic stroke undergoing endovascular therapy.** *Clin Neurol Neurosurg* 2021;210:106978 CrossRef Medline
27. Guenego A, Fahed R, Albers GW, et al. **Hypoperfusion intensity ratio correlates with angiographic collaterals in acute ischaemic stroke with M1 occlusion.** *Eur J Neurol* 2020;27:864–70 CrossRef Medline
28. Norvell DC. **Study types and bias: don’t judge a study by the abstract’s conclusion alone.** *Evid Based Spine Care J* 2010;1:7–10 CrossRef Medline
29. Myint MZ, Yeo LL, Tan BY, et al. **Internal cerebral vein asymmetry is an independent predictor of poor functional outcome in endovascular thrombectomy.** *J Neurointerv Surg* 2022;14:683–87 CrossRef Medline

Femoral Access-Site Complications with Tenecteplase versus Alteplase before Mechanical Thrombectomy for Large-Vessel-Occlusion Stroke

P. Hendrix, M.K. Collins, O. Goren, G.M. Weiner, S.S. Dalal, I. Melamed, M.J. Kole, C.J. Griessenauer, A. Noto, and C.M. Schirmer

ABSTRACT

BACKGROUND AND PURPOSE: IV thrombolysis with alteplase before mechanical thrombectomy for emergent large-vessel-occlusion stroke is associated with access-site bleeding complications. However, the incidence of femoral access-site complications with tenecteplase before mechanical thrombectomy requires exploration. Here, femoral access-site complications with tenecteplase versus alteplase before mechanical thrombectomy for large-vessel-occlusion stroke were compared.

MATERIALS AND METHODS: All patients receiving IV thrombolytics before mechanical thrombectomy for large-vessel-occlusion stroke who presented from January 2020 to August 2022 were reviewed. In May 2021, our health care system switched from alteplase to tenecteplase as the primary thrombolytic for all patients with stroke, facilitating the comparison of alteplase-versus-tenecteplase femoral access-site complication rates. Major (requiring surgery) and minor (managed conservatively) access-site complications were assessed.

RESULTS: One hundred thirty-nine patients underwent transfemoral mechanical thrombectomy for large-vessel-occlusion stroke, of whom 46/139 (33.1%) received tenecteplase and 93/139 (66.9%) received alteplase. In all cases ($n = 139$), an 8F sheath was inserted without sonographic guidance, and vascular closure was obtained with an Angio-Seal. Baseline demographics, concomitant antithrombotic medications, and periprocedural coagulation lab findings were similar between groups. The incidence of conservatively managed groin hematomas (2.2% versus 4.3%), delayed access-site oozing requiring manual compression (6.5% versus 2.2%), and arterial occlusion requiring surgery (2.2% versus 1.1%) was similar between the tenecteplase and alteplase groups, respectively ($P =$ not significant). No dissection, arteriovenous fistula, or retroperitoneal hematoma was observed.

CONCLUSIONS: Tenecteplase compared with alteplase before mechanical thrombectomy for large-vessel-occlusion stroke is not associated with an alteration in femoral access-site complication rates.

ABBREVIATIONS: AIS = acute ischemic stroke; CSC = comprehensive stroke center; INR = international normalized ratio; LVO = large-vessel-occlusion; MT = mechanical thrombectomy; PT = prothrombin time; TPA = alteplase; TNK = tenecteplase

Transfemoral access is the predominant route for mechanical thrombectomy (MT) of large-vessel-occlusion (LVO) acute ischemic stroke (AIS).¹ Access-site complications are potentially underreported in the literature due to a lack of rigorous clinical assessment and charting.^{2,3} A set of prospective LVO MT landmark trials, with mostly (68%–73%)^{4,5} or exclusively (100%)^{6–9}

concomitant alteplase (TPA) administration, provided access-site complication rates in the endovascular treatment arm. A pooled incidence of 1.7% (range, 1.2%–2.9%)^{4,6,7} for severe and 7.0% (range, 3.0%–11.7%)^{2,4,5,8,9} for overall femoral access-site complications provides a framework for TPA-associated access-site complications in LVO MT. More recent trials investigating the safety and efficacy of MT with IV thrombolysis versus MT alone also reported femoral access-site complications. Femoral hematomas^{10–13} and pseudoaneurysms^{10–12} were observed in 0.3%–7.9% and 1.2%–4.4% of the MT with TPA groups compared with 0.7%–4.2% and 0.5%–1.1% of the MT-alone groups, respectively.

The third-generation thrombolytic tenecteplase (TNK) is a bioengineered variant of TPA. It overcomes some of the major shortcomings of TPA, resulting in a decreased plasma clearance, higher fibrin specificity, and improved resistance against plasminogen

Received January 19, 2023; accepted after revision April 10.

From the Departments of Neurosurgery (P.H., O.G., S.S.D., M.J.K., C.M.S.) and Neurology (A.N.), Geisinger Medical Center, Danville, Pennsylvania; Department of Neurosurgery (P.H., G.M.W., I.M., C.M.S.), Geisinger Wyoming Valley Medical Center, Wilkes-Barre, Pennsylvania; Department of Neurosurgery (P.H.), Saarland University Medical Center, Homburg, Germany; Geisinger Commonwealth School of Medicine (M.K.C.), Scranton, Pennsylvania; and Department of Neurosurgery (C.J.G.), Christian Doppler Klinik, Paracelsus Medical University, Salzburg, Austria.

Please address correspondence to Philipp Hendrix, MD, PhD, Department of Neurosurgery, Geisinger Medical Center, 100 N Academy Ave, Danville, PA 17822; e-mail: Hendrix.philipp@gmail.com; @PhilippHendrix

<https://dx.doi.org/10.3174/ajnr.A7862>

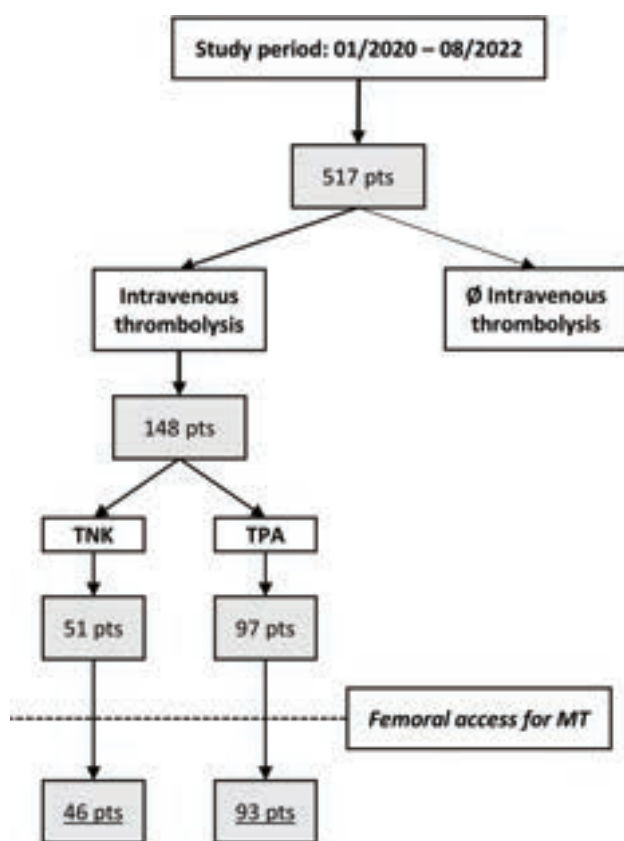


FIGURE. Patient flowchart. “Pts” indicates patients.

activator inhibitor 1.^{14,15} Recently, TNK has received increasing attention as a thrombolytic medication in AIS treatment.^{16–24} On the basis of the mounting evidence and advantages of TNK over TPA, our health care system underwent a system-wide transition of thrombolytic medication from TPA to TNK. Recently, we reported our first-year experience with TNK compared with TPA.²⁵ Compatible with the trial findings of Tenecteplase Versus Alteplase Before Endovascular Therapy for Ischemic Stroke (EXTEND-IA TNK), significantly higher spontaneous recanalization rates with TNK versus TPA in patients with LVO AIS (about 20% versus 10%) were observed.²⁶ Despite similar overall safety profiles (intracranial hemorrhage and mortality), the impact of TNK use on extra- and intracranial hemorrhagic complications in LVO AIS is yet to be explored. Here, we seek to compare the incidence of and analyze risk factors for access-site-related complications with TNK versus TPA before MT for LVO stroke.

MATERIALS AND METHODS

Consecutive patients with LVO AIS admitted to 2 North American comprehensive stroke centers (Geisinger Medical Center, and Geisinger Wyoming Valley Medical Center), part of the same health care system, were reviewed following local institutional review board approval (No. 2022–0571). Patient consent was waived for the retrospective analysis. All patients presenting between January 2020 and August 2022 who had received IV thrombolysis before MT were assessed in the analysis (Figure). In May 2021, our health care system switched from TPA to TNK as the primary thrombolytic for all patients with

AIS, facilitating a comparison of TPA-versus-TNK femoral access complication rates.

Technical Details on Femoral Access

In the hybrid operating room, femoral access was obtained via a 21-ga micropuncture or an 18-ga access needle at the physician’s discretion to insert an 8F short sheath. Sonography was used at the physician’s discretion in all upper extremity accesses (usually radial) but only in selected cases for femoral access. In this cohort, all femoral accesses were obtained without sonography. No patients underwent sonographically guided femoral access in the study period, and none were, therefore, excluded. Vascular closure for 8F sheath access is routinely performed with Angio-Seal (Terumo Medical), following a typical femoral artery angiogram to assess the sheath placement. An Angio-Seal was used in all cases.

Each patient had received IV thrombolytic medication according to current guidelines, which included platelets, $>100,000/\text{mm}^3$, international normalized ratios (INRs), ≤ 1.7 , prothrombin times (PTs), ≤ 15 , and activated partial thromboplastin times, ≤ 40 . IV thrombolysis with TPA (0.9 mg/kg) and TNK (0.25 mg/kg) was administered according to contemporary guidelines. Eligible patients received TPA or TNK either at an outside facility with secondary transfer to the CSC for MT or in the emergency department of the CSC before transfer to the hybrid angio suite. At both CSCs, bridging thrombolysis was performed in each patient eligible for IV thrombolysis. Concomitant antithrombotic medication such as aspirin, clopidogrel, and warfarin (Coumadin), as well as their combinations, did not abrogate the decision to administer IV thrombolysis if coagulation profiles were in range. Following MT and with achievement of access-site hemostasis, patients were transferred to the intensive care unit. To assess potential lasting disruptions of the coagulation system due to the IV thrombolysis, we assessed INRs, PTs, and activated partial thromboplastin times in all patients. For the presented analysis, we considered labs drawn <8 hours since groin access to approximate coagulation profiles <12 hours since IV thrombolysis administration. However, labs were only available in a subset of patients because the timing of additional laboratory panels, including coagulation profiles after MT, was based on the discretion of the on-call critical care team.

Access-Site Complication Types

Minor access-site complications comprised the following: all conservatively managed groin hematomas, conservatively managed pseudoaneurysms, and delayed access-site oozing. Delayed oozing was defined as minor bleeding starting in the post-MT phase in the intensive care unit requiring additional manual compression to achieve hemostasis. Groin hematomas were diagnosed by bedside physical examination. Any bleeding complication was assessed as a composite variable of groin hematomas and delayed oozing.

Major access-site complications were defined as groin hematomas requiring transfusion, pseudoaneurysms requiring thrombin injection or surgical repair, dissections, arterial occlusions, and arteriovenous fistulas. Sonography in conjunction with additional contrast-enhanced CT was performed if indicated. Vascular surgery was consulted in all cases of suspected and diagnosed major access-site complications. Any groin complication was assessed as a composite variable of any minor or major access-site complication.

Table 1: Femoral access-site complications

	TNK (n = 46)	TPA (n = 93)	P Value
Baseline			
Age (IQR)	73 (64–79)	74 (62–83)	.62
Female	24 (52.2%)	44 (64.7%)	.59
Risk factors			
Arterial hypertension ^a	39 (84.8%)	64 (69.6%)	.05
Type 2 diabetes ^a	11 (23.9%)	19 (20.7%)	.66
Dyslipidemia ^a	29 (63.0%)	49 (53.3%)	.27
Coronary artery disease ^a	10 (21.7%)	22 (23.9%)	.78
Atrial fibrillation ^a	13 (28.3%)	38 (41.3%)	.14
Chronic kidney disease ^a	8 (17.4%)	13 (14.1%)	.62
Ischemic stroke ^b	9 (19.6%)	22 (23.7%)	.59
Smoking (ever) ^c	26 (56.5%)	40 (44.0%)	.16
Primary presentation at CSC	26 (56.5%)	29 (31.2%)	.004
LKW to IV thrombolytic (IQR)	109 (90–149)	119 (91–172)	.28
IV thrombolytic to groin puncture (IQR)	74 (48–109)	91 (66–136)	.07
Antithrombotics	23 (50.0%)	45 (48.4%)	.86
Aspirin	18 (39.1%)	31 (33.3%)	
Aspirin and Clopidogrel	3 (6.5%)	5 (5.4%)	
Clopidogrel	0 (0.0%)	1 (1.1%)	
Coumadin	1 (2.2%)	4 (4.3%)	
Aspirin and Coumadin	0 (0.0%)	1 (1.1%)	
Clopidogrel and Coumadin	1 (2.2%)	3 (3.2%)	
Periprocedural			
8F femoral sheath	46 (100.0%)	93 (100.0%)	NA
Sonographically guided access	0 (0.0%)	0 (0.0%)	NA
Angio-Seal closure device	46 (100.0%)	93 (100.0%)	NA
Coagulation labs < 12h			
INR (IQR) ^d	1.07 (0.99–1.12)	1.18 (1.09–1.31)	.001
PT (IQR) ^e	14 (13–15)	15 (14–16)	.001
aPTT (IQR) ^f	30 (28–31)	29 (28–32)	1.00

Note:—IQR indicates interquartile range; LKW, last known well; aPTT, activated partial thromboplastin times; NA, not available.

^aData missing in 1 TPA.

^bData missing in 3 TPAs.

^cData missing in 5 TPAs.

^dData available in 22 and 45 patients with TNK and TPA, respectively.

^eData available in 22 and 46 patients with TNK and TPA, respectively.

^fData available in 18 and 29 patients with TNK and TPA, respectively.

Table 2: Femoral access-site complications

Access-Site Complications	TNK (n = 46)	TPA (n = 93)	P Value
Minor			
Groin hematoma	1 (2.2%)	4 (4.3%)	1.00
Delayed oozing	3 (6.5%)	2 (2.2%)	.33
Pseudoaneurysm (conservative)	0 (0.0%)	1 (1.1%)	1.00
Major			
Arterial occlusion	1 (2.2%)	1 (1.1%)	

Statistical Analysis

The χ^2 , Fisher exact, and Mann-Whitney *U* tests were performed to compare TNK groups with TPA groups, with $P < .05$ considered statistically significant. SPSS, Version 25 (IBM), was used to analyze the data.

RESULTS

A total of 148 patients (TNK $n = 51$, TPA $n = 97$) were identified. Seven patients experienced rapid neurologic recovery averting emergent MT and thus femoral access. In addition, 2 patients underwent upper extremity access (radial \times 1, brachial \times 1) due to previous femoral artery operations. Finally, 139 patients

underwent transfemoral access for LVO MT and were thus included in the analysis (Table 1). If one contrasted TNK ($n = 46$) and TPA ($n = 93$) cases, age, sex, and cardiovascular risk factors except for arterial hypertension were similar between groups. Arterial hypertension was numerically more frequent in the TNK group (84.8%) compared with the TPA group (69.6%) ($P = .05$). Significantly more patients primarily presented to the CSC in the TNK group compared with the TPA group ($P = .004$). Last known well to IV thrombolysis and IV thrombolysis to groin puncture times were similar in both groups ($P = .28$ and $P = .07$, respectively). The overall rate of concomitant antithrombotic medication was 50% in the TNK and 48.4% in the TPA group ($P = .86$).

Coagulation labs within 12 hours of IV thrombolysis were available in a subset of patients (Table 1). The median INR and PT were higher in the TPA subgroups compared with TNK subgroups, compatible with 8/93 (8.6%) patients receiving TPA and 2/46 (4.3%) receiving TNK who had been on Coumadin on admission.

Femoral Access-Site Complications

Nonmajor groin hematomas were observed in 1/46 (2.2%) patients on TNK and 4/93 (4.3%) on TPA ($P =$

1.0) (Table 2). None of these hematomas caused a relevant hemoglobin drop, required transfusion, required surgery or intervention or a prolonged stay, or affected the clinical outcome. In 3/46 (6.5%) and 2/93 (2.2%) TNK and TPA cases, respectively, delayed access-site oozing occurred, hence, requiring additional manual compression at the bedside with subsequent hemostasis in all cases ($P = .33$). A pseudoaneurysm was identified in 1 patient with TPA who also presented with a groin hematoma (1/93, 1.1%). Conservative management was sufficient to treat the pseudoaneurysm. Among the major groin complications, an acute lower extremity ischemia due to arterial occlusion at the access-site occurred in 1/46 (2.2%) patients receiving TNK and 1/93 (1.1%) receiving TPA ($P = 1.0$). Both cases required emergent vascular surgery. If one contrasted the TNK-versus-TPA groups, the occurrence of any groin complication ($P = .53$) and any groin bleeding (0.73) was similar. No dissection, arteriovenous fistula, or retroperitoneal hematoma was observed.

A trend was observed for the associations of coronary artery disease with any groin bleeding complication ($P = .05$) and chronic kidney disease with any groin complication ($P = .09$). Additional analysis demonstrated no significant associations.

DISCUSSION

TNK use for AIS is rapidly increasing in the United States, yet it remains to be determined how it will affect the thrombectomy landscape of emergent LVO. This US 2-center study compares rates of femoral access-site complications with TNK versus TPA before MT. Notably, about half of the TNK and TPA cohorts had concomitant antithrombotic medication. The overall incidence of access-site complications was low, and no significant differences were observed between the TNK and TPA groups.

Thrombolytic medication is the cornerstone of AIS treatment in the 4.5-hour time window. Currently, TNK is only approved for acute ST-elevation myocardial infarction. However, recent studies point to TNK being a noninferior alternative to TPA in AIS treatment.¹⁶⁻²⁴ Genetic modifications at 3 sites of the TPA molecule facilitate decreased clearance of TNK, higher fibrin specificity, and improved resistance against plasminogen activator inhibitor 1. Clinically, these features translate into a longer half-life of TNK paired with improved thrombolytic potency without the additional disruption of the coagulation cascade or bleeding complications.^{14,15} The ideal clot-dissolving agent preferentially acts on solid-phase fibrin bound by plasminogen. Eventually, the thrombolytic medication initiates fibrinolysis by activating plasminogen to plasmin. However, uncontrolled and excessive systemic lysis activates fluid-phase plasminogen, which eventually consumes fibrinogen, plasminogen, and α 2-antiplasmin.¹⁴ Huang et al¹⁵ have demonstrated that TPA more than TNK affects coagulation, especially fibrinolytic cascades. In the present study, a subset of patients had coagulation labs within 12 hours of thrombolysis. We did not identify clinically relevant alterations or differences in coagulation lab findings in either group.

Unless rigorously followed, nonmajor access-site complications such as conservatively managed groin hematomas are likely underrecognized, reflected by only some studies containing detailed information. In the Multicenter Randomized Clinical Trial of Endovascular Treatment for Acute Ischemic Stroke in the Netherlands (MR CLEAN)-NO IV trial, 252/266 patients in the MT with TPA group eventually underwent femoral puncture. The authors reported groin hematomas in 20 patients (7.9%). In the MT alone group, 261/273 patients underwent femoral puncture, and groin hematomas were nonsignificantly lower (11/261; 4.2%).¹² Catapano et al²⁷ reported, in a recent retrospective study on patients receiving TPA undergoing MT, that groin hematomas after transfemoral access were observed in only 1.4% (4/293) of patients. Concomitant use of antithrombotic medication was not addressed. In the present study, half of the patients in both the TNK and TPA cohorts were on antithrombotics before admission. The groin hematoma rates were 2.2% and 4.3% in the TNK and TPA groups, respectively, thus in agreement with the literature. Delayed oozing from the access-site is a known clinical issue not yet dedicatedly reported in the stroke literature. The herein observed rates were low and similar to those observed in cardiology.²⁸ Nevertheless, in the TNK group, delayed oozing was 3 times more frequent than in the TPA group (6.5% versus 2.2%). Whether this finding is related to not enough manual compression after closure device deployment, or disruption of the fibrinolytic cascade cannot be explained with this study.

In the EXTEND-IA TNK study, groin hematomas were observed in 3/101 (3%) in the TPA before MT group and in 1/101 (1%) in the TNK before MT group. One patient in the TPA before MT group (1/101, 1%) had a pseudoaneurysm.²⁶ Pseudoaneurysms in the TPA before MT groups compared with the MT-alone groups in the MR CLEAN-NO IV, Solitaire with the intention for thrombectomy plus IV t-PA versus direct Solitaire stent-retriever thrombectomy in acute anterior circulation stroke (SWIFT DIRECT), and Direct Endovascular Thrombectomy vs Combined IVT and Endovascular Thrombectomy for Patients With Acute Large Vessel Occlusion in the Anterior Circulation (DEVT) trials were observed in 1.2% versus 1.1%, 2.4% versus 0.5%, and 4.4% versus 0.9%, respectively.¹⁰⁻¹² In the present study, 1 patient receiving TPA (1/93, 1.1%) with a groin hematoma was also found to have a small pseudoaneurysm that did not require any intervention and, thus, was considered minor. In summary, reported minor femoral access-site complication rates varied among studies, but differences between TPA and TNK were not apparent.

Major (serious) access-site complications are commonly defined as events causing a relevant hemoglobin drop, requiring blood transfusion, surgery, or an intervention; a prolonged stay; or death. In the prospective stroke trials Endovascular Treatment for Small Core and Anterior Circulation Proximal Occlusion with Emphasis on Minimizing CT to Recanalization Times (ESCAPE), EXTEND-IA, and Mechanical Thrombectomy After Intravenous Alteplase Versus Alteplase Alone After Stroke (THRACE), the serious access-site complication rates were 1.2%, 2.9%, and 2.1% in the endovascular treatment arm, respectively.^{4,6,7} In the Direct Intraarterial Thrombectomy in Order to Revascularize Acute Ischemic Stroke Patients with Large Vessel Occlusion Efficiently in Chinese Tertiary Hospitals: a Multicenter Randomized Clinical Trial (DIRECT MT) trial, major femoral bleeding was encountered in 1/312 (0.3%) patients in the MT with TPA group and in 2/299 (0.7%) in the MT without TPA group.¹³ Gerschenfeld et al²⁹ analyzed a cohort of 588 patients with emergent LVO who received TNK. Major systemic bleeding from the groin puncture was reported in 1 patient. In EXTEND-IA TNK, 1 patient in the TNK before the MT group developed leg ischemia requiring an intervention for femoral artery occlusion.²⁶ In the present study, 1 patient in the TNK (2.2%) and 1 patient in the TPA (1.1%) cohort experienced arterial occlusion and required emergent open vascular surgery. IV thrombolysis per se does not represent a risk factor for arterial occlusion. However, in the acute setting, the threshold to not place a closure device after insertion of an 8F sheath into the femoral artery is likely high, especially when considering that the patient received IV thrombolysis and is on concomitant antithrombotic medication.

Catapano et al²⁷ observed the occurrence of retroperitoneal hematomas in 1.7% of transfemoral cases. Although not observed in the present study, retroperitoneal hematomas have been associated with common femoral artery punctures that are too high and represent a significant risk factor of femoral access-site-related morbidity and mortality.³⁰ While closure devices appear to reduce the risk of pseudoaneurysm after femoral access, they do not appear to mitigate the risk of retroperitoneal hematomas.^{30,31} A shift toward other access sites, such as radial access, may prove beneficial.^{27,32} While radial access has gained significant

attention for cerebral angiography and elective neurointervention, its adoption in emergent stroke care is not as uniformly present in the literature.^{1,33}

Despite the high rate of concomitant antithrombotics in the present study, the overall femoral access-site complication rate was low and similar between the IV thrombolytics TNK and TPA. If TNK continues to prove valuable in stroke treatment, it might replace TPA due to lower cost, ease of administration, and clinical noninferiority. Hence, the data herein provide a framework for the safety of TNK compared with the current standard TPA regarding femoral access-site-related complications surrounding MT for emergent LVO stroke.

Strengths and Limitations

The study is among the first to report real-world data on femoral access-site complication rates with TNK compared with TPA from a recent treatment period in the United States. The femoral accesses analyzed here are homogeneous because, in all cases, sonography use was waived, an 8F sheath was inserted, and the arteriotomy was closed with the same vascular closure device (8F Angio-Seal). The study is predominantly limited by its non-randomized, retrospective character; small sample size; and low event number. Adjustments for potential confounders were considered. Additional, larger, multicenter studies are required to further explore and compare the safety of TNK and TPA before transfemoral MT.

CONCLUSIONS

Despite the high rate of concomitant antithrombotics in the present study, the overall femoral access-site complication rate was low and similar between the IV thrombolytic TNK and TPA.

Disclosure forms provided by the authors are available with the full text and PDF of this article at www.ajnr.org.

REFERENCES

- Siddiqui AH, Waqas M, Neumaier J, et al. **Radial first or patient first: a case series and meta-analysis of transradial versus transfemoral access for acute ischemic stroke intervention.** *J Neurointerv Surg* 2021;13:687–92 CrossRef Medline
- Oneissi M, Sweid A, Tjoumakaris S. **Access-site complications in transfemoral neuroendovascular procedures: a systematic review of incidence rates and management strategies.** *Oper Neurosurg (Hagerstown)* 2020;19:353–63 CrossRef Medline
- Shapiro SZ, Sabacinski KA, Mantripragada K, et al. **Access-site complications in mechanical thrombectomy for acute ischemic stroke: a review of prospective trials.** *AJNR Am J Neuroradiol* 2020;41:477–81 CrossRef Medline
- Goyal M, Demchuk AM, Menon BK, et al; ESCAPE Trial Investigators. **Randomized assessment of rapid endovascular treatment of ischemic stroke.** *N Engl J Med* 2015;372:1019–30 CrossRef Medline
- Jovin TG, Chamorro A, Cobo E, et al; REVASCAT Trial Investigators. **Thrombectomy within 8 hours after symptom onset in ischemic stroke.** *N Engl J Med* 2015;372:2296–306 CrossRef Medline
- Campbell BCV, Mitchell PJ, Kleinig TJ, et al; EXTEND-IA Investigators. **Endovascular therapy for ischemic stroke with perfusion-imaging selection.** *N Engl J Med* 2015;372:1009–18 CrossRef Medline
- Bracard S, Ducrocq X, Mas JL, et al; THRACE Investigators. **Mechanical thrombectomy after intravenous alteplase versus alteplase alone after stroke (THRACE): a randomised controlled trial.** *Lancet Neurol* 2016;15:1138–47 CrossRef Medline
- Saver JL, Goyal M, Bonafe A, et al; SWIFT PRIME Investigators. **Stent-retriever thrombectomy after intravenous t-PA vs. t-PA alone in stroke.** *N Engl J Med* 2015;372:2285–95 CrossRef Medline
- Broderick JP, Palesch YY, Demchuk AM, et al; Interventional Management of Stroke (IMS) III Investigators. **Endovascular therapy after intravenous t-PA versus t-PA alone for stroke.** *N Engl J Med* 2013;368:893–903 CrossRef Medline
- Fischer U, Kaesmacher J, Strbian D, et al; SWIFT DIRECT Collaborators. **Thrombectomy alone versus intravenous alteplase plus thrombectomy in patients with stroke: an open-label, blinded-outcome, randomised non-inferiority trial.** *Lancet* 2022;400:104–15 CrossRef Medline
- Zi W, Qiu Z, Li F, et al; DEVT Trial Investigators. **Effect of endovascular treatment alone vs intravenous alteplase plus endovascular treatment on functional independence in patients with acute ischemic stroke: the DEVT randomized clinical trial.** *JAMA* 2021;325:234–43 CrossRef Medline
- LeCouffe NE, Kappelhof M, Treurniet KM, et al; MR CLEAN-NO IV Investigators. **A randomized trial of intravenous alteplase before endovascular treatment for stroke.** *N Engl J Med* 2021;385:1833–44 CrossRef Medline
- Yang P, Zhang Y, Zhang L, et al; DIRECT-MT Investigators. **Endovascular thrombectomy with or without intravenous alteplase in acute stroke.** *N Engl J Med* 2020;382:1981–93 CrossRef Medline
- Tanswell P, Modi N, Combs D, et al. **Pharmacokinetics and pharmacodynamics of tenecteplase in fibrinolytic therapy of acute myocardial infarction.** *Clin Pharmacokinet* 2002;41:1229–45 CrossRef Medline
- Huang X, Moreton FC, Kalladka D, et al. **Coagulation and fibrinolytic activity of tenecteplase and alteplase in acute ischemic stroke.** *Stroke* 2015;46:3543–46 CrossRef Medline
- Tsivgoulis G, Katsanos AH, Christogiannis C, et al. **Intravenous thrombolysis with tenecteplase for the treatment of acute ischemic stroke.** *Ann Neurol* 2022;92:349–57 CrossRef Medline
- Mahawish K, Gommans J, Kleinig T, et al. **Switching to tenecteplase for stroke thrombolysis: real-world experience and outcomes in a regional stroke network.** *Stroke* 2021;52:e590–93 CrossRef Medline
- Zhong CS, Beharry J, Salazar D, et al. **Routine use of tenecteplase for thrombolysis in acute ischemic stroke.** *Stroke* 2021;52:1087–90 CrossRef Medline
- Gerschenfeld G, Liegey JS, Laborne F-X, et al. **Treatment times, functional outcome, and hemorrhage rates after switching to tenecteplase for stroke thrombolysis: insights from the TETRIS registry.** *Eur Stroke J* 2022;7:358–64 CrossRef Medline
- Menon BK, Buck BH, Singh N, et al; AcT Trial Investigators. **Intravenous tenecteplase compared with alteplase for acute ischaemic stroke in Canada (AcT): a pragmatic, multicentre, open-label, registry-linked, randomised, controlled, non-inferiority trial.** *Lancet* 2022;400:161–69 CrossRef Medline
- Li S, Pan Y, Wang Z, et al. **Safety and efficacy of tenecteplase versus alteplase in patients with acute ischaemic stroke (TRACE): a multicentre, randomised, open label, blinded-endpoint (PROBE) controlled phase II study.** *Stroke Vasc Neurol* 2022;7:47–53 CrossRef Medline
- Ma P, Zhang Y, Chang L, et al. **Tenecteplase vs. alteplase for the treatment of patients with acute ischemic stroke: a systematic review and meta-analysis.** *J Neurol* 2022;269:5262–71 CrossRef Medline
- Katsanos AH, Psychogios K, Turc G, et al. **Off-label use of tenecteplase for the treatment of acute ischemic stroke: a systematic review and meta-analysis.** *JAMA Netw Open* 2022;5:e224506 CrossRef Medline
- Yogendrakumar V, Beharry J, Churilov L, et al. **Tenecteplase improves reperfusion across time in large vessel stroke.** *Ann Neurol* 2023;93:489–99 CrossRef Medline
- Hendrix P, Collins MK, Griessenauer CJ, et al. **Tenecteplase versus alteplase before mechanical thrombectomy: experience from a US healthcare system undergoing a system-wide transition of primary thrombolytic.** *J Neurointerv Surg* 2022 Nov 22. [Epub ahead of print] CrossRef Medline

26. Campbell BC, Mitchell PJ, Churilov L, et al; EXTEND-IA TNK Investigators. **Tenecteplase versus alteplase before thrombectomy for ischemic stroke.** *N Engl J Med* 2018;378:1573–82 CrossRef Medline
27. Catapano JS, Rumalla K, Farhadi DS, et al. **Safety and efficacy of radial versus femoral artery access for mechanical thrombectomy procedures following intravenous administration of tissue plasminogen activator.** *Stroke Vasc Interv Neurol* 2022;2:e000238 CrossRef
28. Wu PJ, Dai YT, Kao HL, et al. **Access site complications following transfemoral coronary procedures: comparison between traditional compression and angioseal vascular closure devices for haemostasis.** *BMC Cardiovasc Disord* 2015;15:34 CrossRef Medline
29. Gerschenfeld G, Smadja D, Turc G; et al; TETRIS Study Group. **Functional outcome, recanalization, and hemorrhage rates after large vessel occlusion stroke treated with tenecteplase before thrombectomy.** *Neurology* 2021;97:e2173–84 CrossRef Medline
30. Farouque HM, Tremmel JA, Raissi Shabari F, et al. **Risk factors for the development of retroperitoneal hematoma after percutaneous coronary intervention in the era of glycoprotein IIb/IIIa inhibitors and vascular closure devices.** *J Am Coll Cardiol* 2005;45:363–68 CrossRef Medline
31. Naddaf A, Williams S, Hasanadka R, et al. **Predictors of groin access pseudoaneurysm complication: a 10-year institutional experience.** *Vasc Endovascular Surg* 2020;54:42–46 CrossRef Medline
32. Kwok CS, Kontopantelis E, Kinnaird T, et al. **Retroperitoneal hemorrhage after percutaneous coronary intervention: incidence, determinants, and outcomes as recorded by the British Cardiovascular Intervention Society.** *Circ Cardiovasc Interv* 2018;11:e005866 CrossRef Medline
33. Shaban S, Rastogi A, Phuyal S, et al. **The association of transradial access and transfemoral access with procedural outcomes in acute ischemic stroke patients receiving endovascular thrombectomy: a meta-analysis.** *Clin Neurol Neurosurg* 2022;215:107209 CrossRef Medline

Early-versus-Late Endovascular Stroke Treatment: Similar Frequencies of Nonrevascularization and Postprocedural Cerebrovascular Complications in a Large Single-Center Cohort Study

E. Maslias, S. Nannoni, B. Bartolini, F. Ricciardi, D. Strambo, S.D. Hajdu, F. Puccinelli, A. Eskandari, V. Dunet, P. Maeder, G. Saliou, and P. Michel



ABSTRACT

BACKGROUND AND PURPOSE: Endovascular treatment of acute ischemic stroke is now performed more frequently in the late window in radiologically selected patients. However, little is known about whether the frequency and clinical impact of incomplete recanalization and postprocedural cerebrovascular complications differ between early and late windows in the real world.

MATERIALS AND METHODS: We retrospectively reviewed all patients with acute ischemic stroke receiving endovascular treatment within 24 hours from 2015 to 2019 and included in the Acute STroke Registry and Analysis of Lausanne. We compared rates of incomplete recanalization and postprocedural cerebrovascular complications (parenchymal hematoma, ischemic mass effect, and 24-hour re-occlusion) in the early (<6 hours) versus late window (6–24 hours, including patients with unknown onset) populations and correlated them with the 3-month clinical outcome.

RESULTS: Among 701 patients with acute ischemic stroke receiving endovascular treatment, 29.2% had late endovascular treatment. Overall, incomplete recanalization occurred in 56 patients (8%), and 126 patients (18%) had at least 1 postprocedural cerebrovascular complication. The frequency of incomplete recanalization was similar in early and late endovascular treatment (7.5% versus 9.3%, adjusted $P = .66$), as was the occurrence of any postprocedural cerebrovascular complication (16.9% versus 20.5%, adjusted $P = .36$). When analyzing single postprocedural cerebrovascular complications, rates of parenchymal hematoma and ischemic mass effect were similar (adjusted $P = .71$, adjusted $P = .79$, respectively), but 24-hour re-occlusion seemed somewhat more frequent in late endovascular treatment (4% versus 8.3%, unadjusted $P = .02$, adjusted $P = .40$). The adjusted 3-month clinical outcome in patients with incomplete recanalization or postprocedural cerebrovascular complications was comparable between early and late groups (adjusted $P = .67$, adjusted $P = .23$, respectively).

CONCLUSIONS: The frequency of incomplete recanalization and of cerebrovascular complications occurring after endovascular treatment is similar in early and well-selected late patients receiving endovascular treatment. Our results demonstrate the technical success and safety of endovascular treatment in well-selected late patients with acute ischemic stroke.

ABBREVIATIONS: adj = adjusted; AIS = acute ischemic stroke; EVT = endovascular treatment; IME = ischemic mass effect; IR = incomplete revascularization; IVT = intravenous thrombolysis; PH = parenchymal hematoma; PPCC = postprocedural cerebrovascular complication; RCT = randomized controlled trial; unadj = unadjusted

The benefit of endovascular treatment (EVT) with stent retrievers or with a direct aspiration first-pass technique for acute ischemic stroke (AIS) is largely confirmed.^{1,2} For the late time window, randomized controlled trials (RCTs) have also proved their effectiveness in radiologically selected patients with anterior circulation stroke,^{3–5} with favorable treatment effects across multiple subgroups.⁶

However, the effectiveness of EVT is potentially reduced by technical problems and complications during EVT, such as embolization into a nonischemic territory or arterial perforation. They can also occur afterward in the form of incomplete recanalization (IR), arterial re-occlusion, and reperfusion injury (ie, parenchymal hematoma [PH] and ischemic mass effect [IME]). In large RCTs, IR was observed in 12%–34.3% of attempted EVTs.^{3–5,7–10} The

Received January 8, 2023; accepted after revision April 26.

From the Stroke Centre (E.M., S.N., D.S., A.E., P. Michel), Neurology Service, Department of Clinical Neurosciences and Department of Diagnostic and Interventional Radiology (B.B., S.D.H., F.P., V.D., P. Maeder, G.S.), Neuroradiology Unit, Lausanne University Hospital and University of Lausanne, Lausanne, Switzerland; and Department of Statistical Science (F.R.), University College London, London, UK.

This work was supported by the Swiss National Science Foundation (Project FN320030-182654/1) and the Swiss Heart Foundation.

Please address correspondence to Errikos Maslias, MD, Neurology Service, Lausanne University Hospital, Rue du Bugnon, 46, 1011 Lausanne, Switzerland; e-mail: Errikos.Maslias@chuv.ch

Indicates open access to non-subscribers at www.ajnr.org

Indicates article with online supplemental data.
<http://dx.doi.org/10.3174/ajnr.A7886>

rate of the other complications during and after EVT was 6%–18.6%.^{3–5,7–10} The large heterogeneity in definitions, neuroimaging techniques, and scales used may explain these variations.

Data on recanalization and postprocedural complications in late-treated patients are scarce^{11,12} and may vary from data in the early time window because patients are selected differently. We had already analyzed intraprocedural complications like arterial access damage, embolization in nonischemic territory, or SAH in early and late EVT.¹³ In this previous study, we found similar complication rates independent of the time window and similar long-term outcomes despite worse short-term deficits in patients with complicated late EVT. When analyzing predictors of intraprocedural complications of EVT, we identified off-hour interventions and smoking to be associated.¹⁴

We now aimed to compare the frequency of complications at the end (IR) and after EVT, ie, postprocedural cerebrovascular complications (PPCCs), between patients treated in the early and late time windows. Such PPCCs include arterial re-occlusion after the end of the procedure, PH, and IME.

MATERIALS AND METHODS

Study Design and Patient Selection

We used the prospectively constructed Acute STroke Registry and Analysis of Lausanne (ASTRAL),¹⁵ which contains all consecutive adults with AIS admitted to Lausanne University Hospital within 24 hours. Here, we retrospectively extracted all patients from January 2015 to December 2019 (modern thrombectomy era) in whom EVT was attempted within 24 hours of last proof of good health, including patients in whom the target occlusion was not reached or was already re-canalized at the time of angiography. Patients with atherosclerotic occlusions due to intracranial stenoses were not excluded. For the current analysis, we considered EVT as “early” if initiated within 6 hours after onset or last proof of good health and as “late” if initiated 6–24 hours after these time points.

The variables collected in ASTRAL, including nonrecanalization and complications during and after EVT, are prespecified as described previously.¹⁵ They include a large range of parameters, such as demographics, medical history, active cerebrovascular risk factors, current medication, clinical symptoms, stroke severity measured by the NIHSS, vital signs, metabolic parameters and stroke mechanism.

Neuroimaging

Until April 2018, the initial neuroimaging of choice on admission was CT (256-detector row Revolution CT; GE Healthcare) and 3T MR imaging thereafter (Magnetom Vida; Siemens). Acute imaging was assessed for ASPECTS and posterior circulation ASPECTS¹⁶ on noncontrast CT or DWI. CTA or MRA was performed before EVT in all patients. After EVT, control cerebral imaging by CT/CTA or MR imaging/MRA was obtained for all patients at 12–48 hours as part of routine clinical practice to evaluate recanalization status. Imaging was also repeated for any nonpalliative patient when clinically indicated, such as a ≥ 2 NIHSS points worsening.

At least 1 senior neuroradiologist (P. Maeder, V.D.) and a senior vascular neurologist (P. Michel) evaluated baseline neuroimaging in a nonblinded fashion to clinical information, but blinded to

each other's results. Controversial situations were reviewed jointly to reach a consensus. Assessment of subacute PH, IME, and re-occlusion was performed jointly. At least 1 interventional neuroradiologist (B.B., S.D.H., F.P., G.S.) assessed all DSA images regarding IR.

EVT Procedure, Recanalization, and Hemicraniectomy

EVT was usually preceded by intravenous thrombolysis (IVT) if the latter could be given within 4.5 hours after onset and there were no contraindications.^{2,17} For later-arriving patients, IVT was given before EVT as per the decision of the treating neurologist, given the absence of randomized trials to judge its added value. EVT was initiated within 6 hours (and up to 8 hours since May 2017)¹⁸ in the presence of a disabling deficit,⁸ a proximal intracranial vessel occlusion,^{17,19} and an ASPECTS of ≥ 5 in MCA circulation strokes, similar to the European criteria.²⁰ Patients arriving later or with an unknown stroke onset were offered treatment if the CTP or DWI-PWI mismatch ratio was >2.0 . Since May 2017, late-arriving patients were treated according to modified DWI or CTP assessment with Clinical Mismatch in the Triage of Wake-Up and Late Presenting Strokes Undergoing Neurointervention With Trevo (DAWN) criteria, ie, with NIHSS ≥ 10 and ASPECTS ≥ 7 or if the stroke was disabling, NIHSS 1–10 and ASPECTS ≥ 8 .⁴ Since January 2018, late-arriving patients were also offered EVT if the core was <70 mL and the mismatch ratio was >1.8 on perfusion imaging, in accordance with Endovascular Therapy Following Imaging Evaluation for Ischemic Stroke (DEFUSE 3) European² and American criteria.²¹

In basilar artery occlusions, EVT was performed up to 6 hours in the absence of extensive brainstem infarct on CT or MR imaging. Since May 2017, this time window was prolonged to 8 hours if posterior circulation ASPECTS was ≥ 7 on CT and up to 24 hours if no transverse irreversible brainstem ischemia was present on MR imaging. The interventional neuroradiology team consisted of 3 senior neuroradiologists until 2019 and 4 thereafter.

A large range of EVT data were analyzed, including time metrics (Online Supplemental Data), technical parameters of the procedure, and degree of reperfusion at the end of the procedure. Decompressive hemicraniectomy for IME was performed according to national guidelines.²²

Primary End Points

We compared the following 4 co-primary end points between patients with early and late windows undergoing EVT, according to the current literature:²³

- 1) IR at the end of EVT: recanalization $<2b$ on modified TICI.
- 2) Arterial re-occlusion on 24-hour neuroimaging, ie, MRA or CTA: re-occlusion of the initially recanalized intracranial artery with a modified TICI of 2b or 3 at the end of EVT.²⁴ Extracranial re-occlusions were not considered.
- 3) PH within 7 days: either PH type 1 or PH type 2 according to the second European Cooperative Acute Stroke Study (ECASS-II),²⁵ independent of clinical worsening; PH was preferred as an end point over symptomatic intracerebral hemorrhage because even PH type 1 is associated with less favorable outcomes.²⁶

- 4) IME within the first 7 days: radiologic supratentorial mass effect causing a ≥ 5 -mm midline shift or cerebellar stroke with obstruction of the fourth ventricle and/or basal cisterns or compression of the brainstem, independent of clinical worsening.

Re-occlusion, IME, and PH within 7 days of EVT were together considered as “any PPCC.”

We also compared, as further outcome, disability at 3 months. A noninterventional neurologist (or neurologist in specialty training) evaluated all patients before EVT and after EVT. The disability at 3 months was estimated in the outpatient stroke clinic by non-blinded stroke neurologists or in a nonblinded structured telephone interview²⁷ by mRS-certified medical personnel. We did not examine SAH or other intraprocedural EVT complications in the current project, given the specific focus on PPCC and our previous publication on such intraprocedural complications.¹³

Secondary End Points

Using unadjusted analyses, we also compared the rate of reperfusion injury (PH or IME), symptomatic intracranial hemorrhage according to ECASS-II,²⁸ Δ -NIHSS at 24 hours (difference between NIHSS at 24 hours and on admission), ischemic stroke and TIA recurrence of < 7 days, length of hospitalization, and disposition and mortality at 3 and 12 months. Furthermore, we compared the Δ -NIHSS at 24 hours and the mRS at 3 months in the early-versus-late EVT populations. Finally, we reported the rates of IR and PPCC separately for the posterior circulation, basilar artery occlusion, and patients with anterior circulation stroke.

Statistical Analysis and Ethical Considerations

Differences between the early and late EVT groups were explored using appropriate statistical testing such as Mann-Whitney U , χ^2 , or Fisher exact tests.

We analyzed each of the 4 co-primary end points separately (IR, re-occlusion at 24 hours, PH, IME) using 4 logistic regression models. We initially performed unadjusted univariate analysis, fitting models with the late/early indicator as the only explanatory variable. Then, we fitted multivariate models, adjusting for covariates selected using stepwise variable selection methods with a .20 significance threshold in univariate analysis.

Clinical long-term outcome for patients who had IR or any of the 3 PPCCs was analyzed using the mRS at 3 months as an ordinal variable (modified Rankin score), ie, with an ordinal logistic regression analysis in which all 6 levels of the mRS were considered.²⁹ Seventy-two patients (10.2%) were lost to 3-month follow-up.

Regarding secondary outcomes, the short-term (Δ -NIHSS) impact of IR and all combined PPCCs was also compared without adjustments (because of low numbers) in the overall cohorts with/without complications, in the overall cohort comparing patients in early-versus-late windows, and in the complication cohort comparing patients with early and late windows.

Given the 4 primary end points, the P value threshold was set at .125 for significance (Bonferroni correction).

ASTRAL is registered with our institution. Patient written information is collected where it is stated that routinely collected clinical data may be used for scientific purposes. Any patient's decision to opt out was respected. Before analysis, the data were anonymized following the principles of the Swiss Human Research

Ordinance. Given that only anonymized data were used, there was no need for local ethics commission approval or patient consent according to the Swiss Federal Act on Research Involving Human Beings. The anonymized data of this study are available from the authors on reasonable request. For reporting, the Strengthening of Reporting of Observational Studies in Epidemiology (STROBE) checklist was applied.

RESULTS

All 701 consecutive patients with AIS receiving EVT during the observation period were included; 70.8% ($n = 496$) were treated early, and 29.2% ($n = 205$), late. Among the 205 late-treated patients, 46 (22.4%) were treated according to a mismatch ratio of > 2.0 on CTP (until May 2017), 20 (9.8%) according to modified DAWN criteria (from May 2017 to January 2018), and 139 (67.8%) according to DEFUSE 3 criteria (after January 2018). Most baseline characteristics were similar between patients receiving early versus late EVT (Online Supplemental Data), but men were underrepresented and late EVT patients received less often IVT.

Frequency of Primary Outcomes

The global rate of incomplete recanalization at the end of the EVT procedure was 8% ($n = 56$). Any cerebrovascular complication within 7 days of EVT occurred in 18% ($n = 126$) of all patients receiving EVT. Radiologic IME within the first 7 days was the most common complication, observed in 9.1%, followed by PH (7.1%) and arterial re-occlusion (5.3%) (Online Supplemental Data).

Comparing patients undergoing early-versus-late EVT, IR rates were similar (adjusted OR [OR_{adj}] for early-versus-late IR = 0.85; 95% CI, 0.41–1.80; adjusted P [P_{adj}] = .66) (Online Supplemental Data and Table). Also, no significant difference was observed in rates of any PPCC (OR_{adj} for early-versus-late EVT = 0.70; 95% CI, 0.33–1.52; P_{adj} = .36).

This absence of differences between early-and-late EVT persisted in separate adjusted analyses of PH (OR_{adj} for early-versus-late EVT = 0.82; 95% CI, 0.29–1.94; P_{adj} = .71), IME (OR_{adj} for early-versus-late EVT = 0.90; 95% CI, 0.43–1.95; P_{adj} = .79), and their combination (reperfusion injury, unadjusted P [P_{unadj}] = .91). Arterial re-occlusion at 24 hours was 2 times more frequent in patients treated early versus late (4% versus 8.3%, P_{unadj} = .02); this difference did not reach statistical significance in the adjusted analysis (OR_{adj} = 0.66; 95% CI, 0.29–2.51; P_{adj} = .40) (Online Supplemental Data). Late EVT was preceded in 66/205 (32.2%) by IVT; this feature did not increase the risk of PH (P value = .58) or influence re-occlusion rates (P value = .43).

Clinical Impact

Overall, patients with IR and those with a PPCC had less favorable short-term and 3-month outcomes in unadjusted analysis (Online Supplemental Data).

When comparing patients with IR with early-versus-late EVT, the adjusted analysis of functional 3-month outcome showed no difference (Table). Similarly, when comparing patients with PPCC with early-versus-late EVT, the long-term clinical outcome was similar (Table).

Clinical outcome at 3 months: shift analysis of mRS comparing early-versus-late EVT

Co-Primary End Points	Unadjusted OR (95%CI)	Adjusted OR (95%CI)
3-Month mRS if IR	2.15 (0.45–15.71)	0.31 (0.00–82.83) ^a
3-Month mRS if PPCC	1.17 (0.45–3.33)	2.64 (0.57–14.67) ^b

^a Adjusted for age, admission NIHSS score, ASPECTS, prehospitalization mRS, hyperglycemia, pre-EVT-thrombolysis, general anesthesia, and year that the EVT was performed.

^b Adjusted for age, admission NIHSS score, prehospitalization mRS, ASPECTS, pre-EVT-thrombolysis, hyperglycemia, general anesthesia, year that the EVT was performed, and start time of groin puncture.

Secondary End Points

The short-term clinical outcome (Δ -NIHSS) in patients with IR with early-versus-late EVT ($P = .18$) and with PPCC was similar ($P = .49$, Online Supplemental Data).

In patients with IR, disposition and mortality at 3 and 12 months were similar (Online Supplemental Data). Mortality at 7 days was nonsignificantly higher in the patients with early EVT. Early stroke recurrence occurred in only 1 patient (from the late EVT group). In the population having at least 1 EVT PPCC, secondary end points were also similar.

When we compared the entire early-versus-late EVT populations (with or without complications), Δ -NIHSS at 24 hours seems less favorable in late EVT. However, the 3-month mRS was similar (Online Supplemental Data).

IR and PPCC in EVT for basilar artery occlusion were similar to EVT for anterior circulation stroke (7.4% and 7.4% versus 8.7% and 14.7%, $P = 1.000$ and $P = .405$, respectively). IR and PPCC for any posterior circulation stroke also did not differ from anterior circulation EVT (13.8% and 13.8% versus 8.7% and 14.7%, $P = .177$ and $P = 1.000$, respectively).

DISCUSSION

In 701 consecutive patients with AIS receiving EVT, we found no difference in the frequency of IR or PPCC between early and late time windows. Long-term clinical outcome in patients with IR or PPCC was also similar in early and late groups.

Our overall rate of IR of 8.7% seems lower than the 12%–41.3% reported in RCTs^{3,4,9,10,30–32} and in a recent large retrospective analysis.³³ This rate may be related to technical progress and improving operator skills, which may also be responsible for the high recanalization rates in our and other recent studies.^{13,34} The similar IR rate is reassuring and adds further support for late EVT.

The overall rate of 3 PPCCs of 18% is similar to the 6.0%–18.6% rate in published early and late EVT RCTs,^{3–5,7–10} with no important difference in the frequency or the clinical outcomes between early-versus-late EVT. Specifically, the PH rate of 7.1% correlates with reported rates in early^{5,8–10} and late EVT.^{3,4} In fact, causality of PH from EVT remains unproven,³⁵ and the risk of PH after EVT depends on numerous factors.^{12,36}

Second, the observed rate of IME of 9.1% seems lower than that in the Multicenter Randomized Clinical Trial of Endovascular Treatment for Acute Ischemic Stroke in the Netherlands (MR CLEAN) study, reporting a midline shift in 46.8%,³⁰ but higher than the 0.9% in DAWN.⁴ An increased risk of reperfusion injury (PH or IME) from prolonged ischemia in patients with late EVT seems to have been counterbalanced by DAWN study's stricter radiologic selection criteria such as a smaller core.

Third, the overall 24-hour re-occlusion rate of 5.3% after EVT is in accordance with reported rates.^{24,37} Most interesting, this complication was non-statistically more frequent in late EVT; the higher IVT rate in the early EVT group seems an unlikely explanation. Possible mechanisms of 24-hour re-occlusion include an unstable occlusion

site with residual thrombus fragments that act as a nidus of highly concentrated platelets and coagulation factors, vessel stenosis that can disrupt the endothelial wall, and multiple recanalization attempts that may induce vessel wall damage.

Similar to published randomized trials,³⁸ basilar artery occlusion and any posterior circulation EVT had IR and PPCC rates similar to those of anterior circulation EVTs, but our sample size might be too small to detect significant differences for this comparison.

Additional important findings of our study were the absence of differences in the duration of hospitalization and mortality between patients with early and late EVT with complications.

The main clinical implication of our study is the confirmation of the relative safety of EVT performed late or in patients with an unknown-onset stroke; this finding should further encourage physicians to offer this treatment whenever the criteria are fulfilled.

The strengths of the study are the enrollment of a large number of consecutive patients with prespecified assessment of complications by noninterventional neurologists. The limitations of our study are its retrospective, nonrandomized character in a single stroke center with an elderly, white population. Second, the definitions of some of the cerebrovascular complications might be contested, given the lack of a precise consensus.²³ Third, the investigated PPCCs are not necessarily causally related to EVT but may be due to the nature of the stroke. Fourth, early-and-late EVT decisions were based on either CT or MR imaging as initial imaging, making the sample more heterogeneous. Also, selection criteria for late EVT differed from those in early EVT because the latter is usually decided without considering perfusion imaging and mismatch criteria. Furthermore, late EVT criteria changed somewhat during the observation period, related to new scientific evidence (DAWN and DEFUSE 3 studies). Even though patients with late EVT had significantly lower ASPECTS on admission brain imaging, IR and PPCC were similar. Due to radiologic selection of patients with late EVT, the overall infarct size was relatively low in both early- and late-presentation groups; thus, the results may not be generalizable to patients with larger infarcts at presentation. Finally, there were a limited number of study outcomes (IR and PPCC), increasing the chance of a type 2 error and a potential risk of overfitting the adjustments for certain outcomes (such as re-occlusions and PH) in the multivariate analysis.

CONCLUSIONS

The frequency of IR and of PPCC after EVT is similar in patients with early and late EVT, as is the clinical outcome after complicated EVT. Our results confirm the safety of EVT in well-selected

patients with late AIS and strengthen the evidence provided by the late EVT RCTs.

Disclosure forms provided by the authors are available with the full text and PDF of this article at www.ajnr.org.

REFERENCES

1. Powers WJ, Rabinstein AA, Ackerson T, et al; American Heart Association Stroke Council. **2018 Guidelines for the Early Management of Patients with Acute Ischemic Stroke: a Guideline for Healthcare Professionals From the American Heart Association/American Stroke Association.** *Stroke* 2018;49:e46–99 CrossRef Medline
2. Turc G, Bhogal P, Fischer U, et al. **European Stroke Organisation (ESO). European Society for Minimally Invasive Neurological Therapy (ESMINT) Guidelines on Mechanical Thrombectomy in Acute Ischaemic Stroke Endorsed by Stroke Alliance for Europe (SAFE).** *Eur Stroke J* 2019;4:6–12 CrossRef Medline
3. Albers GW, Marks MP, Kemp S, DEFUSE-3, et al. **Thrombectomy for stroke at 6 to 16 hours with selection by perfusion imaging.** *N Engl J Med* 2018;378:708–18 CrossRef Medline
4. Nogueira RG, Jadhav AP, Haussen DC, et al; DAWN Trial Investigators. **Thrombectomy 6 to 24 hours after stroke with a mismatch between deficit and infarct.** *N Engl J Med* 2018;378:11–21 CrossRef Medline
5. Goyal M, Demchuk AM, Menon BK, et al; ESCAPE Trial Investigators. **Randomized assessment of rapid endovascular treatment of ischemic stroke.** *N Engl J Med* 2015;372:1019–30 CrossRef Medline
6. Jovin TG, Nogueira RG, Lansberg MG, et al. **Thrombectomy for anterior circulation stroke beyond 6 h from time last known well (AURORA): a systematic review and individual patient data meta-analysis.** *Lancet* 2022;399:249–58 CrossRef Medline
7. Goyal M, Menon BK, van Zwam WH, et al; HERMES Collaborators. **Endovascular thrombectomy after large-vessel ischaemic stroke: a meta-analysis of individual patient data from five randomised trials.** *Lancet* 2016;387:1723–31 CrossRef Medline
8. Berkhemer OA, Fransen PS, Beumer D, et al; MR CLEAN Investigators. **A randomized trial of intraarterial treatment for acute ischemic stroke.** *N Engl J Med* 2015;372:11–20 CrossRef Medline
9. Bracard S, Ducrocq X, Mas JL, et al; THRACE Investigators. **Mechanical thrombectomy after intravenous alteplase versus alteplase alone after stroke (THRACE): a randomised controlled trial.** *Lancet Neurol* 2016;15:1138–47 CrossRef Medline
10. Jovin TG, Chamorro A, Cobo E, et al; REVASCAT Trial Investigators. **Thrombectomy within 8 hours after symptom onset in ischemic stroke.** *N Engl J Med* 2015;372:2296–306 CrossRef Medline
11. Ngankou EH, Gory B, Marnat G, et al; ETIS Registry Investigators. **Thrombectomy complications in large vessel occlusions: incidence, predictors, and clinical impact in the ETIS Registry.** *Stroke* 2021;52:e764–68 CrossRef Medline
12. Salsano G, Pracucci G, Mavilio N, et al. **Complications of mechanical thrombectomy for acute ischemic stroke: Incidence, risk factors, and clinical relevance in the Italian Registry of Endovascular Treatment in acute stroke.** *Int J Stroke* 2021;16:818–27 CrossRef Medline
13. Maslias E, Nannoni S, Ricciardi F, et al. **Procedural complications during early versus late endovascular treatment in acute stroke: frequency and clinical impact.** *Stroke* 2021;52:1079–82 CrossRef Medline
14. Maslias EP, Nannoni S, Hajdu DS, et al. **Predictors of endovascular treatment procedural complications in acute ischemic stroke: a single-center cohort study.** *AJNR Am J Neuroradiol* 2022;43:1743–48 CrossRef Medline
15. Michel P, Odier C, Rutgers M, et al. **The Acute STroke Registry and Analysis of Lausanne (ASTRAL): design and baseline analysis of an ischemic stroke registry including acute multimodal imaging.** *Stroke* 2010;41:2491–98 CrossRef Medline
16. Tei H, Uchiyama S, Usui T, et al. **Posterior circulation ASPECTS on diffusion-weighted MRI can be a powerful marker for predicting functional outcome.** *J Neurol* 2010;257:767–73 CrossRef Medline
17. Michel P, Arnold M, Hungerbühler H, et al. **Thrombolyse de l'attaque cérébrale ischémique: recommandations actualisées.** *Swiss Medical Forum* 2006;6:892–94 CrossRef
18. Saver JL, Goyal M, van der Lugt A, et al; HERMES Collaborators. **Time to treatment with endovascular thrombectomy and outcomes from ischemic stroke: a meta-analysis.** *JAMA* 2016;316:1279–88 CrossRef Medline
19. Michel P, Arnold M, Hungerbühler HJ, et al. **Thrombolyse de l'attaque cérébrale ischémique: recommandations actualisées.** *Swiss Medical Forum* 2006;6:225–28 CrossRef
20. Fiehler J, Cognard C, Gallitelli M, et al. **European Recommendations on Organisation of Interventional Care in Acute Stroke (EROICAS).** *Int J Stroke* 2016;11:701–16 CrossRef Medline
21. Powers WJ, Rabinstein AA, Ackerson T, et al. **Guidelines for the Early Management of Patients with Acute Ischemic Stroke: 2019 Update to the 2018 Guidelines for the Early Management of Acute Ischemic Stroke: a Guideline for Healthcare Professionals from the American Heart Association/American Stroke Association.** *Stroke* 2019;50:e344–418 CrossRef Medline
22. Michel P, Arnold M, Hungerbühler HJ, et al; Swiss Working Group of Cerebrovascular Diseases with the Swiss Society of Neurosurgery and the Swiss Society of Intensive Care Medicine. **Decompressive craniectomy for space occupying hemispheric and cerebellar ischemic strokes: Swiss recommendations.** *Int J Stroke* 2009;4:218–23 CrossRef Medline
23. Sacks D, Baxter B, Campbell BC, et al. **Multisociety Consensus Quality Improvement Revised Consensus Statement for Endovascular Therapy of Acute Ischemic Stroke.** *Int J Stroke* 2018;13:612–32 CrossRef Medline
24. Marto JP, Strambo D, Hajdu SD, et al. **Twenty-four-hour reocclusion after successful mechanical thrombectomy: associated factors and long-term prognosis.** *Stroke* 2019;50:2960–63 CrossRef Medline
25. Larrue V, von Kummer RR, Muller A, et al. **Risk factors for severe hemorrhagic transformation in ischemic stroke patients treated with recombinant tissue plasminogen activator: a secondary analysis of the European-Australasian Acute Stroke Study (ECASS II).** *Stroke* 2001;32:438–41 CrossRef Medline
26. Dzialowski I, Pexman JH, Barber PA, et al; CASES Investigators. **Asymptomatic hemorrhage after thrombolysis may not be benign: prognosis by hemorrhage type in the Canadian alteplase for stroke effectiveness study registry.** *Stroke* 2007;38:75–79 CrossRef Medline
27. Wilson JT, Hareendran A, Grant M, et al. **Improving the assessment of outcomes in stroke: use of a structured interview to assign grades on the modified Rankin Scale.** *Stroke* 2002;33:2243–46 CrossRef Medline
28. Hacke W, Kaste M, Fieschi C, et al. **Randomised double-blind placebo-controlled trial of thrombolytic therapy with intravenous alteplase in acute ischaemic stroke (ECASS II): Second European-Australasian Acute Stroke Study Investigators.** *Lancet* 1998;352:1245–51 CrossRef Medline
29. Lees KR, Bath PM, Schellinger PD, et al; European Stroke Organization Outcomes Working Group. **Contemporary outcome measures in acute stroke research: choice of primary outcome measure.** *Stroke* 2012;43:1163–70 CrossRef Medline
30. Kimberly WT, Dutra BG, Boers AM, et al; MR CLEAN Investigators. **Association of reperfusion with brain edema in patients with acute ischemic stroke: a secondary analysis of the MR CLEAN Trial.** *JAMA Neurol* 2018;75:453–61 CrossRef Medline
31. Saver JL, Goyal M, Bonafe A, et al; SWIFT PRIME Investigators. **Stent-retriever thrombectomy after intravenous t-PA vs. t-PA alone in stroke.** *N Engl J Med* 2015;372:2285–95 CrossRef Medline
32. Ducroux C, Piotin M, Gory B, et al; ASTER Trial Investigators. **First pass effect with contact aspiration and stent retrievers in the Aspiration versus Stent Retriever (ASTER) trial.** *J Neurointerv Surg* 2020;12:386–91 CrossRef Medline

33. Casetta I, Fainardi E, Saia V, et al; Italian Registry of Endovascular Treatment in Acute Stroke. **Endovascular thrombectomy for acute ischemic stroke beyond 6 hours from onset: a real-world experience.** *Stroke* 2020;51:2051–57 CrossRef Medline
34. Nguyen TN, Abdalkader M, Nagel S, et al. **Noncontrast computed tomography vs computed tomography perfusion or magnetic resonance imaging selection in late presentation of stroke with large-vessel occlusion.** *JAMA Neurol* 2022;79:22–31 CrossRef Medline
35. Campbell BC, Hill MD, Rubiera M, et al. **Safety and efficacy of Solitaire stent thrombectomy.** *Stroke* 2016;47:798–806 CrossRef Medline
36. Nawabi J, Knierp H, Schön G, et al. **Hemorrhage after endovascular recanalization in acute stroke: lesion extent, collaterals and degree of ischemic water uptake mediate tissue vulnerability.** *Front Neurol* 2019;10:569 CrossRef Medline
37. Mosimann PJ, Kaesmacher J, Gautschi D, et al. **Predictors of unexpected early reocclusion after successful mechanical thrombectomy in acute ischemic stroke patients.** *Stroke* 2018;49:2643–51 CrossRef Medline
38. Langezaal LCM, van der Hoeven EJ, Mont’Alverne FJ, et al; BASICS Study Group. **Endovascular therapy for stroke due to basilar-artery occlusion.** *N Engl J Med* 2021;384:1910–20 CrossRef Medline

Ultrasound-Guided Radiofrequency Ablation versus Thyroidectomy for the Treatment of Benign Thyroid Nodules in Elderly Patients: A Propensity-Matched Cohort Study

L. Yan, X.Y. Li, Y. Li, and Y. Luo



ABSTRACT

BACKGROUND AND PURPOSE: Ultrasound-guided radiofrequency ablation has been recommended as an alternative to surgery for benign thyroid nodules. However, little is known about the benefit from the application of radiofrequency ablation for benign thyroid nodules in elderly patients. The purpose of this study was to compare the clinical outcomes of radiofrequency ablation versus thyroidectomy for elderly patients with benign thyroid nodules.

MATERIALS AND METHODS: This retrospective study evaluated 230 elderly patients (60 years of age or older) with benign thyroid nodules treated with radiofrequency ablation (R group, $n = 49$) or thyroidectomy (T group, $n = 181$). Complications, thyroid function, and treatment variables, including procedural time, estimated blood loss, hospitalization, and cost, were compared after propensity score matching. The volume, volume reduction rate, symptoms, and cosmetic score were also evaluated in the R group.

RESULTS: After 1:1 matching, each group had 49 elderly patients. The rate of overall complications and hypothyroidism was 26.5% and 20.4% in the T group, respectively, but these complications were totally absent from the R group ($P < .001$, $P = .001$). Patients in the R group had a significantly shorter procedural time (median, 4.8 versus 95.0 minutes, $P < .001$) and lower cost (US \$1979.02 versus US \$2208.80, $P = .013$) than those treated by thyroidectomy. After radiofrequency ablation, the volume reduction rate was 94.1%, and 12.2% of nodules had completely disappeared. The symptom and cosmetic scores were both significantly reduced at the last follow-up.

CONCLUSIONS: Radiofrequency ablation could be considered as a first-line treatment for elderly patients with benign thyroid nodules.

ABBREVIATIONS: IQR = interquartile range; PSM = propensity score matching; PTMC = papillary thyroid microcarcinoma; RFA = radiofrequency ablation; RLN = recurrent laryngeal nerve; US = ultrasound; VRR = volume reduction rate

Thyroid nodules are common in general, with a prevalence of 20%–76% worldwide by ultrasound (US).^{1,2} Thyroid nodules are more common in elderly individuals who have relatively large nodules compared with their young counterparts.^{1,3} With the use of US, Gietka-Czernal detected thyroid nodules in 10% of individuals approximately 20 years of age and in 50% of those older than 60 years of age.⁴ Recently, a study investigated the prevalence of thyroid nodules in China from 6,985,956 individuals. After analysis by age, the prevalence of nodules was decreased in subjects from 18 years of age or younger (30.8%) to 26 years of

age (20.5%) and gradually increased after 26 years of age up to a maximum 71.4% in participants 80 years of age or older.⁵

Most nodules were benign and asymptomatic and could be managed with observation. Only a small proportion grew with local cosmetic or compressive problems and required intervention.⁶ Currently, surgery is the standard treatment for benign thyroid nodules. Because the high prevalence and large nodule size in elderly patients were contributing to an increased number of thyroid surgeries, the risk of general anesthesia and surgery-related complications could not be ignored. Age was a risk factor of complications after thyroid surgery.^{7,8} Any pre-existing comorbidities also increased the risk of complications in elderly patients.^{7,9} Grogan et al⁷ reported that the incidence of complications in young (16–64 years of age), elderly (65–79 years of age), and superelderly (>79 years of age) patients was 1.0%, 2.2%, and 5.0%, respectively. Consequently, elderly patients were a vulnerable population for surgery and often needed special consideration and medical care.⁷ Moreover, some patients needed life-long

Received October 4, 2022; accepted after revision April 28, 2023.

From the Department of Ultrasound, The First Medical Centre, Chinese People's Liberation Army General Hospital, Haidian District, Beijing, China.

Please address correspondence to Yukun Luo, MD, Department of Ultrasound, The First Medical Centre, Chinese PLA General Hospital, No. 28 Fuxing Rd, Haidian District, Beijing, China, 100853; e-mail: lyk301@163.com

Indicates article with online supplemental data.

<http://dx.doi.org/10.3174/ajnr.A7890>

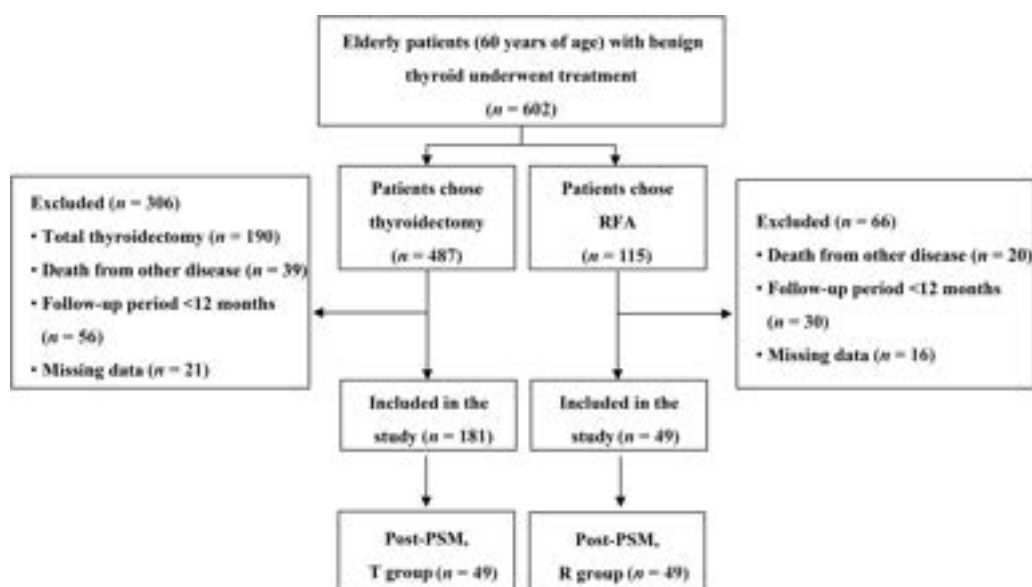


FIG 1. Study flow diagram.

thyroid hormone replacement after surgery. Thyroid hormone replacement was associated with adverse effects on bones and cardiovascular systems, which could be more prominent in elderly patients and postmenopausal women.^{2,10} Thus, elderly patients often preferred the nonsurgical option rather than surgery, even if general anesthesia was possible or a dedicated surgery team was available.¹¹

US-guided radiofrequency ablation (RFA) and other thermal ablation techniques have been recommended as alternatives to surgery for patients with benign thyroid nodules.¹²⁻¹⁶ Well-established data from multiple centers demonstrated that a significant nodular volume reduction could be achieved after ablation with relief of local cosmetic concerns and compressive symptoms.¹⁷⁻²⁴ Although several studies compared the outcomes between RFA and surgery for benign thyroid nodules,^{25,26} little is known about the benefit from the application of RFA in benign thyroid nodules in elderly patients.

Therefore, the purpose of this study was to compare the clinical outcomes of RFA versus thyroidectomy for benign thyroid nodules in elderly patients.

MATERIALS AND METHODS

The Institutional Review Board of the Chinese People's Liberation Army General Hospital approved this retrospective study. Written information consent was obtained from all the patients before RFA or thyroidectomy.

Patients

The inclusion criteria were as follows: 1) 60 years of age or older; 2) nodules confirmed as benign on 2 separate fine-needle aspiration or core-needle biopsy procedures before treatment; 3) maximum diameter of > 2.0 cm; 4) no suspicious malignant features on US, such as marked hypoechoic, irregular margins, taller-than-wide shape, or microcalcifications;¹ 5) solid ($\leq 10\%$ of fluid component) or predominantly solid nodules ($11\% - 50\%$ of fluid component);²⁷

6) cosmetic and/or symptomatic problems reported; 7) serum thyroid hormone and thyrotropin levels within normal ranges; and 8) a follow-up period of > 12 months. The exclusion criteria were as follows: 1) follicular neoplasm or malignancy reported by biopsy; 2) nodule with benign results on biopsy but suspected malignancy on US; and 3) coagulation disorder or serious heart, respiratory, liver, or renal failure.

The electronic medical records of 602 elderly patients with benign thyroid nodules confirmed by biopsy who underwent treatment between May 2014 and December 2018 were reviewed. After the exclusion of patients, 181 patients who underwent thyroidectomy (T group) and 49 patients treated with RFA (R group) were included in this study (Fig 1).

Pretreatment Assessment

All patients underwent laboratory tests that included complete blood count, coagulation tests, and thyroid function tests. The thyroid function tests were as follows: free triiodothyronine (normal range = $2.76 - 6.30$ picomoles per liter [pmol/L]), free thyroxine (normal range = $10.42 - 24.32$ pmol/L), and thyroid stimulating hormone (normal range = $0.23 - 5.50$ milliunits per liter). Before treatment, each nodule underwent US to evaluate the size, location, component, margin, shape, echogenicity, calcification, and vascularity. The nodular volume was calculated as follows: $V = \pi abc/6$ (V is the volume, while a is the largest diameter, b and c are the other 2 perpendicular diameters). The ACR Thyroid Imaging, Reporting and Data System (TI-RADS) score was used to evaluate each nodule.²⁸ Measurements of symptomatic or cosmetic problems was performed using a scoring system according to Thyroid RFA Guidelines from the Korean Society of Thyroid Radiology.¹² The symptom score was self-measured by patients using a 10-cm visual analog scale (grades 0–10).¹² The cosmetic score was evaluated by a physician (1, no palpable mass; 2, no cosmetic problem but palpable mass; 3, a cosmetic problem on swallowing only; and 4, a readily detected cosmetic problem).¹²

RFA

All ablation procedures were performed by an experienced US physician with >20 years' experience in thyroid US and interventional US. Patients were treated under local anesthesia in an outpatient clinic. A bipolar RFA generator (CelonLabPOWER; Olympus Surgical Technologies Europe) and 18-ga bipolar radiofrequency electrodes with 0.9- or 1.5-cm active tips were used (CelonProSurge micro 100-T09; Olympus Surgical Technologies Europe). RFA was performed using recommended ablation techniques, including a hydrodissection technique, a transisthmus approach, and a moving shot technique.¹² The ablation procedure was terminated when the entire nodule had become hyperechoic. Contrast-enhanced sonography was performed immediately after RFA to evaluate the ablated area, which was performed after a bolus injection of SonoVue (2.4 mL; Bracco), followed by 5 mL of normal saline flush. Additional complementary ablation could be performed if any enhancement existed in the ablated area.²⁹

After RFA, the clinical follow-ups were performed at 1, 3, 6, and 12 months and every 12 months thereafter. Volume, volume reduction rate (VRR), cosmetic score, symptom scores, and thyroid function were evaluated at each follow-up visit. The VRR was calculated as follows: $VRR = [(initial\ volume - final\ volume) \times 100\%] / initial\ volume$. Technical success was defined as a >50% volume reduction at last follow-up.²⁷

Thyroidectomy

The thyroidectomy procedures were performed by surgeons with >20 years' experience in thyroid surgery. Patients were treated with lobectomy, with or without isthmusectomy, under general anesthesia in the operating room. After surgery, patients were regularly followed up every 6–12 months by US and thyroid function.

End Points and Definitions

The primary outcomes were complications and hypothyroidism. Complications included were recurrent laryngeal nerve (RLN) injury, hypoparathyroidism, and hypothyroidism. RLN injury was the impaired movement of one or both vocal cords by laryngoscopy.³⁰ Hypoparathyroidism was defined as a parathyroid hormone level after treatment of <15 pg/mL at 24 hours. Permanent RLN injury or hypoparathyroidism was defined as no recovery after 6 months.³⁰

Secondary outcomes were procedural time and treatment cost. The procedural time of surgery was from incision to closure without general anesthesia time. The procedural time of RFA was defined from the electrode inserted in the tumor to ablation terminated without the time of local anesthesia and hydrodissection. The cost of the 2 treatments was based on the medical expenses determined by the government. The cost of RFA included the preoperative examination, ablation procedure, local anesthesia, and radiofrequency needle costs. The cost of surgery included the preoperative examination, surgery, general anesthesia, and hospitalization, such as the hospital bed, nursing costs, and postoperative medication costs.

Statistical Analysis

Statistical analyses were performed using SPSS statistical software, Version 25.0 (IBM) and R statistical and computing

software, Version 3.6.2 (<http://www.r-project.org/>). Because the continuous data in this study were all non-normally distributed, they were expressed as median with interquartile range (IQR) and compared by the Mann-Whitney *U* test. Categorical data are presented as numbers with percentages and compared by the χ^2 or Fisher exact test. Wilcoxon signed-rank tests were used to compare the volume, symptom scores, and cosmetic scores before and after RFA. The Bonferroni correction was used for multiple comparisons. To control potential bias, we matched the 2 groups using propensity score matching (PSM). The propensity to undergo RFA versus thyroidectomy was estimated using a logistic regression model based on age, sex, largest diameter, nodule volume, location, and ACR TI-RADS. The matching algorithm was 1:1 genetic matching with no replacement. Patients' baseline characteristics and primary and secondary outcomes in the 2 groups were compared before and after matching.

RESULTS

Patient Characteristics

Baseline characteristics of elderly patients in the 2 groups are shown in the Online Supplemental Data. Before PSM, elderly patients in the R group had tumors of smaller diameters (median, 4.1 cm; IQR, 1.6 cm versus median, 3.2 cm; IQR, 1.5 cm; $P < .001$) and volume (median, 18.6 mL; IQR, 22.0 mL versus median, 7.4 mL; IQR, 10.1 mL; $P < .001$) than those in the T group. After 1:1 matching, 98 elderly patients were included, with 49 in each group (Fig 2).

Primary Outcomes

The comparisons of complications are summarized in the Online Supplemental Data. Before PSM, the overall incidence of complications was 36.4% (66/181) in the T group and 0% in the R group ($P < .001$). In the T group, 4 elderly patients (2.2%) experienced transient RLN injury. After treatment by dexamethasone, they recovered within 3 months. Three elderly patients (1.7%) had transient hypoparathyroidism and recovered after 7 days. One elderly patient (0.6%) experienced loss of consciousness once after surgery. Three elderly patients (1.7%) had fever and recovered in 3 days after medication. Four elderly patients (2.2%) had wound infection, which resolved in 5 days with antibiotics. One elderly patient (0.6%) had respiratory dysfunction and recovered after 3 days on a ventilator. A total of 50 elderly patients (27.6%) in the T group had hypothyroidism and needed thyroid hormone supplementation. However, thyroid function was not affected in elderly patients after RFA ($P < .001$).

After PSM, the overall incidence of complications (0% versus 26.5%, $P < .001$) and hypothyroidism was significantly lower in the R group than in the T group (0% versus 20.4%, $P = .001$).

Secondary Outcomes

The treatment-related variables are shown in the Online Supplemental Data. After PSM, the procedural time (median, 4.8 minutes; IQR, 4.1 minutes versus median, 95.0 minutes; IQR, 62.0 minutes; $P < .001$) and cost (median, US \$1979.20; IQR, US \$268.40 versus median, US \$2208.80; IQR, US \$886.90; $P = .013$) in the R group were significantly lower than those in the T group.

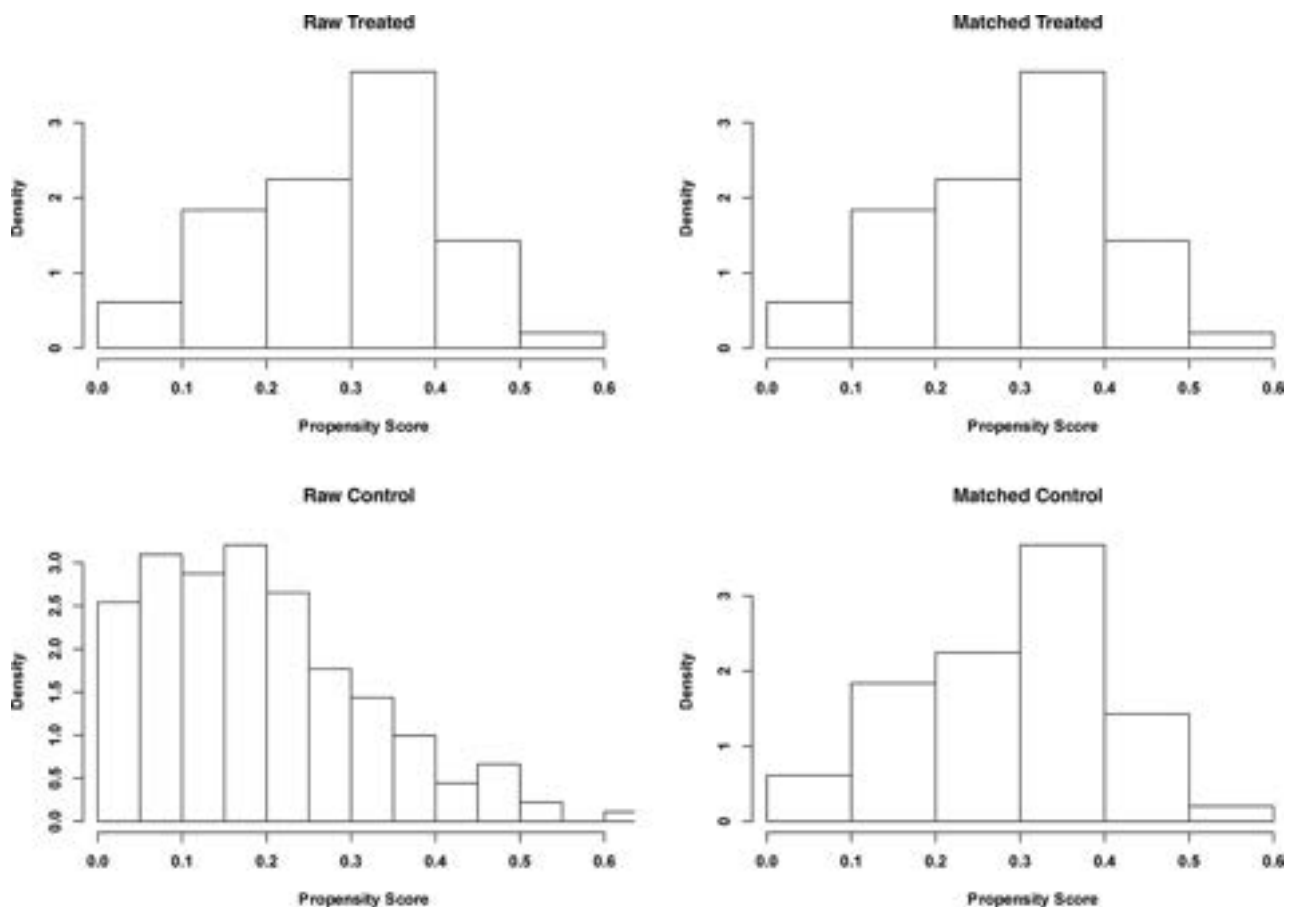


FIG 2. Histogram of PSM.

Other Outcomes

All patients underwent a single-session RFA procedure. During ablation, the median power was 7.5 W, and the mean energy was 1550 J. The Online Supplemental Data show the volume reduction during the follow-up for elderly patients treated by RFA. After ablation, the median volume of the nodules decreased significantly from 7.4 mL (IQR, 10.1 mL) to 0.3 mL (IQR, 1.4 mL) with a VRR of 94.1 (15.0%). Technical efficacy was achieved in all thyroid nodules. Nodule regrowth was not detected. Six ablated nodules (12.2%) disappeared during the follow-up. At the last follow-up, the symptom scores significantly decreased from median, 3 (IQR, 2) to median, 1 (IQR, 1) ($P = .001$), and the median cosmetic scores significantly decreased from median, 3 (IQR, 1.5) to median, 1 (IQR, 1) ($P = .001$). Figure 3 shows a nodule in an elderly patient before and after RFA.

In the T group, the median hospitalization was 8.0 (IQR, 4.0) days, and the median blood loss was 20.0 (40.0) mL. After surgery, the symptom scores significantly decreased from median, 5 (IQR, 4) to median 2 (IQR, 2) ($P < .001$), and the cosmetic scores significantly decreased from median, 4 (IQR, 2) to median, 0 (IQR, 0) ($P = .001$). The final pathology in the T groups was as follows: 113 nodular goiters, 60 thyroid adenomas, 6 Hürthle Cell adenomas, and 2 cases of Hashimoto thyroiditis. Among 113 patients with nodular goiters, 2 patients also had a papillary thyroid microcarcinoma (PTMC) lesion of <2 mm.

DISCUSSION

This study compared the clinical outcomes of RFA versus thyroidectomy for benign thyroid nodules in elderly patients. The results were that the overall incidence of complications and hypothyroidism was 26.5% and 20.4% in the T group, respectively, but they were totally absent from the R group. The procedural time, estimated blood loss, hospitalization, and cost were significantly lower in the R group than in the T group. Moreover, the nodule volume was significantly decreased after RFA with a median VRR of 94.1%. The nodule-related symptoms and cosmetic problems were also clinically improved.

Compared with young individuals, the elderly usually had a relatively large nodule.^{1,3} Therefore, the pressure symptoms or cosmetic problems in the neck including pain, dysphasia, foreign body sensation, discomfort, cough, neck bulging, and tracheal compression, were more prominent and needed treatment. However, because of the complex anatomy in the thyroid and neck, thyroid surgery had a relatively high risk of complications, especially in elderly patients.^{2,7,8,26} RLN injury was the most common major complication of thyroidectomy, and the rate of temporary and permanent injury was 0.4%–7.2% and 0–5.2%, respectively.³¹ It was associated with not only the varied position and intraoperative injury during surgery but also with increased age.^{9,32} Patients 65 years of age or older had a significantly higher rate of RLN injury compared with those younger than 65 years of age (8.0% versus 5.4%, $P < .001$).⁹

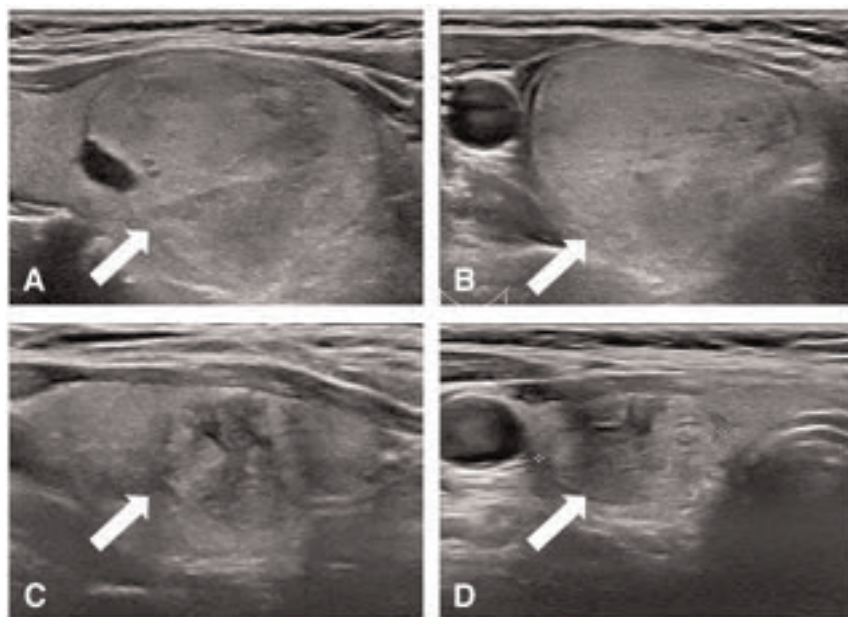


FIG 3. US image of a 61-year-old woman with a benign thyroid nodule in the right thyroid lobe. A and B, Before RFA, US image shows a solid benign nodule confirmed by biopsy in the right thyroid lobe with an initial volume of 14.3 mL (arrow). C and D, At 12 months after RFA, the volume of the ablated nodule was 2.0 mL (arrow) with a VRR of 86.2%.

Hypoparathyroidism was another major complication, mainly caused by the manipulation or incorrect removal of the parathyroid glands. The reported rate of transient and permanent hypoparathyroidism was 25.9%–27% and 1%–2.7% after thyroidectomy, respectively.^{8,33–35} To prevent hypoparathyroidism, the most practical approaches included the identification of the parathyroid glands and protection of the vascular supply; however, these approaches were not always possible during surgery.³⁶ In this study, 4 patients (2.2%) experienced transient RLN injury and 3 patients (1.7%) developed hypoparathyroidism in the T group. In contrast, no patient in the R group had complications. The findings were consistent with those in a previous meta-analysis that reported the rate of temporary injury after RFA for benign thyroid nodules as 0.9% and of permanent injury as 0.04%.³⁷ Moreover, hypoparathyroidism caused by RFA has not been reported yet.³⁷

To avoid complications during ablation, we used several strategies in this study. First, the physician can monitor the electrode tip and treat the nodule accurately by real-time US. Second, the moving shot technique, a transisthmic approach, and hydrodissection techniques were performed to minimize the thermal injury to the adjacent critical structures.¹² Third, the RFA procedure needed only local anesthesia in the outpatient clinic with a shorter procedural time, which also lowered the risk of complications.¹²

Hypothyroidism after RFA was rare,³⁸ and the reported rate of permanent hypothyroidism after RFA was 0.04%.³⁷ This study found that the thyroid function was well-maintained in all elderly patients treated with RFA, whereas 27.6% of elderly patients in the T group developed hypothyroidism and needed thyroid hormone replacement. As a minimally invasive technique, only the targeted nodule was treated during the RFA procedure, and most normal thyroid parenchyma was spared without thermal injury. However, a meta-analysis including 32 studies with 4899 patients

who underwent hemithyroidectomy reported that the incidence of hypothyroidism was from 5.7% to 48.9% and the overall risk of hypothyroidism was 22%.³⁹ Kuo et al⁴⁰ also reported that because of partial removal of the thyroid parenchyma during the thyroidectomy, 22%–33% of patients developed hypothyroidism and needed life-long thyroid hormone replacement. Although thyroid hormone replacement is a safe and generally successful therapy for hypothyroidism, it was difficult to precisely predict the correct replacement dose in elderly individuals.⁴¹ The gastrointestinal absorption of levothyroxine might be lower in elderly patients.⁴¹ The pre-existing comorbidities, such as diabetes, cirrhosis, hypertension, coronary artery disease, respiratory diseases, and malignancy, might also lower the levothyroxine dose required to normalize serum thyroid-stimulating hormone levels.⁴¹ Furthermore, elderly patients were more susceptible to the adverse effects of thyroid hormone replacement, especially arrhythmia and osteoporotic fractures. These issues made it difficult to predict the appropriate levothyroxine dose precisely and carefully in this population.¹⁰

RFA and other thermal ablation techniques have been recommended as an alternative to surgery for benign thyroid nodules.^{12–16} High-level evidence from prospective studies or randomized clinical trials revealed that after ablation, the nodule volume reduction was significant with improvement of clinical symptomatic and cosmetic problems.^{17–24} A meta-analysis reported that the pooled proportion of VRR at 6, 12, 24, 36 months, and last follow-up was 64.5%, 76.9%, 80.1%, 80.3%, and 92.2%, respectively.⁴² This study found that after RFA, the volume was significantly decreased with a median of 94.1% and a complete disappearance rate of 12.2%. Technical efficacy was achieved in all nodules, and nodule-related symptoms and cosmetic problems showed clinical improvement. These results were in line with previous studies suggesting that the efficacy of RFA was also satisfactory and sustainable for elderly patients.⁴²

In this study, 2 elderly patients in the T group were also found to have occult PTMC, suggesting that some benign nodules might have microscopic foci that could not be detected by preoperative US evaluation.⁴³ Therefore, surgery was still the current first-line treatment for benign thyroid nodules.¹ However, in the absence of evidence of extrathyroidal extension, metastatic cervical lymph nodes, or distant metastases, PTMC often had an indolent nature. Current guidelines have recommended active surveillance as a conservative management option to immediate surgery for low-risk PTMC,^{1,44} and this has had favorable results.^{45–47} Although older age was one of the most important factors predicting poor prognosis, Ito et al⁴⁸ reported that the proportion of PTMC progression was lowest in the elderly patients older than 60 years of age and highest in the young patients (younger than 40 years of

age), suggesting that elderly patients with subclinical low-risk PTMC may be the best candidates for active surveillance.

This study had limitations. First, it was a retrospective study. Second, the sample size was relatively small. Third, because elderly patients in the R group had smaller nodules than those in the T group, large nodules in the T group were removed from comparison by PSM. RFA and other thermal ablation techniques have been used for large nodules and nodular retrosternal goiters and have had favorable results.^{17-24,49} However, it was difficult to treat the periphery of a nodule completely by a single-session procedure. Patients with large nodules required multiple treatment sessions to achieve complete ablation.⁵⁰ The comparison between multiple RFA sessions versus thyroidectomy for very large nodules in elderly patients still needs further investigation. Fourth, the baseline disease status of elderly patients in the 2 groups might be different, despite PSM being used in this study to control potential biases. Fifth, because of medical insurance policies, the hospitalization and cost in this study might be different in other countries. In China, patients usually completed pre-treatment examinations after hospitalization, and they were discharged about 3 days after the surgery. Therefore, the hospitalization and cost of elderly patients in other countries need further investigation.

CONCLUSIONS

For elderly patients with benign thyroid nodules, RFA could be considered as a first-line treatment with advantages of a lower incidence of complications and maintenance of thyroid function.

Disclosure forms provided by the authors are available with the full text and PDF of this article at www.ajnr.org.

REFERENCES

- Haugen BR, Alexander EK, Bible KC, et al. **2015 American Thyroid Association Management Guidelines for Adult Patients with Thyroid Nodules and Differentiated Thyroid Cancer: The American Thyroid Association Guidelines Task Force on Thyroid Nodules and Differentiated Thyroid Cancer.** *Thyroid* 2016;26:1–133 CrossRef Medline
- Gharib H, Papini E, Garber JR, et al; AACE/ACE/AME Task Force on Thyroid Nodules. **American Association of Clinical Endocrinologists, American College of Endocrinology, and Associazione Medici Endocrinologi Medical Guidelines for Clinical Practice for the Diagnosis and Management of Thyroid Nodules: 2016 update.** *Endocr Pract* 2016;22:622–39 CrossRef Medline
- Russ G, Lebouilleux S, Leenhardt L, et al. **Thyroid incidentalomas: epidemiology, risk stratification with ultrasound and workup.** *Eur Thyroid J* 2014;3:154–63 CrossRef Medline
- Gietka-Czernel M. **The thyroid gland in postmenopausal women: physiology and diseases.** *Prz Menopauzalny* 2017;16:33–37 CrossRef Medline
- Li Y, Jin C, Li J, et al. **Prevalence of thyroid nodules in China: a health examination cohort-based study.** *Front Endocrinol (Lausanne)* 2021;12:676144 CrossRef Medline
- Hamidi O, Callstrom MR, Lee RA, et al. **Outcomes of radiofrequency ablation therapy for large benign thyroid nodules: a Mayo Clinic case series.** *Mayo Clin Proc* 2018;93:1018–25 CrossRef Medline
- Grogan RH, Mitmaker EJ, Hwang J, et al. **A population-based prospective cohort study of complications after thyroidectomy in the elderly.** *J Clin Endocrinol Metab* 2012;97:1645–53 CrossRef Medline
- Medas F, Tuveri M, Canu GL, et al. **Complications after reoperative thyroid surgery: retrospective evaluation of 152 consecutive cases.** *Updates Surg* 2019;71:705–10 CrossRef Medline
- Gunn A, Oyekunle T, Stang M, et al. **Recurrent laryngeal nerve injury after thyroid surgery: an analysis of 11,370 patients.** *J Surg Res* 2020;255:42–49 CrossRef Medline
- Jonklaas J, Bianco AC, Bauer AJ, et al; American Thyroid Association Task Force on Thyroid Hormone Replacement. **Guidelines for the Treatment of Hypothyroidism: prepared by the American Thyroid Association Task Force on Thyroid Hormone Replacement.** *Thyroid* 2014;24:1670–751 CrossRef Medline
- Ding AS, Xie DX, Zhang L, et al. **Public perceptions of radiofrequency ablation versus standard surgery for benign thyroid nodules.** *Surgery* 2022;172:110–17 CrossRef Medline
- Kim JH, Baek JH, Lim HK, et al; Guideline Committee for the Korean Society of Thyroid Radiology (KSThR) and Korean Society of Radiology. **2017 Thyroid Radiofrequency Ablation Guideline: Korean Society of Thyroid Radiology.** *Korean J Radiol* 2018;19:632–55 CrossRef Medline
- Papini E, Pacella CM, Solbiati LA, et al. **Minimally-invasive treatments for benign thyroid nodules: a Delphi-based consensus statement from the Italian Minimally-Invasive Treatments of the Thyroid (MITT) group.** *Int J Hyperthermia* 2019;36:376–82 CrossRef Medline
- Dobnig H, Zechmann W, Hermann M, et al. **Radiofrequency ablation of thyroid nodules: “Good Clinical Practice Recommendations” for Austria—An interdisciplinary statement from the following professional associations: Austrian Thyroid Association (ÖSDG), Austrian Society for Nuclear Medicine and Molecular Imaging (OGNMB), Austrian Society for Endocrinology and Metabolism (ÖGES), Surgical Endocrinology Working Group (ACE) of the Austrian Surgical Society (OEGCH).** *Wien Med Wochenschr* 2020;170:6–14 CrossRef Medline
- Papini E, Monpeyssen H, Frasoldati A, et al. **2020 European Thyroid Association Clinical Practice Guideline for the Use of Image-Guided Ablation in Benign Thyroid Nodules.** *Eur Thyroid J* 2020;9:172–85 CrossRef Medline
- Ha EJ, Baek JH, Che Y, et al. **Radiofrequency ablation of benign thyroid nodules: recommendations from the Asian Conference on Tumor Ablation Task Force—secondary publication.** *J Med Ultrasound* 2021;29:77–83 CrossRef Medline
- Baek JH, Ha EJ, Choi YJ, et al. **Radiofrequency versus ethanol ablation for treating predominantly cystic thyroid nodules: a randomized clinical trial.** *Korean J Radiol* 2015;16:1332–40 CrossRef Medline
- Cesareo R, Pasqualini V, Simeoni C, et al. **Prospective study of effectiveness of ultrasound-guided radiofrequency ablation versus control group in patients affected by benign thyroid nodules.** *J Clin Endocrinol Metab* 2015;100:460–66 CrossRef Medline
- Deandrea M, Sung JY, Limone P, et al. **Efficacy and safety of radiofrequency ablation versus observation for nonfunctioning benign thyroid nodules: a randomized controlled international collaborative trial.** *Thyroid* 2015;25:890–96 CrossRef Medline
- Jung SL, Baek JH, Lee JH, et al. **Efficacy and safety of radiofrequency ablation for benign thyroid nodules: a prospective multicenter study.** *Korean J Radiol* 2018;19:167–74 CrossRef Medline
- Deandrea M, Garino F, Alberto M, et al. **Radiofrequency ablation for benign thyroid nodules according to different ultrasound features: an Italian multicentre prospective study.** *Eur J Endocrinol* 2019;180:79–87 CrossRef Medline
- Cesareo R, Pacella CM, Pasqualini V, et al. **Laser ablation versus radiofrequency ablation for benign non-functioning thyroid nodules: six-month results of a randomized, parallel, open-label trial (LARA Trial).** *Thyroid* 2020;30:847–56 CrossRef Medline
- Jin H, Lin W, Lu L, et al. **Conventional thyroidectomy vs thyroid thermal ablation on postoperative quality of life and satisfaction for patients with benign thyroid nodules.** *Eur J Endocrinol* 2021;184:131–41 CrossRef Medline

24. Kandil E, Omar M, Aboueisha M, et al. **Efficacy and safety of radiofrequency ablation of thyroid nodules: a multi-institutional prospective cohort study.** *Ann Surg* 2022;276:589–96 CrossRef Medline
25. Che Y, Jin S, Shi C, et al. **Treatment of benign thyroid nodules: comparison of surgery with radiofrequency ablation.** *AJNR Am J Neuroradiol* 2015;36:1321–25 CrossRef Medline
26. Yan L, Deng C, Song Q, et al. **Radiofrequency ablation versus reoperation for benign thyroid nodules that developed after previous thyroid surgery.** *Int J Hyperthermia* 2021;38:176–82 CrossRef Medline
27. Mauri G, Pacella CM, Papini E, et al. **Image-guided thyroid ablation: proposal for standardization of terminology and reporting criteria.** *Thyroid* 2019;29:611–18 CrossRef Medline
28. Tessler FN, Middleton WD, Grant EG, et al. **ACR Thyroid Imaging, Reporting and Data System (TI-RADS): white paper of the ACR TI-RADS Committee.** *J Am Coll Radiol* 2017;14:587–95 CrossRef Medline
29. Zhang M, Luo Y, Zhang Y, et al. **Efficacy and safety of ultrasound-guided radiofrequency ablation for treating low-risk papillary thyroid microcarcinoma: a prospective study.** *Thyroid* 2016;26:1581–87 CrossRef Medline
30. Anuwong A, Ketwong K, Jitpratoom P, et al. **Safety and outcomes of the transoral endoscopic thyroidectomy vestibular approach.** *JAMA Surg* 2018;153:21–27 CrossRef Medline
31. Sun W, Liu J, Zhang H, et al. **A meta-analysis of intraoperative neuromonitoring of recurrent laryngeal nerve palsy during thyroid reoperations.** *Clin Endocrinol (Oxf)* 2017;87:572–80 CrossRef Medline
32. Francis DO, Pearce EC, Ni S, et al. **Epidemiology of vocal fold paralysis after total thyroidectomy for well-differentiated thyroid cancer in a Medicare population.** *Otolaryngol Head Neck Surg* 2014;150:548–57 CrossRef Medline
33. Edafe O, Antakia R, Laskar N, et al. **Systematic review and meta-analysis of predictors of post-thyroidectomy hypocalcaemia.** *Br J Surg* 2014;101:307–20 CrossRef Medline
34. Farkas EA, King TA, Bolton JS, et al. **A comparison of total thyroidectomy and lobectomy in the treatment of dominant thyroid nodules.** *Am Surg* 2002;68:678–82; discussion 682–83 CrossRef Medline
35. Perigli G, Cianchi F, Giudici F, et al. **Thyroidectomy for cancer: the surgeon and the parathyroid glands sparing.** *J Clin Med* 2021;10:4323 CrossRef Medline
36. Puzzello A, Rosato L, Innaro N, et al. **Hypocalcemia following thyroid surgery: incidence and risk factors—a longitudinal multicenter study comprising 2,631 patients.** *Endocrine* 2014;47:537–42 CrossRef Medline
37. Chung SR, Suh CH, Baek JH, et al. **Safety of radiofrequency ablation of benign thyroid nodules and recurrent thyroid cancers: a systematic review and meta-analysis.** *Int J Hyperthermia* 2017;33:920–30 CrossRef Medline
38. Wang N, Zheng B, Wu T, et al. **Thyroid dysfunction following radiofrequency ablation for benign thyroid nodules: more likely to occur within one-week and in high-risk population.** *Int J Hyperthermia* 2021;38:1060–68 CrossRef Medline
39. Verloop H, Louwerens M, Schoones JW, et al. **Risk of hypothyroidism following hemithyroidectomy: systematic review and meta-analysis of prognostic studies.** *J Clin Endocrinol Metab* 2012;97:2243–55 CrossRef Medline
40. Kuo JH, Sinclair CF, Lang B, et al. **A comprehensive review of interventional ablation techniques for the management of thyroid nodules and metastatic lymph nodes.** *Surgery* 2022;171:920–31 CrossRef Medline
41. Biondi B, Cooper DS. **Thyroid hormone therapy for hypothyroidism.** *Endocrine* 2019;66:18–26 CrossRef Medline
42. Cho SJ, Baek JH, Chung SR, et al. **Long-term results of thermal ablation of benign thyroid nodules: a systematic review and meta-analysis.** *Endocrinol Metab (Seoul)* 2020;35:339–50 CrossRef Medline
43. Bernardi S, Dobrinja C, Fabris B, et al. **Radiofrequency ablation compared to surgery for the treatment of benign thyroid nodules.** *Int J Endocrinol* 2014;2014:934595 CrossRef Medline
44. Sugitani I, Ito Y, Takeuchi D, et al. **Indications and strategy for active surveillance of adult low-risk papillary thyroid microcarcinoma: consensus statements from the Japan Association of Endocrine Surgery Task Force on Management for Papillary Thyroid Microcarcinoma.** *Thyroid* 2021;31:183–92 CrossRef Medline
45. Chou R, Dana T, Haymart M, et al. **Active surveillance versus thyroid surgery for differentiated thyroid cancer: a systematic review.** *Thyroid* 2022;32:351–67 CrossRef Medline
46. Kim K, Choi JY, Kim SJ, et al. **Active surveillance versus immediate surgery for low-risk papillary thyroid microcarcinoma patients in South Korea: a cost-minimization analysis from the MAeSTro study.** *Thyroid* 2022;32:648–56 CrossRef Medline
47. Hughes DT, Reyes-Gastelum D, Ward KC, et al. **Barriers to the use of active surveillance for thyroid cancer results of a physician survey.** *Ann Surg* 2022;276:e40–47 CrossRef Medline
48. Ito Y, Miyauchi A, Kihara M, et al. **Patient age is significantly related to the progression of papillary microcarcinoma of the thyroid under observation.** *Thyroid* 2014;24:27–34 CrossRef Medline
49. Li Y, Li X, Xiao J, et al. **Ultrasound-guided microwave ablation combined with ethanol injection for the treatment of solitary nodular retrosternal goiter: a prospective study of 72 patients.** *Eur Radiol* 2023;33:752–62 CrossRef Medline
50. Chen MH, Lin WC, Luo SD, et al. **Residual, regrowth, and new growth of radiofrequency ablation for benign thyroid nodules of different volumes: two-year follow-up results.** *Int J Hyperthermia* 2022;39:1172–78 CrossRef Medline

Improved Myelination following Camp Leg Power, a Selective Motor Control Intervention for Children with Spastic Bilateral Cerebral Palsy: A Diffusion Tensor MRI Study

A. Vuong, S.H. Joshi, L.A. Staudt, J.H. Matsumoto, and E.G. Fowler



ABSTRACT

BACKGROUND AND PURPOSE: Children with spastic cerebral palsy have motor deficits associated with periventricular leukomalacia indicating WM damage to the corticospinal tracts. We investigated whether practice of skilled lower extremity selective motor control movements would elicit neuroplasticity.

MATERIALS AND METHODS: Twelve children with spastic bilateral cerebral palsy and periventricular leukomalacia born preterm (mean age, 11.5 years; age range, 7.3–16.6 years) participated in a lower extremity selective motor control intervention, Camp Leg Power. Activities promoted isolated joint movement including isokinetic knee exercises, ankle-controlled gaming, gait training, and sensorimotor activities (3 hours/day, 15 sessions, 1 month). DWI scans were collected pre- and postintervention. Tract-Based Spatial Statistics was used to analyze changes in fractional anisotropy, radial diffusivity, axial diffusivity, and mean diffusivity.

RESULTS: Significantly reduced radial diffusivity ($P < .05$) was found within corticospinal tract ROIs, including 28.4% of the left and 3.6% of the right posterior limb of the internal capsule and 14.1% of the left superior corona radiata. Reduced mean diffusivity was found within the same ROIs (13.3%, 11.6%, and 6.6%, respectively). Additionally, decreased radial diffusivity was observed in the left primary motor cortex. Additional WM tracts had decreased radial diffusivity and mean diffusivity, including the anterior limb of the internal capsule, external capsule, anterior corona radiata, and corpus callosum body and genu.

CONCLUSIONS: Myelination of the corticospinal tracts improved following Camp Leg Power. Neighboring WM changes suggest recruitment of additional tracts involved in regulating neuroplasticity of the motor regions. Intensive practice of skilled lower extremity selective motor control movements promotes neuroplasticity in children with spastic bilateral cerebral palsy.

ABBREVIATIONS: ACR = anterior corona radiata; AD = axial diffusivity; ALIC = anterior limb of the internal capsule; CC = corpus callosum; CerPed = cerebral peduncle; CP = cerebral palsy; CST = corticospinal tract; EC = external capsule; FA = fractional anisotropy; GMFCS = Gross Motor Function Classification System; GMFM = Gross Motor Function Measure; MD = mean diffusivity; PLIC = posterior limb of the internal capsule; PVL = periventricular leukomalacia; RD = radial diffusivity; SCALE = Selective Control Assessment of the Lower Extremity; SCR = superior corona radiata; SMC = selective motor control; TBSS = Tract-Based Spatial Statistics

Children born prematurely are vulnerable to WM motor tract injury, with the resulting severity of motor impairment dependent on the extent of neuronal damage. The corticospinal

tracts (CSTs) responsible for selective motor control (SMC) are particularly vulnerable to damage due to their anatomic location. Periventricular leukomalacia (PVL), indicating CST damage, is a common MR imaging finding in children with spastic bilateral cerebral palsy (CP).¹ Impaired SMC presents as a lack of isolated joint movement and may include flexor/extensor synergy patterns and mirror movements with reduced force, speed, and timing of movement.^{2,3} SMC can be measured clinically using the Selective Control Assessment of the Lower Extremity (SCALE).² SCALE scores correlate with intralimb coordination⁴ and knee

Received November 4, 2022; accepted after revision April 4, 2023.

From the Departments of Bioengineering (A.V., S.H.J.), Orthopaedic Surgery (A.V., L.A.S., E.G.F.), Neurology (S.H.J.), Ahmanson Lovelace Brain Mapping Center, and Pediatrics (J.H.M.), University of California Los Angeles, Los Angeles, California; and Center for Cerebral Palsy (A.V., L.A.S., E.G.F.), University of California Los Angeles/Orthopaedic Institute for Children, Los Angeles, California.

MR imaging data acquisition and gait assessments were funded by donations and grants from the University of California Los Angeles Children's Discovery and Innovation Institute; Shapiro Family Foundation; United Cerebral Palsy of Los Angeles, Santa Barbara, and Ventura Counties; Waters Foundation; Lena Longo Foundation; and University of California Los Angeles Brain Mapping Center. Additional support was received from the National Center for Advancing Translational Science of the National Institutes of Health under the University of California Los Angeles Clinical and Translational Science Institute grant No. UL1TR001881.

No funders were involved in the preparation of this article. The authors have stated that they had no interests that might be perceived as posing a conflict or bias.

Please address correspondence to Andy Vuong, PhD, Center for Cerebral Palsy at UCLA/OIC, 1000 Veteran Ave, 22-27 Rehabilitation Center, Los Angeles, CA 90095-1795; e-mail: andyvuong@ucla.edu

Indicates open access to non-subscribers at www.ajnr.org

Indicates article with online supplemental data.
<http://dx.doi.org/10.3174/ajnr.A7860>

extension acceleration during gait⁵ and have a larger causal effect on gross motor function than strength, spasticity, contractures, and bony deformities.⁶ SMC is considered a prognostic factor for surgical outcomes.^{7,8}

DTI has been used to assess WM damage in children with spastic CP.⁹⁻¹² Relative to normative data, reduced fractional anisotropy (FA) has been interpreted as a marker of disruption of local tissue structural anisotropy; higher radial diffusivity (RD), as decreased myelination; lower axial diffusivity (AD), as axonal injury; and higher mean diffusivity (MD), as greater overall diffusion.¹³⁻¹⁸ Lower FA,⁹⁻¹² higher RD and MD,^{10,12} and bidirectional results for AD^{10,12} have been reported for children with spastic bilateral CP compared with children with typical development. In children with spastic bilateral CP, significant correlations between DTI measures and the Gross Motor Function Classification System (GMFCS) levels,^{10,11} Gross Motor Function Measure (GMFM),¹² and SCALE scores¹² have been found. SCALE scores were found to correlate positively with FA and negatively with RD in more motor regions of the brain compared with GMFM.¹²

Neuroplasticity as evidenced by changes in the microstructural properties of WM motor tracts in spastic CP is not well-understood. DTI studies examining the response to exercise interventions are limited, and improvements have yet to be clearly demonstrated. Most have focused on upper extremity therapy in children with unilateral CP with contrasting results.¹⁹⁻²¹ No significant changes were found in any DTI measure in cohorts of children and young adults with unilateral CP following constraint-induced therapy¹⁹ and constraint-induced therapy preceded by transcranial direct current stimulation.²¹ In contrast, Kim et al²⁰ found increased FA following a task-specific upper extremity exercise intervention in infants with CP, suggesting that microstructural changes may be more likely in younger participants with greater plasticity.

DTI changes of WM motor regions in children with spastic CP in response to a lower extremity exercise intervention have received little attention. Researchers in India examined FA using tractography following 6 months of daily physical therapy (1.5 hours/day for 24 weeks) that was preceded by botulinum toxin injections and casting for children born full-term with bilateral spastic CP (GMFCS levels I–IV).²² Physical therapy included strengthening, gait training, and stretching. They found significant increases in FA of motor and sensory bundles and GMFM, regardless of botulinum toxin assignment, supporting the efficacy of intensive lower extremity physical therapy. Improved FA, which has not been reported in other studies of lower extremity motor intervention in this population, may be related to the high physical therapy dosage. This dosage is not feasible in most settings and may place a considerable burden on a child and his or her family. Jain et al²³ reported that neither FA nor the apparent diffusion coefficient increased following botulinum toxin injections and 6 months of physical therapy in a cohort of children with spastic bilateral CP. ROIs, however, were defined differently (on the basis of WM perfusion). Most studies of lower extremity interventions in spastic CP to date have not included RD or MD.

While previous CP studies used DTI to observe specific isolated WM motor tracts, full tract reconstruction can be difficult

in cohorts with impaired WM leading to exclusion of participants.^{20,24,25} Additionally, focusing on a priori WM tracts may limit the scope of analysis and underestimate the global extent of WM neuroplasticity. Tract-Based Spatial Statistics (TBSS), a whole-brain voxel-based approach, can be used to observe an intervention effect on all WM tracts, including motor regions of the brain,²⁶ circumventing these issues.

The effect of an intensive lower extremity SMC intervention on WM motor tract microstructure has not been studied in children with spastic bilateral CP born prematurely with PVL. We hypothesized the following: 1) DTI measures would improve following intensive task-specific SMC intervention, and 2) participants with greater baseline SCALE scores would have greater improvement.

MATERIALS AND METHODS

Participants

This study was conducted in an outpatient clinical research setting (Center for CP at the University of California Los Angeles/Orthopaedic Institute for Children and Ahmanson-Lovelace Brain Mapping Center). The institutional review board of the University of California Los Angeles provided ethics approval. Informed assent and consent for research were obtained from the children and their parents or guardians.

Inclusion criteria for all participants were the following: 1) between 5 and 18 years of age, 2) history of prematurity, 3) diagnosis of spastic bilateral CP and PVL as evidenced by a brain scan, 4) the ability to understand and follow verbal directions, 5) the ability to lie still, and 6) the ability to walk with or without assistive devices.

Exclusion criteria were the following: 1) metal implants not verified as MR imaging-safe, 2) programmable implants including ventriculoperitoneal shunts and intrathecal baclofen pumps, 3) dental braces, 4) seizures not controlled by medication, 5) orthopedic surgery or neurosurgery within 1 year of starting the study, and 6) botulinum toxin or casting within 3 months of starting the study.

The participants in the current study were included in a previous publication examining the correlation between baseline DTI outcomes and SCALE in CP and DTI differences relative to a group of children with typical development.¹²

Clinical Assessments

Children with CP were evaluated by experienced physical therapists using standardized protocols. SCALE was used to assess SMC.² Specific isolated movement patterns at the hip, knee, ankle, and subtalar and toe joints were evaluated bilaterally. SCALE scores for each limb ranged from 0 (absent SMC) to 10 (normal SMC). Left and right limb scores were summed for a total possible SCALE score of 20 points.

Lower Extremity SMC Intervention

Camp Leg Power, the lower extremity SMC intervention, included practice of skilled, isolated joint movements, isokinetic knee exercises at variable speeds, ankle-controlled video gaming, gait and functional training, and sensory enrichment using a summer camp format. Under the supervision of experienced physical



FIG 1. Flowchart detailing the recruitment and screening process leading to the total number of participants included in the study.

therapists, each participant had 15 camp sessions for 3 hours/day during a 1-month period. Skilled, isolated movements of the hip, knee, ankle, and subtalar and toe joints were practiced. By means of a Biodex System 4 Pro Dynamometer (Biodex Medical Systems), isokinetic knee extension and flexion exercises were performed bilaterally for a minimum of 10 sessions. Each participant was trained at speeds up to 300°/s, depending on his or her initial ability to produce torque and was progressed to higher speeds on the basis of ability during each session. Participants operated video games using ankle dorsiflexion and plantar flexion movements on a robotic device²⁷ for at least 5 minutes per limb for a minimum of 10 sessions. Additionally, gait and functional training in activities that emphasized intra- and interlimb control were practiced. These included kicking, navigating obstacles, stair climbing, and treadmill/overground walking encouraging maximal step length. Barefoot sensory enrichment activities were performed including walking on different surfaces.

MR Imaging Protocols

Before MR imaging sessions, children viewed a slide presentation describing procedures and practiced lying still while listening to recordings of scanner sounds. All T1WI and DWI scans were acquired using a 32-channel coil on a 3T Magnetom Prisma MR imaging scanner (Siemens) without sedation. T1-weighted MPRAGE images were obtained using TR = 2500 ms; TE = 1.8, 3.6, 5.39, and 7.18 ms; FOV = 256 × 256 mm²; and isotropic voxel resolution = 0.8 × 0.8 × 0.8 mm³. DWI scans were obtained using a single-shot, spin-echo, echo-planar acquisition with 6 reference images ($b = 0$ s/mm²), 52 gradient directions ($b = 1500$ s/mm²), TR = 3231 ms, TE = 89.6 ms, FOV = 210 × 210 mm², echo spacing = 0.69 ms, and isotropic voxel resolution = 1.5 × 1.5 × 1.5 mm³. All DWI scans were corrected for EPI susceptibility and eddy current distortions using FSL's topup tool (<https://fsl.fmrib.ox.ac.uk/fsl/fslwiki/topup/ExampleTopupFollowedByApplytopup>) and eddy tool (<https://fsl.fmrib.ox.ac.uk/fsl/fslwiki/eddy>), respectively, and FA, RD, AD, and MD maps were generated using DTIFit (http://fsl.fmrib.ox.ac.uk/fsl/fsl-4.1.9/fdt/fdt_dtifit.html).²⁸ All DTI maps underwent a nonlinear registration to the standard space. Subsequently, the mean FA image was projected in the standard space FMRIB58_FA (https://fsl.fmrib.ox.ac.uk/fsl/fslwiki/FMRIB58_FA) and thresholded at FA = 0.2 to create a skeletonized version.²⁶ The nonlinear transformations were applied to the FA, RD, AD, and MD maps and projected on the mean FA skeleton in preparation for statistical analysis.²⁹

Statistical Analysis

TBSS, a whole-brain voxel-based approach, was used to assess pre- and postdifferences in FA, RD, AD, and MD.²⁶ The mean WM skeleton used was derived from and overlaid on the FMRIB58 standard-space FA template. Statistical analyses were

performed using paired *t* tests (5000 permutations). In addition, correlation analyses between pre- and post-DTI differences within each voxel and total SCALE score were performed. All results were corrected for multiple comparisons using the threshold-free cluster enhancement procedure implemented in Randomise (<https://fsl.fmrib.ox.ac.uk/fsl/fslwiki/Randomise/UserGuide>).³⁰ Voxels with significant findings ($P < .05$) were displayed on the mean WM skeleton.

ROI analyses were performed to quantify voxels with significant postintervention differences ($P < .05$). Using the Johns Hopkins University ICBM-DTI-81 WM atlas labels (<http://neuro.debian.net/pkgs/fsl-jhu-dti-whitematter-atlas.html>),³¹ we transferred ROIs to all images produced in the TBSS pipeline after nonlinear warping to the standard Montreal Neurological Institute 152 space and skeletonization. Significant pre- and postdifferences ($P < .05$) within ROIs were quantified by performing voxel counts in FSL (<http://www.fmrib.ox.ac.uk/fsl>). ROIs located along the descending pathways of the CSTs were parcellated bilaterally to analyze WM motor regions: 1) area inferior to the cerebral peduncle (sub-CerPed), 2) cerebral peduncle (CerPed), 3) posterior limb of the internal capsule (PLIC), and 4) superior corona radiata (SCR). Secondary ROIs were the anterior limb of the internal capsule (ALIC), external capsule (EC), anterior corona radiata (ACR), and the corpus callosum (CC) genu and body. The percentages of significant voxels ($P < .05$) in relation to the total number of voxels within ROIs were calculated.

RESULTS

Twelve children with spastic bilateral CP (2 females, 10 males; mean age, 11.5 [SD, 2.8] years; age range, 7.3–16.6 years) participated. They were born preterm with a mean gestational age of 28.9 weeks, ranging from 24 to 33 weeks. Using baseline T2WI scans, a neurologist or neuroradiologist examined CST brain regions between the cortex and medulla. All demonstrated findings consistent with clinical findings of spastic bilateral CP, namely PVL and/or ventricular enlargement, particularly in the posterior horns of the lateral ventricles. GMFCS levels were the following: I ($n = 3$), II ($n = 1$), III ($n = 7$), and IV ($n = 1$). Total SCALE scores ranged from 1 to 18. Five participants were right-handed, and 7 participants were left-handed. Figure 1 details the recruitment and screening process leading to the total number of participants included in the study.

The mean WM skeleton used is shown in Fig 2A. Significant postintervention decreases in RD ($P < .05$) were found throughout major WM tracts, including the CSTs, ALIC, EC, ACR, and CC (Fig 2B). Within the CSTs, RD decreased in the bilateral PLIC and left SCR as seen on the coronal and axial views. In the

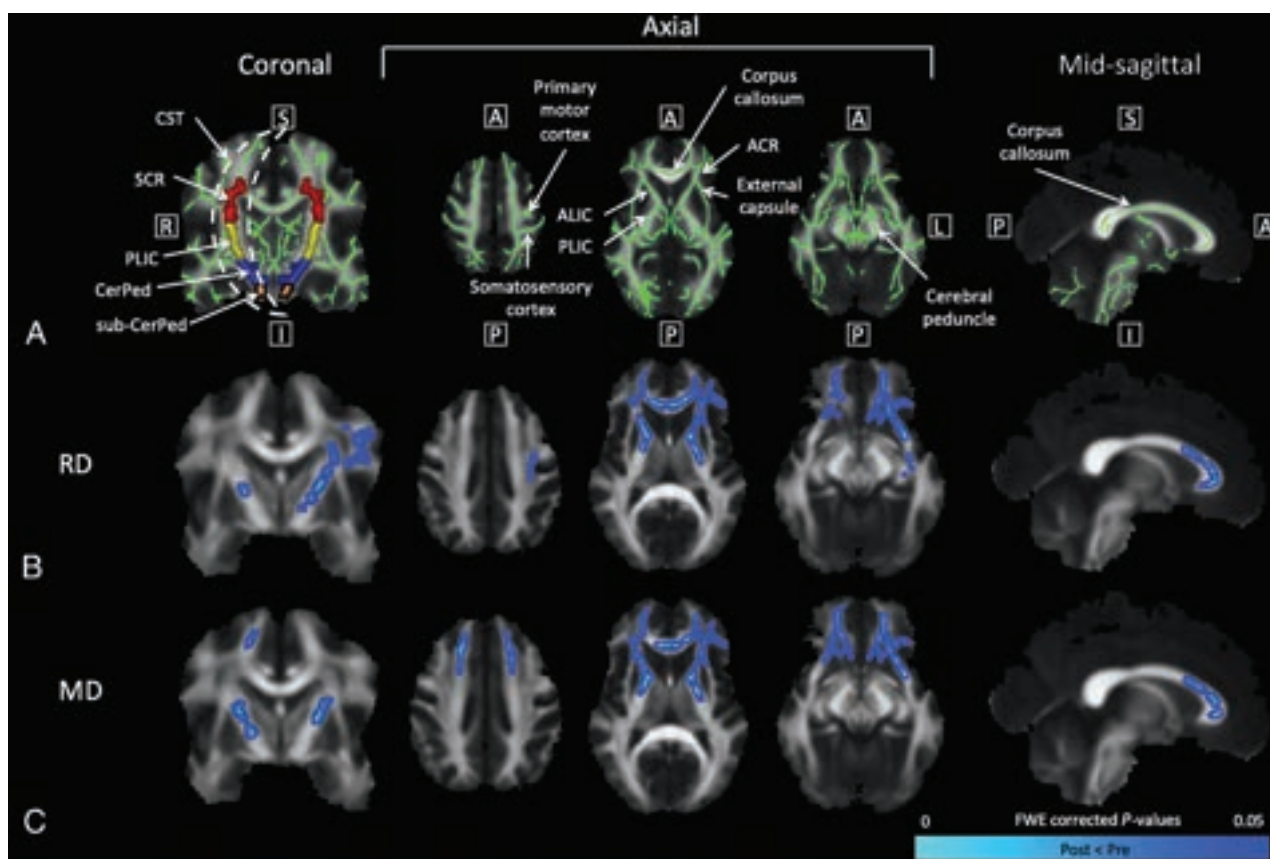


FIG 2. TBSS results show significant reductions in RD and MD ($P < .05$) after lower extremity SMC intervention. Coronal slices were selected at the level of the CSTs. From left to right, axial slices were selected at the level of the primary motor cortex, PLIC, and CerPed, respectively. Mid-sagittal slices were selected at the level of the CC. A, The WM skeleton is shown in green with additional arrows labeling the somatosensory cortex, ALIC, ACR, and EC. In the coronal view, ROIs for the SCR (red), PLIC (yellow), CerPed (blue), and sub-CerPed (orange) are shown. Significant pre- and postdifferences for the CP group ($P < .05$) are shown for RD (B) and MD (C). The colormap (blue-light blue) denotes a significant decrease in the DTI measure ($P < .05$). A indicates anterior; FWE, family-wise error; I, inferior; L, left; P, posterior; R, right; S, superior.

superior axial section, decreased RD can be viewed in the left motor and somatosensory cortices. Significant decreases in MD ($P < .05$) were found in similar regions of the brain (Fig 2C): the CSTs (bilateral PLIC and left SCR), ALIC, EC, ACR, and CC. In addition, decreased MD was apparent in both frontal lobes. No significant increases in RD or MD ($P < .05$) were found, and no significant changes in FA or AD ($P < .05$) were found in either direction. Significant correlations ($P < .05$) were not found between changes in DTI measures and total SCALE scores.

The number of voxels with significant decreases in RD and MD ($P < .05$) within motor and nonmotor WM ROIs is shown in the Table. RD and MD decreased within ROIs for the bilateral ALIC, bilateral PLIC, bilateral EC, bilateral ACR, left SCR, and CC genu and body. In all bilateral ROIs presented, a greater percentage change was seen in the left hemisphere of the brain compared with the right for both RD and MD, with the exception of MD in the bilateral ALIC. Additional ROIs containing voxels with significant decreases in RD ($P < .05$) are shown in the Online Supplemental Data.

DISCUSSION

This study showed significantly decreased RD and MD ($P < .05$) in the WM motor regions after an intensive lower extremity SMC

intervention in children with spastic bilateral CP. No significant postintervention increases in RD or MD ($P < .05$) were found. Few studies of children with spastic CP have analyzed postintervention DTI changes beyond FA. Following the intervention, RD and MD decreased in key CST regions, including the bilateral PLIC, left SCR, and left primary motor cortex. While decreased RD of the WM tracts is indicative of improved myelination,^{16,18} the meaning of decreased MD is less clear.^{17,32} We suggest, however, that the decreased MD is driven by intervention-guided neuroplastic changes related to altered uniformity in microstructural tissue complexity.^{17,32-34} In children with typical development, myelination is rapidly developed during infancy³⁵ and is dynamically regulated throughout adolescence,³⁶ but deficits have been widely reported for children with spastic CP and PVL.^{12,37-39} It has been theorized that task-based interventions focused on practicing new complex motor skills, as performed in this study, promote myelination.⁴⁰⁻⁴³ Others have reported improved CST myelination (using DTI tract-based quantitative susceptibility mapping) in children with spastic CP following cord blood stem cell therapy and usual rehabilitation therapy,⁴⁴⁻⁴⁶ precluding direct comparisons.

Our current findings of improved myelination of the CC genu and body are consistent with potential neuroplastic

Voxel counts of WM ROIs^a

ROI	Voxel Count	Voxels with Significant Pre- and Post-Decreases	
		RD (%)	MD (%)
R ALIC	792	278 (35.1)	400 (50.5)
L ALIC	819	341 (41.6)	205 (25.0)
R PLIC	845	30 (3.6)	98 (11.6)
L PLIC	858	244 (28.4)	114 (13.3)
R EC	1331	19 (1.4)	41 (3.1)
L EC	1431	320 (22.4)	164 (11.5)
R ACR	1619	365 (22.5)	569 (35.1)
L ACR	1613	897 (55.6)	802 (49.7)
L SCR	1279	180 (14.1)	84 (6.6)
Genu of CC	1758	914 (52.0)	710 (40.4)
Body of CC	3138	201 (6.4)	256 (8.2)

Note:— R indicates right; L, left.

^aSignificance set at ($P < .05$).

changes in response to SMC-focused therapy activities. In a study of rats trained in a spatial learning and memory task, WM changes in the CC as evidenced by DTI changes in FA and apparent diffusion coefficient were accompanied by increased myelin basic protein expression.⁴⁷ These findings support the association between acquisition of new complex motor skills and increased CC myelination. The CC is an important WM structure that is believed to play a role in bilateral coordination,⁴⁸ especially inhibition of physiologic mirroring that normally diminishes with age during early childhood.⁴⁹ Loss of transcallosal inhibition is one proposed cause of acquired obligatory mirror movements in patients with upper motor neuron lesions.^{50–52} These abnormal mirror movements in CP contribute to SMC deficits and lower SCALE scores.² Lower FA in transcallosal fibers in the CC body has been associated with upper extremity mirroring in children with spastic CP and PVL.⁵³ We previously demonstrated a correlation between SCALE scores and DTI indices in the CC in a cross-sectional analysis of this cohort.¹²

Significant postintervention decreases in RD and MD ($P < .05$) in other WM regions, including the ALIC, ACR, EC, sensorimotor cortex, and frontal lobes suggest recruitment of neighboring WM tracts directly adjacent or within close proximity to the CSTs. Prior studies of adults recovering from stroke have demonstrated significant changes in functional connectivity among the primary motor cortices,^{54,55} as well as postintervention (repetitive transcranial magnetic stimulation and occupational therapy) changes in similar WM regions.⁵⁶ Although motor improvement in children with spastic CP is made more complex by ongoing processes in the developing brain, similar patterns and principles of neuroplasticity likely apply. These neighboring WM regions with reduced RD and MD are areas of the brain that contain rich interconnections among the cortex, thalamus, and association regions.^{57–61} Therefore, it is plausible that coactivation and improved myelination of these additional WM tracts are necessary in regulating neuroplasticity of the brain motor regions.

Lower extremity interventions aimed specifically at developing and improving SMC in CP are limited and have primarily focused on the ankle joint.^{27,62} DTI changes following more generalized lower extremity rehabilitation have focused on FA. Two

studies with botulinum toxin and 6 months of general lower extremity exercise in children with CP reported increased FA in the PLIC of the CSTs⁶³ and in motor fiber bundles,²² regions where we found decreased RD and MD. Additionally, increased FA was found in 2 motor tracts (CSTs and PLIC) and 5 association tracts (CC, inferior and superior longitudinal fasciculus, uncinate, and cingulum) following intensive voice treatment (14 weeks) in children with CP and secondary dysarthria.⁶⁴ While the DTI measures analyzed did not include RD, these studies support the ideas in the present study that recruitment and activation of the CSTs play a critical role in responsiveness to intensive lower extremity intervention and practicing new complex motor skills. It is possible that improved myelination preceded or accompanied improvements in FA in these previous studies, but RD was not assessed. A longer intervention duration and a younger CP cohort may be required to promote improvements in FA.

Significant postintervention decreases in RD and MD ($P < .05$) were not associated with SCALE scores in this analysis, despite the significant correlation between RD and SCALE at baseline.¹² Isolated, skilled movements require good CST function; therefore, we hypothesized that children with higher SCALE scores would have greater capacity to learn and perform skilled movements, resulting in greater myelination. One explanation may be that children with lower SCALE scores are more likely to move in synergistic patterns, have lower levels of physical activity, and experience ankle and foot constraints due to greater dependence on orthotics. Therefore, the Camp Leg Power intervention was more novel for these participants, and greater motor learning may have occurred than was expected.

This study was limited by a relatively small sample size due to MR imaging exclusion criteria. Children with spastic CP commonly have shunts, baclofen pumps, and orthopedic surgery requiring metal implants.⁶⁵ In addition, involuntary movements are common and sometimes exaggerated by noise, further limiting a good MR imaging acquisition. The inclusion of a control group of children with spastic bilateral CP who did not undergo the Camp Leg Power intervention would strengthen these findings. Trivedi et al⁶³ included a control group of children with typical development and did not find significant within-group differences in FA or MD over a much longer time period. A randomized, controlled trial with a larger cohort would confirm our results. An additional limitation was that ROI analyses of the CSTs at the level of the primary motor cortex were not performed because this region is not included in the Johns Hopkins University WM atlas labels. Younger children with greater potential for plasticity⁶⁶ may be more likely to show improvement but are more difficult to scan without sedation. Efforts are currently underway to adapt SCALE and develop a lower extremity SMC intervention for infants and toddlers.

CONCLUSIONS

Intensive practice of skilled lower extremity SMC movements by children with spastic bilateral CP and PVL born prematurely was associated with increased myelination of WM motor tracts, including the CSTs and CC. Improved myelination of neighboring WM tracts suggests additional neuroplasticity associated with

skilled lower extremity SMC learning. A longer intervention duration at earlier ages may optimize WM neuroplasticity.

ACKNOWLEDGMENTS

We would like to thank the children and their families for participating in this study.

Disclosure forms provided by the authors are available with the full text and PDF of this article at www.ajnr.org.

REFERENCES

- Bax M, Tydeman C, Flodmark O. **Clinical and MRI correlates of cerebral palsy: the European Cerebral Palsy Study.** *J Am Med Assoc* 2006;296:1602–08 CrossRef Medline
- Fowler EG, Staudt LA, Greenberg MB, et al. **Selective Control Assessment of the Lower Extremity (SCALE): development, validation, and interrater reliability of a clinical tool for patients with cerebral palsy.** *Dev Med Child Neurol* 2009;51:607–14 CrossRef Medline
- Kennedy PR. **Corticospinal, rubrospinal and rubro-olivary projections: a unifying hypothesis.** *Trends Neurosci* 1990;13:474–79 CrossRef Medline
- Fowler EG, Goldberg EJ. **The effect of lower extremity selective voluntary motor control on interjoint coordination during gait in children with spastic diplegic cerebral palsy.** *Gait Posture* 2009;29:102–07 CrossRef Medline
- Goldberg EJ, Requejo PS, Fowler EG. **Joint moment contributions to swing knee extension acceleration during gait in individuals with spastic diplegic cerebral palsy.** *Gait Posture* 2011;33:66–70 CrossRef Medline
- MacWilliams BA, Prasad S, Shuckra AL, et al. **Causal factors affecting gross motor function in children diagnosed with cerebral palsy.** *PLoS One* 2022;17:e0270121 CrossRef Medline
- Goldberg EJ, Fowler EG, Oppenheim WL. **Case reports: the influence of selective voluntary motor control on gait after hamstring lengthening surgery.** *Clin Orthop Relat Res* 2012;470:1320–26 CrossRef Medline
- Staudt LA, Peacock WJ. **Selective posterior rhizotomy for treatment of spastic cerebral palsy.** *Pediatric Physical Therapy* 1989;1:3–9 CrossRef
- Ceschin R, Lee VK, Schmithorst V, et al. **Regional vulnerability of longitudinal cortical association connectivity: associated with structural network topology alterations in preterm children with cerebral palsy.** *Neuroimage Clin* 2015;9:322–37 CrossRef Medline
- Arrigoni F, Peruzzo D, Gagliardi C, et al. **Whole-brain DTI assessment of white matter damage in children with bilateral cerebral palsy: evidence of involvement beyond the primary target of the anoxic insult.** *AJNR Am J Neuroradiol* 2016;37:1347–53 CrossRef Medline
- Lee JD, Park HJ, Park ES, et al. **Motor pathway injury in patients with periventricular leukomalacia and spastic diplegia.** *Brain* 2011;134:1199–210 CrossRef Medline
- Vuong A, Fowler EG, Matsumoto J, et al. **Selective motor control is a clinical correlate of brain motor tract impairment in children with spastic bilateral cerebral palsy.** *AJNR Am J Neuroradiol* 2021;42:2054–61 CrossRef Medline
- Basser PJ, Jones DK. **Diffusion-tensor MRI: theory, experimental design and data analysis: a technical review.** *NMR Biomed* 2002;15:456–67 CrossRef Medline
- Assaf Y, Pasternak O. **Diffusion tensor imaging (DTI)-based white matter mapping in brain research: a review.** *J Mol Neurosci* 2008;34:51–61 CrossRef Medline
- Winkiewicz PJ, Sabisz A, Naumczyk P, et al. **Understanding the physiopathology behind axial and radial diffusivity changes: what do we know?** *Front Neurol* 2018;9:92 CrossRef Medline
- Song SK, Sun SW, Ramsbottom MJ, et al. **Dysmyelination revealed through MRI as increased radial (but unchanged axial) diffusion of water.** *Neuroimage* 2002;17:1429–36 CrossRef Medline
- Vos SB, Jones DK, Jeurissen B, et al. **The influence of complex white matter architecture on the mean diffusivity in diffusion tensor MRI of the human brain.** *Neuroimage* 2012;59:2208–16 CrossRef Medline
- Lazari A, Lipp I. **Can MRI measure myelin? Systematic review, qualitative assessment, and meta-analysis of studies validating microstructural imaging with myelin histology.** *Neuroimage* 2021;230:117744 CrossRef Medline
- Rickards T, Sterling C, Taub E, et al. **Diffusion tensor imaging study of the response to constraint-induced movement therapy of children with hemiparetic cerebral palsy and adults with chronic stroke.** *Arch Phys Med Rehabil* 2014;95:506–14.e1 CrossRef Medline
- Kim JH, Kwon YM, Son SM. **Motor function outcomes of pediatric patients with hemiplegic cerebral palsy after rehabilitation treatment: a diffusion tensor imaging study.** *Neural Regen Res* 2015;10:624–30 CrossRef Medline
- Nemanich ST, Mueller BA, Gillick BT. **Neurite orientation dispersion and density imaging quantifies corticospinal tract microstructural organization in children with unilateral cerebral palsy.** *Hum Brain Mapp* 2019;40:4888–900 CrossRef Medline
- Chaturvedi SK, Rai Y, Chourasia A, et al. **Comparative assessment of therapeutic response to physiotherapy with or without botulinum toxin injection using diffusion tensor tractography and clinical scores in term diplegic cerebral palsy children.** *Brain Dev* 2013;35:647–53 CrossRef Medline
- Jain KK, Paliwal VK, Yadav A, et al. **Cerebral blood flow and DTI metrics changes in children with cerebral palsy following therapy.** *J Pediatr Neurol* 2015;34:63–73 CrossRef
- Hodge J, Goodyear B, Carlson H, et al. **Segmental diffusion properties of the corticospinal tract and motor outcome in hemiparetic children with perinatal stroke.** *J Child Neurol* 2017;32:550–59 CrossRef Medline
- Kwon JY, Chang W, Chang HJ, et al. **Changes in diffusion tensor tractographic findings associated with constraint-induced movement therapy in young children with cerebral palsy.** *Clin Neurophysiol* 2014;125:2397–403 CrossRef Medline
- Smith SM, Jenkinson M, Johansen-Berg H, et al. **Tract-Based Spatial Statistics: voxelwise analysis of multi-subject diffusion data.** *Neuroimage* 2006;31:1487–505 CrossRef Medline
- Wu YN, Hwang M, Ren Y, et al. **Combined passive stretching and active movement rehabilitation of lower-limb impairments in children with cerebral palsy using a portable robot.** *Neurorehabil Neural Repair* 2011;25:378–85 CrossRef Medline
- Basser PJ, Mattiello J, Leblond D. **Estimation of the effective self-diffusion tensor from the NMR spin echo.** *J Magn Reson B* 1994;103:247–54 CrossRef Medline
- Andersson JL, Sotiropoulos SN. **An integrated approach to correction for off-resonance effects and subject movement in diffusion MR imaging.** *Neuroimage* 2016;125:1063–78 CrossRef Medline
- Smith SM, Nichols TE. **Threshold-free cluster enhancement: addressing problems of smoothing, threshold dependence and localisation in cluster inference.** *Neuroimage* 2009;44:83–98 CrossRef Medline
- Mori S, Oishi K, Jiang H, et al. **Stereotaxic white matter atlas based on diffusion tensor imaging in an ICBM template.** *Neuroimage* 2008;40:570–82 CrossRef Medline
- Thomas B, Eyssen M, Peeters R, et al. **Quantitative diffusion tensor imaging in cerebral palsy due to periventricular white matter injury.** *Brain* 2005;128:2562–77 CrossRef Medline
- Scheck SM, Pannet K, Raffelt DA, et al. **Structural connectivity of the anterior cingulate in children with unilateral cerebral palsy due to white matter lesions.** *Neuroimage Clin* 2015;9:498–505 CrossRef Medline
- Scheck SM, Boyd RN, Rose SE. **New insights into the pathology of white matter tracts in cerebral palsy from diffusion magnetic resonance imaging: a systematic review.** *Dev Med Child Neurol* 2012;54:684–96 CrossRef Medline

35. Poduslo SE, Jang Y. **Myelin development in infant brain.** *Neurochem Res* 1984;9:1615–26 CrossRef Medline
36. Corrigan NM, Yarnykh VL, Hippe DS, et al. **Myelin development in cerebral gray and white matter during adolescence and late childhood.** *Neuroimage* 2021;227:117678 CrossRef Medline
37. Billiards SS, Haynes RL, Folkerth RD, et al. **Myelin abnormalities without oligodendrocyte loss in periventricular leukomalacia.** *Brain Pathol* 2008;18:153–63 CrossRef Medline
38. Kinney HC. **Human myelination and perinatal white matter disorders.** *J Neurol Sci* 2005;228:190–92 CrossRef Medline
39. Volpe JJ. **Brain injury in premature infants: a complex amalgam of destructive and developmental disturbances.** *Lancet Neurol* 2009;8:110–24 CrossRef Medline
40. Bloom MS, Orthmann-Murphy J, Grinspan JB. **Motor learning and physical exercise in adaptive myelination and remyelination.** *ASN Neuro* 2022;14:175909142210975 CrossRef Medline
41. Baraban M, Mensch S, Lyons DA. **Adaptive myelination from fish to man.** *Brain Res* 2016;1641:149–61 CrossRef Medline
42. de Faria O Jr, Gonsalves DG, Nicholson M, et al. **Activity-dependent central nervous system myelination throughout life.** *J Neurochem* 2019;148:447–61 CrossRef Medline
43. Lakhani B, Borich MR, Jackson JN, et al. **Motor skill acquisition promotes human brain myelin plasticity.** *Neural Plast* 2016;2016:7526135 CrossRef Medline
44. Englander ZA, Sun J, Case L, et al. **Brain structural connectivity increases concurrent with functional improvement: evidence from diffusion tensor MRI in children with cerebral palsy during therapy.** *Neuroimage Clin* 2015;7:315–24 CrossRef Medline
45. Sun JM, Song AW, Case LE, et al. **Effect of autologous cord blood infusion on motor function and brain connectivity in young children with cerebral palsy: a randomized, placebo-controlled trial.** *Stem Cells Transl Med* 2017;6:2071–78 CrossRef Medline
46. Zhang L, Ellor S, Sun JM, et al. **DTI tract-based quantitative susceptibility mapping: an initial feasibility study to investigate the potential role of myelination in brain connectivity change in cerebral palsy patients during autologous cord blood cell therapy using a rotationally-invariant quantitative measure.** *J Magn Reson Imaging* 2021;53:251–58 CrossRef Medline
47. Blumenfeld-Katzir T, Pasternak O, Dagan M, et al. **Diffusion MRI of structural brain plasticity induced by a learning and memory task.** *PLoS One* 2011;6:e20678 CrossRef Medline
48. Wahl M, Lauterbach-Soon B, Hattingen E, et al. **Human motor corpus callosum: topography, somatotopy, and link between microstructure and function.** *J Neurosci* 2007;27:12132–38 CrossRef Medline
49. Mayston MJ, Harrison LM, Stephens JA. **A neurophysiological study of mirror movements in adults and children.** *Ann Neurol* 1999;45:583–94 CrossRef Medline
50. Beaulé V, Tremblay S, Théoret H. **Interhemispheric control of unilateral movement.** *Neural Plast* 2012;2012:627816 CrossRef Medline
51. Riddell M, Kuo HC, Zewdie E, et al. **Mirror movements in children with unilateral cerebral palsy due to perinatal stroke: clinical correlates of plasticity reorganization.** *Dev Med Child Neurol* 2019;61:943–49 CrossRef Medline
52. Nass R. **Mirror movement asymmetries in congenital hemiparesis: the inhibition hypothesis revisited.** *Neurology* 1985;35:1059–62 CrossRef Medline
53. Koerte I, Pelavin P, Kirmess B, et al. **Anisotropy of transcallosal motor fibres indicates functional impairment in children with periventricular leukomalacia.** *Dev Med Child Neurol* 2011;53:179–86 CrossRef Medline
54. Li Y, Wang D, Zhang H, et al. **Changes of brain connectivity in the primary motor cortex after subcortical stroke: a multimodal magnetic resonance imaging study.** *Medicine (Baltimore)* 2016;95:e2579 CrossRef Medline
55. Liu J, Qin W, Zhang J, et al. **Enhanced interhemispheric functional connectivity compensates for anatomical connection damages in subcortical stroke.** *Stroke* 2015;46:1045–51 CrossRef Medline
56. Ueda R, Yamada N, Abo M, et al. **White matter changes follow low-frequency repetitive transcranial magnetic stimulation plus intensive occupational therapy for motor paralysis after stroke: a DTI study using TBSS.** *Acta Neurol Belg* 2021;121:387–96 CrossRef Medline
57. Safadi Z, Grisot G, Jbabdi S, et al. **Functional segmentation of the anterior limb of the internal capsule: linking white matter abnormalities to specific connections.** *J Neurosci* 2018;38:2106–17 CrossRef Medline
58. Karababa F, Bayazit H, Kılıçaslan N, et al. **Microstructural changes of anterior corona radiata in bipolar depression.** *Psychiatry Investig* 2015;12:367–71 CrossRef Medline
59. Nolze-Charron G, Dufort-Rouleau R, Houde JC, et al. **Tractography of the external capsule and cognition: a diffusion MRI study of cholinergic fibers.** *Exp Gerontol* 2020;130:110792 CrossRef Medline
60. Chayer C, Freedman M. **Frontal lobe functions.** *Curr Neurol Neurosci Rep* 2001;1:547–52 CrossRef Medline
61. Zhao M, Marino M, Samogin J, et al. **Hand, foot and lip representations in primary sensorimotor cortex: a high-density electroencephalography study.** *Sci Rep* 2019;9:19464 CrossRef Medline
62. Wu YN, Ren Y, Hwang M, et al. **Efficacy of robotic rehabilitation of ankle impairments in children with cerebral palsy.** *Annu Int Conf IEEE Eng Med Biol Soc* 2010;2010:4481–84 CrossRef Medline
63. Trivedi R, Gupta RK, Shah V, et al. **Treatment-induced plasticity in cerebral palsy: a diffusion tensor imaging study.** *Pediatr Neurol* 2008;39:341–49 CrossRef Medline
64. Reed A, Cummine J, Bakhtiari R, et al. **Changes in white matter integrity following intensive voice treatment (LSVT LOUD®) in children with cerebral palsy and motor speech disorders.** *Dev Neurosci* 2017;39:460–71 CrossRef Medline
65. Thompson RM, Fowler EG, Culo B, et al. **MRI safety and imaging artifacts evaluated for a cannulated screw used for guided growth surgery.** *Magn Reson Imaging* 2020;66:219–25 CrossRef Medline
66. Mundkur N. **Neuroplasticity in children.** *Indian J Pediatr* 2005;72:855–57 CrossRef Medline

Doppler Ultrasound Flow Reversal in the Superior Sagittal Sinus to Detect Cerebral Venous Congestion in Vein of Galen Malformation

S. Schwarz, F. Brevis Nuñez, N.R. Dürr, F. Brassel, M. Schlunz-Hendann, A. Feldkamp, T. Rosenbaum, U. Felderhoff-Müser, K. Schulz, C. Dohna-Schwake, and N. Bruns



ABSTRACT

BACKGROUND AND PURPOSE: Vein of Galen malformation is a rare congenital cerebrovascular malformation. In affected patients, increased cerebral venous pressure constitutes an important etiologic factor for the development of brain parenchymal damage. The aim of this study was to investigate the potential of serial cerebral venous Doppler measurements to detect and monitor increased cerebral venous pressure.

MATERIALS AND METHODS: This was a retrospective monocentric analysis of ultrasound examinations within the first 9 months of life in patients with vein of Galen malformation admitted at <28 days of life. Categorization of perfusion waveforms in the superficial cerebral sinus and veins into 6 patterns was based on antero- and retrograde flow components. We performed an analysis of flow profiles across time and correlation with disease severity, clinical interventions, and congestion damage on cerebral MR imaging.

RESULTS: The study included 44 Doppler ultrasound examinations of the superior sagittal sinus and 36 examinations of the cortical veins from 7 patients. Doppler flow profiles before interventional therapy correlated with disease severity determined by the Bicêtre Neonatal Evaluation Score (Spearman $\rho = -0.97$, $P = < .001$). At this time, 4 of 7 patients (57.1%) showed a retrograde flow component in the superior sagittal sinus, whereas after embolization, none of the 6 treated patients presented with a retrograde flow component. Only patients with a high retrograde flow component (equal or more than one-third retrograde flow, $n = 2$) showed severe venous congestion damage on cerebral MR imaging.

CONCLUSIONS: Flow profiles in the superficial cerebral sinus and veins appear to be a useful tool to noninvasively detect and monitor cerebral venous congestion in vein of Galen malformation.

ABBREVIATIONS: AV = arteriovenous; BNES = Bicêtre Neonatal Evaluation Score; cMRI = cerebral MR imaging; FP = flow profile; MPV = median prosencephalic vein of Markowski; SSS = superior sagittal sinus; US = ultrasound; VGAM = Vein of Galen (aneurysmal) malformation

Vein of Galen (aneurysmal) malformation (VGAM) is a rare, complex, congenital cerebrovascular malformation. Arteriovenous (AV) fistulas or malformations between the persistent median prosencephalic vein of Markowski (MPV) and various arterial

feeding vessels or both result in intracerebral shunts between the arterial and venous systems.¹ This arteriovenous connection causes a loss of cerebral arterial resistance with redistribution of blood to the detriment of the brain and other organ systems, sometimes culminating in high-output cardiac failure. Despite modern therapeutic interdisciplinary interventions, the mortality in neonatal manifestation is approximately 40%, and 50% of survivors have poor neurodevelopmental outcomes.²⁻⁴

Besides reduced arterial cerebral organ perfusion, increased cerebral venous pressure plays a key role in the development of progressive parenchymal brain damage. Arterialization of the MPV and the cerebral sinus causes a massive increase in cerebral venous pressure, with subsequent functional outflow obstruction, leading to congestion, venous ischemia, and hydrocephalus mal-resorptivus.⁵⁻⁸ Cerebral venous hypertension can be exacerbated by high venous return due to excessive shunt volumes with cardiac volume overload and backward failure of the right heart.⁹

Received February 14, 2023; accepted after revision May 3.

From the Clinic for Pediatrics and Adolescent Medicine (S.S., F.B.N., A.F., T.R.), Clinic for Radiology and Neuroradiology (N.R.D., F.B., M.S.-H., K.S.), and Center for Pediatric Interventional Radiology/Neuroradiology and Interventional Treatment of Vascular Malformations (F.B.), Sana Clinics Duisburg, Duisburg, Germany; and Clinic for Pediatrics I (U.F.-M., C.D.-S., N.B.) and Centre for Translational Neuro- and Behavioural Sciences (U.F.-M., C.D.-S., N.B.), University Hospital Essen, University of Duisburg-Essen, Essen, Germany.

Please address correspondence to Simone Schwarz, MD, Clinic for Pediatrics and Adolescent Medicine, Neonatal and Pediatric Intensive Care Unit, Sana Clinics Duisburg, Zu den Rehwiesen 9-11, 47055 Duisburg, Germany; e-mail: simone.schwarz@sana.de

Indicates open access to non-subscribers at www.ajnr.org

Indicates article with online supplemental data.

<http://dx.doi.org/10.3174/ajnr.A7891>

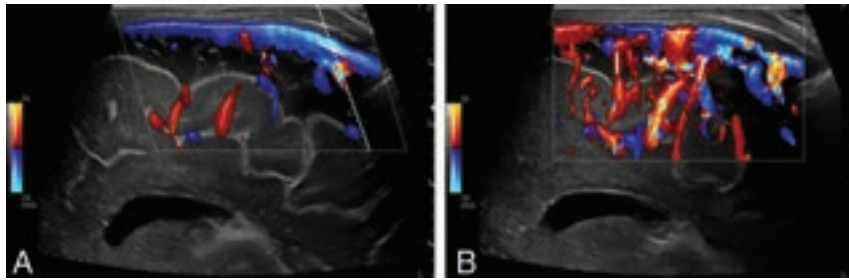


FIG 1. Doppler imaging protocol of the SSS and cortical veins in a median sagittal section. A, SSS in median sagittal section in color-coded Doppler US with tilted Doppler beam (*dotted line*) and corresponding angular correction (*white line*). B, Cortical arteries and veins in sagittal section in color-coded Doppler US show possible measurement points (*white lines*).

Furthermore, a maturation disorder of the sinu-jugular connection due to flow stress in the vessel wall may lead to bilateral stenosis of the jugular bulb, further increasing cerebral venous pressure.^{10–12} Thus, venous congestion may persist even after marked reduction of the shunt volume.

Cerebral venous congestion leads mainly to white matter injury and subependymal atrophy, making it one of the main factors for progressive brain damage in VGAM.^{3,10} To date, there is no tool for early noninvasive detection and serial assessment of cerebral venous congestion. Currently, the best method is cerebral MR imaging (cMRI), which only shows indirect signs and direct parenchymal damage due to chronic venous congestion, such as congested veins, congestive edema, microhemorrhages, calcifications, and atrophy.^{13–15}

The aim of this study was to investigate the potential of serial venous ultrasound (US) Doppler measurements to detect and monitor increased cerebral venous pressure in VGAM.

MATERIALS AND METHODS

This retrospective, monocentric study included all neonates with VGAM younger than 28 days admitted to the tertiary care neonatal intensive care unit at the Sana Hospital Duisburg between January and June 2022. All examinations were performed by a board-certified neonatologist with >10 years of experience in cerebral US and Doppler US (S.S.) according to a standardized local protocol.

Eligible patients were identified via the electronic patient administration system, and clinical data were collected from the digital patient management systems including the PACS. The Bicêtre Neonatal Evaluation Score (BNES), a validated clinical score with therapeutic and prognostic significance, was recorded before the first cMRI to assess disease severity (Online Supplemental Data).^{16,17}

Approval of the study was granted by the Ethics Committee of the Medical Faculty of the University Hospital Essen (22–10801-BO).

US Protocol

To assess the time course of US Doppler flow profiles (FPs), we analyzed the examination before the first cMRI (T1), after the first cMRI/embolization (T2), after 5–7 days (T3), and before discharge (T4) of each patient during the first inpatient stay. After discharge, the available examinations were evaluated on an individual basis.

All US scans were obtained using 1 of 2 high-end US machines (LOGIQ S8/LOGIQ E10s R3; GE Healthcare) equipped with high-resolution linear transducers (ML5-15-D or ML4-20-D; GE Healthcare). Venous cerebral US Doppler flow measurements were documented only in calm, preferably sleeping, infants. US Doppler FPs in the superior sagittal sinus (SSS) were recorded using a median sagittal section (Fig 1). First, the SSS was visualized in a longitudinal section at a low penetration depth in B-mode and color-coded Doppler US with flow displayed over the entire vessel

section. Next, an angle-corrected pulsed Doppler time-frequency analysis of intravascular flow in a far posterior vessel segment before the junction of any VGAM drainage veins was performed. The sample volume was adapted until the entire width of the vessel was captured. Visual and acoustic reassurance of an optimal time-frequency Doppler signal ensured that the sample volume passed through the center of the vessel. Doppler FPs in the cortical veins were measured with the same transducer, following the same optimization steps (Fig 2B). The FPs were only evaluated for this study if the Doppler flow curves had sufficient image quality, ie, correct positioning of the sample volume, correct wall filter, correct pulse repetition frequency, and sufficient Doppler signal for at least 5 seconds.

Classification of US Doppler FPs

Following Ikeda et al,¹⁸ the FPs were classified into 6 different types (Fig 2): FP1: low alterations of the flow amplitude, minimum velocity never less than half of the maximum velocity; FP2: increased undulation, minimum speed less than half of the maximum speed; FP3: increased undulation, minimum speed dropping to 0 cm/s or retrograde flow; FP4: retrograde flow component with pulsatile retrograde flow; FP5: high retrograde flow, equal or more than one-third retrograde flow of the total Doppler flow; and FP6: complete retrograde flow.

MR Imaging

Timing of endovascular therapy was determined by interdisciplinary consensus based on clinical and sonographic findings. The first cMRI was performed with the patient under the same anesthesia as in the first procedure. Assessment of the first cMRI and the follow-up cMRI after 1–10 months was retrospectively performed by an experienced neuroradiologist (N.R.D.), blinded to the clinical course using a structured report and a previously described scoring system for structural brain abnormalities.¹⁹ Damage to the brain parenchyma was classified as no lesion, mild lesion, moderate lesion, and severe lesion. All structural abnormalities were documented, especially signs of brain atrophy, medullary lesions, ischemic or hemorrhagic infarcts or their remnants, hemorrhages, and damage due to venous congestion.

Endovascular Therapy

In most centers, endovascular therapy of a VGAM is performed via a transarterial approach with exclusive embolization of the arterial feeders apart from the point of shunting. According to our clinical routine, combined therapy with arterial and venous

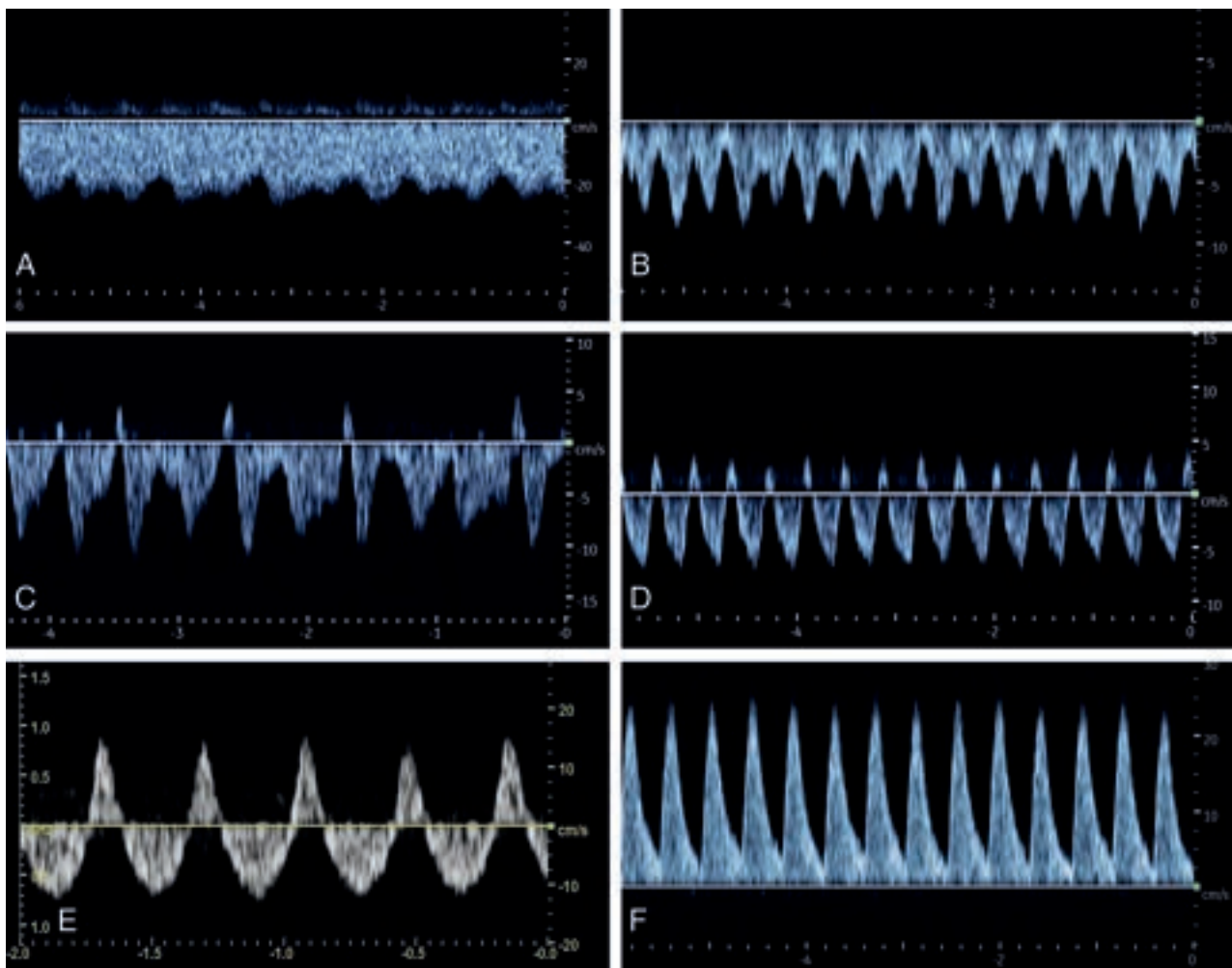


FIG 2. Classification of Doppler FPs of the SSS in neonates with vein of Galen malformation. *A*, FP1: Doppler FP with low fluctuation, minimum velocity, never less than half of the maximum velocity. *B*, FP2: Increased fluctuations of the flow velocities with minimum velocity less than half of the maximum velocity. *C*, FP3: Doppler FP with intermittent retrograde flow. *D*, FP4: Doppler FP with pulsatile retrograde flow. *E*, FP5: Doppler FP with a high retrograde flow (equal or more than one-third retrograde flow of the total Doppler flow). *F*, FP6: Doppler FP with complete retrograde flow.

access was performed for precise occlusion of AVFs, with high flow exactly at the shunting point with coils and/or ethylene-vinyl alcohol. To obtain direct access to the inflowing artery at the entry point of the dilated persistent MPV, we introduced superselective arterial feeder probing in combination with retrograde transvenous access using the “looping technique” or “kissing microcatheter technique.”²⁰

Statistical Analyses

Categoric variables are summarized as counts and relative frequencies; continuous variables are presented as median and range. The Spearman ρ was calculated to assess the association of FPs in the SSS and BNES. SAS Enterprise Guide 8.3 (SAS Institute) was used to perform statistical analyses.

RESULTS

A total of 7 neonates with VGAM with a median gestational age of 38 1/7 (range, 34 2/7–41 6/7) and a median birth weight of 3380 g (range, 2220–4250 g) were admitted in the study period (Fig 3 and Online Supplemental Data). They were admitted as

inpatients at a median age of 2 days (range, 1–13 days) with a median BNES of 18 (range, 7–21). According to Lasjaunias,¹⁶ 3 of 7 (42.9%) of the AV malformations were choroidal, 3 of 7 (42.9%) were mural, and 1 of 7 (14.3%) was a mixed type.¹⁷

One patient was treated palliatively due to severe brain parenchymal damage at the initial presentation and died in the second week of life. All other patients underwent endovascular therapy at a median of 4.5 days (range, 1–14 days) after birth in the Department of Interventional Neuroradiology and were discharged alive. One neonate experienced intraventricular hemorrhage and posthemorrhagic hydrocephalus after the intervention. No other neonates developed complications from the procedure (Online Supplemental Data).

US Doppler Flow Measurements during Initial Therapy

All 7 patients underwent a standardized US before and 1 day after the first embolization and after cMRI in the palliative case (T1 + T2). All survivors were examined before discharge (T4), and 5 of the 6 survivors underwent an additional examination 5–7 days after embolization (T3). Thus, 26 Doppler US examinations of

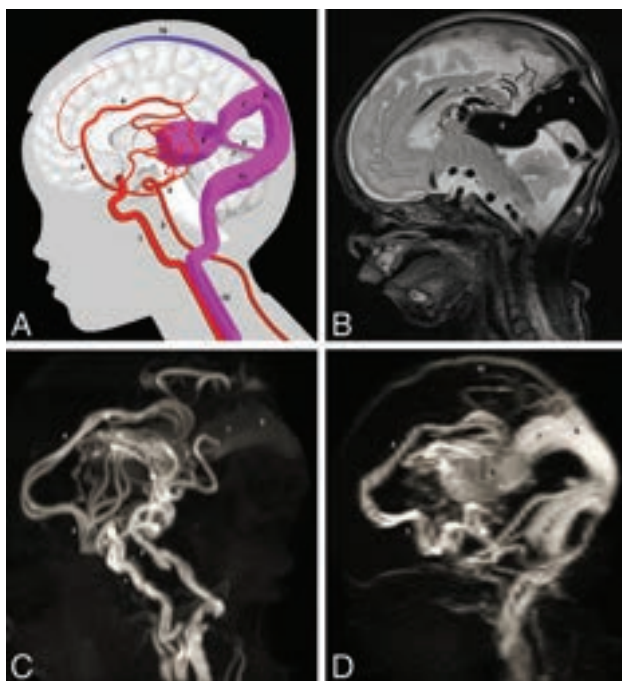


FIG 3. Scheme and MR imaging of a VGAM. A, Simplified scheme of VGAM. B, Sagittal T2-weighted MR image. C, Arterial TOF-MRA. D, Venous TOF-MRA. 1) internal carotid artery; 2) basilar artery; 3) anterior cerebral artery; 4) pericallosal artery; 5) posterior cerebral artery; 6) dilated MPV; 7) falcine sinus; 8) straight sinus; 9) accessory confluence; 10) SSS; 11) transverse sinus; 12) internal jugular vein.

the SSS and 25 examinations of the cortical veins were included in this analysis (Fig 4A).

Overall, 4 of 7 (57.1%) of the Doppler flow measurements at T1 showed a retrograde flow component in the SSS. After embolization, no patient had a retrograde flow component. One week after the first embolization, patient 5 developed an increasing retrograde flow component that progressed to complete retrograde flow in the SSS and cortical veins until discharge.

At all time points, correlating abnormal FPs in the cortical veins were observed only when the SSS had a high retrograde flow component (FP5 + 6) (Online Supplemental Data).

Before interventional therapy, US Doppler FPs correlated with disease severity determined by BNES ($\rho = -0.97$; 95% CI, -0.995 to -0.787 ; $P = < .0001$). Pathologic FPs occurred more frequently with low BNESs (Fig 4B).

Correlation to Congestion Damage on cMRI

Only 2 patients showed severe venous congestion damage on cMRI (Online Supplemental Data). Patient 1 showed severe cerebral damage on the first cMRI. Patient 5 showed cerebral injury with moderate atrophy, white matter damage, and hydrocephalus ex-vacuo and malresorptivus due to venous congestion on the second MR imaging. Both patients had high or complete retrograde flow in the SSS and cortical veins before cMRI. No other patient showed similarly abnormal US Doppler FPs in the SSS or the cerebral veins at any time (Fig 5).

US Doppler Flow Measurements during Follow-up

Only in patient 5 could serial Doppler measurements be evaluated after discharge. In the other patients, no or only single

examinations were performed during follow-up. None of these examinations showed retrograde flow components in the SSS or the cortical veins. Finally, 21 examinations could be included in this analysis.

Patient 5 showed a highly pathologic, retrograde, arterialized FP in both the SSS and cortical veins at re-admission. This pathologic FP developed during the first hospital stay (Fig 6A and Online Supplemental Data). At discharge (at the age of 9 weeks) and re-admission (at the age of 14 weeks), the SSS showed an arterialized FP toward the frontal base. At re-admission, there was also retrograde arterialized flow in the cortical veins. Direction of flow in the SSS and the cortical veins remained unchanged even after further embolization. Severe occlusion of the venous outflow due to bilateral stenosis of sinu-jugular junctions was finally diagnosed by MR imaging and invasive angiography, followed by endovascular therapy with bilateral balloon dilation and additional stent implantation on the left side. With each dilation step, the Doppler US flow direction in the SSS and cortical veins became less arterialized until almost complete normalization at the end of the intervention (Fig 6B). The examination at re-admission due to status epilepticus at 9 months of age showed again an arterialized, retrograde flow in the SSS and cortical veins with a significant increase of cerebral damage due to venous congestion on cMRI (Online Supplemental Data). Restenosis of the sinu-jugular junction could be excluded. After $>90\%$ occlusion of the VGAM, complete normalization of the FP in the SSS was observed.

DISCUSSION

This retrospective observational study evaluated the use of US Doppler FPs of the superficial cerebral sinus and veins to detect venous congestion in VGAM serving as a bedside, broadly available, and noninvasive method for serial assessment during therapy. Sufficient occlusion of the VGAM corresponded to normalization of US Doppler FPs. Vice versa, persistent pathologic flow correlated with cerebral damage as measured on cMRI.

Normal US Doppler flow patterns of the cerebral veins are characterized by a continuous flat or sometimes slightly undulating profile. In the cerebral sinus, amplitude fluctuations up to a triphasic forward flow are more common.²¹⁻²³ These fluctuations correspond to the cardiac action and respiratory movements.²⁴ Recent advances in US technology allow the assessment of small cortical and medullary veins and analysis of intravascular flow even at low venous flow velocities.²⁵

In this study, infants with VGAM frequently showed pathologic spectral US Doppler waveforms in the SSS with retrograde flow components, preinterventionally correlating with disease severity measured by the BNES. The proportion of pathologic FPs in the SSS decreased after partial superselective embolization, likely due to effective shunt reduction with concomitant pressure reduction in the cerebral venous system.⁵

In 1 patient, retrograde arterialized flow in the SSS occurred before discharge. Retrospectively, the increasing flow reversal resembled a venous outflow occlusion caused by bilateral stenosis of the jugular bulb. Serial US examinations during the endovascular reopening demonstrated the resolution of the FP abnormalities in real-time. After 5 months, complete retrograde flow in the SSS as well as in the cortical veins reoccurred, accompanied by

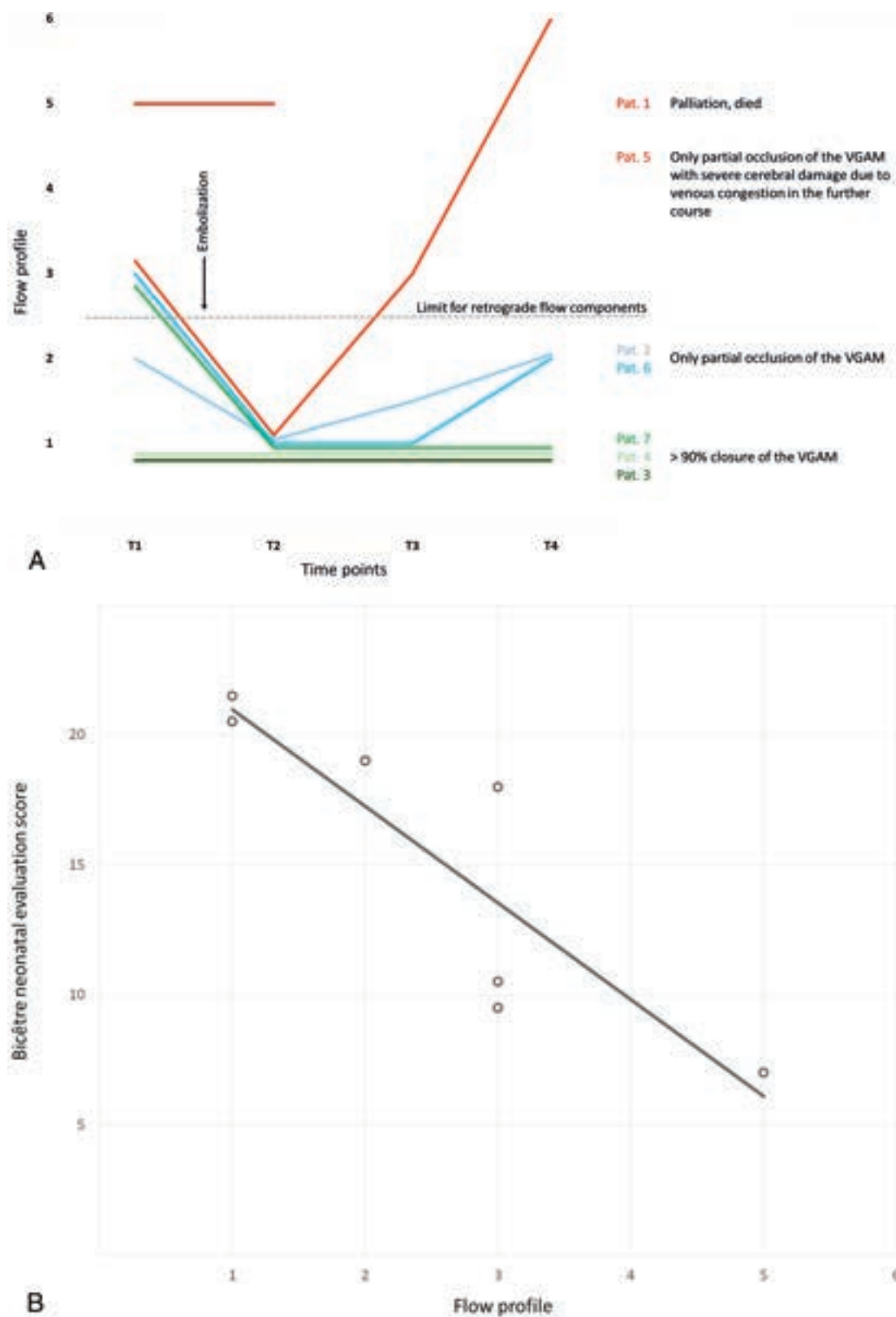


FIG 4. A, Individual course of the FPs in the SSS across time per patient. T1 = US Doppler measurement before embolization/first cMRI; T2 = US Doppler measurement 1 day after embolization/first cMRI; T3 = US Doppler measurement 5–7 days after embolization; T4 = US Doppler measurement before discharge. B, Association between Doppler FPs and BNES before therapy. Spearman rank correlation coefficient $\rho = -0.97$ (95% CI, -0.995 to -0.787 ; $P < .0001$). Pat. indicates patient.

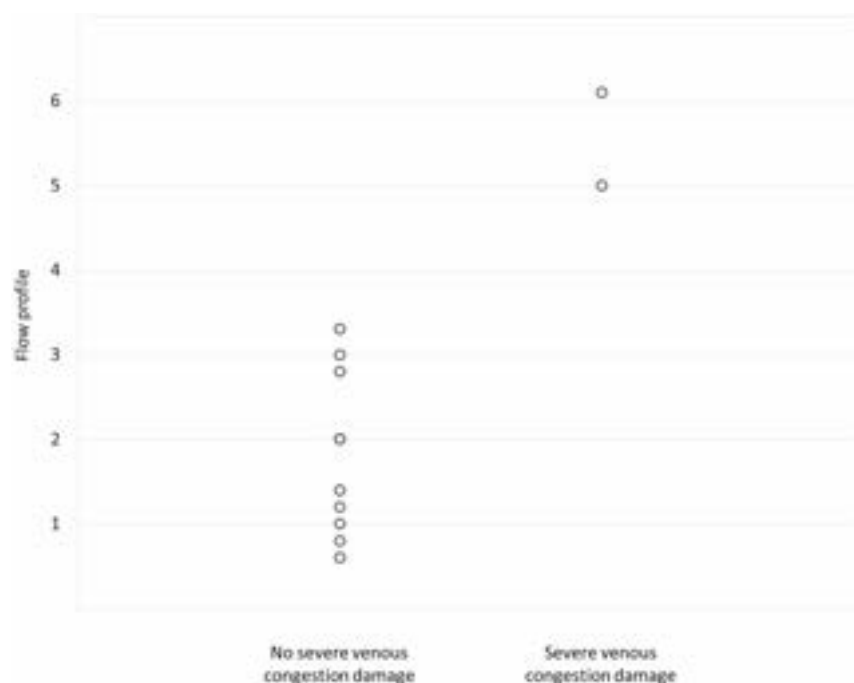


FIG 5. Relationship between the FP in the SSS at T1 and T4 and the damage due to venous congestion detectable in the first and second cMRI.

exacerbation of the cMRI findings. Consequently, almost complete embolization of the AV malformation resulted in a permanent normalization of the FPs.

A potential explanation for retrograde US Doppler flow components is the fluctuation of right atrial pressure during the cardiac cycle in patients with elevated central venous pressure. Tanaka et al²⁶ described pathologic FPs in the corresponding internal cerebral veins in 2 preterm infants with high-grade intraventricular hemorrhage. They attributed the retrograde flow components to increased venous pulsation caused by increased atrial contraction waves. The reverse flow corresponded to A and V waves, probably generated by an increase in right atrial pressure.²⁶ This may also play an important role in patients with VGAM with backward failure of the right heart. Another reason for insufficient venous outflow of the SSS in VGAM could be arterialized pressure in the confluence of sinuses or accessory confluence of sinuses. Quisling and Mickle⁶ performed invasive venous pressure measurements within the Galen aneurysm/straight sinus complex in patients with Galen AVFs and vein of Galen aneurysms. The pressure was above the normal range (<5 cm H₂O) in all cases and varied between 9 and 55 cm H₂O. Values >20 cm H₂O were associated with an increased incidence of cerebral calcifications as a typical sign of congestion damage. Venous outflow obstruction might be exacerbated by peak pressure during systole, possibly explaining the pulsatile reflux into the SSS sometimes observed.

Fluctuations in central venous pressure can be transmitted into the intracranial veins only in the absence of mechanical outflow obstruction. Probably, mechanical outflow obstruction initially leads to rising prestenotic pressure, increasing the pulsatile reflux into the SSS. Later, the complete or partial venous outflow from the AV malformation across the SSS directs the arterialized retrograde flow toward the frontal base. If the pressure in the SSS

exceeds the pressure in the afferent cortical veins, this scenario may result in a loss of normal ventriculocortical venous flow direction in the cortex and subcortical white matter. In the absence of sufficient collateral outflow tracts, this loss leads to venous congestion with subsequent parenchymal damage. Therefore, highly retrograde Doppler flow in the SSS is associated with pathologic FPs in the cortical veins and cerebral congestion damage on cMRI.

Real-time assessment of cerebral venous pressure is a diagnostic challenge. Accurate measurement can only be performed intracranially during angiography and is, therefore, not feasible as a routine diagnostic method for serial assessment. Currently, the only noninvasive tool to detect venous congestion is the appearance of indirect signs or direct parenchymal damage due to chronic venous congestion measured by cMRI.^{6,13-15} Alterations on cMRI occur as late signs when damage has already occurred. In addition, cMRI scans cannot be repeated serially due to logistic and financial limitations and frequently require sedation or even anesthesia. Noninvasive methods for serial screening, monitoring, and follow-up of venous congestion would, therefore, be of great benefit for individual therapeutic management in VGAM.

Our study is limited by the sample size and retrospective design. This limitation is because VGAM is extremely rare, with approximately 1:58 100 live births per year in Germany.²⁷ The limited number of patients limits the possibility of conducting advanced statistical analyses. Furthermore, the criterion standard used to diagnose venous congestion in this study, namely cMRI, has a time lag between the onset of venous congestion and the manifestation of parenchymal damage detectable by this method.

Intracranial venous pressure is particularly influenced by central venous pressure, which, in turn, depends on volume status, cardiac function, and right ventricular and pulmonary artery

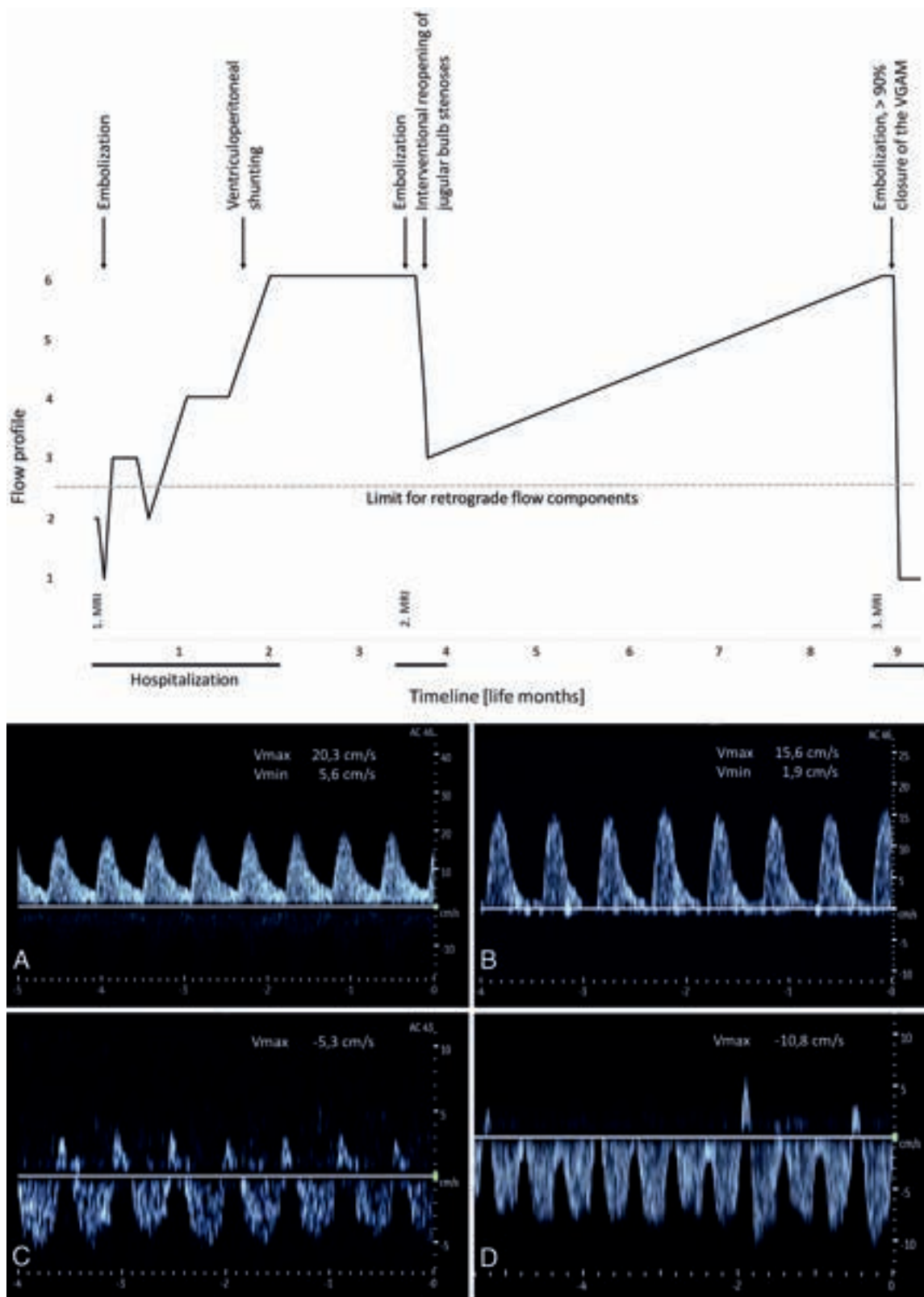


FIG 6. A, Timeline of the FPs in the SSS during 9 life months in patient 5. B, Course of Doppler FPs in the SSS under endovascular interventional therapy of stenosis of the jugular bulb in patient 5 (in the angiography room at the age of 16 weeks). A (upper left), An US Doppler FP in the SSS directly before balloon dilation on the left showing an arterialized retrograde flow. B (upper right), After balloon dilation and stent implantation on the left side decrease in flow velocities with reduced retrograde flow. C (bottom left), After additional balloon dilation on the right side, further reduction of the retrograde flow component and normalization of the flow direction. D (bottom right), At 24 hours after the procedure, further normalization of the US Doppler FP and increased undulation with minor retrograde components. Vmax indicates maximum velocity; Vmin, minimum velocity.

pressures. Therefore, both central venous pressure and cerebral venous US Doppler FPs may be affected not only by embolization itself but also by supportive measures or changes of the cardiocirculatory status. These include drug therapies (preload-lowering agents, inotropes, vasodilators, and sedation) and changes in circulatory conditions due to spontaneous closure or reopening of the ductus arteriosus (including prostaglandin E1 therapy) and must indispensably be considered when interpreting serial measurements.

Direct sonographic determination of the actual venous pressure is impossible. In VGAM, Doppler US in the SSS and cortical veins allows only a semiquantitative assessment of current hemodynamics caused by obstructed outflow of the superficial veins and thus an indirect estimate of venous congestion in the cerebral cortex. The outflow from the deep cerebral veins, which are directly affected by the increase in pressure in the persistent MPV, cannot be estimated with this method. Venous congestion leads to the formation of various venous collaterals. The veins involved in the collateral circuits exhibit sectional retrograde flow and may persist even after complete closure of all AV shunts of the VGAM, contributing to physiologic drainage of the brain parenchyma.

Yet, in patients with VGAM, US Doppler flow measurements of the superficial cerebral sinus and veins appear to have great potential to improve patient care and possibly neurologic outcome by providing the possibility of noninvasively monitoring cerebral venous hemodynamics in real-time. The data presented suggest that it is reasonable to integrate the US assessment of venous cerebral outflow in patients with VGAM into routine care. Further prospective studies should investigate the relevance of cerebral venous Doppler measurements for intensive care and endovascular therapy management in these neonates and in the prenatal diagnostics of fetuses with VGAM.

Besides this specific patient group, our study also points to the general potential of cerebral venous US Doppler flow measurements toward an understanding of cerebral venous hemodynamics in neonates. Abnormalities of venous US Doppler FPs cannot be expected only in VGAM but also in other diseases with cerebral venous outflow or upper cardiac inflow congestion. With ongoing technical advancements,²⁸ the cerebral venous system deserves increased attention both scientifically and in clinical practice to evaluate the clinical relevance of different venous Doppler waveforms in neonates with complex hemodynamic conditions.

CONCLUSIONS

Flow reversal in the SSS measured with spectral Doppler US is a promising new diagnostic parameter for the assessment of venous congestion in VGAM. Relevant retrograde flow may indicate cerebral venous outflow obstruction due to increased central or cerebral venous pressure or mechanical occlusions and should prompt further diagnostic measures. As US techniques evolve, the potential of cerebral venous Doppler waveforms should be more systematically explored.

ACKNOWLEDGMENTS

The authors would like to thank Mr Yannick Schulz for graphic assistance.

Disclosure forms provided by the authors are available with the full text and PDF of this article at www.ajnr.org.

REFERENCES

1. Raybaud CA, Strother CM, Hald JK. **Aneurysms of the vein of Galen: embryonic considerations and anatomical features relating to the pathogenesis of the malformation.** *Neuroradiology* 1989;31:109–28 CrossRef Medline
2. Taffin H, Maurey H, Ozanne A, et al. **Long-term outcome of vein of Galen malformation.** *Dev Med Child Neurol* 2020;62:729–34 CrossRef Medline
3. Lecce F, Robertson F, Rennie A, et al. **Cross-sectional study of a United Kingdom cohort of neonatal vein of Galen malformation.** *Ann Neurol* 2018;84:547–55 CrossRef Medline
4. Chow ML, Cooke DL, Fullerton HJ, et al. **Radiological and clinical features of vein of Galen malformations.** *J Neurointerv Surg* 2015;7:443–48 CrossRef Medline
5. Chang D, Babadjouni R, Nisson P, et al. **Transvenous pressure monitoring guides endovascular treatment of vein of Galen malformation: a technical note.** *Pediatr Neurosurg* 2021;56:401–06 CrossRef Medline
6. Quisling RG, Mickle JP. **Venous pressure measurements in vein of Galen aneurysms.** *AJNR Am J Neuroradiol* 1989;10:411–17 CrossRef Medline
7. Kortman H, Navaei E, Raybaud CA, et al. **Deep venous communication in vein of Galen malformations: incidence, imaging, and implications for treatment.** *J Neurointerv Surg* 2021;13:290–93 CrossRef Medline
8. Meila D, Grieb D, Melber K, et al. **Hydrocephalus in vein of Galen malformation: etiologies and therapeutic management implications.** *Acta Neurochir (Wien)* 2016;158:1279–84 CrossRef Medline
9. Cory MJ, Durand P, Sillero R, et al. **Vein of Galen aneurysmal malformation: rationalizing medical management of neonatal heart failure.** *Pediatr Res* 2023;93:39–48 CrossRef Medline
10. Saliou G, Dirks P, Sacho RH, et al. **Decreased superior sagittal sinus diameter and jugular bulb narrowing are associated with poor clinical outcome in vein of Galen arteriovenous malformation.** *AJNR Am J Neuroradiol* 2016;37:1354–58 CrossRef Medline
11. Brew S, Taylor W, Reddington A. **Stenting of a venous stenosis in vein of Galen aneurysmal malformation: a case report.** *Interv Neuroradiol* 2001;7:237–40 CrossRef Medline
12. Gupta G, Rallo MS, Goldrich DY, et al. **Management of jugular bulb stenosis in pediatric vein of Galen malformation: a novel management paradigm.** *Pediatr Neurosurg* 2021;56:584–90 CrossRef Medline
13. Alvarez H, Garcia Monaco R, Rodesch G, et al. **Vein of Galen aneurysmal malformations.** *Neuroimaging Clin N Am* 2007;17:189–206 CrossRef Medline
14. Issa R, Barakat A, Salman R, et al. **Vein of Galen malformation, a cause of intracranial calcification: case report and review of literature.** *J Radiol Case Rep* 2019;13:13–18 CrossRef Medline
15. El Mekabaty A, Pearl MS, Mershon B, et al. **Susceptibility weighted imaging in infants with staged embolization of vein of Galen aneurysmal malformations.** *J Neuroradiol* 2019;46:214–21 CrossRef Medline
16. Lasjaunias PL. *Vascular Diseases in Neonates, Infants and Children: Interventional Neuroradiology Management.* Springer-Verlag; 1997
17. Lasjaunias PL, Chng SM, Sachet M, et al. **The management of vein of Galen aneurysmal malformations.** *Neurosurgery* 2006;59:S184–94; discussion S3–13 CrossRef Medline
18. Ikeda T, Amizuka T, Ito Y, et al. **Changes in the perfusion waveform of the internal cerebral vein and intraventricular hemorrhage in the acute management of extremely low-birth-weight infants.** *Eur J Pediatr* 2015;174:331–38 CrossRef Medline
19. Woodward LJ, Anderson PJ, Austin NC, et al. **Neonatal MRI to predict neurodevelopmental outcomes in preterm infants.** *N Engl J Med* 2006;355:685–94 CrossRef Medline
20. Meila D, Hannak R, Feldkamp A, et al. **Vein of Galen aneurysmal malformation: combined transvenous and transarterial method using a “kissing microcatheter technique.”** *Neuroradiology* 2012;54:51–59 CrossRef Medline

21. Dean LM, Taylor GA. **The intracranial venous system in infants: normal and abnormal findings on duplex and color Doppler sonography.** *AJR Am J Roentgenol* 1995;164:151–56 CrossRef Medline
22. Liu LY, Hong JL, Wu CJ. **A preliminary study of neonatal cranial venous system by color Doppler.** *Biomed Res Int* 2019;2019:7569479 CrossRef Medline
23. Taylor GA. **Intracranial venous system in the newborn: evaluation of normal anatomy and flow characteristics with color Doppler US.** *Radiology* 1992;183:449–52 CrossRef Medline
24. Deeg KH. **Duplex sonographic diagnosis of perinatal hemorrhagic stroke.** *Ultraschall Med* 2017;38:484–98 CrossRef Medline
25. Parodi A, Govaert P, Horsch S, et al; eurUS.brain group. **Cranial ultrasound findings in preterm germinal matrix haemorrhage, sequelae and outcome.** *Pediatr Res* 2020;87:13–24 CrossRef Medline
26. Tanaka K, Sakamoto R, Imamura H, et al. **Reversal of blood flow in deep cerebral vein in preterm intraventricular hemorrhage: two case reports.** *BMC Pediatr* 2020;20:517 CrossRef Medline
27. Brevis Nunez F, Dohna-Schwake C. **Epidemiology, diagnostics, and management of vein of Galen malformation.** *Pediatr Neurol* 2021;119:50–55 CrossRef Medline
28. Baranger J, Demene C, Frerot A, et al. **Bedside functional monitoring of the dynamic brain connectivity in human neonates.** *Nat Commun* 2021;12:1080 CrossRef Medline

Subarachnoid Space Measurements in Apparently Healthy Fetuses Using MR Imaging

A. Wandel, T. Weissbach, E. Kotorza, and T. Ziv-Baran



ABSTRACT

BACKGROUND AND PURPOSE: The fetal subarachnoid space size serves as an indicator of normal brain development. The subarachnoid space is commonly measured by an ultrasound examination. Introduction of MR imaging for fetal brain evaluation enables standardization of MR imaging–driven subarachnoid space parameters for a more accurate evaluation. This study aimed to determine the normal range of MR imaging–derived subarachnoid space size in fetuses according to gestational age.

MATERIALS AND METHODS: A cross-sectional study based on a retrospective assessment of randomly selected brain MR images of apparently healthy fetuses performed between 2012 and 2020 at a large tertiary medical center was performed. Demographic data were collected from the mothers' medical records. Subarachnoid space size was measured at 10 reference points using the axial and coronal planes. Only MR imaging scans obtained between weeks 28 and 37 of pregnancy were included. Scans with low-quality images, multiple pregnancy, and cases with intracranial pathologic findings were excluded.

RESULTS: Overall, 214 apparently healthy fetuses were included (mean maternal age, 31.2 [SD, 5.4] years). Good interobserver and intraobserver agreement was observed (intraclass correlation coefficient > 0.75 for all except 1 parameter). For each gestational week, the 3rd, 15th, 50th, 85th, and 97th percentiles of each subarachnoid space measurement were described.

CONCLUSIONS: MR imaging–derived subarachnoid space values at a specific gestational age provide reproducible measurements, probably due to the high resolution of MR imaging and adherence to the true radiologic planes. Normal values for brain MR imaging could provide valuable reference information for assessing brain development, thus being an important tool in the decision-making process of both clinicians and parents.

ABBREVIATIONS: GA = gestational age; ICC = intraclass correlation coefficient; SAS = subarachnoid space; US = ultrasound

The subarachnoid space (SAS) is located between the arachnoid membrane and the pia mater. Trabecular delicate connective tissue and intercommunicating channels containing CSF fill this space.^{1–4} Normally, the cavity is small. An enlarged cavity is associated with CNS malformations and syndromes, including macrocephaly, communicating hydrocephalus, brain atrophy, and benign enlargement of the SASs.^{2–4} A normal-sized SAS reflects normal brain development with intact production and

absorption of CSF. Assessment of macrocephaly resulting from macrocrania, hydrocephalus, or SAS abnormality^{5,6} is based on the occipitofrontal circumference and defined as a head circumference of 2 SDs above the mean or the 98th percentile for gestational age (GA).⁷ Evaluation of head circumference is also important for indicating the need for a cesarean delivery when the increased head circumference may impair vaginal delivery.⁸ Previous studies reported measurements of the SAS in neonates, infants, and children, using different imaging methods such as ultrasound (US),^{9–14} CT,^{15–17} and MR imaging.¹⁸ Only a few studies have described the range of the normal SAS at the prenatal period, which was measured by transabdominal US,^{19,20} transvaginal US,^{9,21} and in only one study by MR imaging.²²

There are some technical limitations for the US examinations. Pilu et al²⁰ reported that after 29 weeks of pregnancy, the Sylvian cistern could not be detected as a fluid-filled space; after 30–32 weeks, a decreased size of the fetal cisterns and the increased calcification of the fetal calvaria make it difficult to precisely evaluate the SAS.^{18,20} Transabdominal US is associated with technical

Received February 11, 2023; accepted after revision April 4.

From the Sackler School of Medicine (A.W., T.W., E.K.) and School of Public Health (T.Z.-B.), Sackler Faculty of Medicine, Tel Aviv University, Tel Aviv, Israel; Department of Diagnostic Radiology (A.W.), Shamir Medical Center, Zerifin, Israel; and Antenatal Diagnostic Unit (T.W., E.K.), Department of Obstetrics and Gynecology, and Gertner Institute for Epidemiology and Health Policy Research (E.K.), Sheba Medical Center, Tel HaShomer, Israel.

E. Kotorza and T. Ziv-Baran contributed equally to this work.

Please address correspondence to Ayelet Wandel, MD, Sackler School of Medicine, Tel Aviv University, Tel Aviv, Israel; e-mail: ayeletwandel@yahoo.com

Indicates article with online supplemental data.

<http://dx.doi.org/10.3174/ajnr.A7864>

difficulties in obtaining the coronal planes. Corbacioglu Esmer et al⁹ described the normal SAS value of 154 fetuses, though it was possible to evaluate the sinocortical width in only 88% of fetuses and the anterior craniocortical width in only in 78% of fetuses. Maligner et al²¹ reported a better ability to evaluate the SAS using transvaginal US and concluded that dilation of the SAS alerts obstetricians to a possible intracranial pathology requiring further investigation. Later, they described a limited measurement accuracy of the head circumference of prenatal US and demonstrated an inconsistency between prenatal and postnatal head circumferences.¹⁹ Yaniv et al²³ reported discrepancy in fetal head biometry between US and MR imaging performed in fetuses with suspected microcephalus. These reports are consistent with the known advantages and disadvantages of the US compared with the MR imaging examination of the fetal brain.²³ To the best of our knowledge, a wide-scale evaluation of the normal measurements of the SAS is still unavailable. Therefore, the purpose of this study was to establish normal values of the SAS in the fetal brain measured using MR imaging during 28–37 gestational weeks.

MATERIALS AND METHODS

Research Design and Subjects

A cross-sectional study based on a retrospective assessment of randomly selected brain MR images of apparently healthy fetuses obtained at 28–37 weeks of pregnancy was performed. All scans were obtained between 2012 and 2020 at Sheba Medical Center, a large tertiary referral, university-affiliated medical center. Demographic data were collected from mothers' medical records. Only good-quality images in terms of alignment, sharpness, and well-defined planes were included.

Approximately 20 scans were selected for each week of pregnancy. GA at MR imaging was calculated from the last menstruation and as corrected by the crown-rump length measured on an US performed in the first trimester. Women with multiple pregnancy and cases with intracranial pathologic findings at MR imaging that may indicate a CNS abnormality were excluded from the study. Fetuses with isolated mild extracranial anomalies, maternal cytomegalovirus infection without evidence of fetal involvement, and healthy fetuses with a maternal history of anomalies in previous gestations were included, as was acceptable in similar studies.^{24,25} For fetuses that underwent multiple MR imaging, only 1 scan was included.

MR Imaging Technique

Fetal brain MR images were obtained using a 1.5T system (Optima MR450w with GEM Suite; GE Healthcare). Examination protocol consisted of single-shot fast spin-echo T2-weighted images in 3 orthogonal planes. T1-weighted fast-spoiled gradient-echo sequences in the axial plane using a half-Fourier technique (number of excitations = 0.53) were performed with the following parameters: section thickness of 3 mm, no gap, flexible coil (8-channel cardiac coil). The FOV was determined by the size of the fetal head with a range of 240 × 240 mm to 300 × 300 mm; acquisition time was between 40 and 45 seconds with matrix = 320/224, TE = 90 ms, TR = 1298 ms, pixel bandwidth =

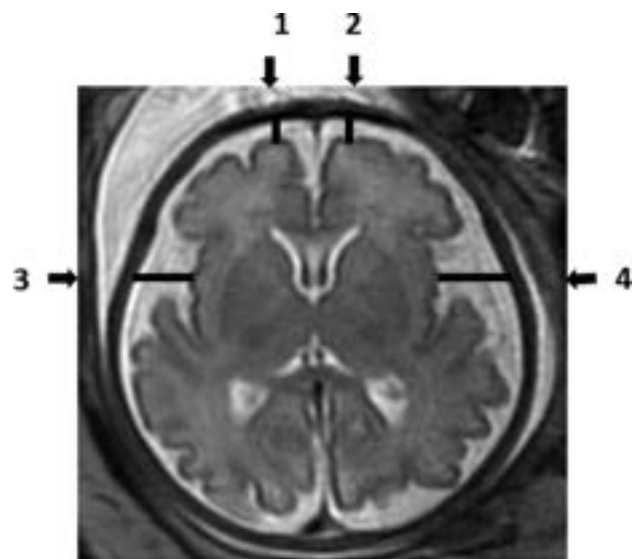


FIG 1. Axial T2-weighted fetal brain image demonstrating the measurements of the subarachnoid space: 1) Right frontal gyrus. 2) Left frontal gyrus. 3) Right insula gyrus. 4) Left insula gyrus.

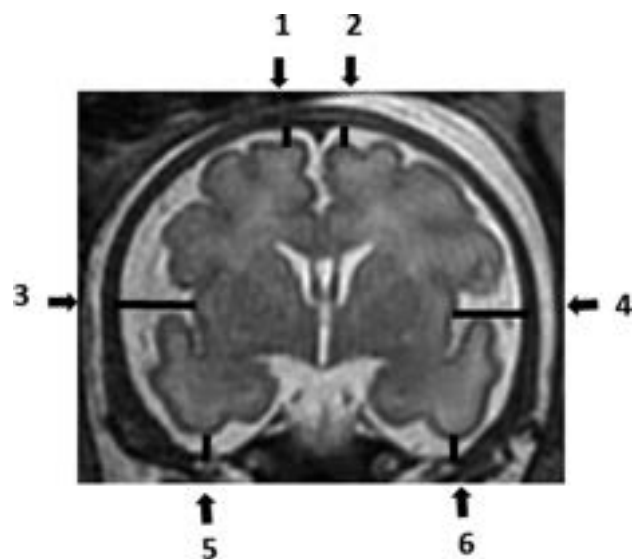


FIG 2. Coronal T2-weighted fetal brain image demonstrating the measurements of the subarachnoid space: 1) Right frontal gyrus. 2) Left frontal gyrus. 3) Right insula gyrus. 4) Left insula gyrus. 5) Right inferior temporal gyrus. 6) Left inferior temporal gyrus.

122 Hz/pixel; specific absorption rate values = 1.1–1.7 W/kg. DWI sequence and the calculated ADC map were included.^{25,26}

Measurements

Each MR imaging examination was routinely read by 2 expert physicians to detect any abnormality. Measurements of the SAS size, which was identified by a high signal (white color) at T2-weighted imaging, were analyzed manually by a single reader (A.W.) on the PACS reading workstation. Measurements were recorded in 2D slices. The SAS was measured in millimeters, in 4 locations of the axial section (Fig 1), and in 6 locations of the coronal section (Fig 2). All measurements were obtained at the level

of midinsula from the cortex to the internal margin of the cranium as shown in Figs 1 and 2: axial section - right frontal gyrus, left frontal gyrus, right insula gyrus, left insula gyrus; coronal section - right frontal gyrus, left frontal gyrus, right insula gyrus, left insula gyrus, right inferior temporal gyrus, and left inferior temporal gyrus.

For the evaluation of interobserver agreement, 40 random fetuses (3–4 cases per each gestational week) were remeasured by another operator (T.W.).

A previous study showed that the SAS was not associated with fetal sex.⁹ Therefore, fetuses whose sex could not be determined were also included in the study.

Statistical Methods

The intraclass correlation coefficient (ICC) was used to evaluate the intraobserver and interobserver agreement. Intraclass correlation values were considered according to previously published threshold values. Intraclass correlation values of <0.5, between 0.5 and 0.75, between 0.75 and 0.9, and >0.90 were considered poor, moderate, good, and excellent reliability, respectively.²⁷ A histogram and a quantile-quantile plot were applied to define the distribution of each SAS measurement. Measurement percentiles were generated using the Generalized Additive Model for Location, Scale, and Shape. Models for normal or log-normal distributions with cubic spline smoothing were built. The paired samples *t* test and Mann-Whitney test were used to compare the left and right sides. All statistical analyses were performed with R statistical and computing software (Version 4.1.0, 2021; <http://www.r-project.org/>).

Ethics Approval

The study was approved by the institutional review board. Informed consent was waived because of the retrospective nature of the study.

RESULTS

Two hundred fourteen fetuses who had met the inclusion criteria were measured; 101 fetuses were male, 70 were female, and for 43 fetuses, sex was not recorded. The mean maternal age was 31.2 (SD, 5.4) years. The number of fetuses analyzed in each gestational week ranged between 19 and 26 (Online Supplemental Data).

Forty random fetuses were remeasured to evaluate the intra- and interobserver agreement. Overall, good intra- and interobserver agreement was observed. Excellent, good, and moderate intraobserver agreement was observed in 4, 5, and 1 measurement, respectively. Similarly, excellent, good, and moderate interobserver agreement was observed in 2, 6, and 2 measurements, respectively. ICC values are presented in the Table.

The fetuses' measurements were used to evaluate the SAS percentiles. Percentiles according to GA are detailed in the Online Supplemental Data, while the 3rd, 15th, 50th, 85th, and 97th percentiles are summarized in Online Supplemental Data and presented in Figs 3 and 4.

Figure 3 shows an increase in the axial left and right frontal space up to a GA of 31 weeks, with a decrease at a higher GA. Figure 4 demonstrates measurements of the coronal left and right insula, which reached the highest values at 31 weeks of pregnancy and sharply decreased at higher GAs. Measurements of the right and left insula in both axial and coronal views showed a small

Intraobserver and interobserver agreement

Type of Agreement and SAS Location	ICC (95% CI)
Intraobserver	
Ax. Rt. Fr.	0.761 (0.573–0.870)
Ax. Lt. Fr.	0.670 (0.431–0.816)
Ax. Rt. In.	0.865 (0.760–0.926)
Ax. Lt. In.	0.869 (0.762–0.929)
Cr. Rt. Fr.	0.942 (0.889–0.969)
Cr. Lt. Fr.	0.950 (0.908–0.973)
Cr. Rt. In.	0.911 (0.737–0.962)
Cr. Lt. In.	0.933 (0.767–0.973)
Cr. Rt. It.	0.890 (0.803–0.940)
Cr. Lt. It.	0.877 (0.780–0.933)
Interobserver	
Ax. Rt. Fr.	0.742 (0.562–0.854)
Ax. Lt. Fr.	0.700 (0.499–0.830)
Ax. Rt. In.	0.858 (0.740–0.923)
Ax. Lt. In.	0.877 (0.718–0.941)
Cr. Rt. Fr.	0.913 (0.842–0.953)
Cr. Lt. Fr.	0.893 (0.807–0.942)
Cr. Rt. In.	0.884 (0.792–0.937)
Cr. Lt. In.	0.919 (0.852–0.956)
Cr. Rt. It.	0.893 (0.808–0.942)
Cr. Lt. It.	0.890 (0.798–0.941)

Note:—Ax. indicates axial; Cr., coronal; Fr., frontal; It., inferior temporal; In., Insula; Lt., left; Rt., right.

increase at 32 weeks of pregnancy but can be considered constant in all GAs analyzed.

There were no significant differences between left- and right-sided measurements in the axial section of the frontal location ($P = .893$) as well as the coronal section of the insula ($P = .610$) and inferior temporal space ($P = .975$). Nonclinical-but-statistically significant differences were observed in axial section at the insula (mean difference = 0.14 mm, $P = .007$) and in the coronal section at the frontal location (mean difference = 0.05 mm, $P = .002$).

DISCUSSION

MR imaging is considered the most exact noninvasive technique to assess structures of the developing brains of fetuses.^{28,29} A systematic review revealed that MR imaging confirmed US-positive findings in 65.4% of the fetuses and provided additional information for about 22.1% of the fetuses. MR imaging gave additional information that changed the clinical management in 30% of fetuses. The review also reported a sensitivity of 97% (95% CI, 95%–98%) and specificity of 70% (95% CI, 58%–81%) in the MR images.³⁰ The ability of MR imaging to detect brain abnormalities that had not been found during US examinations increases the use of MR imaging. The ability of MR imaging to accurately demonstrate the SAS measurements makes it essential to widely determine the normal values of the SAS.

To date, only Watanabe et al²² reported an MR imaging evaluation of the healthy fetal SAS in 2005. The data by Watanabe et al on SAS MR imaging measurements were published more than 15 years ago, and since then, MR imaging technology has evolved to higher resolutions. Moreover, Watanabe et al evaluated the SAS measurement at 3 locations only (frontal, parietal, and cisterna magna). Therefore, there are limited data on the normal

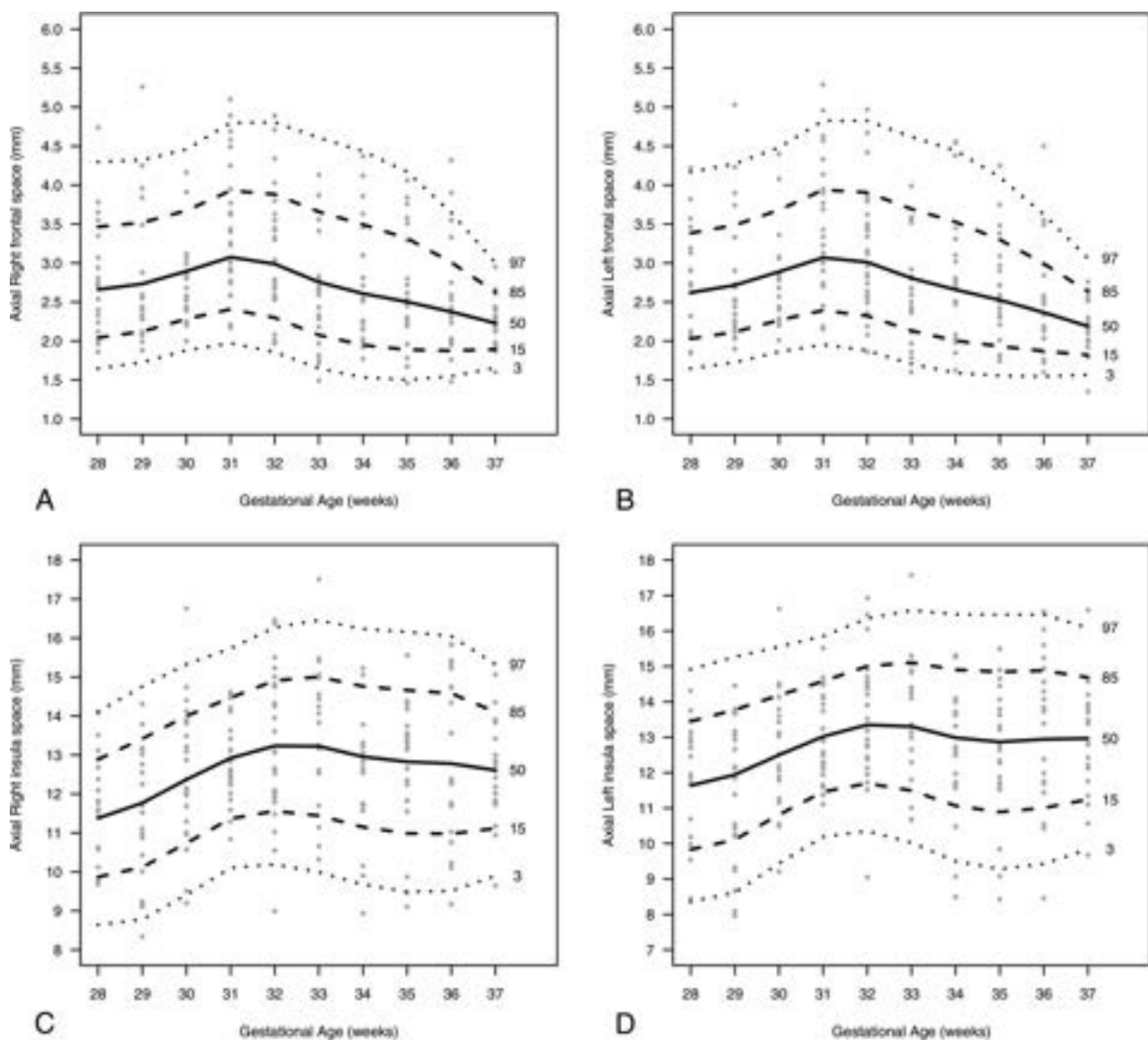


FIG 3. A nomogram presenting the SAS size (millimeters) in the axial plane according to the 3rd, 15th, 50th, 85th, 97th percentiles and GA (weeks). A, Right frontal. B, Left frontal. C, Right insula; D, Left insula.

size of the SAS, and most of the previous research was based on US examinations. In MR imaging, T2-weighted images provide an accurate demonstration of the CSF within the SAS, which enables more precise measurements.²² Hence, the current study aimed to define MR imaging–derived measurements of the SAS in fetuses with apparently normal brains, in an attempt to provide normal valuable reference data for the SAS during the pregnancy.

In an attempt to compare available literature, we found that MR imaging has provided similar data for SAS measurements and a good agreement with previously published data.²² As mentioned above, the previous study used 3 reference areas only (frontal SAS in an axial scan, parietal SAS in an axial scan, and the cisterna magna in a sagittal scan), while the current study uses 10 well-demarcated anatomic measurements.²²

The distribution of CSF across the brain is uneven; therefore, a measurement of 10 well-established anatomic points enables a

precise assessment of brain development. The 10 locations for measurements enable overcoming artifacts caused by movement and better assessment of the SAS.

US examination is a real-time, safe exploration and has been a low-cost means of diagnosis for many years. The image quality of the US is operator-dependent and can be hampered by maternal obesity, decreased amniotic fluid, fetal positioning, and calvarial ossification. In addition, its relative lack of diagnostic specificity usually requires MR imaging detection of US abnormalities.³¹ Transabdominal and transvaginal US depict the SAS measurements in 2 axial sections only (sinocortical and craniocortical width).^{9,21} The use of MR imaging for evaluation of the fetal brain, especially for fetuses with suspected abnormalities on US, provides an additional accurate measurement of SAS dimensions and calls for a standardized nomenclature of a normal-width fetal SAS. Measurements of the SAS are important parameters to

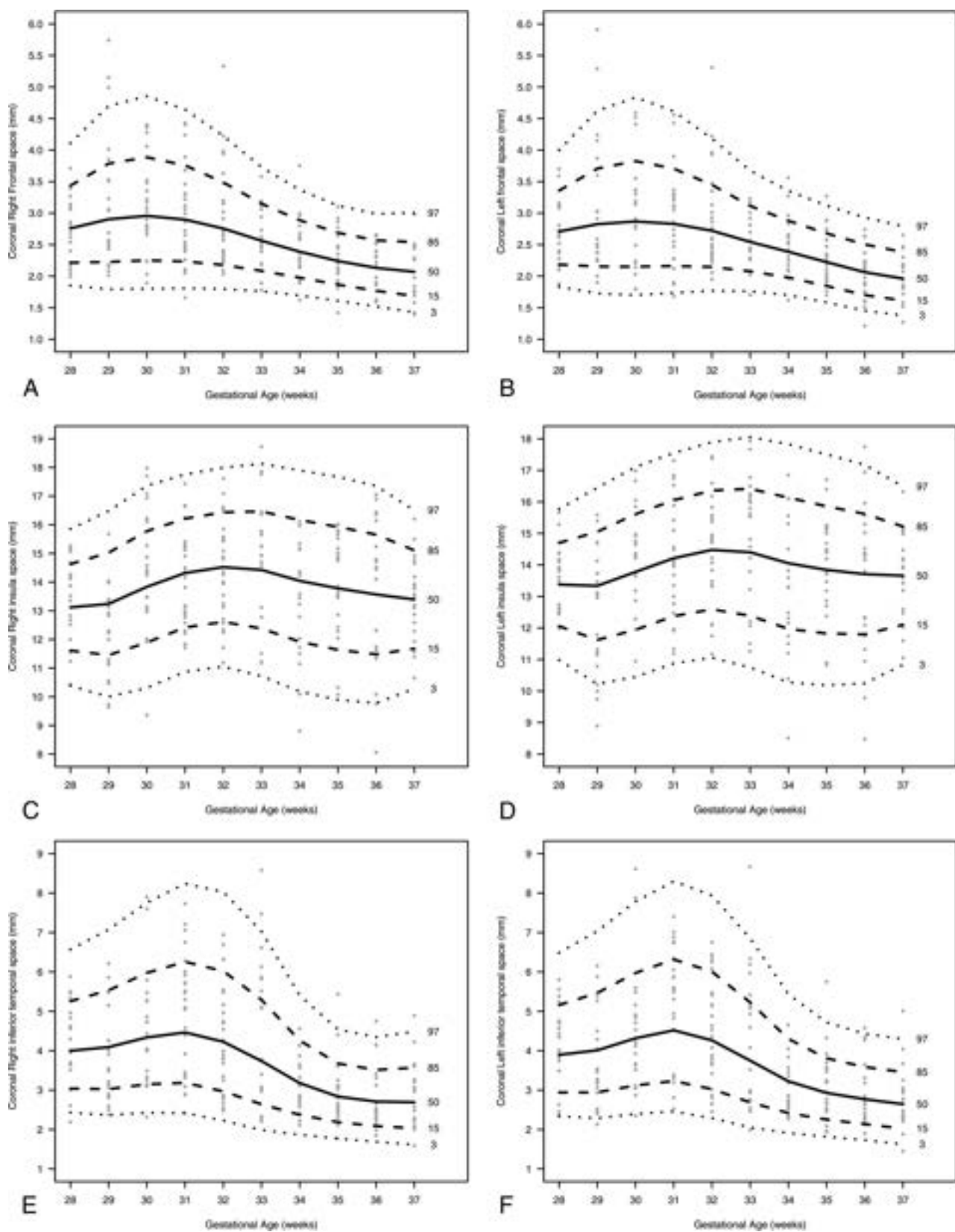


FIG 4. A nomogram presenting the SAS size (millimeters) in the coronal plane according to 3rd, 15th, 50th, 85th, 97th percentiles, and GA (weeks): A, Right frontal. B, Left frontal. C, Right insula. D, Left insula. E, Right inferior temporal. F, Left inferior temporal.

evaluate possible CNS abnormalities. The measurements of the SAS are independent of laterality, as previously described.^{9,21,22}

Our study has several limitations. First, it includes a retrospective random sample of MR images obtained in a single medical center. However, this is a tertiary referral, university-affiliated medical center that performs a large volume of MR images each year. Second, intraobserver and interobserver changes may have an impact on study results. Therefore, intraobserver and interobserver agreement have been evaluated before the nomograms were built. Third, we could not evaluate the development of the children to exclude those with impaired development. Hence, we referred to the study population as apparently healthy. Fourth, because our medical center is a referral center, usually only a small percentage of the women who underwent MR imaging at our medical center also give birth there. Therefore, of the 214 studied fetuses, only 72 (33.6%) were born at our medical center, and almost all neonates were considered healthy at birth (5-minute Apgar, ≥ 8 , 98.6%; birth at ≥ 37 weeks, 87.5%; normal length of hospitalization, 93.1%; emergency cesarean delivery, 0%). Fifth, because fetal brain MR images are usually obtained at 28+ weeks of pregnancy, only a few scans at <28 weeks of pregnancy were available; thus, normal values could not be achieved for this GA.

CONCLUSIONS

The increased use of MR imaging for the diagnosis of fetal brain pathologies requires a standardization of the normal anatomic development. Using normal values may help to make uniform the way the physicians read the scans. This work provides percentiles of 10 SAS anatomic measurements of apparently healthy fetal brains according to the GA.

Disclosure forms provided by the authors are available with the full text and PDF of this article at www.ajnr.org.

REFERENCES

- Mortazavi MM, Quadri SA, Khan MA, et al. **Subarachnoid trabeculae: a comprehensive review of their embryology, histology, morphology, and surgical significance.** *World Neurosurg* 2018;111:279–90 CrossRef Medline
- Barkovich MJ, Li Y, Desikan RS, et al. **Challenges in pediatric neuroimaging.** *Neuroimage* 2019;185:793–801 CrossRef Medline
- Piatt JH Jr. **Unexpected findings on brain and spine imaging in children.** *Pediatr Clin North Am* 2004;51:507–27 CrossRef Medline
- Suara RO, Trouth AJ, Collins M. **Benign subarachnoid space enlargement of infancy.** *J Natl Med Assoc* 2001;93:70–73 Medline
- Biran-Gol Y, Malinger G, Cohen H, et al. **Developmental outcome of isolated fetal macrocephaly.** *Ultrasound Obstet Gynecol* 2010;36:147–53 CrossRef Medline
- Marcante KJ, Kliegman RM, Schuh AM, eds. *Nelson Essentials of Pediatrics, Ninth Edition.* Elsevier; 2022:6
- Nellhaus G. **Head circumference from birth to eighteen years: practical composite international and interracial graphs.** *Pediatrics* 1968;41:106–14 CrossRef Medline
- Burke N, Burke G, Breathnach F, et al; Perinatal Ireland Research Consortium. **Prediction of cesarean delivery in the term nulliparous woman: results from the prospective, multicenter Genesis study.** *Am J Obstet Gynecol* 2017;216:598.e1–11 CrossRef Medline
- Corbacioglu Esmer A, Yuksel A, Aksu Uzunhan T, et al. **Evaluation of fetal subarachnoid space using transabdominal ultrasonography**

- and normal values during pregnancy.** *Springerplus* 2016;5:1439 CrossRef Medline
- Frankel DA, Fessell DP, Wolfson WP. **High resolution sonographic determination of the normal dimensions of the intracranial extra-axial compartment in the newborn infant.** *J Ultrasound Med* 1998;17:411–15; quiz 417–18 CrossRef Medline
- Govaert P, Pauwels W, Vanhaesebrouck P, et al. **Ultrasound measurement of the subarachnoid space in infants.** *Eur J Pediatr* 1989;148:412–13 CrossRef Medline
- Lam WW, Ai VH, Wong V, et al. **Ultrasonographic measurement of subarachnoid space in normal infants and children.** *Pediatr Neurol* 2001;25:380–84 CrossRef Medline
- Libicher M, Tröger J. **US measurement of the subarachnoid space in infants: normal values.** *Radiology* 1992;184:749–51 CrossRef Medline
- Narli N, Soyupak S, Yildizdas HY, et al. **Ultrasonographic measurement of subarachnoid space in normal term newborns.** *Eur J Radiol* 2006;58:110–12 CrossRef Medline
- Fukuyama Y, Miyao M, Ishizu T, et al. **Developmental changes in normal cranial measurements by computed tomography.** *Dev Med Child Neurol* 1979;21:425–32 CrossRef Medline
- Kleinman PK, Zito JL, Davidson RI, et al. **The subarachnoid spaces in children: normal variations in size.** *Radiology* 1983;147:455–57 CrossRef Medline
- Pedersen H, Gyldensted M, Gyldensted C. **Measurement of the normal ventricular system and supratentorial subarachnoid space in children with computed tomography.** *Neuroradiology* 1979;17:231–37 CrossRef Medline
- McArdle CB, Richardson CJ, Nicholas DA, et al. **Developmental features of the neonatal brain: MR imaging, Part II: ventricular size and extracerebral space.** *Radiology* 1987;162:230–34 CrossRef Medline
- Malinger G, Lev D, Ben-Sira L, et al. **Can syndromic macrocephaly be diagnosed in utero?** *Ultrasound Obstet Gynecol* 2011;37:72–81 CrossRef Medline
- Pilu G, De Palma L, Romero R, et al. **The fetal subarachnoid cisterns: an ultrasound study with report of a case of congenital communicating hydrocephalus.** *J Ultrasound Med* 1986;5:365–72 CrossRef Medline
- Malinger G, Lerman-Sagie T, Achiron R, et al. **The subarachnoid space: normal fetal development as demonstrated by transvaginal ultrasound.** *Prenat Diagn* 2000;20:890–93 CrossRef
- Watanabe Y, Abe S, Takagi K, et al. **Evolution of subarachnoid space in normal fetuses using magnetic resonance imaging.** *Prenat Diagn* 2005;25:1217–22 CrossRef Medline
- Yaniv G, Katorza E, Tsehmaister Abitbol V, et al. **Discrepancy in fetal head biometry between ultrasound and MRI in suspected microcephalic fetuses.** *Acta Radiol* 2017;58:1519–27 CrossRef Medline
- Kertes I, Hoffman D, Yahal O, et al. **The normal fetal cavum septum pellucidum in MR imaging: new biometric data.** *Eur J Radiol* 2021;135:109470 CrossRef Medline
- Ber R, Bar-Yosef O, Hoffmann C, et al. **Normal fetal posterior fossa in MR imaging: new biometric data and possible clinical significance.** *AJNR Am J Neuroradiol* 2015;36:795–802 CrossRef Medline
- Polat A, Barlow S, Ber R, et al. **Volumetric MRI study of the intrauterine growth restriction fetal brain.** *Eur Radiol* 2017;27:2110–18 CrossRef Medline
- Koo TK, Li MY. **A guideline of selecting and reporting intraclass correlation coefficients for reliability research.** *J Chiropr Med* 2016;15:155–63 CrossRef Medline
- Choudhri AF. *Pediatric Neuroradiology.* Thieme; 2016
- Garel C. *MRI of the Fetal Brain: Normal Development and Cerebral Pathologies.* Springer; 2004
- Rossi AC, Prefumo F. **Additional value of fetal magnetic resonance imaging in the prenatal diagnosis of central nervous system anomalies: a systematic review of the literature.** *Ultrasound Obstet Gynecol* 2014;44:388–93 CrossRef Medline
- Nagaraj UD, Kline-Fath BM. **Clinical applications of fetal MRI in the brain.** *Diagnostics (Basel)* 2022;12:764 CrossRef Medline

Why, How Often, and What Happens When We Fail: A Retrospective Analysis of Failed Fluoroscopically Guided Lumbar Punctures

M. Gerasymchuk, J.C. Durieux, and A.P. Nayate



ABSTRACT

BACKGROUND AND PURPOSE: Important information regarding fluoroscopically guided lumbar puncture (FGLP) performance and referrals is lacking. The purpose of our study was to elucidate the success rate for initial FGLP attempts and re-attempts, reasons for unsuccessful FGLPs, and the relationship between clinical indications and whether patients will undergo a fluoroscopically guided re-attempt, among others.

MATERIALS AND METHODS: This retrospective study analyzed failed FGLP attempts in hospitalized adult patients at an academic hospital between June 2016 and March 2022. Unsuccessful FGLPs were labeled as insufficient CSF egress. FGLP reports and patients' clinical charts were analyzed for pertinent information such as clinical indication, reason for failure, whether patients received IV fluid before fluoroscopically guided spinal puncture attempt, and which patients returned for another FGLP attempt. Patients' ages and sex were analyzed using descriptive statistics. The OR was used to investigate the relationship between the clinical indications to perform FGLP and whether patients returned for a re-attempt.

RESULTS: Sixty-three of 1389 (4.5%) patients (median age, 62 years) had failed the initial FGLPs administered by 39 trainees. Twenty-eight of 63 (44.4%) patients (median age, 64 years) underwent a re-attempt within a median of 2 days after the first attempt, and 27/28 (96.4%) re-attempts were successful. A dry tap, no egress of CSF was the top reason (58.7%) for failed FGLP, and 12/13 of patients had a successful FGLP after IV hydration. Twenty-seven of 63 (43%) patients did not undergo a repeat attempt, and 100% were subsequently discharged from the hospital. There was no difference ($P > .05$) in the likelihood of patients returning for a repeat FGLP based on the clinical indications.

CONCLUSIONS: Initial and repeat FGLPs have very high success rates. No difference exists in the likelihood of patients returning for a re-attempt based on clinical indication.

ABBREVIATIONS: BMI = body mass index; FG = fluoroscopically guided; FGLP = fluoroscopically guided lumbar puncture; LP = lumbar puncture

Lumbar punctures (LPs) are a commonly performed procedure to obtain CSF. Typically, LPs are performed successfully without imaging guidance, with a reported success rate of ~72%.¹ When unsuccessful, these procedures are performed on adults using image guidance, usually under fluoroscopy in the radiology department. A prior study demonstrated a high success rate in the performance of fluoroscopically guided lumbar punctures (FGLPs), with most of the unsuccessful attempts occurring due to an inability to collect CSF, even though the needle was located in the spinal canal (dry tap).² Other reasons for unsuccessful

FGLP attempts included degenerative changes preventing entry of the LP needle into the spinal canal, and marked obesity precluding proper guidance and visualization and entry into the spinal canal, among others.

A failed FGLP attempt poses potential challenges to patient management, particularly if CSF analysis is crucial to determine appropriate treatment. In addition, failed FGLPs can negatively impact the proper function of the FGLP service because, in our experience, repeat FGLPs will require further analysis regarding the site of entry of the spinal needle (ie, cervical or lumbar) and whether the patient has been hydrated, among others. A properly functioning and efficient FGLP service is particularly important because FGLP referrals continue to increase.³

Prior studies have analyzed the optimization of performing FGLPs,⁴⁻⁶ complications,^{7,8} training,^{2,9} and the impact on workflow and residency training,^{10,11} and many studies have analyzed neuroradiologists' performance and miss rates for both attendings

Received November 21, 2022; accepted after revision April 11, 2023.

From the Department of Radiology, University Hospitals Cleveland Medical Center, Cleveland, Ohio.

Please address correspondence to Ameya Nayate, MD, Department of Radiology, University Hospitals Cleveland Medical Center, 11100 Euclid Ave, BSH 5056, Cleveland, OH 44106; e-mail: Ameya.Nayate@UHhospitals.org; @UHneurorads

<http://dx.doi.org/10.3174/ajnr.A7867>

and trainees regarding the interpretation of diagnostic studies.^{12,13} However, there is not much information regarding multiple factors related to FGLP performance and referral, potentially helping streamline the process. The purpose of our study was to elucidate the success rate for initial FGLPs and re-attempts, the reasons for unsuccessful FGLPs, and the relationship between clinical indications and whether patients will undergo an FGLP re-attempt, among others.

MATERIALS AND METHODS

The present study was approved by the local institutional review board and is compliant with the Health Insurance Portability and Accountability Act.

Procedure Technique and Operators

Following a written informed consent for the diagnostic LP procedure, all patients underwent FGLP and cervical spinal puncture by means of a C-arm fluoroscopy machine in 1 neurointerventional suite. FGLPs were primarily performed by radiology residents and neuroradiology fellows under the supervision of a neuroradiology attending (range, 7–12 attendings) or independently during nonregular working hours, in a workflow that is similar to that in other academic hospitals;¹⁴ attending experience in FGLPs ranged from 1–20+ years. The level of supervision varied among attendings, ranging from directly observing the entire setup and performance of FGLP to being present in a reading room located less than a 20-second walk from the fluoroscopy room and assisting in the procedure as needed.

The range of experience in performing prior FGLPs was large for trainees, varying from the first FGLP attempt (R1s) to having performed >25 FGLPs (R3–R4s and neuroradiology fellows).

Before the FGLP attempt, typically, the lumbar level to access and approach was discussed between the supervising attending and trainee performing the FGLP. We primarily attempt to enter the spinal canal at L2–3 or L3–4 but ultimately leave it to the supervising attending's discretion, often after the attending has reviewed relevant spinal imaging, if available.

The initial FGLP was typically attempted by the trainee, and if unsuccessful, the supervising attending would attempt it if the patient agreed. All cervical punctures were performed by 1 attending.

Fluoroscopically guided (FG) spinal punctures were performed using techniques as dictated by the American Society of Neuroradiology guidelines and American College of Radiology–American Society of Neuroradiology–Society for Pediatric Radiology parameters with the patient in a prone or lateral position, including the use of local anesthetic¹⁵ and iodine and chlorhexidine to clean the skin. The lumbar spinal canal was accessed using the interlaminar or interspinous approach, and the cervical spinal canal was accessed at the level of C1–2 via a lateral approach using a Quincke 22-ga needle. A successful FGLP or cervical spinal puncture involved confirmation of the spinal needle in the spinal canal on fluoroscopy (ideally in the center of the canal, confirmed using anterior-posterior and/or lateral views) and egress of the CSF, enough for collection, after the removal of the stylet.

Patient Population

The patient charts of all hospitalized (inpatient/emergency department) adult patients (older than 18 years of age) who underwent

FGLPs from June 1, 2016, to March 31, 2022, were retrospectively reviewed.

The primary indication to perform FGLPs was to administer intrathecal chemotherapy or sample the CSF to detect malignancy, infection, CSF opening pressure, and other diseases. As per the standard guidelines in the radiology department, most patients had at least 1 failed attempt at bedside LP. Direct FGLP was available for patients requiring intrathecal chemotherapy, myelography, or cisternography and for patients with pre-existing conditions, such as morbid obesity, that could substantially reduce the chance of a successful non-image-guided LP. The decision to forgo a non-image-guided LP attempt was determined by the supervising neuroradiologist, similar to methods in other institutions.¹⁴

Data Collection

Data were collected retrospectively by 1 neuroradiology fellow through month-by-month review of FG spinal punctures performed in a 1 neurointerventional suite by reviewing our imaging database (Centricity; athenaIDX). All radiology reports of unsuccessful FGLPs from June 1, 2016, to March 31, 2022, were analyzed, and the clinical indication, demographic data, spinal levels at which the LP was attempted, training year of the operator, reason for failure, and whether the patient returned for another FGLP attempt (within 1 month) were documented from the radiology report.

Unsuccessful FGLPs were cases with an inability to enter the spinal canal evidenced by lack of CSF egress and on fluoroscopy; an inability to collect CSF in tubes even though the needle was confirmed to be in the spinal canal on fluoroscopy; or for patient-related factors including the patient requesting termination of procedure due to pain, discomfort, or anxiety or the patient being confused and not able to follow directions or lie still. Figure 1 summarizes reasons for failure. We recorded the number of days between the initial and second FGLP attempts.

For patients with an initial failed FGLP due to a dry tap, we analyzed their clinical charts to determine whether they received IV fluids; specifically, we determined whether the clinician's note mentioned starting or continuing IV fluids to assure success of a repeat FG spinal puncture, and/or we looked at the patient's order set to ensure that patient received IV fluids. For patients with failures due to a high body mass index (BMI), we recorded their BMI obtained on the closest date to the first FGLP attempt. For patients who had initial failed FGLPs due to patient-related factors including discomfort, anxiety, and so forth, we determined whether the patient received antianxiety or pain medication or anesthesia before the repeat FG spinal puncture.

We reviewed pertinent clinical information for patients who did not return for a repeat FGLP to determine whether additional tests or procedures were performed as a substitution for an image-guided LP, such as infusion of chemotherapy through a shunt reservoir.

Data Analysis

The age and sex of study participants were described using descriptive statistics. To assess the relationship between the patient's age, sex, lumbar levels attempted, resident's training year, and clinical indication to undergo LP and the likelihood of patients

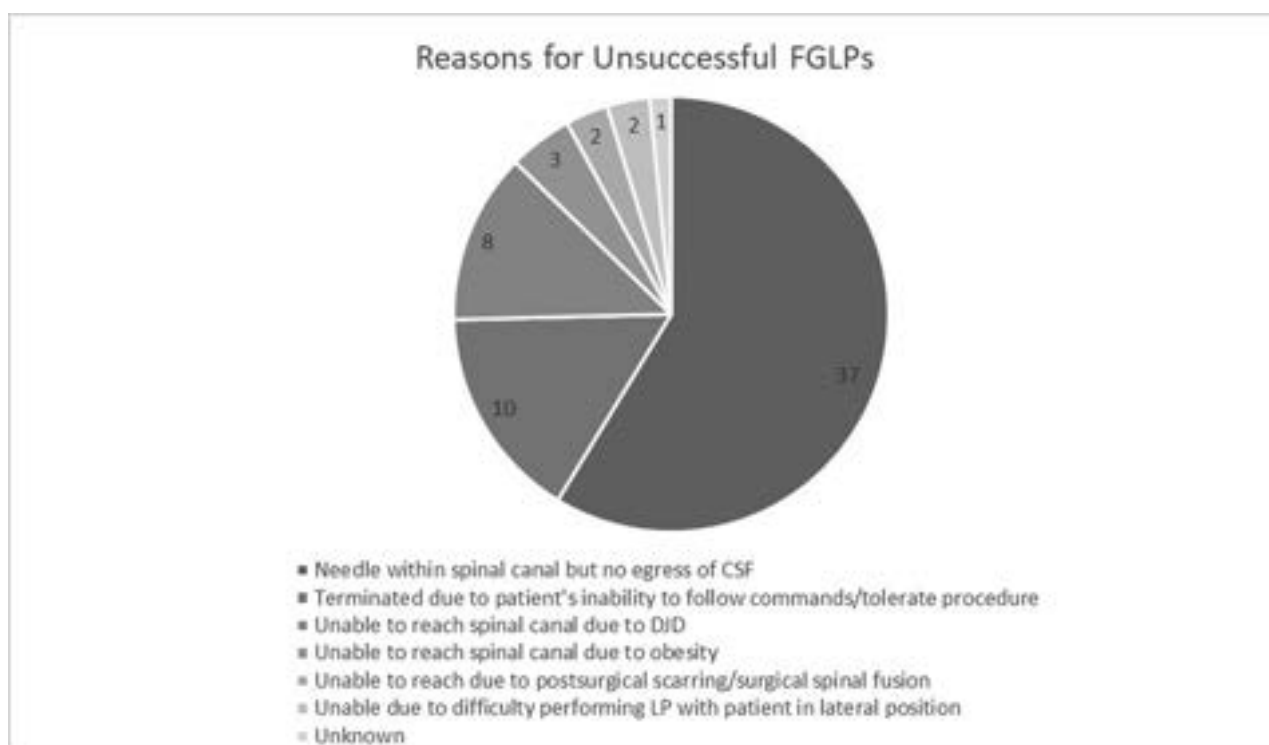


FIG 1. Breakdown of reasons for unsuccessful FGLPs. DJD indicates degenerative joint disease.

returning for repeat spinal puncture compared with patients who did not return following a failed LP, we fit logistic regression models with 95% profile likelihood confidence intervals. *P* values < .05 were considered statistically significant.

RESULTS

From June 1, 2016, to March 31, 2022, 1389 FGLPs were performed on inpatients or patients in the emergency department. Sixty-three of 1389 (4.5%) patients (mean age = 59.8 [SD, 16.2] years; range = 18–93 years; median = 62 years; 55% women and 45% men) had failed initial attempts by 39 trainees at obtaining CSF. Sixty of 63 (95.2%) FGLPs were attempted under supervision of an attending, while the remaining 3 were performed by the resident during the weekend or weekday after hours. Of the 63 failed attempts, 21 failures were by R1s, 10 by R2s, 17 by R3s, 7 by R4s, 4 by neuroradiology fellows, and 4 failures were by 2 residents who were performing the FGLP together. The median failure rate was 1 per resident (range = 1–4 failures). Lumbar level-by-level failure rates on an initial attempt in the 63 patients were as follows: sole attempts at L2–3 = 3 (4.8%), L3–4 = 15 (23.8%), and L4–5 = 7 (11.1%); 2 levels attempted (L1–2 and L5–S1) = 23 (36.5%); and 3 levels attempted (L2–3 and L5/L6/S1) = 11 (17.5%). For 4 patients (6.3%), it was unclear which levels were attempted, but for 3, it was likely at 1 level. Patients' clinical indications for the FGLPs were the following: concern for infectious process in the CSF = 25 (39.7%), concern for a neoplasm in the CSF = 15 (23.8%), testing for normal pressure hydrocephalus = 2 (3.2%), and all remaining categories including concern for MS, encephalitis, and so forth = 21 (33.3%).

Twenty-eight of 63 patients (61% women and 39% men, mean age = 58.6 [SD, 18.1] years, median = 64 years) returned

to undergo a second FG spinal puncture (5 cervical and 23 lumbar approaches; mean = 4 [SD, 5.9] days after the first FGLP attempt, median = 2 days, range = 1–28 days). Twenty-seven of 28 (96.4%) had a successful repeat FG spinal puncture.

Failure Due to Lack of Egress of CSF through the LP Needle Confirmed in the Spinal Canal on Fluoroscopy

Thirty-seven of 63 (58.7%) failures were due to lack of egress of CSF through the LP needle, though the needle tip was within the spinal canal (46% women and 54% men, mean age = 59 [SD, 17.3] years, median age = 61 years, age range = 18–92 years). The mean lumbar spinal levels attempted on the initial failed FGLP were 1.9 (SD, 0.76) levels, median = 2 levels. A sole approach at levels L2–3 was 2 (5.4%); L3–4, 7 (18.9%); and L4–5, 4 (10.8%). Twenty-four patients (64.9%) had attempts at multiple levels. For 33 patients (89.2%), FGLP was attempted with the patient in the prone position and 1 patient was in the lateral position, and for 3 patients, positioning was unknown.

Fifteen of 37 patients (40.5%) (47% women and 53% men, mean age = 57.7 [SD, 18.6] years, median age = 64 years, age range = 18–82 years) returned to undergo FGLP at another date (mean = 4.7 [SD, 7.5] days, median = 2 days, range = 1–28 days) after the first attempt, of which 14/15 (93.3%) had a successful repeat FGLP. See Fig 2 for the breakdown.

Failure Due to Degenerative Changes

Eight of 63 (12.7%) failures were due to an inability to access the spinal canal due to degenerative changes as documented in the radiology report: 63% women and 37% men, mean age = 68.3 (SD, 9.8) years, median age = 65.5 years. The mean number of

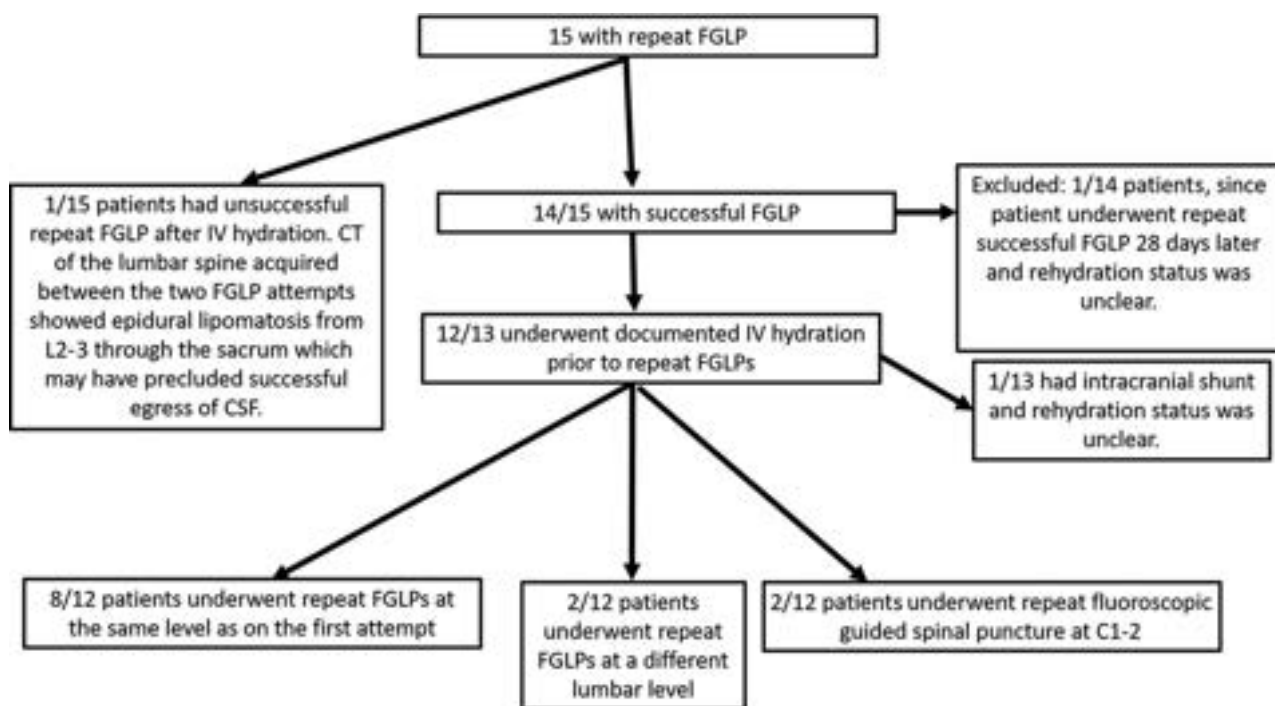


FIG 2. Breakdown of patients with initial dry taps who returned for repeat FG spinal punctures.

FGLP attempts at multiple lumbar levels after the initial failed FGLP was 2.4 (SD, 1.1), median = 2.

Two of 8 (25%) returned to undergo a repeat FGLP (range = 1–5 days after the first FGLP attempt). Both of these were successful and were performed at the C1–2 level.

Failure Due to Patients' High BMI, Postsurgical Scarring, and Other Factors

High BMI. Three patients had failed initial FGLPs due to an inability to adequately visualize the bony landmarks under fluoroscopy and an inability to reach to the spinal canal with the needle due to large body habitus (mean BMI = 48.3, range = 35.8–56.3). Two patients had initial FGLP attempts while in the lateral position either due to intubation or an inability to lie prone. One patient had a repeat successful non-image-guided LP on the inpatient floor, a second patient had a successful repeat FGLP with the use of a longer needle (14 days after the first failed FGLP), and the last patient did not have a repeat LP attempt and went for brain biopsy.

Postsurgical Scarring or Instrumentation. One patient had a failed FGLP due to the inability of the LP needle to pierce through the postsurgical scarring in the lumbar spinal soft tissues. A repeat FGLP was not attempted because the patient's symptoms resolved. One patient had a failed FGLP due to lumbar instrumentation. The patient underwent a successful cervical puncture the following day.

Other Factors. Ten patients had initial failed FGLPs due to an inability to follow commands and/or pain and anxiety. Six of 10 patients returned to undergo a repeat FGLP (mean = 2.2 [SD, 1.5] days, median = 2 days). See Fig 3 for outcomes.

Two patients had initial unsuccessful attempts while in the lateral decubitus position and 1 and 3 days later had successful FGLPs (1 under anesthesia). For 1 patient, the reason for the initial FGLP failure could not be determined, and the patient had a subsequent successful FGLP 2 days later. The Table 1 summarizes some of the data presented above.

Factors Associated with Patients Returning for a Repeat FGLP Attempt

No clear relationship ($P < .05$) was seen regarding multiple factors and whether the patient returned for a repeat FGLP (Table 2).

Patients Who Did Not Return for Repeat FGLP Attempts

Of the 35 patients who did not return for an FG spinal puncture, 5 had substitute procedures to determine the cause of their symptoms or to instill intrathecal agents, including placement of an Ommaya reservoir or other type of intracranial shunt or brain biopsy. One patient died from hypotension and hypoxia the day following the unsuccessful FGLP attempt, and the primary cause of death was ruled lymphoma. Two patients underwent successful LP attempts on the inpatient floor without image guidance.

The remaining 27/63 (43%) patients (52% men and 48% women, mean age = 59.2 [SD, 15] years, median = 62 years) did not undergo a further FGLP attempt because they improved clinically, other reasons for symptomatology were revealed, or the patient declined, among others. One hundred percent of the patients were successfully discharged to home or a care facility (median = 5 days, range = 0–16 days after admission).

DISCUSSION

Our findings, obtained from a large academic hospital, demonstrate a success rate of 95.5% FGLPs on the first FGLP attempt

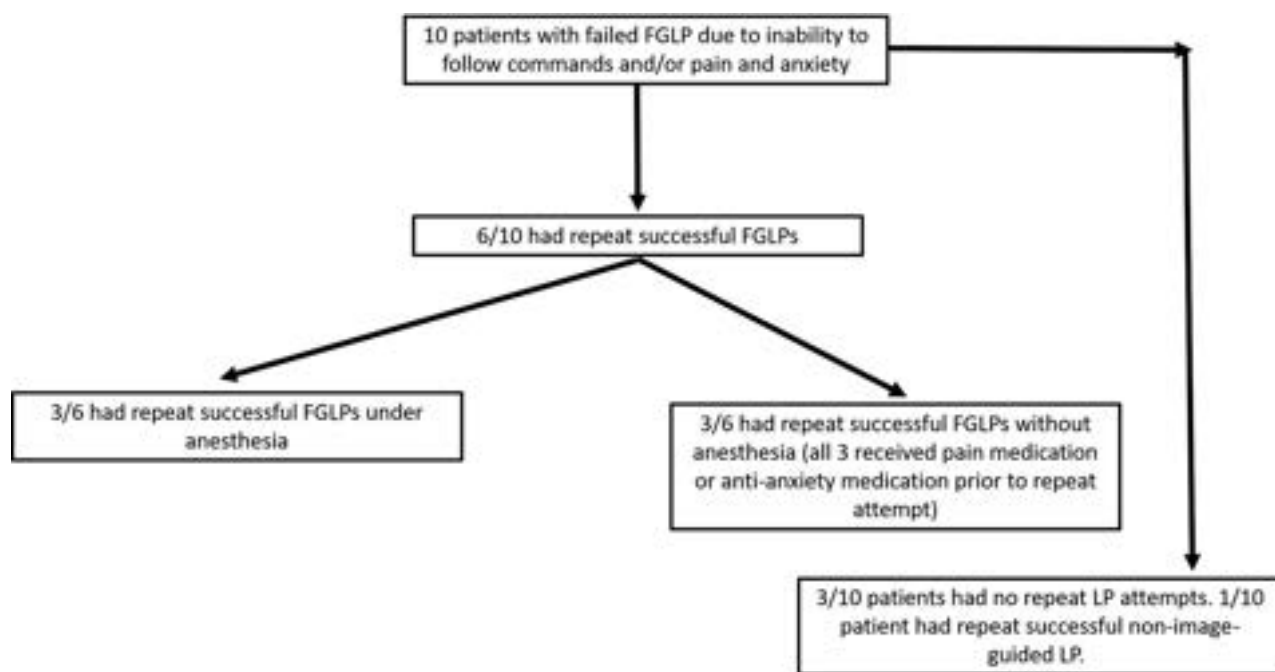


FIG 3. Outcomes of patients with initial failed FGLPs due to an inability to follow commands and/or pain and anxiety.

Table 1: Breakdown of data on failed and repeat spinal punctures

Reason for Initial FGLP Failure (No.)	No. of Patients Who Returned for a Repeat Spinal Puncture/No. of Patients with Initial FGLP Failure	No. of Successful Repeat Spinal Punctures/No. of Patients Who Returned for a Repeat Spinal Puncture Attempt
Lack of egress of CSF in the LP needle confirmed in the spinal canal (<i>n</i> = 37)	15/37 (40.5%)	14/15 (93.3%)
Degenerative changes (<i>n</i> = 8)	2/8 (25%)	2/2 (100%)
Patient's inability to follow commands and/or due to pain and anxiety (<i>n</i> = 10)	6/10 (60%)	6/6 (100%)
High BMI (<i>n</i> = 3)	1/3 (33%)	1/1 (100%)
Patient in lateral decubitus position (<i>n</i> = 2)	2/2 (100%)	2/2 (100%)
Postsurgical scarring or instrumentation (<i>n</i> = 2)	1/2 (50%)	1/1 (100%)
Unknown (<i>n</i> = 1)	1/1 (100%)	1/1 (100%)
Total (<i>n</i> = 63)	28/63 (44%)	27/28 (96%)

Table 2: Factors associated with whether the patient will return for a repeat FGLP and the reason for the failed LP

	Unadjusted OR (95% CI)
Factors	
Age	0.99 (0.96–1.02)
Sex (male/female)	0.7 (0.25–1.86)
Lumbar levels attempted (>1 vs 1)	0.84 (0.31–2.28)
Resident year	1.04 (0.7–1.54)
Clinical indication (infection or neoplasm vs other)	0.55 (0.19–1.52)
Reason for failed LP	
Cannot enter spinal canal vs dry tap	0.77 (0.24–2.37)
Cannot enter spinal canal vs other ^a	1.74 (0.48–6.66)

^aPatient was unable to undergo the procedure due to anxiety, pain, inability to follow commands, and so forth.

and 96.4% (27/28) after patients returned for a second fluoroscopically guided cervical or lumbar puncture. Success rates are higher compared with a non-image-guided approach, ~72%,¹ and a sonographically guided approach, 90%,¹⁶ primarily related

to the ability to clearly visualize osseous structures and advancement of the LP needle in real time. Our success rate was slightly lower than the 99% success rate reported in another article with a smaller sample;² the reasons could be multifactorial, including differences in the patient population and procedural expertise. Although in our study and the prior study, the miss rate was low, it is still important to analyze because FG spinal puncture is typically the last remaining option in many patients to obtain CSF, and if it is unsuccessful, it could directly impact their care. Furthermore, planning and performing FGLPs can be time-intensive^{6,10} and impact workflow as well as residency training in diagnostic neuro-radiology;¹¹ therefore, knowledge of potential reasons for failure is critical. Most important, our findings show that even if initially unsuccessful, repeat FG spinal punctures have a high success rate of 96% and can be reassuring for patients, ordering clinicians, and radiologists.

In our sample, most of the failed FGLPs were due to lack of egress of CSF through the LP needle, even though the needle tip was confirmed in the spinal canal and demonstrated no kinking,

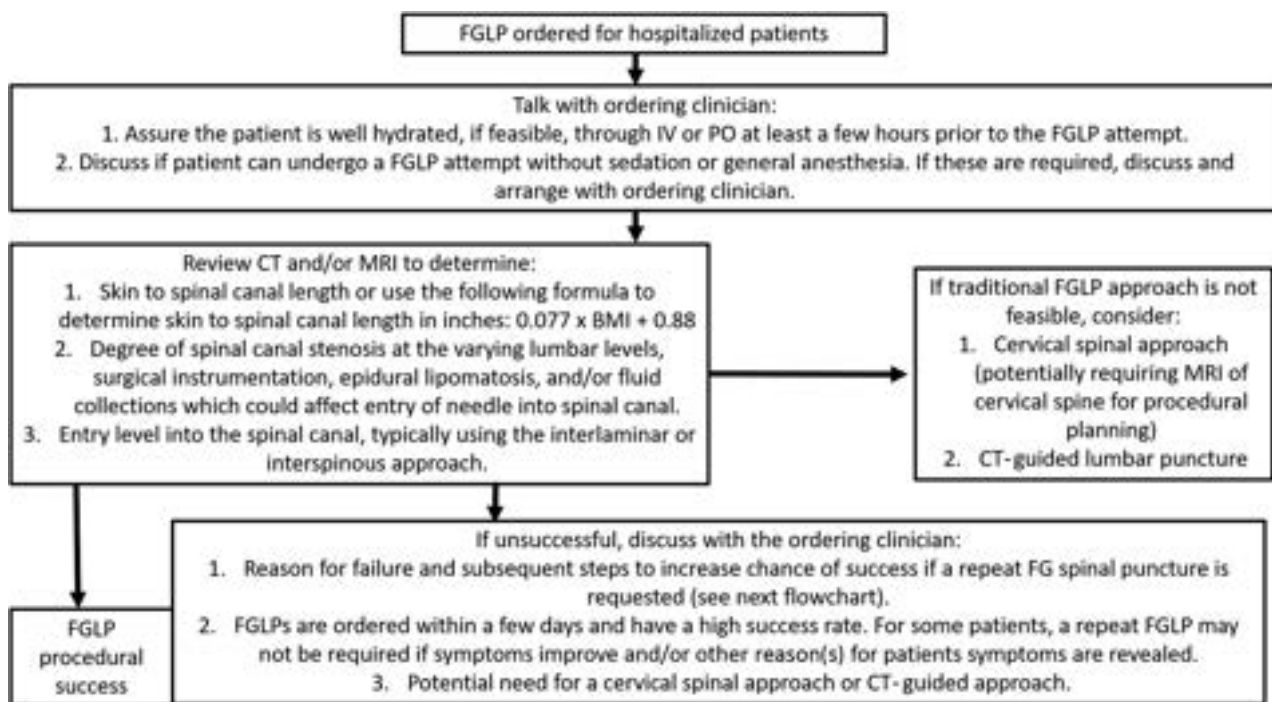


FIG 4. Flowchart to determine how to prepare for and perform an FG spinal puncture. PO indicates by mouth.

which could preclude outflow of CSF, ie, a dry tap. A prior article with a smaller sample size and conducted at another institution demonstrated that most of the FGLP misses, 44%, were due to dry taps,² which is slightly lower than our findings (58.7%). Dry taps are believed to be due to low CSF volume and pressure, often due to dehydration.⁴ In our experience, ordering clinicians are aware that patients need to be hydrated before FGLPs, and we often specifically request that hospitalized patients are hydrated before the FGLP attempt. Even so, 37 patients in our sample still had initial dry FGLP taps. We followed the same maneuvers to acquire CSF as suggested by Hudgins et al;⁴ however, we do not use the “gentle suction” technique using a syringe, primarily due to procedural inexperience. Using this technique may provide some CSF flow but often remains slow.⁴ Many patients require ≥ 10 mL of CSF for proper analysis, and collecting adequate CSF, if egressing is slow, may be impractical because many relatively ill, elderly, and/or obese patients cannot remain in position for an extended time.

Of the 15 hospitalized patients who returned for a repeat FGLP while still hospitalized, 13 had documented IV hydration and 12 had successful FGLPs. Most had a repeat attempt at the same lumbar level as on the initial attempt. Imaging in the sole patient with the unsuccessful FGLP demonstrated epidural lipomatosis from L2–3 through the sacrum, which likely precluded successful egress of CSF because epidural lipomatosis a known factor for failed LPs.¹⁷ The patient was subsequently discharged because symptoms had resolved.

In 8 patients, the lumbar spinal canal could not be accessed due to degenerative changes. Most of these patients were older than 65 years of age, and advanced age is highly associated with degenerative disease of the lumbar spine.¹⁸ Only 2 patients returned for a repeat attempt and underwent successful cervical

spinal punctures. Although not often performed, cervical spinal punctures remain a viable option to access the spinal canal for CSF sampling and/or myelography.^{19,20} If operators do not feel comfortable performing cervical punctures, accessing the spinal canal under CT guidance is an alternative option,⁴ though it results in an increase in the radiation dose. The percentage of unsuccessful FGLPs due to degenerative changes was overall low because fluoroscopy generally well-defines the spinal canal entry sites, typically the interlaminar or interspinous spaces.

A high BMI is a known factor for failed non-image-guided LPs.²¹ Even under fluoroscopy, due to increased soft tissue in the flank, ensuring a straight entry into the spinal canal can be difficult. Most interesting, only 3 patients had FGLP failures, primarily due to the patient’s high BMI. Our high success rate in patients with high BMIs is likely because we measure the skin-to-midspinal canal distance on CT or MR imaging before performing FGLPs to determine the correct needle length. If no prior imaging is available, we use the formula detailed by Nayate et al⁵ to determine the inches from the skin to the spinal canal.

FGLPs require patients to remain still for several minutes and can cause discomfort. Inpatients are often ill and cannot follow directions or remain still, are anxious, and cannot bear the discomfort. Clinicians strive to avoid unnecessarily sedating patients, and often the initial FGLP is attempted on patients and is subsequently terminated due to reasons stated above. In our sample, in only 10 patients did the initial FGLP attempts fail for reasons stated above. This low number is likely because we typically discuss the case with the ordering physician and ask if the patient can undergo the procedure without requiring sedation or anesthesia. Most of patients returned for a repeat FGLP (one-half with anesthesia and one-half without), and 100% had a repeat successful FGLP.

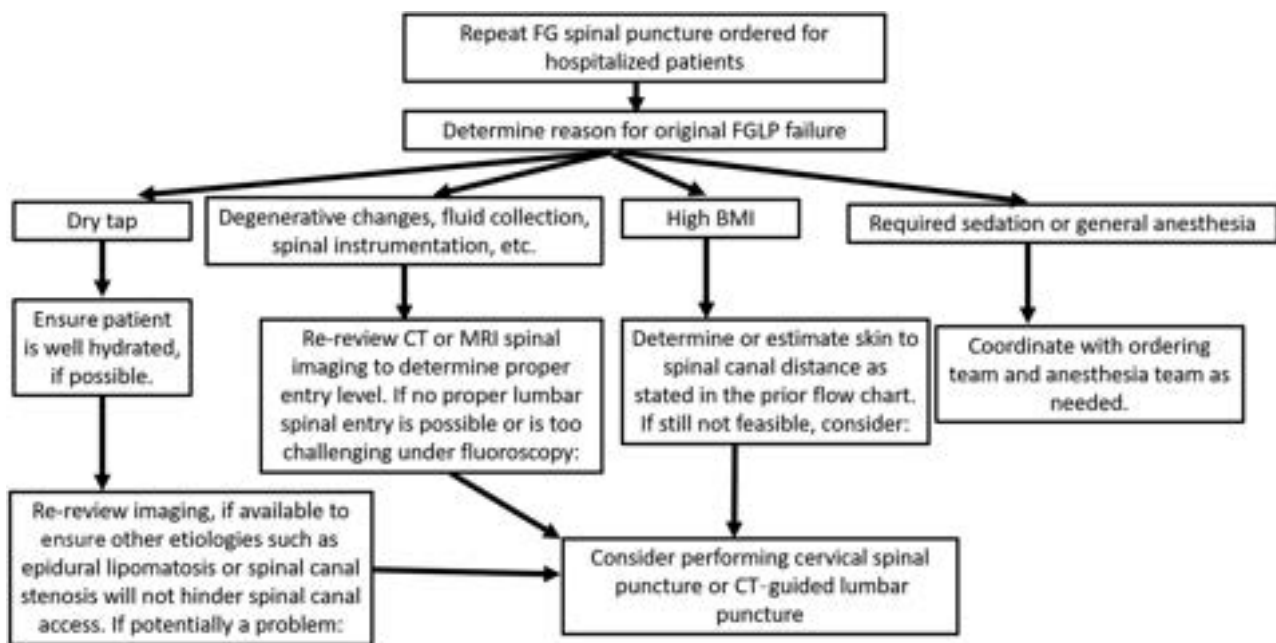


FIG 5. Flowchart for patients who return for a repeat FG spinal puncture.

We hypothesized that most patients would return for a repeat FGLP. However, >40% of patients did not return for FGLPs because their symptoms resolved, patients declined further attempts, or they were planning to undergo FGLP as an outpatient. All of these patients were successfully discharged, typically a few days after the failed FGLP attempt. There was no difference between the likelihood of patients returning for a repeat FG spinal puncture or not based on the clinical indication. Of the approximately 44.4% of our sample that returned for a repeat FGLP, most returned within 2 days, which is expected because if there is concern for CSF pathologic processes, timely detection is needed for treatment planning and to reduce morbidity/mortality. Using this logic, we suspect that other radiology departments have similar referral timing for repeat FGLPs and therefore can adjust their FGLP schedule to allow return of these patients. An orderly functioning FGLP service is critical because FGLP referrals continue to increase³ and occupancy of a FGLP procedure room can be an hour or longer.⁶

Well-organized scheduling, planning, and performing of FGLPs can sometimes be challenging; therefore, we have provided a flowchart (Figs 4 and 5) that can be followed to potentially ease the process.

Our study has some limitations. First, our findings are based on the FGLPs performed at a single institution; although 39 trainees performed FGLPs under the supervision of 7–12 attendings, there was a broad range of operator skill. Our hospital is a tertiary academic center, and our radiology department performs FGLPs on patients with a large range of BMIs, medical conditions, degenerative changes, and other patient-related factors that are typically seen in hospital systems that service a substantial patient population. Second, we had a small sample size, but the high success rate of the repeat FGLPs supports our findings and assertions. Third, in some patients, multiple factors could have caused

the failed FGLP attempt, but we focused on the primary cause as stated in the dictation and after review of the FGLP procedural images and patients' charts. Fourth, we did not review CT or MR imaging of the lumbar spine in all patients to determine degree of degenerative changes because grading degenerative changes is often subjective and not standardized. Fifth, we did not objectively determine which patients with dry taps were initially dehydrated nor determine the amount of IV fluid they received because it is beyond the scope of this article but is the focus of our next research project.

CONCLUSIONS

We demonstrated a 95.5% success rate for FGLPs performed at our tertiary academic hospital and a near-equivalent success rate for patients who returned to undergo a second FG spinal puncture attempt after an initial failed FGLP attempt. Patients had a repeat FG spinal puncture within a median of 2 days after the initial failed attempt. A dry tap was the most common reason for a failed FGLP, and most patients had a successful FGLP after they were hydrated. More than 40% of patients did not require a repeat FGLP because their symptoms resolved, the patient declined further attempts, or other reasons for their symptoms were determined, which no longer required CSF sampling. There was no difference in the likelihood of patients returning for a repeat FG spinal puncture based on the clinical indication.

Disclosure forms provided by the authors are available with the full text and PDF of this article at www.ajnr.org.

REFERENCES

- Williams P, Tait G, Wijeratne T. Success rate of elective lumbar puncture at a major Melbourne neurology unit. *Surg Neurol Int* 2018;9:12 CrossRef Medline

2. Nayate AP, Schmitt JE, Mohan S, et al. **Trends in fluoroscopy time in fluoroscopy-guided lumbar punctures performed by trainees over an academic year.** *Acad Radiol* 2017;24:373–80 CrossRef Medline
3. Johnson DR, Waid MD, Rula EY, et al. **Comparison of radiologists and other specialists in the performance of lumbar puncture procedures over time.** *AJNR Am J Neuroradiol* 2021;42:1174–81 CrossRef Medline
4. Hudgins PA, Fountain AJ, Chapman PR, et al. **Difficult lumbar puncture: pitfalls and tips from the trenches.** *AJNR Am J Neuroradiol* 2017;38:1276–83 CrossRef Medline
5. Nayate AP, Nasrallah IM, Schmitt JE, et al. **Using body mass index to predict needle length in fluoroscopy-guided lumbar punctures.** *AJNR Am J Neuroradiol* 2016;37:572–78 CrossRef Medline
6. Bakrakov D, Siddique Z, Mangla R, et al. **Retrospective comparative analysis of fluoroscopic-guided lumbar puncture in the routine prone versus lateral decubitus position.** *Cureus* 2021;13:e18799 CrossRef Medline
7. Rodriguez D, Branstetter BF 4th, Agarwal V, et al. **Incidence of complications following fluoroscopically guided lumbar punctures and myelograms.** *AJR Am J Roentgenol* 2016;206:20–25 CrossRef Medline
8. Eskey CJ, Ogilvy CS. **Fluoroscopy-guided lumbar puncture: decreased frequency of traumatic tap and implications for the assessment of CT-negative acute subarachnoid hemorrhage.** *AJNR Am J Neuroradiol* 2001;22:571–76 Medline
9. Yang H, Schaffer K, Liu L, et al. **Benchmarking lumbar puncture fluoroscopy time during fellowship training.** *AJNR Am J Neuroradiol* 2017;38:656–58 CrossRef Medline
10. Lee MH, Schemmel AJ, Pooler BD, et al. **Workflow dynamics and the imaging value chain: quantifying the effect of designating a nonimage-interpretive task workflow.** *Curr Probl Diagn Radiol* 2017;46:275–81 CrossRef Medline
11. Richards TJ, Schmitt JE, Wolansky LJ, et al. **Radiology performed fluoroscopy-guided lumbar punctures decrease volume of diagnostic study interpretation: impact on resident training and potential solutions.** *J Clin Imaging Sci* 2021;11:39 CrossRef Medline
12. Babiarz LS, Yousem DM. **Quality control in neuroradiology: discrepancies in image interpretation among academic neuroradiologists.** *AJNR Am J Neuroradiol* 2012;37–42 CrossRef Medline
13. Masur JH, Schmitt JE, Lalevic D, et al. **Am I ready to be an independent neuroradiologist? Objective trends in neuroradiology fellows' performance during the fellowship year.** *AJNR Am J Neuroradiol* 2021;42:815–23 CrossRef Medline
14. Richards TJ, Durieux JC, Nayate AP. **How are we handling fluoroscopy-guided lumbar puncture requests? A nationwide survey of practice trends.** *AJNR Am J Neuroradiol* 2022;43:1827–33 CrossRef Medline
15. Kieffer S, Mukundan S, Rollins N. **ACR–ASNR–SPR practice guideline for the performance of myelography and cisternography.** 2013. <https://www.asnr.org/wp-content/uploads/2016/12/Myelography.pdf>. Accessed November 1, 2022
16. Gottlieb M, Holladay D, Peksa GD. **Ultrasound-assisted lumbar punctures: a systematic review and meta-analysis.** *Acad Emerg Med* 2019;26:85–96 CrossRef Medline
17. Yamanaka D, Kawano T, Shigematsu-Locatelli M, et al. **Failure of lumbar puncture in a patient with spinal epidural lipomatosis: a case report.** *JA Clin Rep* 2016;2:14 CrossRef Medline
18. Hicks GE, Morone N, Weiner DK. **Degenerative lumbar disc and facet disease in older adults: prevalence and clinical correlates.** *Spine* 2009;34:1301–06 CrossRef Medline
19. Yousem DM, Gujar SK. **Are C1-2 punctures for routine cervical myelography below the standard of care?** *AJNR Am J Neuroradiol* 2009;30:1360–63 CrossRef Medline
20. Gerasymchuk M, Labak C, Hoffer S, et al. **“The Up and Down Approach” to localize and exclude sites of intraspinal CSF leaks.** *Curr Probl Diagn Radiol* 2022;52:10–13 CrossRef Medline
21. Edwards C, Leira EC, Gonzalez-Alegre P. **Residency training: a failed lumbar puncture is more about obesity than lack of ability.** *Neurology* 2015;84:e69–72 CrossRef Medline

Efficacy of Epidural Blood Patching or Surgery in Spontaneous Intracranial Hypotension: A Systematic Review and Evidence Map

T.J. Amrhein, J.W. Williams, Jr., L. Gray, M.D. Malinzak, S. Cantrell, C.R. Deline, C.M. Carr, D.K. Kim, K.M. Goldstein, and P.G. Kranz



ABSTRACT

BACKGROUND: Spontaneous intracranial hypotension is an important cause of treatable secondary headaches. Evidence on the efficacy of epidural blood patching and surgery for spontaneous intracranial hypotension has not been synthesized.

PURPOSE: Our aim was to identify evidence clusters and knowledge gaps in the efficacy of treatments for spontaneous intracranial hypotension to prioritize future research.

DATA SOURCES: We searched published English language articles on MEDLINE (Ovid), the Web of Science (Clarivate), and EMBASE (Elsevier) from inception until October 29, 2021.

STUDY SELECTION: We reviewed experimental, observational, and systematic review studies assessing the efficacy of epidural blood patching or surgery in spontaneous intracranial hypotension.

DATA ANALYSIS: One author performed data extraction, and a second verified it. Disagreements were resolved by consensus or adjudicated by a third author.

DATA SYNTHESIS: One hundred thirty-nine studies were included (median, 14 participants; range, 3–298 participants). Most articles were published in the past decade. Most assessed epidural blood patching outcomes. No studies met level 1 evidence. Most were retrospective cohort or case series (92.1%, $n = 128$). A few compared the efficacy of different treatments (10.8%, $n = 15$). Most used objective methods for the diagnosis of spontaneous intracranial hypotension (62.3%, $n = 86$); however, 37.7% ($n = 52$) did not clearly meet the International Classification of Headache Disorders-3 criteria. CSF leak type was unclear in 77.7% ($n = 108$). Nearly all reported patient symptoms using unvalidated measures (84.9%, $n = 118$). Outcomes were rarely collected at uniform prespecified time points.

LIMITATIONS: The investigation did not include transvenous embolization of CSF-to-venous fistulas.

CONCLUSIONS: Evidence gaps demonstrate a need for prospective study designs, clinical trials, and comparative studies. We recommend using the International Classification of Headache Disorders-3 diagnostic criteria, explicit reporting of CSF leak subtype, inclusion of key procedural details, and using objective validated outcome measures collected at uniform time points.

ABBREVIATIONS: EBP = epidural blood patching; ICHD-3 = International Classification of Headache Disorders-3; QOL = quality of life; SIH = spontaneous intracranial hypotension


Spontaneous intracranial hypotension (SIH) is a condition caused by a noniatrogenic spinal CSF leak that leads to considerable disability, typically in the form of an orthostatic headache (ie, improved with recumbency).¹ Morbidity due to SIH is

compounded by cranial nerve dysfunction, causing a variety of symptoms including diplopia, tinnitus, muffled hearing, and disequilibrium, among many others. SIH is now recognized as an important treatable cause of headache. During the past decade, increased awareness of this disorder has led to substantial growth in both patient diagnoses as well as research publications.

Received February 23, 2023; accepted after revision April 21.

From the Department of Radiology (T.J.A., L.G., M.D.M., P.G.K.), Duke University Medical Center, Durham, North Carolina; Division of General Internal Medicine (J.W.W., K.M.G.) and Duke University Medical Center Library (S.C.), Duke University School of Medicine, Durham, North Carolina; Durham Center of Innovation to Accelerate Discovery and Practice Transformation (J.W.W., K.M.G.), Durham Veterans Affairs Health Care System, Durham, North Carolina; Spinal CSF Leak Foundation (C.R.D.), Spokane, Washington; and Department of Radiology (C.M.C., D.K.K.), Mayo Clinic, Rochester, Minnesota.

Please address correspondence to T.J. Amrhein, MD, Department of Radiology, Box 3808, Duke University Medical Center, Durham, NC 27710; e-mail: timothy.amrhein@duke.edu; @TimAmrheinMD

 Indicates article with online supplemental data.
<http://dx.doi.org/10.3174/ajnr.A7880>

The treatment of SIH requires closure of the spinal CSF leak. The primary methods are via epidural blood patching (EBP) or surgical repair.² Data on SIH treatment efficacy are limited. For example, reported responses to EBP range from 36%–90%.^{3–10} This wide range suggests that the true effect is not yet determined. Data for the efficacy of surgical repair are even more sparse. Furthermore, the efficacy of treatments may be impacted by leak subtypes (eg, disc osteophyte spur, nerve root diverticula, or CSF-venous fistula) or affected by differences in technical characteristics of the treatment (eg, EBP targeted to the leak site versus nontargeted). As a result, there is considerable uncertainty about the optimal treatment for any given patient, and there are currently neither consensus guideline recommendations nor widely accepted algorithms for management. This lack of consensus has resulted in a heterogeneity of treatment approaches.

Standardization of treatment algorithms for SIH will be best reached through the development of strong evidence supporting decision-making. Thus, future research should be directed toward specific-yet-unanswered questions regarding SIH treatment efficacy. Developing these questions requires a thorough understanding of the current state of the literature. Therefore, we aimed to systematically map the available evidence for the efficacy of SIH treatments. This review addressed 2 key objectives: first, to describe the published literature that evaluates the efficacy of epidural patching for treatment of patients with SIH, and second, to describe the published literature that evaluates the efficacy of surgery for treatment of patients with SIH. The results of this work will allow us to gain a better understanding of the landscape of existing research on these topics, including a systematic description of study characteristics; evidence clusters to guide subsequent systematic reviews and meta-analyses; and evidence gaps that may guide funding agencies and investigators toward prioritization of future research to fulfill unmet needs.

MATERIALS AND METHODS

This systematic review and evidence map adhered to Preferred Reporting Items for Systematic Reviews and Meta Analyses Extension for Scoping Reviews (PRISMA-ScR) guidelines.¹¹ The protocol was published and registered a priori in Open Science Framework (OSF, 10.17605/OSF.IO/NWJU7; <https://osf.io/>) and has not been subject to amendments.¹² All steps of this study were pilot-tested by the team before implementation.

Data Sources and Searches

The MEDLINE (Ovid), Web of Science (Clarivate), and EMBASE (Elsevier) databases were searched for published English language citations. The search was developed and conducted by a professional medical librarian in consultation with the author team and included a mix of database-specific subject headings and keywords representing SIH (including CSF leaks, low CSF volume headaches, low-pressure headaches, and hypotensive headaches) and terms related to EBP or surgical techniques for the treatment of SIH. Search hedges or database filters were used to remove publication types such as editorials, letters, case reports, comments, and animal-only studies as appropriate for each database. The searches were independently peer-reviewed by another librarian using a modified Peer

Review of Electronic Search Strategies checklist.¹³ Complete reproducible search strategies for all databases are detailed in the Online Supplemental Data. The original searches were conducted on December 10, 2020; a search update was conducted on October 20, 2021, to identify newly published studies. The reference lists of key studies and all included systematic reviews were hand-searched to identify additional citations not previously captured.

Inclusion and Exclusion Criteria

We included experimental, observational, and systematic review studies that assessed the efficacy of EBP or surgery for the treatment of patients of any age or sex with a reported diagnosis of SIH.

We excluded studies of patients with cranial CSF leaks, iatrogenic spinal CSF leaks (eg, post-dural puncture or postoperative), those with headaches not secondary to SIH, and mixed populations of patients with and without SIH without subgroup analyses. Single case reports, small case series (<3 cases), clinical guidelines, narrative reviews, editorials, and protocols were excluded. There was no limitation on date of publication.

Study Selection

The titles and abstracts of all articles identified by electronic searches were screened independently by 2 authors for relevance. Articles included by either investigator by title and abstract review advanced to full-text screening where they were again independently dual-screened. Disagreements between authors during full-text screening were resolved by consensus or by a third investigator when consensus could not be reached. All results were tracked in Covidence (<https://www.covidence.org/>), a web-based data-synthesis software program, and duplicates were removed.¹⁴ EndNote reference management software (Clarivate) was used during drafting of the manuscript. Articles that met the criteria for inclusion underwent data extraction.

Data Extraction

One author abstracted data from each included study using a customized data-extraction form within Covidence. Abstracted data were then verified by a second author. Disagreements were resolved by consensus or adjudicated by a third author when consensus could not be reached. Extracted data elements included study design, study setting, number of patients included, patient demographics, method of SIH diagnosis, treatment-intervention characteristics (eg, type of EBP or surgery), outcome measures used, and timing of outcome assessment. Article authors were contacted for clarification or supplemental data when necessary.

Data Synthesis and Analysis

We tabulated included studies and summarized key study characteristics (eg, study design, patient demographics, details of treatment intervention) using tabular and graphic formats, including bubble plots to display evidence clusters and identify gaps. Areas of interest included the number of publications across time, clusters and gaps in study designs (such as a preponderance of retrospective designs or the absence of particular designs), patterns of both strengths and deficiencies in the reporting of diagnostic features (eg, International Classification of Headache Disorders-3 [ICHD-3] criteria, CSF leak subtypes), procedural details (eg, targeting

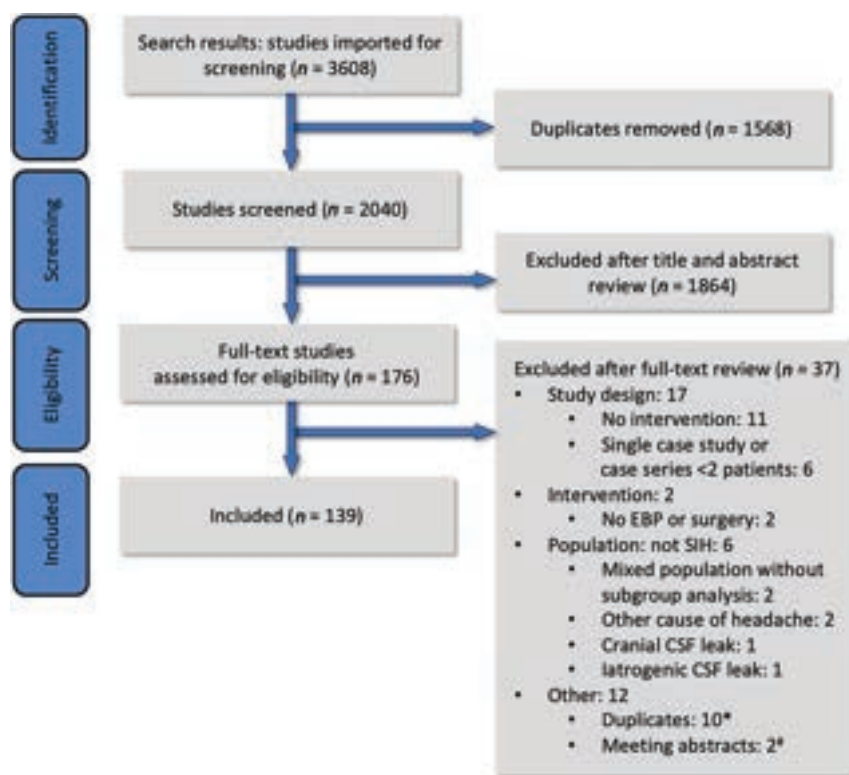


FIG 1. Evidence map or the Preferred Reporting Items for Systematic Reviews and Meta-Analyses flow chart. The asterisk indicates Martin 2019,²⁶ Ohtonari 2012,²⁷ Urbach 2020,²⁸ Beck 2019,²⁹ Pagani-Estevez 2019,³⁰ Levi 2019,³¹ Franzini 2013,³² Watanabe 2011,³³ Beck 2019,²⁹ Angelo 2011,³⁴ hash, Ferrante 2016,³⁵ Ferrante 2015.³⁶

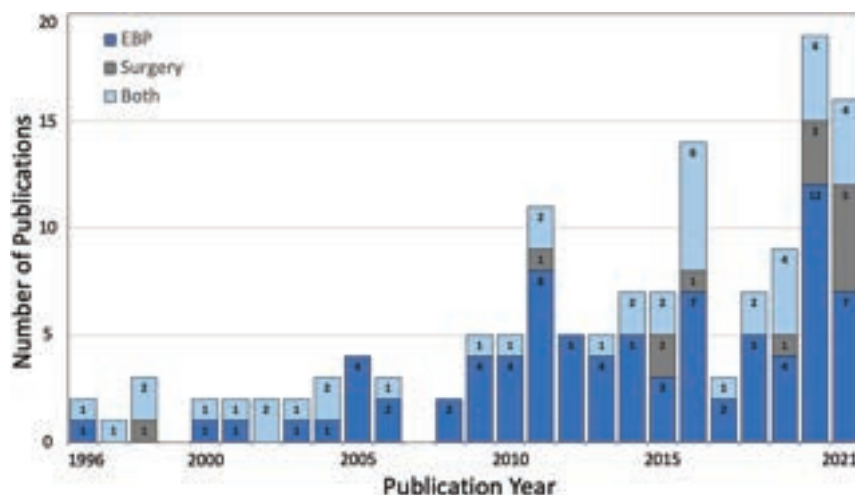


FIG 2. Timeline of included publications.

EBP, patch material used), and measures of efficacy (eg, patient symptoms, quality of life, imaging biomarkers). Proportions were assessed by 2-tailed χ^2 tests for significance. Two-tailed t tests were used to compare means. Linear regression was used to assess continuous variables such as the mean number of patients included per study across time. All statistical analyses were conducted using an open-source statistical analysis program (R statistical and computing software; Version 3.4.1; <http://www.r-project.org>). A P value $< .05$ was considered statistically significant.

Certainty of Evidence

A critical appraisal of the methodologic quality and risk of bias for individual studies as well as grading of the strength of evidence was not performed because this is an evidence mapping review.¹⁵

Role of Funding Source

This study was not supported by external funding sources.

Standard Protocol Approvals, Registrations, and Patient Consent

This Health Insurance Portability and Accountability Act-compliant study was deemed exempt from institutional review board oversight. The protocol for this study was registered with Open Science Framework on December 8, 2020.

Data Availability Statement

Anonymized data not published within this article will be made available by request from any qualified investigator.

RESULTS

The primary literature search identified 3608 studies. After duplicate articles were removed, a total of 2040 underwent title and abstract screening. Of these, 176 were moved on to full-text review, and a total of 139 were included in the evidence map (Fig 1 and Online Supplemental Data).

Characteristics of Included Studies

Most included studies (66.2%, 92 of 139) were published in the past decade. The number of studies published per year has progressively increased, particularly during the past 5–10 years (Fig 2). Most studies assessed outcomes after EBP. Very few studies investigated surgical approaches alone. Articles were published by authors at institutions throughout the world, though the greatest number came

from the United States, followed by South Korea and Japan (Fig 3). Most studies were generated from either dedicated SIH referral centers or universities. Studies that included surgery were more likely to come from referral centers (62.5%, 35 of 56) than those that included EBP (28.8%, 36 of 125), possibly due to the complexity of these operative procedures ($P < .001$). The number of patients per study has significantly increased with time (mean, 29.8 [SD 41.9] patients; range, 3–298 patients; $P < .001$). Characteristics of included studies can be found in the Online Supplemental Data.

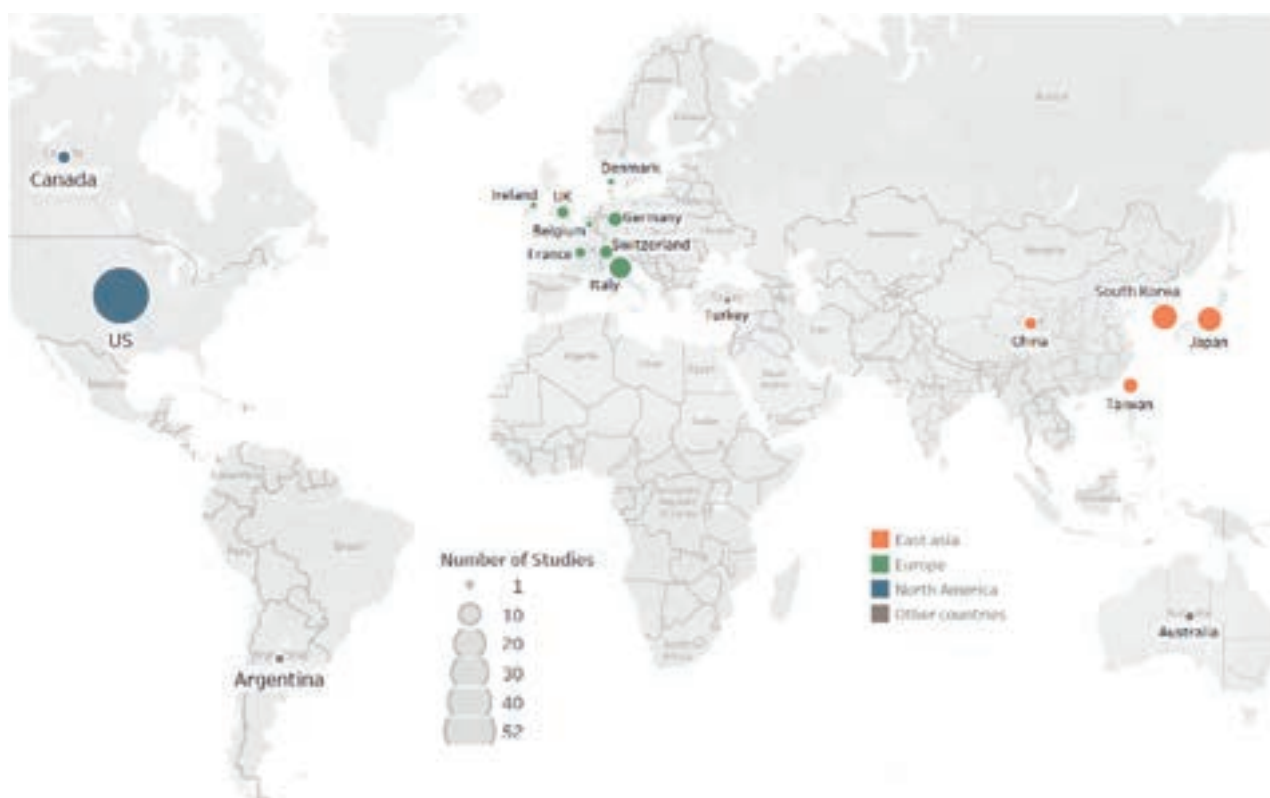


FIG 3. Countries of origin for included studies.

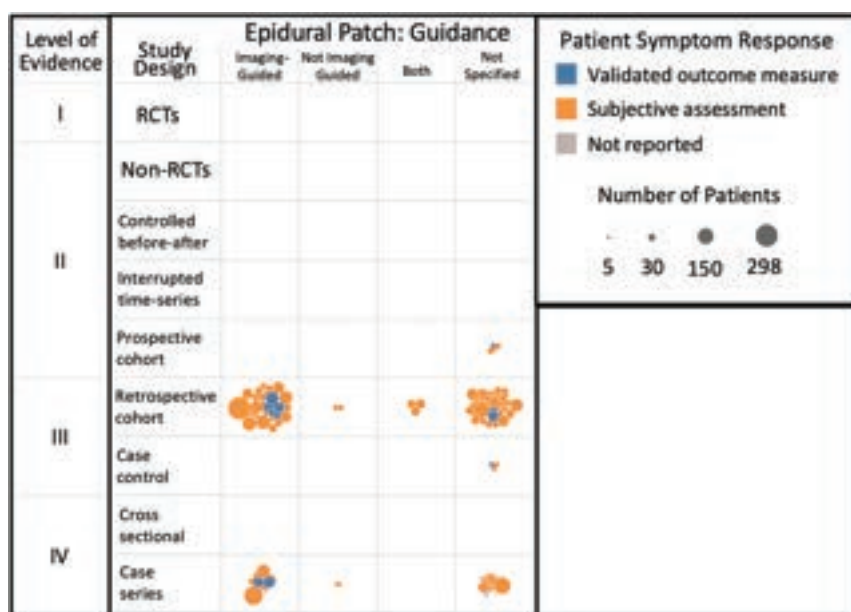


FIG 4. Evidence map of studies investigating treatments for SIH that included epidural patching and describing imaging-guidance methods. Note that each circle represents a single study with the area of the circle proportional to the study sample size; and colors represent the method of assessing a patient's symptomatic response in each study, either a validated outcome measure (blue), subjective (nonvalidated) assessment (orange), or not reported (gray). RCT indicates randomized controlled trial.

There were no studies that met level 1 evidence (ie, no randomized controlled trials). Most study designs were retrospective cohort studies (56.1%, 78 of 139) or case series (36%, 50 of

139), with only a few prospective cohort studies (3.6%, 5 of 139) (Figs 4–7). However, the evidence level of studies has slowly increased with time. For example, 52.8% of all published studies from 1996 to 2001 were case series, compared with 24.5% from 2017 to 2021. This interval reduction in the percentage of case studies reflects an increasing quality of study design. Furthermore, during the past 5 years, 67.8% of studies were a retrospective cohort design (increased from 30.6% in 1996–2001), and the first systematic reviews were published (3.8%, $n = 3$).

There were very few studies that included a comparison of 2 active treatments, and none were published before 2007. Of those published, most (66.7%, 10 of 15) were published only within the past 5 years.

The following subsections report results for the cohort of studies that included EBP and the cohort of studies that included surgery, as well as report key characteristics about included studies

such as the methods of SIH diagnosis, the included CSF leak subtypes, and the outcome measures used to assess the efficacy of treatment.

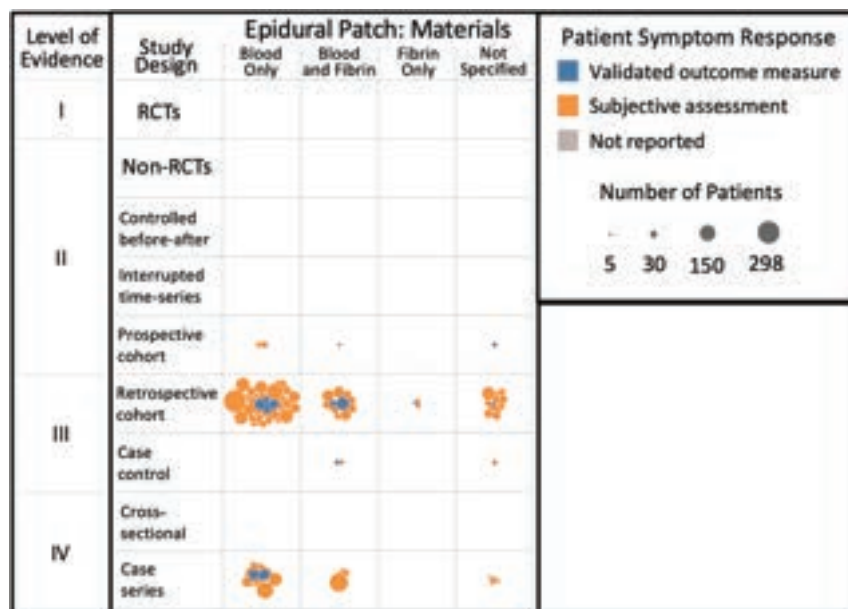


FIG 5. Evidence map of studies investigating treatments in SIH that included epidural patching and described the patching material used. RCT indicates randomized controlled trial.

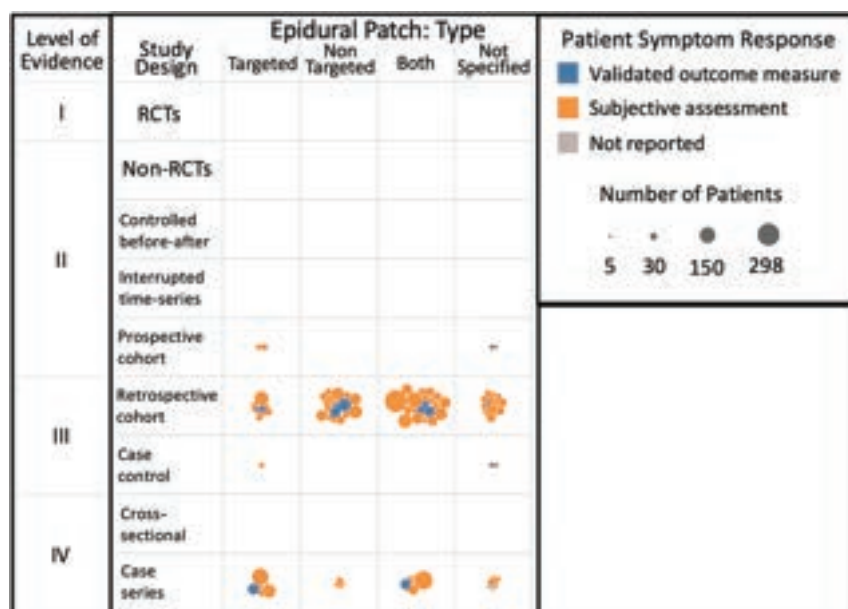


FIG 6. Evidence map of studies investigating treatments in SIH that included epidural patching and described targeted or nontargeted approaches. RCT indicates randomized controlled trial.

Epidural Patching

Most studies (57.6%, 72 of 125) that investigated the efficacy of epidural patching did not specify whether imaging guidance was used to direct needle placement (Fig 4). Moreover, several of the studies reporting the use of imaging guidance did not specify the type of guidance (ie, fluoroscopy or CT).

Nearly one-quarter of the epidural patching studies did not specify the patching material used (22.4%, 28 of 125). Most studies that did report the patching material used autologous blood (56.8%, 71 of 125). Very few studies investigated the efficacy of procedures using fibrin glue alone (3.2%, 4 of 125) (Fig 5).

The largest proportion of studies on epidural patching (28.8%, 36 of 125) did not specify whether needle placements were targeted to a site of CSF leak or were nontargeted (Fig 6). When specified, more studies reported on procedures that were nontargeted (24.8%, 31 of 125) than targeted (19.2%, 24 of 125). Many studies reported a heterogeneous mixture of both targeted and nontargeted approaches (27.2%, 34 of 125), but nearly all of these studies did not include a comparison between these subgroups.

Surgery

There were fewer studies that investigated outcomes after surgical treatment of SIH than after epidural patching ($n = 56$ versus 125, respectively). Studies that assessed outcomes after surgical treatment of SIH had significantly smaller sample sizes (mean, 9.9 [SD 12.8] patients; range, 1–69 patients) compared with EBP (mean, 30.1 [SD 43.6] patients; range, 1–298 patients) ($P < .001$). More than half of investigations on surgical treatment included <10 patients.

Most surgical studies (66.1%, 37 of 56) either did not specify the surgical approach used or included a heterogeneous mixture of multiple surgical approaches, typically in the form of case series (Fig 7). The most commonly reported surgical techniques included intradural and extradural approaches to dural repair (some using fat-packing, muscle flaps, fibrin glue, or Gelfoam; Phadia), nerve root ligation or clipping, electrocautery of epidural veins for CSF-to-venous fistulas, and nerve root sleeve meningeal diverticulum repair.

SIH: Diagnosis

Greater than one-third of the included studies either did not specify the diagnosis method (13.8%, 19 of 138) or used a subjective criterion such as physician reporting of perceived patient improvement (23.9%, 33 of 138). The remainder of the included studies used an objective method to establish a patient diagnosis of SIH (62.3%, 86 of 138) (Fig 8A). The proportion of studies using objective diagnostic criteria was similar between studies investigating treatment with EBP and those investigating treatment with surgery.

Greater than half of the included studies used diagnosis methods that satisfy current ICHD-3 criteria for a diagnosis of SIH (58.7%, 81 of 138). However, in a substantial number of studies, it was not possible to determine whether included patients

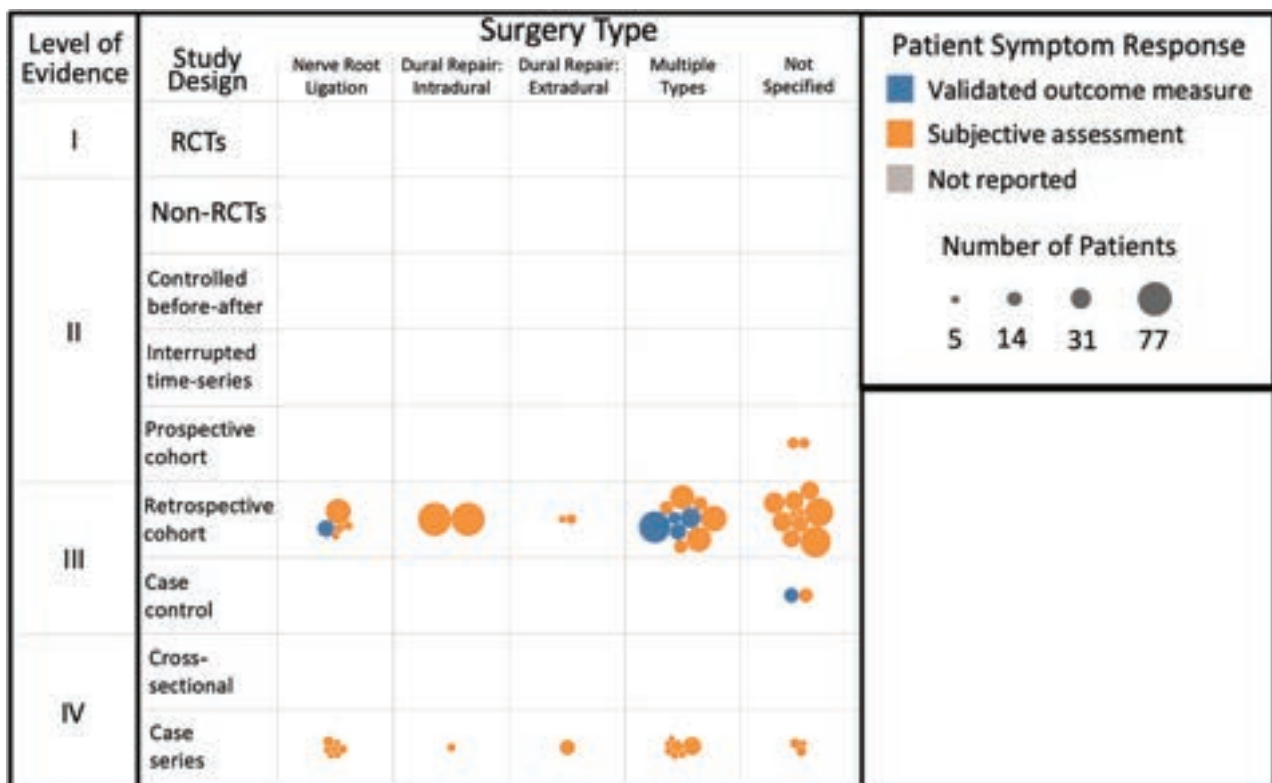


FIG 7. Evidence map of studies investigating treatments in SIH that included surgery. RCT indicates randomized controlled trial.

satisfied the ICHD-3 criteria (37.7%, 52 of 138). In a small number of studies, reporting of methodologic details was sufficient to determine that the included patients did not meet ICHD-3 diagnostic criteria (3.6%, 5 of 138) (Fig 8B).¹⁶

Types of CSF Leaks

SIH is caused by 3 known types of spinal CSF leaks: nerve root sleeve diverticula, disc osteophyte spurs, and CSF-to-venous fistulas.¹ Most studies provided insufficient detail to determine which type or types of CSF leaks were included in their investigations (Fig 8C). For example, 77.7% (108 of 139) of studies either did not report the type of CSF leaks included (56.8%, 79 of 139) or their reporting was unclear, making it impossible to tell what subtypes were included (20.9%, 29 of 139). Studies including surgical treatments were significantly more likely to report the specific subtypes of CSF leaks than studies investigating treatment with EBP (48.2%, 27 of 56 versus 17.6%, 22 of 125, $P < .001$).

Outcome Measures

Nearly all of the studies made use of subjective nonvalidated reporting of changes in patient symptoms to assess treatment efficacy (84.9%, 118 of 139). In fact, only 12.2% (17 of 139) used validated outcome measures, most commonly a Pain Numeric Rating Scale (Figs 4–7 and 9A).

There were almost no studies that included measures of quality of life (QOL). Only 1 study (0.7%) reported results from a validated QOL measure (modified Rankin scale), and 98.6% (137 of 139) did not report on QOL at all (Fig 9B). A single study subjectively reported QOL changes.

Posttreatment brain MR imaging and spine imaging are sometimes used as noninvasive biomarkers for successful resolution of SIH.¹⁷ Most of the included studies (61.2%, 85 of 139) did not report on posttreatment changes in imaging (Fig 9C). When a change was reported, it was typically in the form of a subjective interpretation of the imaging (eg, “imaging improved”), which was the case in 37.4% (52 of 139) of the studies. Only 2 studies (1.4%) used objective outcome measures such as the Bern score.¹⁸ Studies including surgery were more likely to obtain posttreatment imaging (53.6%, 30 of 56) than those including EBP (37.6%, 47 of 125) ($P = .04$). However, these studies typically included only subjective assessments of the imaging.

There were very few studies that had predetermined and set postprocedural time points for the collection of outcome measures. Far more commonly, patient outcomes were collected at variable times after treatment. In 34.6% (47 of 136) of studies, the timing of outcome collection was not reported at all.

DISCUSSION

We identified and reviewed 139 studies that reported the efficacy of surgery and EBP, the 2 most common treatments for patients with SIH. We found no studies providing level 1 evidence for the efficacy of either treatment and identified no published clinical trials. Most published studies were retrospective, typically either case series or smaller cohort studies. In general, important study details were often missing, including methodologic details such as how a diagnosis of SIH was established and what specific subtypes of CSF leaks were being treated. Furthermore, procedural characteristics were often lacking, which made it difficult to

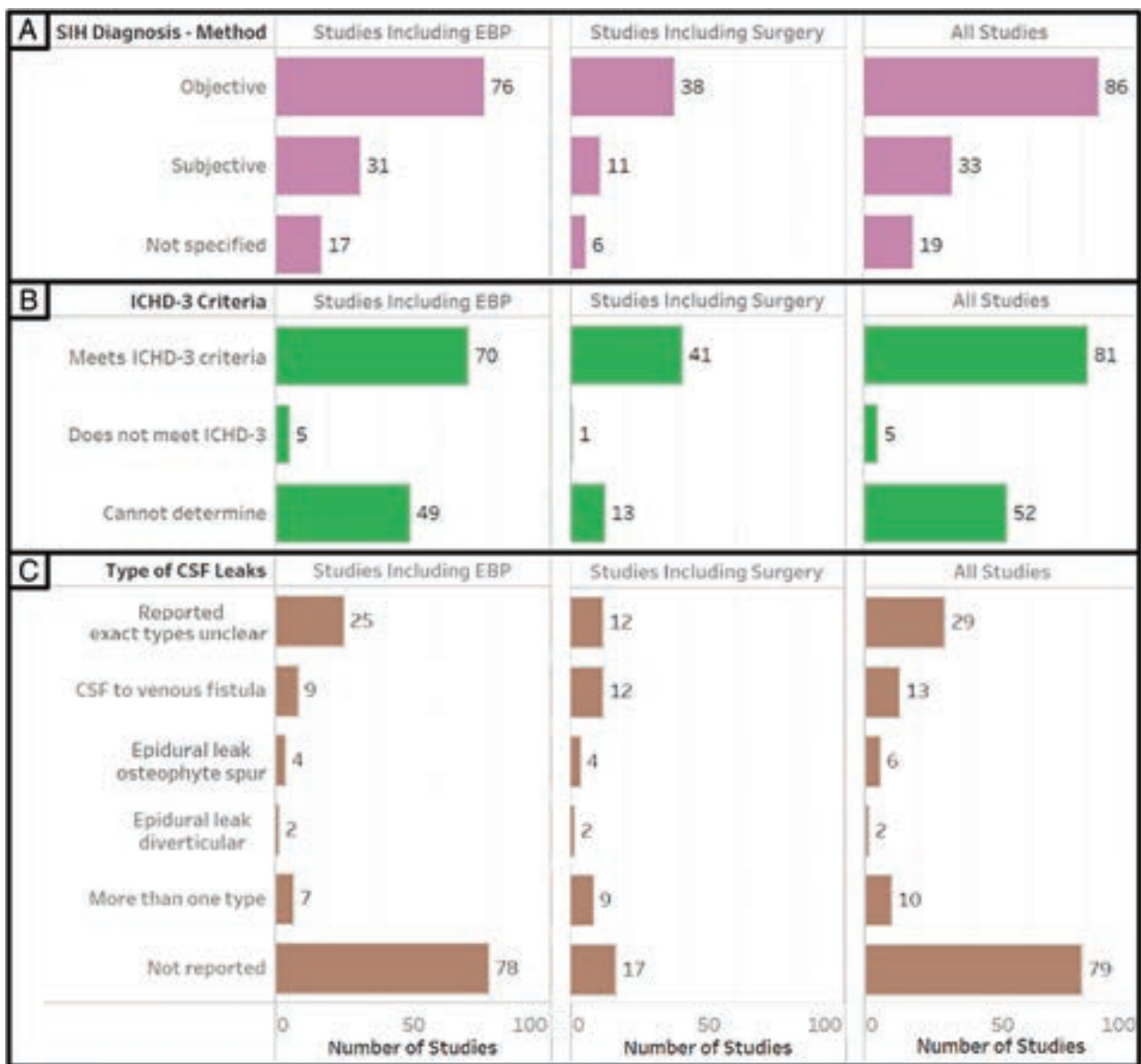


FIG 8. Methods of SIH diagnosis and types of CSF leaks.

determine important information such as whether imaging guidance or targeting was used in EBP or exactly what type of surgery was performed. Finally, patient-outcome assessment typically used subjective, nonvalidated measures collected at variable or unspecified time intervals.

The results of this evidence map suggest that the current efficacy estimates for EBP and surgery in SIH should be interpreted with caution. The incomplete description of patient characteristics in many of the included studies makes it difficult to understand how the study cohort compares with the broader SIH population, limiting applicability. For example, in some studies, the methods for establishing an SIH diagnosis were ambiguous, leading to uncertainty about the diagnosis itself. Additionally, we found that 77.7% of the studies did not adequately describe the subtypes of CSF leaks that were being treated. There may prove to be substantial differences in the treatment outcomes between patients with different subtypes of CSF leaks, which could skew

the results of individual studies, possibly leading to spurious conclusions. Similarly, the absence of key procedural details in many instances makes it difficult, if not impossible, to understand the impact of certain decisions on the efficacy of treatments, such as whether to use a targeted approach or to include fibrin glue in EBP. Finally, the use of subjective, nonvalidated outcome measures without prespecified or uniform collection times leads to uncertainty about the usefulness of the collected data. Without establishing content validity, a chosen outcome measure may not truly capture the intended information of interest. For example, the use of outcome measures focused on patients' pain may not accurately reflect the severity of disease if morbidity is due to cranial nerve dysfunction, fatigue, or cognitive dysfunction. Moreover, collecting outcomes at variable time points makes it challenging to compare cohorts of patients and could introduce bias (eg, outcomes only collected when the patient is symptomatic and returning to clinic).

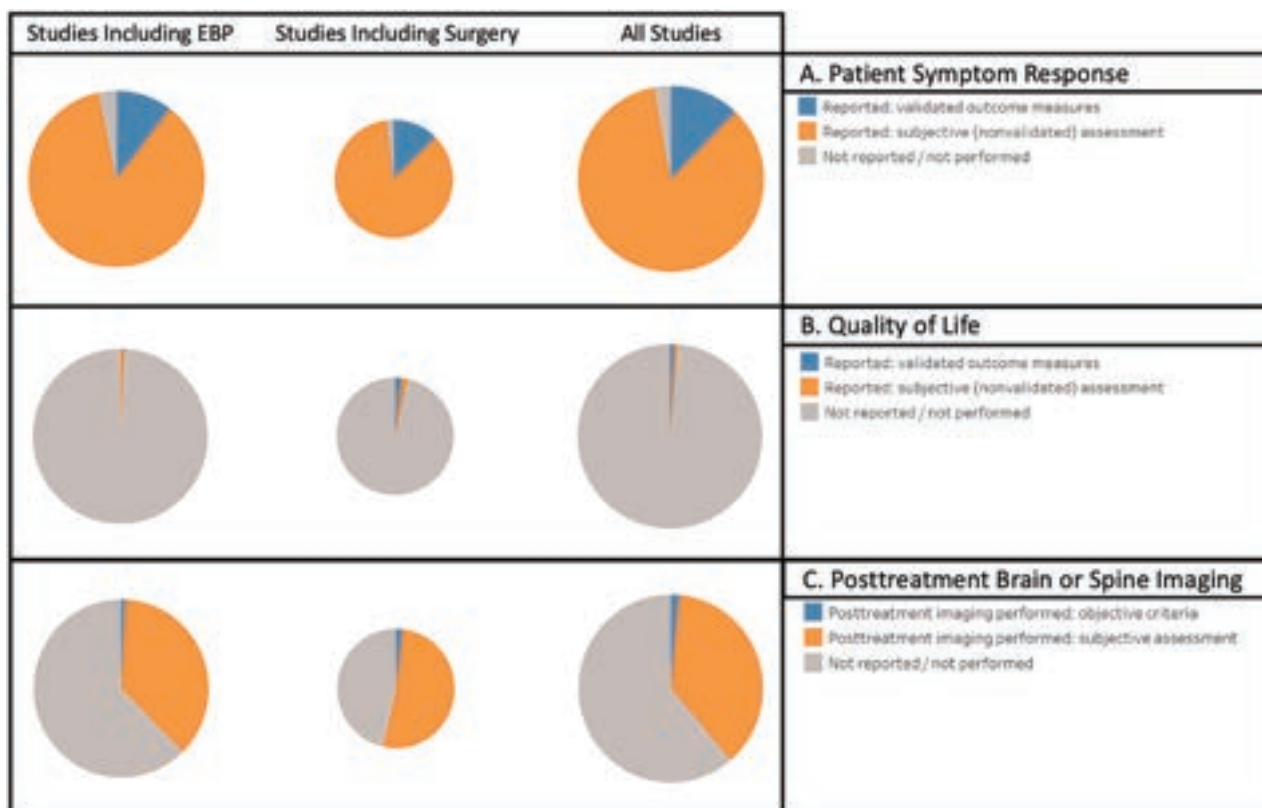


FIG 9. Outcome measures.

To our knowledge, this represents the first systematic review to map the evidence for the efficacy of EBP and surgery in the treatment of SIH. We identified 3 previously published systematic reviews of SIH, but none of these mapped the current evidence to describe characteristics of the literature nor did they identify evidence clusters and knowledge gaps. Two also included meta-analyses.^{19,20} The article by D'Antona et al¹⁹ is a general review of SIH containing a small subsection on treatment, which provides some summary estimates about conservative approaches, EBP, and surgery. The study by Signorelli et al²⁰ focused on factors affecting the outcome of EBP in SIH. Their review and analysis included only 6 articles, all retrospective. This small number was presumably due to the strict inclusion criteria used, such as the need for the studies to be comparative. This finding is in keeping with our findings that there are few prospective or comparative studies of EBP. Shlobin et al²¹ published a systematic review of patients with SIH with CSF-to-venous fistulas. The purpose of their review was to provide a comprehensive picture of CSF-to-venous fistulas, rather than to focus solely on treatment or map the evidence, as in the present study. They found 16 articles that met the inclusion criteria and performed a patient-level meta-analysis on 18 patients from 7 of these studies. Similarly, they found either only retrospective case series or cohort studies.

Given the considerable clinical and methodologic heterogeneity of the SIH literature, there was resultant statistical heterogeneity in many of the meta-analyses in these 2 studies, which raises some concern about the pooled estimates because they could lead to misleading conclusions. This heterogeneity is reflected in large

I^2 values (a measure of variation due to study heterogeneity rather than chance) for the meta-analyses, many >75% (considered high heterogeneity) and some in excess of 95%.^{19,20} In fact, very few published meta-analyses have $I^2 > 90\%$.²² Sources of heterogeneity are not identified, calling into question the value of the pooled estimates. In addition, many of the meta-analyses consisted of predominantly small studies. Although random effects analysis is appropriate, it can lend undue weight to smaller studies, skewing the estimated summary effect. Given the resultant uncertainty regarding the reported estimates, caution should be used before changing practice on the basis of these results.

The current study adds to these prior systematic reviews by providing clear descriptions of study design and methodology, including details about SIH diagnostic criteria, patient characteristics, procedure specifics, and the outcome measures used. Furthermore, this investigation maps the breadth of the literature rather than focusing on a narrow question in a small subset of studies. It, therefore, provides a better perspective to identify knowledge gaps and to suggest designs that might address these unmet needs. The results of this investigation reveal several evidence gaps and clear opportunities for methodologic improvement, which, when addressed through future research, will serve to improve the state of the literature and advance our knowledge about SIH treatment efficacy. First, the dearth of prospective studies and the absence of any level 1 evidence or clinical trials demonstrate a clear unmet need. Similarly, there are few comparative studies. Thus, future research should be directed toward designing comparative prospective studies beginning with cohort designs followed by

randomized controlled trials, preferably with a multicenter approach to maximize patient enrollment and generalizability. These efforts may be best facilitated through development of a research infrastructure among a consortium of dedicated research institutions. Furthermore, there are very few studies investigating surgical treatments of SIH. Dedicated effort to determine the efficacy of SIH treatments other than EBP (ie, surgery and the newly developed venous embolization of CSF-venous fistulas) should be pursued.²³ Second, future research should endeavor to reduce the potential for bias through adherence to sound methodologic practices and to improve interpretability through the clear reporting of key components of the study design. We recommend that objective SIH diagnostic criteria be used for patient inclusion, which should follow the current ICHD criteria at the time of the study (currently ICHD-3).¹⁶ Similarly, investigators should report the subtypes of spinal CSF leaks included in their cohort and whether there are efficacy differences among these subgroups of patients with SIH.

The following key procedural details should also be included at a minimum so that results may be better interpreted. For EBP, we strongly recommend including whether imaging guidance was used and the type (eg, CT fluoroscopy), whether the needles were targeted to the site of a known CSF leak or nontargeted, and the type of patch material used (eg, blood, fibrin glue, or both). For surgery, we recommend describing the operative approach or approaches in detail or providing references to previously described techniques. Critically, we recommend reporting symptom and disability outcome measures that are validated for use in SIH and that these measures be collected at prespecified uniform time points. To our knowledge, there are currently no validated outcome measures for use in SIH. Thus, effort should be directed toward validating existing measures or generating new ones. Until these efforts are completed, we recommend using objective measures validated for use in other headache disorders, such as the Headache Impact Test-6 and EuroQol-5D (<https://euroqol.org/>).^{24,25} Finally, the use of changes in imaging (eg, resolution of SIH findings on brain MR imaging) as an outcome measure should include either an objective scoring system or description.¹⁸

This study is a protocol-driven, methodologically rigorous evidence map. However, there are several potential limitations to this investigation. It is possible that our search inadvertently excluded studies that would have otherwise met the criteria for inclusion. This issue could have occurred due to the use of narrower search terms that included the “spontaneous” concept. However, we followed best practices for search development and reviewed a random sample of studies from the more expansive search to ensure that the probability of this exclusion was minimal, at best. Furthermore, we did not search the gray literature because this was deemed unlikely to have identified relevant studies and, therefore, did not warrant the substantial additional effort. This investigation did not include the few studies that reported the efficacy of transvenous embolization of CSF-to-venous fistulas because this newer treatment method was developed after the protocol for this review was established and there are so few publications on this promising new intervention to date. Additionally, the authors recognize that some of our recommendations are dependent on presumptions that are yet to be proved.

For example, if nontargeted patching is equivalent in efficacy to targeted patching, then identifying the CSF leak subtype and localizing the leak with advanced myelography techniques may not be necessary. Finally, given that evidence mapping is a relatively new approach to critically appraising the literature, the standards are evolving. We followed current best practices, but these may be subject to change.

CONCLUSIONS

This systematic review and evidence map summarize the current state of the literature investigating the efficacy of EBP and surgery in the treatment of SIH based on 139 articles. Most studies were retrospective, and there was no published level 1 evidence. Identified gaps include the need for studies comparing the efficacy of different treatments as well as more sophisticated study designs such as prospective cohorts and randomized controlled trials. There remain many opportunities for the improvement in study methodology. We recommend that future research use the ICHD diagnostic criteria for SIH, explicitly report the specific subtypes of CSF leaks, include key procedural details such as whether EBP was imaging-guided and targeted and the type of patching material used or provide details about the surgical approach, and use objective outcome measures preferably validated for use in SIH and collected at uniform prespecified time points.

ACKNOWLEDGMENTS

The authors would like to thank Reginald Lerebours from Duke University Medical Center for his assistance with the power analysis for the initial screening search and Eric Monson for his assistance in generating the figures for this article.

Disclosure forms provided by the authors are available with the full text and PDF of this article at www.ajnr.org.

REFERENCES

1. Amrhein TJ, Kranz PG. **Spontaneous intracranial hypotension: imaging in diagnosis and treatment.** *Radiol Clin North Am* 2019;57:439–51 CrossRef Medline
2. Kranz PG, Gray L, Malinzak MD, et al. **Spontaneous intracranial hypotension: pathogenesis, diagnosis, and treatment.** *Neuroimaging Clin N Am* 2019;29:581–94 CrossRef Medline
3. Ferrante E, Arpino I, Citterio A, et al. **Epidural blood patch in Trendelenburg position pre-medicated with acetazolamide to treat spontaneous intracranial hypotension.** *Eur J Neurol* 2010;17:715–19 CrossRef Medline
4. He FF, Li L, Liu MJ, et al. **Targeted epidural blood patch treatment for refractory spontaneous intracranial hypotension in China.** *J Neurol Surg B Skull Base* 2018;79:217–23 CrossRef Medline
5. Wu JW, Hseu SS, Fuh JL, et al. **Factors predicting response to the first epidural blood patch in spontaneous intracranial hypotension.** *Brain* 2017;140:344–52 CrossRef Medline
6. Cho KI, Moon HS, Jeon HJ, et al. **Spontaneous intracranial hypotension: efficacy of radiologic targeting vs blind blood patch.** *Neurology* 2011;76:1139–44 CrossRef Medline
7. Chung SJ, Lee JH, Im JH, et al. **Short- and long-term outcomes of spontaneous CSF hypovolemia.** *Eur Neurol* 2005;54:63–67 CrossRef Medline
8. Berroir S, Loisel B, Ducros A, et al. **Early epidural blood patch in spontaneous intracranial hypotension.** *Neurology* 2004;63:1950–51 CrossRef Medline

9. Sencakova D, Mokri B, McClelland RL. **The efficacy of epidural blood patch in spontaneous CSF leaks.** *Neurology* 2001;57:1921–23 CrossRef Medline
10. Ahn C, Lee E, Lee JW, et al. **Two-site blind epidural blood patch versus targeted epidural blood patch in spontaneous intracranial hypotension.** *J Clin Neurosci* 2019;62:147–54 CrossRef Medline
11. Tricco AC, Lillie E, Zarin W, et al. **PRISMA Extension for Scoping Reviews (PRISMA-ScR): checklist and explanation.** *Ann Intern Med* 2018;169:467–73 CrossRef Medline
12. Amrhein TJ, Kranz PG, Cantrell S, et al. **Efficacy of epidural blood patching or surgery in spontaneous intracranial hypotension: an evidence map protocol.** *Syst Rev* 2022;11:116 CrossRef Medline
13. McGowan J, Sampson M, Salzvedel DM, et al. **PRESS Peer Review of Electronic Search Strategies: 2015 Guideline Statement.** *J Clin Epidemiol* 2016;75:40–46 CrossRef Medline
14. **Covidence systematic review software.** Veritas Health Innovation, [online]. www.covidence.org
15. Bragge P, Clavisi O, Turner T, et al. **The Global Evidence Mapping Initiative: scoping research in broad topic areas.** *BMC Med Res Methodol* 2011;11:92 CrossRef Medline
16. International Headache Society. **The International Classification of Headache Disorders 3rd edition.** <https://www.ichd-3.org/7-headache-attributed-to-non-vascular-intracranial-disorder/7-2-headache-attributed-to-low-cerebrospinal-fluid-pressure/7-2-3-headache-attributed-to-spontaneous-intracranial-hypotension/>. Accessed March 15, 2023
17. Sulioti G, Gray L, Amrhein TJ. **Popping the balloon: abrupt onset of a spinal CSF leak and spontaneous intracranial hypotension in idiopathic intracranial hypertension, a case report.** *Headache* 2022;62:208–11 CrossRef Medline
18. Dobrocky T, Grunder L, Breiding PS, et al. **Assessing spinal cerebrospinal fluid leaks in spontaneous intracranial hypotension with a scoring system based on brain magnetic resonance imaging findings.** *JAMA Neurol* 2019;76:580–87 CrossRef Medline
19. D'Antona L, Jaime Merchan MA, Vassiliou A, et al. **Clinical presentation, investigation findings, and treatment outcomes of spontaneous intracranial hypotension syndrome: a systematic review and meta-analysis.** *JAMA Neurol* 2021;78:329–37 CrossRef Medline
20. Signorelli F, Caccavella VM, Giordano M, et al. **A systematic review and meta-analysis of factors affecting the outcome of the epidural blood patching in spontaneous intracranial hypotension.** *Neurosurg Rev* 2021;44:3079–85 CrossRef Medline
21. Shlobin NA, Shah VN, Chin CT, et al. **Cerebrospinal fluid-venous fistulas: a systematic review and examination of individual patient data.** *Neurosurgery* 2021;88:931–41 CrossRef Medline
22. Higgins JP, Thompson SG, Deeks JJ, et al. **Measuring inconsistency in meta-analyses.** *BMJ* 2003;327:557–60 CrossRef Medline
23. Brinjikji W, Garza I, Whealy M, et al. **Clinical and imaging outcomes of cerebrospinal fluid-venous fistula embolization.** *J Neurointerv Surg* 2022;14:953–56 CrossRef Medline
24. Yang M, Rendas-Baum R, Varon SF, et al. **Validation of the Headache Impact Test (HIT-6) across episodic and chronic migraine.** *Cephalalgia* 2011;31:357–67 CrossRef Medline
25. EuroQol Group. **EuroQol: a new facility for the measurement of health-related quality of life.** *Health Policy* 1990;16:199–208 CrossRef Medline
26. Martin R, Louy C, Babu V, et al. **A two-level large-volume epidural blood patch protocol for spontaneous intracranial hypotension: retrospective analysis of risk and benefit.** *Reg Anesth Pain Med* 2019 Sep 20. [Epub ahead of print] CrossRef Medline
27. Ohtonari T, Ota S, Nishihara N, et al. **A novel technique of multiple-site epidural blood patch administration for the treatment of cerebrospinal fluid hypovolemia.** *J Neurosurg* 2012;116:1049–53 CrossRef Medline
28. Urbach H, Fung C, Dovi-Akue P, et al. **Spontaneous intracranial hypotension.** *Dtsch Arztebl Int* 2020;117:480–87 CrossRef Medline
29. Beck J, Raabe A, Schievink WI, et al. **Posterior approach and spinal cord release for 360 degrees repair of dural defects in spontaneous intracranial hypotension.** *Neurosurgery* 2019;84:E345–51 CrossRef Medline
30. Pagani-Estevez GL, Cutsforth-Gregory JK, Morris JM, et al. **Procedural predictors of epidural blood patch efficacy in spontaneous intracranial hypotension.** *Reg Anesth Pain Med* 2019;44:212–20 CrossRef
31. Levi V, Di Laurenzio NE, Franzini A, et al. **Lumbar epidural blood patch: effectiveness on orthostatic headache and MRI predictive factors in 101 consecutive patients affected by spontaneous intracranial hypotension.** *J Neurosurg* 2019;132:809–17 CrossRef Medline
32. Franzini A, Messina G, Chiapparini L, et al. **Treatment of spontaneous intracranial hypotension: evolution of the therapeutic and diagnostic modalities.** *Neurol Sci* 2013;34(Suppl 1):S151–55 CrossRef Medline
33. Watanabe K, Hashizume K, Kawaguchi M, et al. **Fluoroscopically guided epidural blood patch with subsequent spinal CT scans in the treatment of spontaneous cerebrospinal fluid hypovolemia.** *J Neurosurg* 2011;114:1731–35 CrossRef Medline
34. Angelo F, Giuseppe M, Eliana M, et al. **Spontaneous intracranial hypotension: diagnostic and therapeutic implications in neurosurgical practice.** *Neurol Sci* 2011;32 Suppl 3:S287–90 CrossRef Medline
35. Ferrante E, Olgiati E, Sangalli V, et al. **Early pain relief from orthostatic headache and hearing changes in spontaneous intracranial hypotension after epidural blood patch.** *Acta Neurol Belg* 2016;116:503–08 CrossRef Medline
36. Ferrante E, Rubino F, Arpino I, et al. **Treatment of orthostatic headache from spontaneous intracranial hypotension syndrome: single institutional experience of 326 cases.** *J Headache Pain* 2015;16:A125 CrossRef Medline

Utility of Photon-Counting Detector CT Myelography for the Detection of CSF-Venous Fistulas

A.A. Madhavan, L. Yu, W. Brinjikji, J.K. Cutsforth-Gregory, F.R. Schwartz, I.T. Mark, J.C. Benson, and T.J. Amrhein



ABSTRACT

SUMMARY: CSF-venous fistulas are an increasingly recognized type of CSF leak that can be particularly challenging to detect, even with recently improved imaging techniques. Currently, most institutions use decubitus digital subtraction myelography or dynamic CT myelography to localize CSF-venous fistulas. Photon-counting detector CT is a relatively recent advancement that has many theoretical benefits, including excellent spatial resolution, high temporal resolution, and spectral imaging capabilities. We describe 6 cases of CSF-venous fistulas detected on decubitus photon-counting detector CT myelography. In 5 of these cases, the CSF-venous fistula was previously occult on decubitus digital subtraction myelography or decubitus dynamic CT myelography using an energy-integrating detector system. All 6 cases exemplify the potential benefits of photon-counting detector CT myelography in identifying CSF-venous fistulas. We suggest that further implementation of this imaging technique will likely be valuable to improve the detection of fistulas that might otherwise be missed with currently used techniques.

ABBREVIATIONS: CTM = CT myelography; CVF = CSF-venous fistula; DSM = digital subtraction myelography; EID = energy-integrating detector; LDDSM = lateral decubitus digital subtraction myelography; PCD = photon-counting detector; SIH = spontaneous intracranial hypotension; SR = standard resolution; T3D = low-energy threshold; UHR = ultra-high-resolution mode; VMI = virtual monoenergetic image

Spontaneous intracranial hypotension (SIH) is caused by a spinal CSF leak from a dural tear (type 1), leaking meningeal diverticulum (type 2), or a CSF-venous fistula (CVF, type 3).¹ Localization of the causative CSF leak requires imaging techniques with high spatial and temporal resolution, such as decubitus digital subtraction myelography (DSM) and dynamic CT myelography (CTM).^{2,3} CVFs can be particularly challenging to detect because they may opacify with contrast only intermittently, and they sometimes require very dense intrathecal contrast for the draining vein to become visible. Procedural modifications such as imaging during inspiration and use of conebeam CT with DSM have recently been shown to increase the yield of detecting CVFs.⁴⁻⁶ Despite optimal techniques, however, CVFs are sometimes missed.

Photon-counting detector (PCD) CT is a recent advancement that has multiple benefits over conventional energy-integrating detector (EID) CT.^{7,8} EIDs convert incident x-rays into visible light, which subsequently encounters a photodiode that generates

an electric signal proportional to the total energy deposited. As a result of this process, the energy information of each individual x-ray photon is lost. In contrast, PCDs convert the energy of each individual x-ray photon directly into an electric pulse and record the energy information on the basis of the pulse height, allowing more precise discrimination of individual photon energy. This photon-counting process permits a more optimal energy-weighting of individual photons and leads to multiple benefits over EIDs. First, electronic noise is substantially reduced by applying a low-energy threshold, leading to improved signal- and contrast-to-noise ratios. Second, photons can be binned into different energy ranges, and subsequent postprocessing can be performed to obtain virtual monoenergetic images (VMIs) without impairing scan speed or increasing the dose. The SNR of the VMIs is also typically better than can be achieved with modern dual-energy CT. Finally, because PCDs do not require physical septa between detector elements, detector pixel size can be made smaller compared with EIDs, yielding superior spatial resolution (up to 40 line pairs/cm). Due to these advantages, PCD CTM can theoretically detect CVFs that may not be apparent on DSM or EID CTM. One case of a CVF seen on PCD CTM has been reported, but its added value over DSM and EID CTM is yet to be demonstrated.⁹

Here, we report 6 cases of CVFs that were identified on PCD CT. The CVFs were occult on decubitus DSM or EID CTM in 5 cases.

Received March 15, 2023; accepted after revision April 26.

From the Division of Neuroradiology (A.A.M., L.Y., W.B., I.T.M., J.C.B.), Department of Radiology and Department of Neurology (J.K.C.-G.), Mayo Clinic, Rochester, Minnesota; and Division of Neuroradiology (F.R.S., T.J.A.), Department of Radiology, Duke University Medical Center, Durham, North Carolina.

Please address correspondence to Ajay Madhavan, MD, Division of Neuroradiology, Department of Radiology, Mayo Clinic, 200 First St SW, Rochester, MN 55905; e-mail: madhavan.ajay@mayo.edu

<http://dx.doi.org/10.3174/ajnr.A7887>

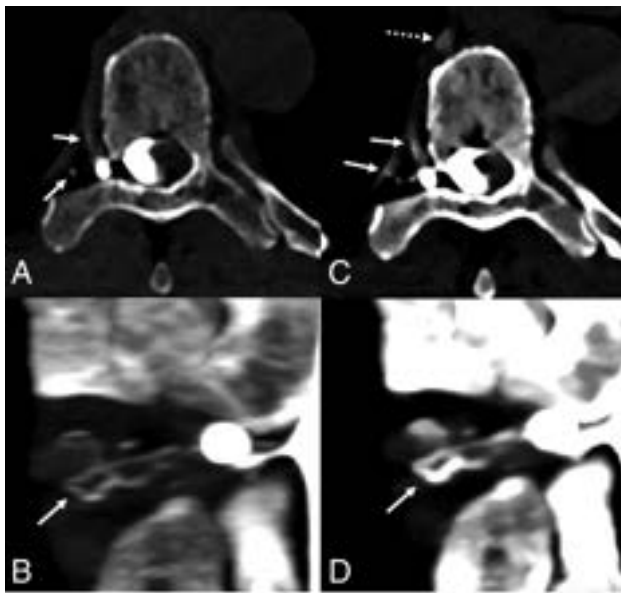


FIG 1. A 70-year-old man with 18 months of orthostatic headaches and brain MR imaging demonstrating diffuse pachymeningeal enhancement (not shown). Axial and coronal T3D reconstructions from a right lateral decubitus PCD CTM (A and B) at a section thickness of 0.2 mm demonstrate exquisite delineation of tiny veins draining a right T6 CVF (A and B, arrows). Axial and coronal 40-keV reconstructions at the identical time point and window/level settings, both at a section thickness of 0.4 mm (minimum allowable), demonstrate improved conspicuity of the iodine signal within the same veins (C and D, solid arrows) and within the more distal azygous vein (C, dashed arrow), though with slightly diminished anatomic characterization. PCD CT confers excellent spatial resolution and spectral information, which have a complementary role and can both be useful in imaging CVFs. The patient underwent transvenous Onyx embolization of the CVF.

MATERIALS AND METHODS

Patient Selection

This is a retrospective series including patients from 2 separate institutions specializing in the diagnosis and treatment of SIH. Medical records were searched for all consecutive patients who underwent PCD CTM for the indication of SIH from April 2022 to March 2023. All myelographic images, including EID CTMs, DSMs, and PCD CTMs were reviewed by 2 neuroradiologists blinded to the radiologic reports. Cases demonstrating a definitive CVF on PCD CTM were included in this case series. Clinical information and brain MR imaging findings from each included case were recorded. This study was deemed exempt by both institutional review boards.

Myelographic Examination Technique

The technique for lateral decubitus digital subtraction myelography (LDDSM) has been previously described and was used for the included patients.¹⁰ For decubitus EID CTM, lumbar puncture was performed on the CT table, and 10–11 mL of iodinated contrast was injected immediately before performing a single scan of the entire spine. The needle was removed, and scanning was repeated with the patient in the contralateral decubitus position without injection of more contrast. The scanning protocol used a previously described technique.³

The PCD CTM technique varied slightly by participating institution. At the first institution, the patient was placed in the PCD CT scanner (NAEOTOM Alpha; Siemens) in the right lateral decubitus Trendelenburg position. A 20-ga spinal needle was advanced into the subarachnoid space at L3–L4 under CT guidance. Five milliliters of Omnipaque 300 (GE Healthcare) was injected intrathecally. Multiple low-dose monitoring scans at C7–T1 were performed every 5 seconds to dynamically monitor contrast flow. A series of 3–6 scans of the entire spine was initiated manually when intrathecal contrast reached C7–T1. All scans were performed at end inspiration with a 5-second interval between scans. The needle was removed, the patient was rotated to the left lateral decubitus position, and the process was repeated after placing a new spinal needle, injecting 5–6 mL of contrast, and performing 3–6 additional scans.

Among the 3–6 scans in each position, the first 2–4 scans were obtained with standard resolution (SR) mode (144×0.4 mm detector collimation), and the last 1–2 scans, with ultra-high-resolution (UHR) mode (120×0.2 mm detector collimation). All scans had a rotation time of 0.5 seconds, CAREkeV image quality level of 200. Automatic exposure control was on, with a manual kilovolt of 140. All scans were reconstructed separately at 40 keV, 55 keV, and at a low-energy threshold (referred to as T3D by the manufacturer and including photon energies from 20 keV to 140 keV), all with a Br40-3 kernel (quantum iterative reconstruction strength setting of 3). SR scans were reconstructed at 0.4 mm, and UHR scans were reconstructed at 0.2 mm. Pitch was 1.2 (SR) or 1.0 (UHR), and the mean time per scan was 5.0 seconds (SR) and 12.0 seconds (UHR).

At the second institution, lumbar puncture and contrast injection were performed under conventional fluoroscopy with a tilting table with the patient in the right lateral decubitus position, also at L3–L4 with an injection of 10 mL of Isovue-M 300 (Bracco). Patients were transferred to PCD CT while maintaining decubitus and Trendelenburg positioning, and a single scan in the UHR mode was obtained, in both cases approximately 10 minutes after contrast injection. Patients were rotated to the prone and left lateral decubitus positions, and 2 additional UHR scans were obtained in each position. Scans were reconstructed at 0.2 mm with T3D.

RESULTS

Patient Cohort

In total, 12 patients underwent PCD CTM during the study period (3 with prior negative findings on DSM, 8 with prior negative findings on EID CTM, and 1 with no prior myelographic studies). Of these, 6/12 had a definite CVF identified on PCD CTM by review of both neuroradiologists (figures/patients, 1–6), while the other 6 PCD CTMs had negative findings. In one of the cases with positive findings (patient 1), the PCD CTM was the first myelographic study performed. In another 3 patients (patients 2–4), LDDSM was performed initially and had negative findings. In the final 2 patients (patients 5 and 6), decubitus dynamic EID CTM was performed initially and had negative findings. Patients 1–4 were from the first institution, and patients 5 and 6 were from the second institution.

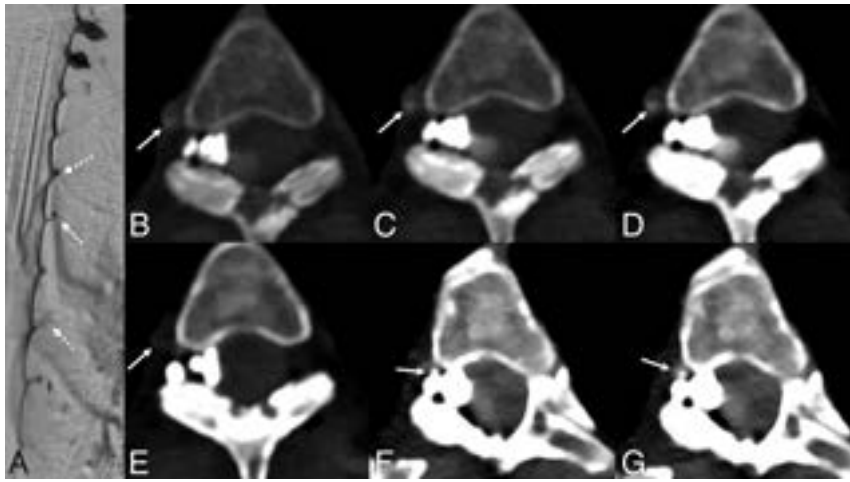


FIG 2. A 65-year-old woman with several years of orthostatic headaches and brain MR imaging demonstrating diffuse pachymeningeal enhancement and brain sag (not shown). Representative image from a right lateral decubitus DSM (A) shows multiple meningeal diverticula that remained stable during dynamic imaging (A, *dashed arrows*), with no evidence of a CVF. Axial images from a right lateral decubitus PCD CTM at the same time point (B–D) reconstructed at a T3D (B), 55 keV (C), and 40 keV (D) demonstrate a right T3 CVF (B–D, *arrows*), which is most apparent at 40 keV. The CVF is not apparent during imaging 30 seconds later, even at 40 keV (E, *arrow*). Additional images at adjacent slices, both from the earlier time point at 40 keV (F and G), show that this venous enhancement, though discontinuous, does, in fact, arise from a prominent meningeal diverticulum (F and G, *arrows*). In this case, the high degree of temporal resolution and spectral imaging conferred by PCD CT were necessary to confidently make the diagnosis. The patient underwent successful transvenous Onyx embolization of the right T3 CVF.

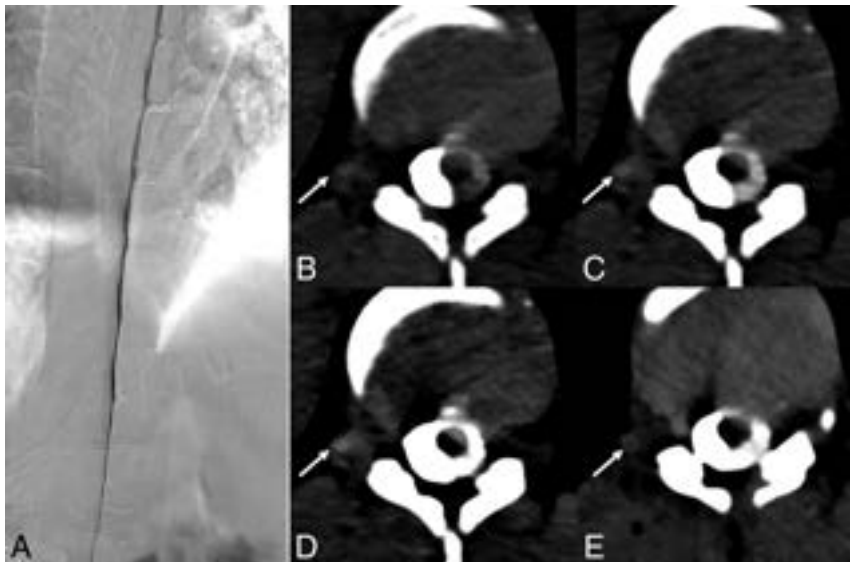


FIG 3. A 36-year-old woman with several years of orthostatic headaches, tinnitus, and MR imaging demonstrating brain sag without pachymeningeal enhancement (not shown). A representative image from a right lateral decubitus DSM (A) shows no evidence of a CVF. Axial images from a right lateral decubitus PCD CTM at the same time point (B–D) reconstructed at a T3D (B), 55 keV (C), and 40 keV (D) demonstrate a subtle right T1 CVF (B–D, *arrows*), most apparent at 40 keV. An axial 40-keV image obtained 20 seconds later (E) no longer shows this subtle venous opacification (E, *arrow*). The patient underwent Onyx embolization of this right T1 fistula.

Clinical and Conventional Imaging Findings

All 6 patients met International Classification of Headache Disorders (ICHD-3) criteria for SIH. Contrast-enhanced brain MR imaging showed brain sagging and/or pachymeningeal enhancement in patients 1, 2, 3, 5, and 6. Patient 4 had normal findings on

brain MR imaging. All 6 patients had no evidence of extradural fluid on spine MR imaging (patients 1–4) or conventional CTM (patients 5 and 6).

Additional Advanced Myelography Findings

LDDSM for patients 2–4 and decubitus EID CTM for patients 5 and 6 were negative for CVF on review by both neuroradiologists. Although multiple meningeal diverticula were present, no levels had any findings suspicious for CVF or other leaks.

PCD CTM for all 6 patients was positive for a single definitive CVF on review by both neuroradiologists (Figs 1–6). In the cases from the first institution, the CVFs were most apparent at 40 keV using 0.4-mm reconstructions (Figs 1–4). In the cases from the second institution, the CVFs were most apparent using 0.2-mm T3D reconstructions (Figs 5 and 6). Mean dose-length product for patients 1–4 was 7223 mGy-cm, while the mean dose-length product for patients 5 and 6 was 1602 mGy-cm.

Treatment

Patients 1–4 underwent transvenous Onyx (Medtronic) embolization of their CVFs. Patients 5 and 6 underwent CT-guided epidural blood and fibrin glue patching at the level of the CVF. These are the preferred initial methods of treatment at each respective institution based on the availability of resources and institutional experience with each method of treatment. All patients have had symptomatic resolution to date, with the time since treatment ranging from 3 weeks to 6 months.

DISCUSSION

We have described 6 patients with SIH with CVFs identified using lateral decubitus PCD CTM. In 5 patients (patients 2–6), the CVF was occult using decubitus DSM or EID CTM. In all 6 cases, precise localization of the CVF on PCD CTM was instrumental in permitting targeted treatment.

Decubitus dynamic EID CTM and DSM are both excellent techniques for localization of CVFs.^{3,10} Precise techniques for both modalities vary considerably across different institutions. Some of these variations include differences in timing between contrast injection and imaging, duration of imaging/frame rate (for DSM), number of scans obtained (for CTM),

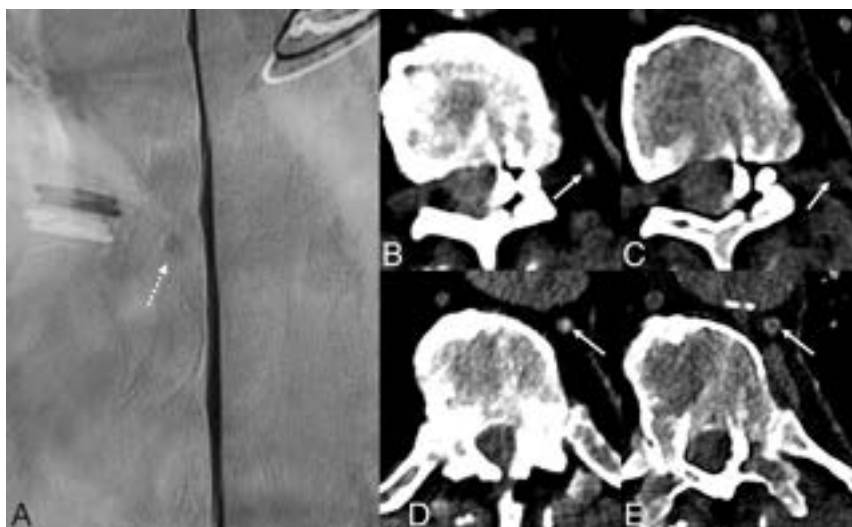


FIG 4. An 80-year-old man with several years of orthostatic headaches but normal brain MR imaging findings (not shown). Representative image from a left lateral decubitus DSM centered at T10 (A) shows a small meningeal diverticulum (A, dashed arrow) but no evidence of a CVF. Axial 40-keV images at 2 adjacent slices from a left lateral decubitus PCD CTM (B and D) demonstrate opacification of a paraspinal vein (B, arrow) and the azygous and hemiazygous vein (D, arrow), consistent with a CVF. Axial 40-keV images at the same slices obtained 30 seconds later (C and E) no longer show contrast within these veins (C and E, arrows). The patient underwent transvenous Onyx embolization of the left T10 CVF.

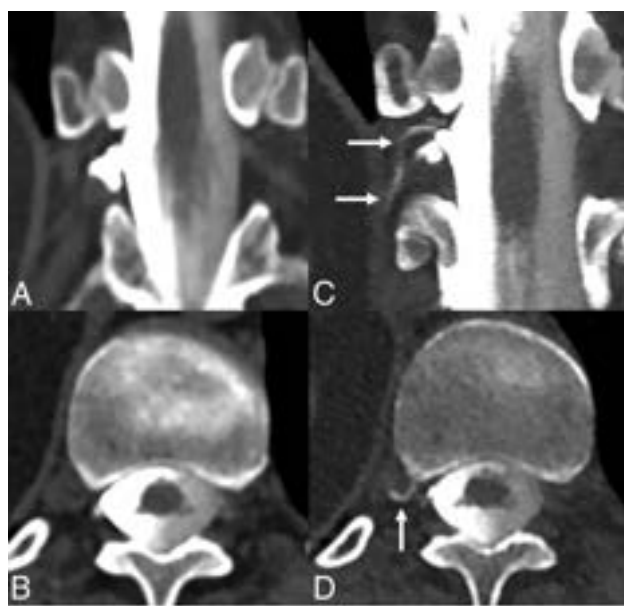


FIG 5. A 55-year-old woman with SIH according to the ICHD-3 criteria, including dural enhancement and venous distention on brain MR imaging (not shown). Coronal and axial images from a right lateral decubitus dynamic CTM (A and B) on an EID scanner reconstructed at 0.6 mm show no clear CVF. Subsequent PCD CTM with the patient in the right lateral decubitus position, including 0.2-mm coronal and axial reconstructions (C and D), shows a clear right T11 CVF (C and D, arrows).

and respiratory instructions during imaging.^{3,4,10} Some institutions prefer a 2-day myelographic technique, while others perform a same-day bilateral technique.¹¹ Despite considerable improvement in technique at many centers, CVFs can be missed, even in patients meeting the ICHD-3 criteria for SIH with no evidence of type 1 or 2 leaks. Our series suggests that PCD CTM could have a role in

identifying CVFs in patients with negative findings on DSM or dynamic EID CTM (Figs 2–6). Furthermore, PCD CTM may be a reasonable initial myelographic test to localize CVFs as this technology becomes more accessible (Fig 1).

PCD CTM may theoretically be more sensitive for CVF detection for many reasons. First, it has superior spatial resolution compared with the most current EID scanners. PCD CT allows an axial section thickness of 0.2–0.4 mm (depending on the scan mode) compared with 0.6 mm on most modern EID CT scanners. This permits more exquisite visualization of tiny veins draining a CVF, or in some cases, it simply allows better discrimination of a thin contrast column within a vein (Figs 1 and 6). Some previously reported CVFs drain predominantly into the internal epidural venous plexus, and high spatial resolution may be particularly beneficial to evaluate these.¹² Second, PCD CT allows simultaneous spectral and high-spatial-resolution

imaging with decreased noise. While EID-based dual-energy CT scanners can also create VMIs, the spatial resolution and SNR are inferior. One study on EID CT suggested that 50-keV VMIs offer the best SNR.¹³ In our series, monoenergetic reconstructions as low as 40 keV retained acceptable noise while maximizing iodine conspicuity (Figs 1–4). Finally, PCD CT has excellent temporal resolution, with an average scan length of 5.0 seconds in SR mode in this study, though scan lengths are longer in the UHR mode. This high temporal resolution minimizes motion degradation of images and permits sampling of multiple time points during a relatively short interval. While EID CT can achieve similar scan speeds, it cannot simultaneously provide high spatial resolution, and obtaining VMIs with a dual-energy technique usually requires slower scan modes.⁸

Certainly, further study will be needed to definitively determine whether PCD CTM provides superior sensitivity for CVF detection. Nonetheless, we believe the combination of high temporal and spatial resolution, as well as the spectral imaging capabilities allowed by photon energy thresholding, may make PCD CTM more sensitive. While many modalities provide these advantages in isolation, PCD CTM confers all of them in concert.

Our study has limitations, the most noteworthy being its small sample size. Because PCD CT is relatively new in our clinical practices, access to these scanners is limited, and we have been able to offer this examination to only a small number of patients. Further study will be needed once our patient database grows. Additionally, not all 6 patients underwent the exact same myelographic work-up, and there was some variation in precise examination techniques. Although we believe that the superior imaging provided by PCD CT aided in the detection of CVFs in patients 2–6, there are many other factors that influence the conspicuity

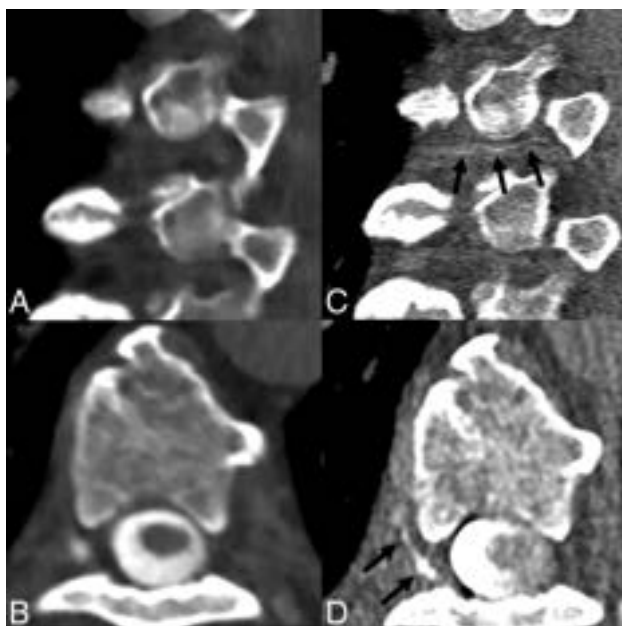


FIG 6. A 65-year-old woman with SIH confirmed by the ICHD-3 criteria, as well as brain MR imaging showing dural enhancement and venous distention (not shown). Sagittal and axial images during decubitus dynamic EID CTM (A and B, 0.625-mm section thickness) show no evidence of a CVF. Subsequent right lateral decubitus PCD CTM (C and D, 0.2-mm section thickness) demonstrates a clear right T6 CVF (C and D, arrows).

of CVFs, such as timing between contrast injection and imaging. CVF conspicuity can fluctuate on the order of seconds, and this fluctuation could confound our findings.¹⁴ There was also variation in the number of scans obtained during each PCD CTM; further study on the temporal characteristics of CVFs will be helpful to determine how many are actually needed. This will help minimize the radiation dose as the examination technique is refined. For reference, the dose for PCD CTM in patients 1–4 was generally higher than the reported doses for dynamic EID CTM in the literature (which, in turn, is higher than reported doses for DSM), likely due to the high number of scans obtained.^{15,16}

As PCD CTM becomes increasingly available, a more consistent imaging protocol can be developed. This will allow prospective and more precise comparison among LDDSM, EID CTM, and PCD CTM. Despite its limitations, our study suggests that PCD CTM has the potential to improve the diagnosis of CVFs, and additional investigation of this technique may prove useful to patients.

ACKNOWLEDGMENT

This work was a collaboration between the Mayo Clinic and Duke Health. The authors acknowledge the support of the Mayo Clinic CT Clinical Innovation Center and Siemens, who owns the

PCD CT system used at the Mayo Clinic. No funding was used for the present study.

Disclosure forms provided by the authors are available with the full text and PDF of this article at www.ajnr.org.

REFERENCES

- Schievink WI, Maya MM, Jean-Pierre S, et al. A classification system of spontaneous spinal CSF leaks. *Neurology* 2016;87:673–79 CrossRef Medline
- Kranz PG, Gray L, Amrhein TJ. Decubitus CT myelography for detecting subtle CSF leaks in spontaneous intracranial hypotension. *AJNR Am J Neuroradiol* 2019;40:754–56 CrossRef Medline
- Mamlouk MD, Ochi RP, Jun P, et al. Decubitus CT myelography for CSF-venous fistulas: a procedural approach. *AJNR Am J Neuroradiol* 2021;42:32–36 CrossRef Medline
- Mark IT, Amans MR, Shah VN, et al. Resisted inspiration: a new technique to aid in the detection of CSF-venous fistulas. *AJNR Am J Neuroradiol* 2022;43:1544–47 CrossRef Medline
- Amrhein TJ, Gray L, Malinzak MD, et al. Respiratory phase affects the conspicuity of CSF-venous fistulas in spontaneous intracranial hypotension. *AJNR Am J Neuroradiol* 2020;41:1754–56 CrossRef Medline
- Madhavan AA, Cutsforth-Gregory JK, Benson JC, et al. Conebeam CT as an adjunct to digital subtraction myelography for detection of CSF-venous fistulas. *AJNR Am J Neuroradiol* 2023;44:347–50 CrossRef Medline
- Leng S, Bruesewitz M, Tao S, et al. Photon-counting detector CT: system design and clinical applications of an emerging technology. *Radiographics* 2019;39:729–43 CrossRef Medline
- Rajendran K, Petersilka M, Henning A, et al. First clinical photon-counting detector CT system: technical evaluation. *Radiology* 2022;303:130–38 CrossRef Medline
- Schwartz FR, Malinzak MD, Amrhein TJ. Photon-counting computed tomography scan of a cerebrospinal fluid venous fistula. *JAMA Neurol* 2022;79:628–29 CrossRef Medline
- Kim DK, Brinjikji W, Morris PP, et al. Lateral decubitus digital subtraction myelography: tips, tricks, and pitfalls. *AJNR Am J Neuroradiol* 2020;41:21–28 CrossRef Medline
- Carlton Jones L, Goadsby PJ. Same-day bilateral decubitus CT myelography for detecting CSF-venous fistulas in spontaneous intracranial hypotension. *AJNR Am J Neuroradiol* 2022;43:645–48 CrossRef Medline
- Kranz PG, Gray L, Malinzak MD, et al. CSF-venous fistulas: anatomy and diagnostic imaging. *AJR Am J Roentgenol* 2021;217:1418–29 CrossRef Medline
- Albrecht MH, Vogl TJ, Martin SS, et al. Review of clinical applications for virtual monoenergetic dual-energy CT. *Radiology* 2019;293:260–71 CrossRef Medline
- Mark I, Madhavan A, Oien M, et al. Temporal characteristics of CSF-venous fistulas on digital subtraction myelography. *AJNR Am J Neuroradiol* 2023;44:492–95 CrossRef Medline
- Mamlouk MD, Shen PY, Dahlin BC. Modified dynamic CT myelography for type 1 and 2 CSF leaks: a procedural approach. *AJNR Am J Neuroradiol* 2023;44:341–46 CrossRef Medline
- Nicholson PJ, Guest WC, van Prooijen M, et al. Digital subtraction myelography is associated with less radiation dose than CT-based techniques. *Clin Neuroradiol* 2021;31:627–31 CrossRef Medline

Conebeam CT as an Additional Tool in Digital Subtraction Myelography for the Detection of Spinal Lateral Dural Tears

N. Lützen, T. Demerath, F. Volz, J. Beck, and H. Urbach

ABSTRACT

SUMMARY: Lateral dural tears as a cause spontaneous intracranial hypotension occur in ~20% of patients. Common imaging modalities for their detection are lateral decubitus digital subtraction myelography or dynamic CT myelography. Reports on the use of conebeam CT are scarce. We show 3 patients in whom the targeted use of conebeam CT during digital subtraction myelography was helpful in confirming the site of the leak.

ABBREVIATIONS: CBCT = conebeam CT; DCTM = dynamic CT myelography; DSM = digital subtraction myelography; SIH = spontaneous intracranial hypotension; SLEC = spinal longitudinal extradural CSF collection

Spontaneous intracranial hypotension (SIH) typically causes orthostatic headaches but can also lead to serious impairment, with coma as the most severe complication.

Patients with SIH who show a spinal longitudinal extradural CSF collection (SLEC) on MR imaging of the spine usually have an underlying ventral (type 1 leak) or lateral dural tear at the site of the nerve root sleeve (type 2 leak); patients negative for SLEC, on the other hand, may have a CSF-venous fistula.¹

Patients positive for SLEC who are suspected of having a lateral dural tear undergo either digital subtraction myelography (DSM), usually in the angiography suite, or dynamic CT myelography (DCTM) with multiple scans with the patient in the lateral decubitus position. Today, there is no consensus on which method is more beneficial for detecting type 2 leaks. The radiation dose has been reported to be 3-fold higher in DCTM² but may provide better spatial coverage and resolution. However, conebeam CT (CBCT) may offer comparable cross-sectional images by flat panel detector in the angiographic suite but was only reported once showing spinal dural tears.³ It seems reasonable to start diagnostics with a less radiation-intensive technique with high temporal resolution such as DSM and supplement it with targeted use of CBCT in the same session to confirm or exclude unclear findings by providing 3D images. This approach combines the best features of the 2 techniques, DSM

and DCTM, potentially resulting in higher spatial resolution and a lower overall radiation dose.

In this brief report, we focus on type 2 leaks only. We demonstrate 3 patients in whom CBCT was helpful in detecting a lateral leak during DSM and discuss all 3 different imaging techniques.

Cases

Case 1. A 47-year-old man was admitted to a local hospital with confusion and personality changes. Bilateral subdural hematomas were detected on cranial CT and surgically treated. Due to the young age of the patient, we performed an MR imaging of the spine, revealing an SLEC. However, MR imaging of the head disclosed only minimal postoperative findings and a Bern SIH score of 1, and the patient could not recall the orthostatic headache.⁴ Because there were suspicious nerve root sleeve diverticula at the L1/2 level on both sides, we performed a DSM on the left and subsequently on the right side, each followed by CBCT (Fig 1). Imaging findings were subtle, most likely due to a slow-flow leak and only visible on CBCT. Intraoperative findings confirmed a lateral dural tear on both sides. After surgical repair, no recurrence of subdural hematomas was noted at the last clinical follow-up at 2 months.

Case 2. A 37-year-old woman presented with typical orthostatic headache. MR imaging of the head from an outside hospital showed a high probability of SIH (Bern SIH score 9), an SLEC on spinal MR imaging, and a suspicious left-sided dorsal dural tear at the T7/8 level on DCTM. An epidural blood patch initially improved symptoms and imaging (Bern SIH score 2), but the SLEC persisted on MR imaging 11 months later. Accordingly, the patient asked for closure of the leak. We repeated imaging with the patient in the left lateral position, but only, the subsequent

Received February 19, 2023; accepted after revision April 6.

From the Departments of Neuroradiology (N.L., T.D., H.U.) and Neurosurgery (F.V., J.B.), Medical Center, University of Freiburg, Faculty of Medicine, Freiburg, Germany.

Please address correspondence to Niklas Lützen, MD, Department of Neuroradiology, University Medical Center Freiburg, Breisacher Str 64, 79106 Freiburg, Germany; e-mail: niklas.luetzen@uniklinik-freiburg.de; @Niklas_Luetzen
<http://dx.doi.org/10.3174/ajnr.A7866>

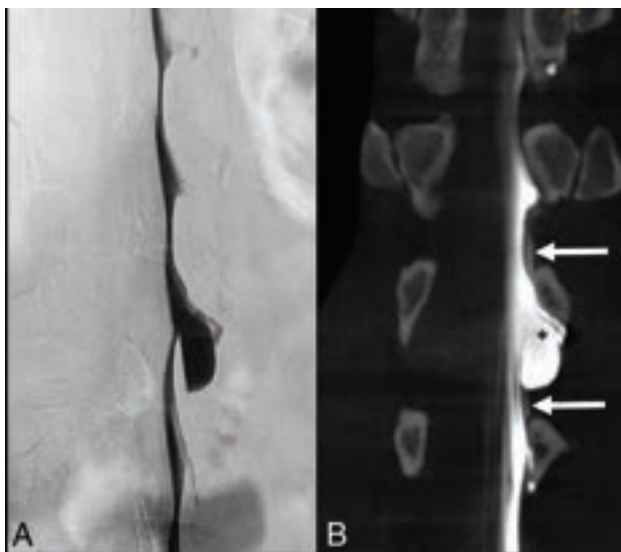


FIG 1. A 47-year-old man with SIH, resulting in bilateral subdural hematomas. DSM with the patient in left lateral decubitus position does not demonstrate a contrast extradural outflow at the level of a suspicious meningeal diverticulum at L1/2 (A). Subsequent CBCT in a coronal reconstruction reveals a subtle extradural contrast collection next to the diverticulum (arrows in B), confirming a slow-flow type 2 leak. The high spatial resolution of CBCT also indicates an accompanying arachnoid outpouching with an interrupted dura (medial-cranial to the *asterisk* in B), appearing like a meningeal diverticulum (later confirmed by surgery). CBCT settings are the following: 3D-(5sDCT Body), 49-cm zoom, 90 kV, 544 mA, 90 images/sec in a 4.83-second runtime (397 total images).

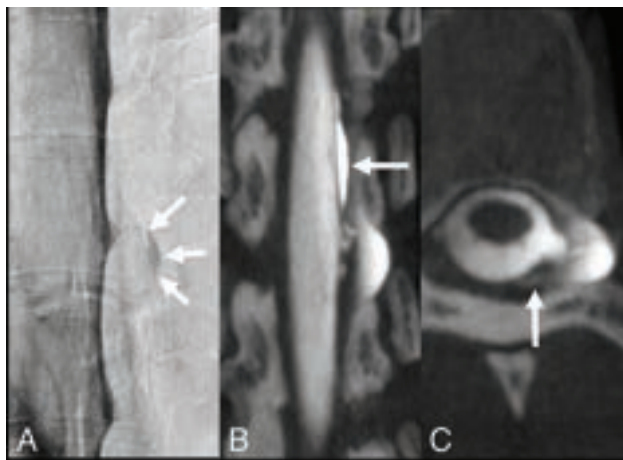


FIG 2. A 37-year-old woman with SIH and a persistent SLEC on MR imaging of the spine months after the epidural blood patch. Anterior-posterior DSM with the patient in the left lateral decubitus position shows a slightly contrast-filled prominent diverticulum at T7/8 (arrows in A) without extradural contrast egress. Coronal CBCT clearly demonstrates an epidural contrast collection (arrow in B) next to the diverticulum. Axial CBCT shows a type 2 leak with more posterior contrast leakage (arrow in C) (caused by encapsulation and neomembranes as reported from the operation), previously not visible on DSM due to superimpositions. CBCT settings are the following: 3D-(4sDCT Body Care), 49-cm zoom, 90 kV, 134 mA, 90 images/sec in 3.53-second runtime (248 total images).

CBCT demonstrated the contrast outflow (Fig 2B, -C), which was most likely superimposed during previous biplane DSM. CBCT suggested that the leak at T7/8 might originate from the nerve root

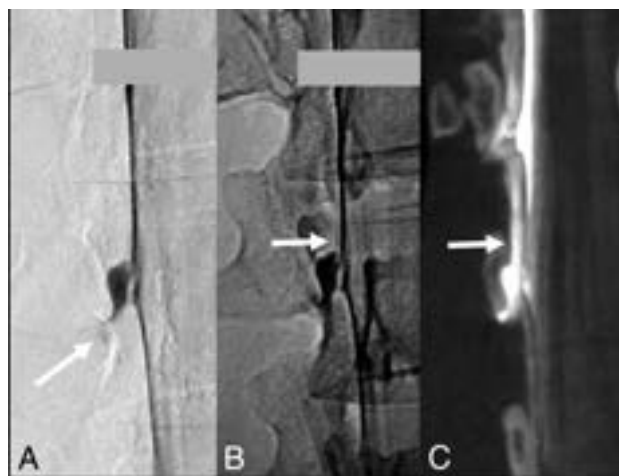


FIG 3. A 26-year-old woman severely impaired by SIH. DSM with the patient in a right lateral decubitus position shows a small but remarkable diverticulum at the L1/2 level. A subtle contrast flickering is visible at the bottom of the diverticulum (arrow in A). Delay single x-ray shows a faint hyperdense line as a questionable indication of extradural contrast outflow (arrow in B). Subsequent CBCT in a coronal reconstruction confirms the findings as a type 2 leak (arrow in C). CBCT settings are the following: 3D-(4sDCT Body Care) 49-cm zoom, 90 kV, 404 mA, 90 images/sec in 3.53-second runtime (248 total images).

sleeve, which was confirmed by surgery. Six weeks later, the Bern SIH score was zero, and the patient had recovered completely at clinical follow-up after 2 months.

Case 3. A 26-year-old woman presented with a variety of symptoms, starting with head and neck pain, later accompanied by dizziness, nausea, and photosensitivity. The Bern SIH score was 7, and spinal MR imaging showed an SLEC. DSM revealed unclear findings next to a suspicious diverticulum (Fig 3A, -B), most likely due to a slow-flow leak. Immediately, supplemented CBCT and subsequent surgery confirmed the lateral leak at L1/2 right side (Fig 3C). The SLEC disappeared on spinal MR imaging 6 weeks after the operation, and symptoms completely resolved after 4 months of clinical follow-up.

MATERIALS AND METHODS

In all patients, DSM and CBCT were performed on a flat panel detector unit (Artis icono biplane; Siemens) with the patients in the lateral decubitus position while awake, with ~10 mL of contrast agent (300 mg iodine/mL). DSM settings in all patients were the following: 60-second run (1 frame per second) with additional fluoroscopy and single x-ray imaging. For DSM, the table was tilted 6°–8° head down, and patients continued shallow breathing. Settings for the CBCT slightly differed among patients and were, therefore, specified in the legend of each figure. For CBCT, the table was returned to horizontal to avoid contrast agent runoff, and patients held their breaths during the CBCT acquisition (4- to 5-second run).

DISCUSSION

In this report, we demonstrate the value of cross-sectional CBCT to detect type 2 leaks in 3 patients. These leaks were not detectable

on DSM, either due to their slow flow or low volume, respectively, or superimposition of the thecal sac.

DSM is a technique comprising series with and without subtraction and may be supplemented by fluoroscopy and single x-rays. The temporal and spatial resolution (0.2 mm) is excellent, and the radiation dose is only one-third of the dose in DCTM.² It allows full control over the intrathecal contrast column (by gradually tilting the table). Downsides are planar rather than cross-sectional images and limited detector coverage. Motion artifacts during DSM may be an issue. However, because type 2 leaks are usually located in the less-breath-dependent lower spine,¹ motion artifacts are often minimized with continuous shallow breathing. As reported previously, this technique is well-suited for high-flow leaks.⁵ In our experience, approximately three-fourths of patients with lateral leaks (in a cohort of 30 patients with type 2 leaks) can definitely be identified by DSM, presenting high-flow leaks. At our institution, further CT scans are performed in the remaining cases (CT following DSM or DCTM another day) to visualize underlying slow flow or leaks previously superimposed at DSM. This procedure is increasingly being replaced by CBCT, as illustrated here.

DCTM has been frequently reported as a diagnostic tool for type 2 leaks.^{6–8} CT is readily available, offers a great advantage with cross-sectional imaging, and is feasible to capture the entire spine. However, temporal and spatial (0.4–0.6 mm) resolution is relatively lower compared with DSM, and the radiation dose is high (often requiring multiple scans).^{2,6} A recent study modified this technique to lower the radiation dose.⁸

CBCT is usually applied to better illustrate complex anatomic vascular structures in 3D. A flat panel detector generates conebeam data sets while the C-arm rotates around the patient, providing highest spatial resolution (up to 0.14 mm) and high contrast resolution.³ In 2013, Chu and McAuliffe³ suggested using CBCT to identify the time point of dural contrast egress for high-volume lateral dural leaks in patients with SIH, because true dynamic examinations were rarely used at this time. Today, the advantage of CBCT may be more to selectively confirm or exclude questionable findings during DSM without delay so that the contrast egress can still be assigned to the actual site of leak (which may not be possible after transporting the patient to the CT scanner). Depending on institutional standards, this information could reduce or omit further CT investigations. The radiation dose of CBCT is assumed to

be comparable with that of conventional CT,⁹ but this assumption has not been evaluated in spinal imaging of patients with SIH so far. Moreover, the high spatial resolution of CBCT may provide additional insight into underlying anatomy. In the future, targeted use of CBCT could also be helpful to detect ventral dural leaks (type 1) with the patient in the prone position by clarifying indeterminate findings during DSM.

CONCLUSIONS

In selected cases with equivocal DSM findings, simultaneous CBCT acquisition may help reveal lateral dural CSF leaks.

Disclosure forms provided by the authors are available with the full text and PDF of this article at www.ajnr.org.

REFERENCES

1. Farb RI, Nicholson PJ, Peng PW, et al. **Spontaneous intracranial hypotension: a systematic imaging approach for CSF leak localization and management based on MRI and digital subtraction myelography.** *AJNR Am J Neuroradiol* 2019;40:745–53 CrossRef Medline
2. Nicholson PJ, Guest WC, van Prooijen M, et al. **Digital subtraction myelography is associated with less radiation dose than CT-based techniques.** *Clin Neuroradiol* 2021;31:627–31 CrossRef Medline
3. Chu E, McAuliffe W. **Use of flat panel DynaCT myelography to locate the site of CSF leak.** *J Med Imaging Radiat Oncol* 2013;57:455–59 CrossRef Medline
4. Dobrocky T, Grunder L, Breiding PS, et al. **Assessing spinal cerebrospinal fluid leaks in spontaneous intracranial hypotension with a scoring system based on brain magnetic resonance imaging findings.** *JAMA Neurol* 2019;76:580–87 CrossRef Medline
5. Piechowiak EI, Pospieszny K, Haeni L, et al. **Role of conventional dynamic myelography for detection of high-flow cerebrospinal fluid leaks.** *Clin Neuroradiol* 2021;31:633–41 CrossRef Medline
6. Dobrocky T, Mosimann PJ, Zibold F, et al. **Cryptogenic cerebrospinal fluid leaks in spontaneous intracranial hypotension: role of dynamic CT myelography.** *Radiology* 2018;289:766–72 CrossRef Medline
7. Madhavan AA, Verdoorn JT, Shlapak DP, et al. **Lateral decubitus dynamic CT myelography for fast cerebrospinal fluid leak localization.** *Neuroradiology* 2022;64:1897–903 CrossRef Medline
8. Mamlouk MD, Shen PY, Dahlin BC. **Modified dynamic CT myelography for type 1 and 2 CSF leaks: a procedural approach.** *AJNR Am J Neuroradiol* 2023;44:341–46 CrossRef Medline
9. Jones AK, Odisio BC. **Comparison of radiation dose and image quality between flat panel computed tomography and multidetector computed tomography in a hybrid CT-angiography suite.** *J Appl Clin Med Phys* 2020;21:121–27 CrossRef Medline

In the article “Surgical or Endovascular Treatment of MCA Aneurysms: An Agreement Study” (Boisseau W, Darsaut TE, Fahed R, et al. *AJNR Am J Neuroradiol* 2022;43:1437–44. 10.3174/ajnr.A7648), Roland Jabre, MD, was accidentally omitted from the author list. His affiliation is the Department of Surgery, Division of Neurosurgery, Center Hospitalier de l’Université de Montréal, Montreal, Québec, Canada.

The authors regret the error.

<http://dx.doi.org/10.3174/ajnr.A7893>